

A Thesis Submitted for the Degree of PhD at the University of Warwick

Permanent WRAP URL:

<http://wrap.warwick.ac.uk/128302>

Copyright and reuse:

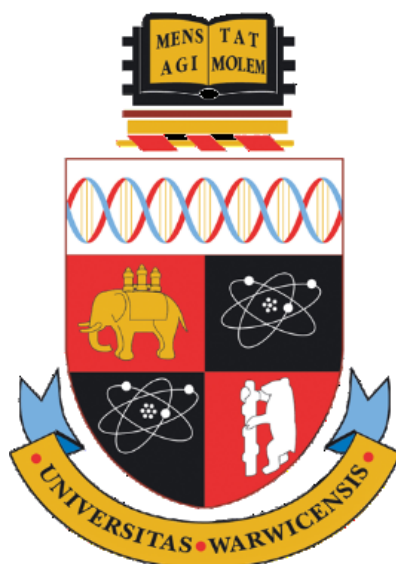
This thesis is made available online and is protected by original copyright.

Please scroll down to view the document itself.

Please refer to the repository record for this item for information to help you to cite it.

Our policy information is available from the repository home page.

For more information, please contact the WRAP Team at: wrap@warwick.ac.uk



Investigating the roles of turnover and mobility in the actomyosin ring of *Schizosaccharomyces pombe*

by

Thomas Harold Cheffings

Thesis

Submitted for the degree of

Doctor of Philosophy in Mathematical Biology and Biophysical Chemistry

MOAC DTC, University of Warwick

September 2018

THE UNIVERSITY OF
WARWICK

Contents

List of figures.....	iv
List of tables.....	vi
Acknowledgements.....	vii
Declarations	ix
Abstract.....	x
List of abbreviations	xi
List of Proteins.....	xii
1. Introduction.....	1
1.1. Cell division and cytokinesis.....	1
1.2. Cytokinesis in bacterial cells	2
1.3. Cytokinesis in plant cells.....	3
1.4. Cytokinesis in other eukaryotes.....	4
1.5. Fission yeast as a model organism: Advantages and disadvantages	5
1.6. Morphology of the fission yeast cell	6
1.7. The fission yeast actin cytoskeleton.....	7
1.7.1. Actin patches.....	8
1.7.2. Actin cables.....	9
1.7.3. Actomyosin ring.....	9
1.8. The actomyosin ring 'life cycle' in <i>S. pombe</i>	10
1.8.1. Division site selection	11
1.8.2. Ring formation	13
1.8.3. Ring dwell/maturation phase	16
1.8.4. Ring contraction	16
1.8.5. Ring disassembly.....	18
1.9. Major components of the contracting actomyosin ring.....	19
1.9.1. Tropomyosin.....	19
1.9.2. Myosin motor proteins	19
1.9.3. Actin nucleators.....	21
1.9.4. Actin crosslinkers	22
1.9.5. Membrane anchors	22
1.9.6. Actin severing/disassembly proteins	23
1.10. Possible mechanisms of actomyosin ring contractility.....	25
1.11. Interplay between actomyosin ring contraction and septation....	30
1.12. Aims, significance, and layout of this thesis.....	32
2. Materials and methods	35
2.1. Fission yeast strains.....	35
2.2. Media used, culturing, and strain saving	38
2.3. Drugs used.....	38
2.4. Yeast genetics (classic and molecular).....	39
2.4.1. Strain construction <i>via</i> mating.....	39
2.4.2. Tetrad dissection.....	39
2.4.3. Free spore analysis.....	40

2.4.4.	Strain construction <i>via</i> transformation of fission yeast cells.....	40
2.4.5.	C-terminal tagging of proteins with fluorophores from Pfa6A vectors	41
2.4.6.	Yeast genomic DNA purification.....	42
2.5.	Molecular cloning	43
2.5.1.	PCR	43
2.5.2.	PCR from genomic DNA.....	43
2.5.3.	Restriction digestion and ligation.....	43
2.5.4.	Purification of PCR product.....	44
2.5.5.	Plasmid extraction.....	44
2.5.6.	Transforming <i>E. coli</i> cells.....	44
2.5.7.	Creation of fission yeast strain with extra copy of <i>imp2</i>	44
2.6.	Yeast cell biology methods	46
2.6.1.	Cell cycle synchronisation.....	46
2.6.2.	Fission Yeast Spheroplasting	47
2.6.3.	Cell fixation and staining with Calcofluor white and DAPI.....	48
2.7.	Microscopy and data analysis.....	48
2.7.1.	Spinning disk microscopy	48
2.7.2.	FRAP procedure (for experiments performed by Anton Kamnev)49	
2.7.3.	Agarose slide preparation	50
2.7.4.	Imaging using the cell suspension method	50
2.7.5.	Imaging using the CellASIC microfluidic system	50
2.7.6.	Image Acquisition	51
2.7.7.	Image processing and quantification	51
2.7.8.	Measuring contraction rate of actomyosin rings	53
2.7.9.	Measuring shortening rates of peeling bundles	53
2.7.10.	Measuring the timing of the first peeling event.....	54
2.7.11.	Comparing LifeAct density in contracting actomyosin rings.....	54
2.7.12.	Measuring myosin-II fluorescence signal in actomyosin rings.....	55
2.7.13.	Fitting of Gaussian mixture models to histograms of peeling event times	55
2.7.14.	Statistical analysis	56
3.	Experimental results and discussion.....	57
3.1.	Investigating the effect of reduced actin turnover in contracting actomyosin rings.....	57
3.2.	Ring peeling is not an artefact of defective ring formation	59
3.3.	Quantification of the ring peeling phenotype	61
3.4.	Timing of peeling events relative to the onset of ring contraction64	
3.5.	Dependence of ring peeling on the individual myosin species in the ring	69
3.6.	Imaging ring peeling using the actin marker LifeAct	72
3.7.	Localisation of other ring proteins in peeling rings	75
3.8.	Model of ring peeling in <i>adf1</i> mutant cells	77
3.9.	Genetic interaction between <i>adf1</i> -M3 and mutations that partially compromise ring anchoring.....	78
3.10.	Attempting to rescue the peeling phenotype by increasing membrane anchoring of the ring	83
3.11.	Effect of <i>adf1</i> mutations on septation	84
3.12.	Attempting to recreate and rescue the ring peeling phenotype through drug treatment of cells.....	86

3.13. Effect of the <i>adf1</i> -M3 mutation on the amount of myosin and actin in the ring	90
3.14. Blocking ring contraction in <i>adf1</i> -M3 cells	94
3.15. Discussion.....	96
3.15.1. Why do we observe different ring peeling behaviour with different mutants/treatments?.....	96
3.15.2. What is the cause of ring peeling in <i>adf1</i> mutant cells?	98
3.15.3. Perturbing actin turnover in other organisms.....	101
4. Ring modelling results and discussion	105
4.1. Description of the original model	105
4.1.1. Extracting tension information from simulation data	112
4.2. Modifying the ring structure and dimensionality.....	113
4.3. Altering the model geometry from flat to cylindrical.....	117
4.4. Making the myosin-actin interactions more realistic	120
4.5. Adding in Myp2 clusters to the ring model	125
4.6. Attempting to more accurately model the structure of the nodes.....	129
4.7. Mathematical description of ring modelling, and lists of ring parameters	135
4.7.1. The original model:	135
4.7.2. Combining myosin clusters and formin dimers into nodes.....	144
4.7.3. Making the simulation 3D (still using flat geometry)	145
4.7.4. Using a 3D cylindrical geometry.....	148
4.7.5. Making the myosin actin interactions more realistic.....	150
4.7.6. Generating heatmaps of ring tension	153
4.7.7. Including Myp2 clusters in the ring simulation	154
4.7.8. Modelling the node structure with increased resolution	158
4.8. Discussion	168
4.8.1. Weaknesses of the original model.....	168
4.8.2. Evidence of ring peeling/tension heterogeneity in our simulations	171
4.8.3. Further limitations of the model, and potential future modifications	172
5. Modelling FRAP recovery curves in the fission yeast ring.....	176
5.1. Mathematical modelling of FRAP recovery.....	179
5.2. Estimating k_{off} and k_{on}	184
5.3. Using the model to calculate the mobile fractions of various ring proteins.....	187
5.4. Discussion	189
6. Conclusions, and future directions	190
7. Bibliography	194
8. Appendix.....	211
8.1. Estimation of observed changes in LAGFP fluorescence from changes in the cellular ratio of [F-actin]:[G-actin]	211

List of figures

Figure 1.1: <i>S. pombe</i> cellular morphology and actin structures.....	8
Figure 1.2: Division site specification in <i>S. pombe</i>	12
Figure 1.3. Mechanisms of actomyosin ring assembly in <i>S. pombe</i>	15
Figure 1.4: Localisation of myosins to the AMR.....	20
Figure 1.5: Mechanisms of actomyosin contractility (<i>in vitro</i>).....	27
Figure 1.6: Mechanisms of actomyosin ring contraction, and its coordination with septation in <i>S. pombe</i>	30
Figure 3.1: Contracting rings in <i>adf1</i> -M2 and <i>adf1</i> -M3 cells display a ring peeling phenotype.....	58
Figure 3.2: Rings in <i>adf1</i> -1 cells also display a ring peeling phenotype.....	60
Figure 3.3: Initial quantification of ring peeling phenotype.....	62
Figure 3.4: Quantification of the timing of peeling events.....	66
Figure 3.5: Ring peeling depends on three Myosin species.....	70
Figure 3.6: Ring peeling depends on three myosin species II.....	73
Figure 3.7: Protein localisation within peeling rings.....	77
Figure 3.8: Genetic interaction between <i>adf1</i> -M3 and <i>pxl1Δ/ΔSH3</i> mutations.....	79
Figure 3.9: Examining ring contraction in <i>adf1</i> -M3 $\Delta SH3$ cells.....	81
Figure 3.10: Attempting to rescue the peeling phenotype by increasing membrane anchoring of the ring.....	83
Figure 3.11: Effect of <i>adf1</i> mutants on septation.....	85
Figure 3.12: Drug treatment of fission yeast cells to recreate the phenotype.....	88
Figure 3.13: Effect of Adf1-M3 on protein levels in contracting rings....	92
Figure 3.14: Effect of blocking ring constriction in Adf1-M3 cells.....	96
Figure 4.1: Diagram of components and forces in original ring model.....	107
Figure 4.2: Making the model 3D, and utilising different geometries..	116
Figure 4.3: Modifying the myosin-actin interactions.....	123
Figure 4.4: Adding in Myp2 clusters.....	128
Figure 4.5: Modelling individual myosin heads within clusters.....	130

Figure 4.6: testing and implementing new model of myosin clusters.	134
Figure 5.1: Preliminary experiments and considerations for analysis of FRAP experiments.....	178
Figure 5.2: Investigating protein turnover within the ring, as a function of AMR age.....	188

List of tables

Table 2.1: Fission yeast strains used in this thesis.	35
Table 4.1: List of parameter values used in the original simulation.	141
Table 4.2: List of temporal parameters used in the original model.	142
Table 4.3: List of parameter values used in 3D flat geometry simulation with nodes.	147
Table 4.4: List of parameter values used in 3D cylindrical geometry simulation with nodes.	149
Table 4.5: List of parameter values used in 3D flat geometry simulation with more realistic node-actin interactions.	151
Table 4.6: List of temporal parameters used in the ring model where node-actin interactions were made to be more realistic.	153
Table 4.7: List of parameter values used in 3D flat geometry simulation with after the inclusion of Myp2 clusters.	156
Table 4.8: List of temporal parameters used in the ring model where Myp2 clusters were included.	157
Table 4.9: List of parameter values used for simulations where we attempted to account for the node microstructure.	167

Acknowledgements

I would first and foremost like to thank my wife, (Dr) Yi-Fang Wang, for her encouragement and advice throughout my PhD, as without this I do not think that I would have made it to the end of my studies.

An equal amount of gratitude must also be extended to my supervisors, Prof. Mohan Balasubramanian and Prof. Nigel Burroughs, for giving me the opportunity to work with them over these past four years, and for their guidance and patience over this time.

I am also very grateful to all other members of the Balasubramanian lab, past and present, for all of their instruction, advice, and friendship during my time here. Whilst every member has contributed to my experience during my PhD, I would like to give a special mention to a few individuals, in no particular order:

- Rebecca Hogg, for her help when I initially entered the lab (with virtually no biology wet-lab experience!), by teaching me the basic methods of yeast cell biology
- Junqi ('Jacky') Huang and Ting Gang Chew, for the many discussions I had with them, their instruction in the use of FIJI/ImageJ for image processing and analysis, and their advice and encouragement
- Anton Kamnev, for his instruction and help with using our microscopes, and for also giving me the opportunity to collaborate with him on his FRAP project
- Tomoyuki Hatano, for his help with some of the molecular genetics work that I performed
- Saravanan Palani, for help with certain protocols, and for contributing a large amount of personality (along with Jacky and Anton, when they were here) to the Balasubramanian lab

Thanks must go to Prof. Ben O'Shaughnessy and his lab, for sharing their simulation code with me, which greatly helped with my attempts to simulate the actomyosin ring. Additionally, I would also like to thank Prof. Thomas Pollard, Prof. Kathleen Gould and Dr. Jim Karagiannis for the gifts of strains and plasmids used for the work presented in this thesis.

I would also like to thank Erick Martins Ratamero for his help with making my MATLAB code run more efficiently.

Thanks must go to my advisory committee members, Rob Cross, Matt Turner, and Till Bretschneider, for their comments and advice during my advisory committee meetings.

Finally, I would like to thank all my friends and family for their support over these years, for which I am very grateful.

Declarations

This thesis is presented in accordance with the regulations for the degree of Doctor of Philosophy at the University of Warwick. This thesis has been written solely by myself, and has not been submitted in any previous application for any degree. The work presented in this thesis is my own, except in the instances where collaborative work was performed, and these instances are clearly noted in figure captions and the main text.

Thomas Cheffings,
12th September 2018

Abstract

In many eukaryotes cytokinesis is facilitated by the contraction of an actomyosin ring. The exact mechanisms that lead to this contractility are unknown, although a number of models posit that actin turnover in the ring is essential. The effect of reduced actin dynamics during ring formation has been well studied in *Schizosaccharomyces pombe*; however the corresponding effects on ring contraction are not well understood.

By using mutants of the fission yeast actin severing protein Adf1, we observed that contracting actomyosin rings display a 'peeling' phenotype. In these cells bundles of actin and myosin peel off from one side of the ring, and are then pulled across to the opposite side, which typically occurs 3 times during cytokinesis. We also found that this phenotype is dependant on the activity of the three myosin species present in the ring.

We hypothesise that reduced actin turnover leads to a non-uniform distribution of tension around the ring, which causes regions of higher tension to peel off. This model predicts that *adf1* mutant cells might be sensitive to additional mutations that compromise membrane anchoring of the ring, and that the tension imbalance could lead to non-uniform septum ingression during cytokinesis. Subsequent experiments confirmed these predictions, which further supported our model.

We also attempted to recreate the phenotype *in silico*, by adapting a previously used mathematical model of the actomyosin ring. However, in doing so we encountered a number of problems, as we realised that certain parts of the model were unrealistic, and attempting to fix these aspects introduced new problems. As a result of this, we were unable to achieve this goal in the available timeframe.

Finally, we also used mathematical modelling to analyse FRAP experiments, to more accurately extract information on the mobile fractions of ring proteins from FRAP recovery curves. Application of this method enabled the identification of interesting behaviour from the membrane anchoring protein Cdc15, potentially linking its mobility to its function in the ring.

List of abbreviations

ADF – Actin depolymerising factor
AIC - Akaike information criterion
AMR – Actomyosin ring
CDF – Cumulative distribution function
CHD – Calponin homology domain (actin binding domain)
CS – Cold sensitive
CW – Calcofluor White (cell wall stain in *S. pombe*)
DAPI – 4', 6-diamidino-2-phenylindole (nuclear envelope stain in *S. pombe*)
ddH₂O – double distilled water
DMSO – Dimethyl sulfoxide
ELN – Extra low nitrogen
F-BAR – FCH (Fer and CIP4 Homology) and BAR (Bin1 Amphiphysin Rvs161/167p)
FRAP – Fluorescence recovery after photobleaching
GMM – Gaussian mixture model
IQGAP – IQ domain-containing GTPase activating protein
Lat A – Latrunculin A (actin polymerisation inhibiting drug)
LAGFP – LifeAct-GFP
mNG – mNeonGreen
OD – Optical density
PBS – Phosphate-buffered saline
RCF – Relative centrifugal force
ROI – Region of interest
SCPR – Search, capture, pull and release
SIN – Septation initiation network
SPB – Spindle pole body
tdT – tdTomato
TS – Temperature sensitive
WT – Wild type
YEA – Yeast extract with adenine

List of Proteins

This section provides a reference for proteins that are specifically discussed in the results sections. Proteins that are only discussed in the introduction are not included.

Protein name (<i>S. pombe</i>)	Generic name	Function
Act1	Actin	Forms filamentous actin (F-actin), which is vital for a range of cellular processes, particularly cytokinesis
Adf1	Cofilin/ADF	Actin severing and depolymerising protein. Essential for actin turnover in the cell – the AMR is unable to form when Adf1 is absent or inactive
Ain1	α -actinin	Actin crosslinking protein that localises to the AMR. Contains one CHD (calponin homology domain), and dimerises <i>in vivo</i>
Bgs1	β -glucan synthase	Synthesises the primary septum as the AMR contracts. AMR contraction/septation is blocked when it is absent or inactive.
Blt1	-	Present in nodes from early interphase, and the AMR until the completion of ring contraction. Interacts with Cdc15, but is also important for recruiting signalling proteins necessary for the progression of the cell through cytokinesis.
Cdc12	Formin	Nucleates actin filaments for the AMR in <i>S. pombe</i> .
Cdc15	-	Scaffolding and membrane anchoring protein in <i>S. pombe</i> AMR. Membrane anchoring is mediated by its F-BAR domain, and the protein also contains an SH3 domain which mediates interactions with the rest of the ring.
Clp1	Cdc14 related phosphatase	Phosphatase important for the progression of <i>S. pombe</i> cells through cytokinesis. Is believed to de-phosphorylate Cdc15, which ‘opens up’ the protein, and allows its SH3 domains to bind to other proteins.
Cyk3	Nebulin	Contains an SH3 domain, and interacts with the SH3 domains of Imp2 and Cdc15, a process which is likely mediated by additional proteins. Its exact function remains unclear.
Fim1	Fimbrin	Actin binding protein with a CHD. Unlike Ain1, mainly localises to actin patches, with much weaker localisation detected in the AMR.
Imp2	-	Similar to Cdc15 in terms of structure, and believed to fulfil similar functions. Unlike Cdc15, Imp2 only joins the ring after it is fully formed.
Myo2	Type II myosin	Essential type II myosin in <i>S. pombe</i> . Present in the AMR from formation until the end of contraction. Essential for ring formation, and

		believed to contribute most of the tension for ring contraction.
Myo51	Type V myosin	Involved in ring formation, by transporting nonmedially nucleated filaments to the division site, and helping to align them with the ring. Not believed to be important for ring contraction.
Myp2	Type II myosin	Non-essential type II myosin. Joins the AMR immediately prior to the onset of ring contraction. May help with tension generation in contracting rings, but exact function is not known.
Nda3	Beta tubulin	Subunit of microtubules. The cold sensitive mutant Nda3-KM311 prevents the formation of microtubules, which prevents cells entering anaphase, and is useful for generating large numbers of cells with AMRs.
Pxl1	Paxillin	LIM domain containing protein, localises to the ring before the onset of contraction, and plays a role in stabilising the ring by binding to the SH3 domains of Cdc15 and Imp2, and linking to other ring components.
Rgf3	RhoGEF (Guanine nucleotide exchange factor)	Rgf3 is a positive regulator of Rho1, the <i>S. pombe</i> homolog of RhoA. Rho1 is involved in regulating cell wall biosynthesis during cytokinesis.
Rlc1	Myosin II regulatory light chain	The regulatory light chain of both Myo2 and Myp2. Commonly used as a ring marker in fluorescence microscopy experiments by tagging with fluorescent proteins.
Rng2	IQGAP	Essential ring protein which acts as a scaffold for other ring components during ring formation. Contains a number of domains, including IQ domain, CHD, and rasGAP (GTPase activating protein), so the protein likely has a number of roles.
Spg1	-	Septum promoting GTPase, and an important protein in controlling the onset of septation in <i>S. pombe</i> (part of the SIN).

1. Introduction

1.1. Cell division and cytokinesis

One of the fundamental traits of all living organisms is the ability to reproduce, as this is necessary for the growth and continued evolution of a given species. At the cellular level, reproduction is facilitated by the process of cell division, which can be either mitotic or meiotic, depending on the type of cell involved. However, rather than being a single process, cell division consists of a series of individual events, each of which is tightly regulated both temporally and spatially, in order to ensure that they occur at the right time and place within the cell, and in the correct sequence. Although there are a wide variety of mechanisms employed to complete these tasks in different organisms [1–6], there are nonetheless a number of fundamental similarities in these processes that are shared across many domains of life (with viruses being a notable exception).

In mitotic cell division, the mother cell must first undergo DNA replication, so that each daughter cell can receive a full copy of the mother's genome. Subsequently, the mother cell must then segregate the two copies of the genome, and position them so that one copy will be located in each of the nascent daughter cells, a process known as mitosis or karyokinesis. The final stage of cell division is then the physical separation of the two daughter cells, by deposition of new membrane material (and possibly new cell wall material, depending on the organism) between the two sets of segregated DNA.

This last stage of cell division is referred to as cytokinesis, and this requires the prior assembly of a division apparatus at the division site, which then facilitates the partitioning of the mother cell into the two daughter cells [4]. Improper cytokinesis can lead to an incorrect distribution of chromosomes between daughter cells, and this can subsequently lead to tumorigenesis in human or animal cells [7–11]. Therefore, studying cytokinesis will hopefully improve our

understanding of how cells become cancerous, and potentially lead to new treatments. Additionally, it is hoped that studying cytokinesis in bacterial cells can lead to new antimicrobial drugs that specifically target the cytokinetic machinery [12,13], which would help combat the rising problem of antibiotic resistance.

As would be expected, the composition of this division apparatus, and the mechanisms that it employs to divide the mother cell, vary significantly across the different domains and kingdoms of life [4], and we shall highlight some of these different mechanisms below.

1.2. Cytokinesis in bacterial cells

In many bacterial cells, the division apparatus consists of a ring-shaped structure that is positioned at the division site, which is believed to contract concomitantly with cell wall synthesis, leading to the successful division of the cell [2]. This is commonly referred to as the Z-ring, and it is composed of a large number of ~125 nm long protofilaments of the bacterial tubulin homolog FtsZ, which interact with membrane-bound proteins at the division site such as ZipA and FtsA [14].

How this Z-ring generates contractile force remains poorly understood, as traditional force-generating proteins such as kinesins and dyneins have not been identified in any bacterial species. However, a number of *in vitro* experiments performed with FtsZ confined within liposomes suggest that FtsZ alone may be sufficient to generate the contractile force within Z-rings [15,16]. One proposed explanation for this is that the energy from GTP hydrolysis within FtsZ polymers promotes bending of the protofilaments, leading to the generation of an inwards force [14]. Others have suggested that increased affinity for bundling between FtsZ polymers can lead to condensation, and therefore contraction, of the Z ring [17,18]. It has also been suggested that, *in vivo*, Z-ring contraction is not the principle force generator for cytokinesis, with the process of septum synthesis taking this role, while the Z-ring simply acts as a scaffold for the septum synthesis machinery [19]. A

mixture of further modelling and experimental work will be necessary to determine exactly how the Z-ring leads to successful division within bacterial cells.

1.3. Cytokinesis in plant cells

Unlike bacteria, plant cells belong to the eukaryotic domain of life, which, among other things, means that they contain the eukaryotic tubulin and actin proteins, rather than their prokaryotic variants, as well as the myosin, kinesin, and dynein motor proteins, which interact with these cytoskeletal filaments. However, they do not contain type II myosins [20], which only evolved in the common ancestor of metazoan, fungal, and amoeboid cells. For this reason, cytokinesis in plant cells is vastly different from other, type II myosin-containing eukaryotes: In fungi, amoeba, and metazoans, cytokinesis is completed by the construction of a cell-cell barrier that originates at the plasma membrane, and which is grown centripetally inwards (section 1.4), a process which also takes place in bacterial cells. However, in plant cells, the opposite approach is taken, with the cell-cell barrier originating from the centre of the division plane, and growing outwards until it merges with the plasma membrane [21,22]. This is facilitated by a structure called the phragmoplast, which is formed from the mitotic spindle at the end of anaphase, and serves as a track for the directed trafficking of vesicles to the phragmoplast midzone, where construction of the new cell-cell barrier occurs [22]. This cell-cell barrier is called the cell plate, and as it expands outwards the phragmoplast microtubules are also pushed outwards, ensuring that vesicles are continually transported to the outermost region of the growing cell plate, where they are most needed. As the cell plate grows it eventually merges with the plasma membrane, after which the phragmoplast disappears, and the separation of the two daughter cells is complete, although subsequent maturation of the cell plate into a stiff cell wall structure is also necessary [21,22].

1.4. Cytokinesis in other eukaryotes

In terms of their cytokinetic behaviour, all other eukaryotic cells can (for the purposes of this thesis) be broadly divided into two main categories: Those that contain genes encoding type II myosins, and those that do not. This latter group includes organisms belonging to the genera *Giardia* and *Trypanosoma*, among others. Not much is known about how these organisms complete cytokinesis, although in general it is believed to be tubulin dependent and largely actin independent [23,24]. In *Giardia*, it is thought that flagella-based forces initiate the separation of the daughter cells, and help to coordinate membrane trafficking to the furrow [24]. In *T. brucei* cells, cytokinesis is more complex, requiring large-scale morphological remodelling of the mother cell, however actin is believed to play a minimal role in this, with these processes dependent on remodelling of the microtubule cytoskeleton [23].

In eukaryotic species that evolved from a myosin II containing ancestor, specifically fungi, amoeba, and metazoa, normal cytokinesis is dependent on both actin and type II myosin, which form a contractile ring structure at the division site, called the actomyosin ring [1,25]. While actin and myosin are its namesake constituents, there are a range of other proteins which also play an important role in actomyosin ring function, including, but not limited to, actin nucleators, actin crosslinkers, actin severing proteins, actin capping proteins, membrane anchoring proteins, and various phosphatases and kinases that regulate the function of all of these proteins [25]. Most, if not all, of these proteins are present in the actomyosin ring of every organism which uses this structure, and considering the diversity of the organisms that this entails, and the diversity of the mechanisms that are employed by the other organisms that we have discussed, this is a remarkable level of conservation [25]. Therefore, it is likely that the mechanisms which facilitate the formation and contraction of this actomyosin ring are also conserved across these organisms.

Because of this conservation, much of the work that has been performed on actomyosin-based cytokinesis has focused on a relatively small number of model organisms. These include the budding yeast *Saccharomyces cerevisiae* [26], the fission yeast *Schizosaccharomyces pombe* [1,25], the slime mould *Dictyostelium discoideum* [27], embryos of the nematode *Caenorhabditis elegans* [28], and cultured mammalian cells such as HeLa cells and COS-7 cells [3].

1.5. Fission yeast as a model organism: Advantages and disadvantages

Of particular importance for this thesis is the fission yeast *S. pombe*. Like the other organisms listed above, the vast majority of cytokinesis genes present in human cells are also present in *S. pombe* [25]. However, fission yeast cells also have a number of advantages over more complex cell types when it comes to the study of actomyosin based cytokinesis (hereafter just referred to as *cytokinesis*). Firstly, fission yeast cells are very amenable to genetic manipulation, and their haploid genome facilitates the relatively easy generation of mutant strains, and the subsequent phenotypic analysis of these mutations, when compared to diploid cell types. The high growth rate of fission yeast cells is also an advantage, as this speeds up the process of generating new strains, and therefore the rate at which new experiments can be performed. Fission yeast cells are also well suited for fluorescence microscopy-based analysis, in part due to the ease with which proteins can be fluorescently labelled, but also because the cells are non-motile, and their cellular morphology (rod shaped) tends to ensure that always they lie flat against the coverslip, with their actomyosin ring perpendicular to the imaging plane, which can greatly simplify image quantification.

However, perhaps the main advantage of fission yeast is that, before it was first used to study cytokinesis, it was already well established as a model organism for studying cell cycle regulation [29]. As such, many of the techniques employed for its genetic and biochemical

analysis had already been developed and optimised, and because of the close links between cell cycle regulation and cytokinesis, many of the available mutated genes also had overlapping roles in cytokinesis as well as cell cycle regulation.

There are also a number of disadvantages with using *S. pombe* as a model organism for cytokinesis. For a start, it is quite evolutionarily distant from human cells, with one billion years of divergence since their common ancestor, which will have inevitably lead to some differences between these cells [25,30]. Perhaps the most obvious of these is the presence of a cell wall, and a correspondingly high internal turgor pressure, in *S. pombe* [31]. This complicates the process of actomyosin ring contraction, because the ring cannot contract in the absence of cell wall synthesis [32], which is a process that does not occur in mammalian cytokinesis. Additionally, fission yeast cells undergo a closed mitosis, where the mitotic spindle is formed inside the nucleus, whilst metazoan cells undergo an open mitosis, allowing the position of the mitotic spindle to directly regulate the position of the actomyosin ring [3]. Furthermore, the relatively small size of fission yeast cells can make it difficult to discern different structures/regions in the cell when using fluorescence microscopy. However, this is less of a problem nowadays, due to the improved resolution of modern microscopes, and the increasing usage of super-resolution techniques such as STORM and 3D-SIM [33].

Overall, *S. pombe* has proven to be an invaluable model organism for the purpose of cytokinesis research, and its use has led to the most complete inventory of cytokinesis genes in any organism [25], as well as the development of some of the first molecularly explicit mathematical models for the processes of ring formation [34] and ring contraction [35].

1.6. Morphology of the fission yeast cell

The shape of a fission yeast cell is, to a good approximation, cylindrical, with a hemispherical cap at each end, and with a diameter of around 4

μm in wild type (WT) cells (Figure 1.1). The length of a cell depends upon the time since its last division, with new daughter cells having an end-to-end length of around 7 μm . New daughter cells only grow through addition of cell wall material at the cell-tip that was present in the mother cell, referred to as the old end. However, during G2 phase, a transition from monopolar to bipolar growth occurs, leading to subsequent cell growth at both ends. When the cells reach a length of around 14 μm they are ready to enter mitosis, and all cell growth ceases. The subsequent division then cleaves the cell in half, once again generating two daughter cells with a length of 7 μm each (Figure 1.1).

1.7. The fission yeast actin cytoskeleton

There are three F-actin structures in fission yeast: Actin patches, actin cables, and the actomyosin ring (Figure 1.1) [36]. These differ from each other in a number of ways, including their localisation, their nucleators, the length of actin filaments within these structures, and their overall function within the cell. All three of these undergo continuous turnover, with disassembly of old filaments and nucleation and polymerisation of new filaments [37]. Each of these structures competes for the limited G-actin pool in the cell (although the actomyosin ring is obviously only present during mitosis and cytokinesis) [38,39].

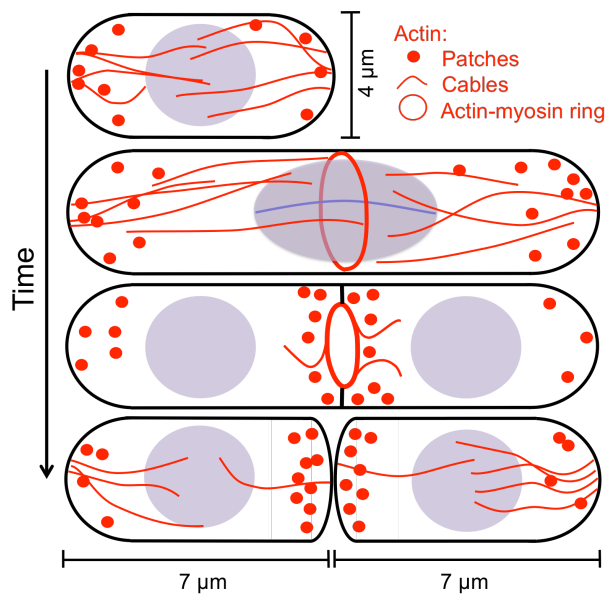


Figure 1.1: *S. pombe* cellular morphology and actin structures

Diagram of the morphology of a fission yeast cell throughout the cell cycle. The various actin structures within the cell are also depicted (purple circle/oval is the nucleus).

1.7.1. Actin patches

Actin patches are the most abundant actin structure during interphase, and are also the brightest when actin is observed through fluorescence microscopy [36]. Patches are involved in endocytosis, and tend to form at the tips of interphase *S. pombe* cells, and around the division site in mitotic cells (Figure 1.1) [36]. They are principally nucleated by the Arp2/3 complex [40], which forms a branched network of actin filaments, with lengths of around 100 to 200 nm [41]. Actin patches are very dynamic structures, undergoing continuous assembly and disassembly, and with typical lifetimes of around 10 – 20s [36]. Actin patches are an essential cellular structure, as endocytotic internalisation in yeast cells depends entirely on the presence of actin filaments nucleated by the Arp2/3 complex [42].

1.7.2. Actin cables

Actin cables are the other F-actin structure that is present in interphase cells, and these aid in intracellular cargo transport by providing a track for the type V myosin Myo52 [43]. A single actin cable actually consists of multiple individual actin filaments, crosslinked into a bundle that extends from the cell tip towards the nucleus in the centre (Figure 1.1) [36], with an overall length of between 3 to 7 μm , depending on the length of the cell. Cables are nucleated from the cell tips by the formin For3 [44], which is part of the polarisome at the cell tips. Cables are less abundant than patches, and are not as easily observed by fluorescence microscopy [44], which makes studying their behaviour more difficult. Actin cables are a non-essential structure, as *for3 Δ* cells are viable, and actin cables are not observed within these cells, although *for3 Δ* cells do exhibit some minor morphological defects compared to WT cells [44].

1.7.3. Actomyosin ring

The final actin structure in fission yeast is the actomyosin ring (AMR), which is believed to be responsible for generating the contractile force that drives cell division during cytokinesis [1]. There are different estimates of the number and length of actin filaments found within the ring, with one paper reporting that there are between 1000 – 2000 filaments present, with average lengths of around 0.6 μm , although the number of rings observed in this study was very low [45]. More recent work has suggested that there are actually around 300 filaments, with average lengths of approximately 0.9 μm [46]. Actin filaments in the AMR are primarily nucleated by the formin Cdc12 [47]. Additionally, For3 also localises to the ring, where it most likely also contributes to maintaining actin in the ring [44]. However, its role is minor, as *for3 Δ* cells were not observed to display any specific cytokinesis defects, while *cdc12* is an essential gene, and in its absence the AMR cannot form [44,48].

The AMR begins to form near the end of G2 phase, with the recruitment of various ring proteins to a series of nodes localised around the cell middle [49,50], and its construction is completed during anaphase. The ring then maintains a constant radius until the end of anaphase, at which point ring contraction begins, and the mother cell is physically cleaved into two daughter cells (Figure 1.1).

At the beginning of this introductory chapter, we stated that reproduction (i.e. replication of the mother cell's DNA, and then the repackaging of this DNA into separate daughter cells) is one of the essential traits of living organisms. Therefore, it is not surprising that the AMR is an essential structure, since without it cell division cannot occur, and *S. pombe* cells are subsequently unable to reproduce. Furthermore, the ring must also be contractile in order to fulfil its function, as shown by experiments using *S. pombe* cells expressing an actin translocation mutant of their essential type II myosin. These cells were still able to form an AMR, but in the absence of their non-essential type II myosin they were unable to divide, because the AMRs that they formed were non-contractile [51].

1.8. The actomyosin ring 'life cycle' in *S. pombe*

The AMR is a transient structure (although less so than individual actin cables and patches), and its life cycle can be divided into four main stages: specification of the division site, ring assembly, ring contraction, and ring disassembly. Because ring assembly in *S. pombe* is completed before the end of anaphase, there is also a dwell/maturation phase, where the ring is fully formed, but is waiting for the completion of anaphase before it starts to contract. We shall discuss each of these stages below.

1.8.1. Division site selection

In *S. pombe*, the future division site is specified by the location of a set of cortical puncta, called nodes. These form around the division plane in the cell middle [52], and after the transition from G2 to Mitosis has been triggered, these gradually accumulate contractile ring proteins until the start of anaphase, at which point they subsequently condense to form the AMR [52].

A particularly important node protein for division site specification and ring formation in WT cells is the anillin Mid1, and at the onset of mitosis two distinct populations of Mid1p use independent but complementary mechanisms to specify the division site [25]. One population of Mid1 is present in the nodes, where it co-localises with the SAD-like kinase Cdr2 [52]. Cortical protein gradients of the DYRK kinase Pom1, which emanate from the cell tips, have been proposed to inhibit the formation of these Cdr2-containing nodes until the cell reaches either a certain length (14 μm) or surface area (it is not yet certain exactly which mechanism is employed by cells [53–55]). At this point the concentration of Cdr2 in nodes at the cell middle is thought to be high enough to trigger the onset of mitosis, by inhibiting the G2/M kinase Wee1p [53,54]. This process leads to the formation of Mid1 nodes on the inner edge of the plasma membrane, around the cell middle (Figure 1.2A).

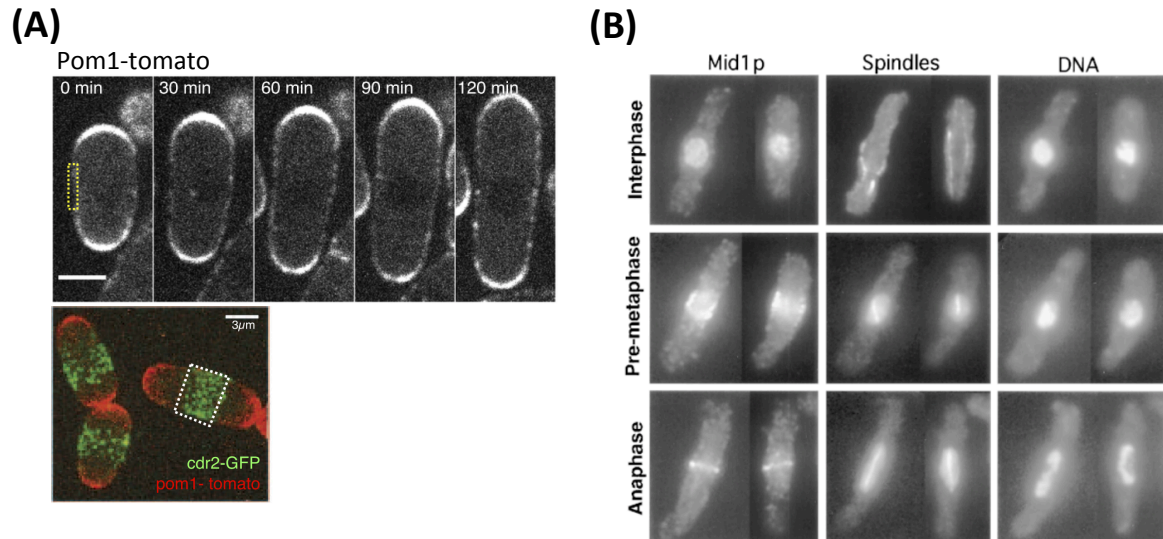


Figure 1.2: Division site specification in *S. pombe*

- (A) Fluorescence images showing how Pom1 inhibits the formation of interphase nodes, containing Cdr2, away from the cell middle, helping to specify the future division site (adapted from Pan, *et al*, 2014).
- (B) Immunofluorescence images of *S. pombe* cells, showing how Mid1 is released from the nucleus as the cell enters mitosis (adapted from Bähler, *et al*, 1998).

The second interphase population of Mid1 is localised to the nucleus. Directly before the onset of mitosis this Mid1 pool is released into the cytoplasm by the Polo kinase Plo1, and subsequently diffuses to the plasma membrane (Figure 1.2B) [56]. Because the nucleus is held in the middle of the cell by interphase microtubules, this means that the nuclear Mid1 is more likely to diffuse to the medial membrane, rather than towards the cell tips (where node formation is inhibited anyway by a tip occlusion mechanism, as described in the following paragraph). So, whilst microtubules are not directly responsible for specifying the division site, as is seen in metazoan cells, they are nonetheless indirectly involved by controlling the position of the nucleus [57]. The combination of these two mechanisms ensures that the future ring is correctly positioned to divide the mother cell into two equal-sized daughters.

While Mid1 is an important protein for division site specification and ring formation, rings can form in its absence, although there does not appear to be a way to specifically target these to the cell middle [58,59]. However, in *mid1Δ* cells it is still necessary to prevent the ring from

forming across the cell tips, as its subsequent contraction would lead to incorrect segregation of genetic material between the two daughter cells, and cause problems with polarised growth of the daughter cells. Because of this, there is a third, Mid1-independent mechanism, which acts as a failsafe to ensure that the division septum cannot form at the very tips of the cell. A tip complex, consisting of Tea1, Tea4 and Pom1, inhibits division septum assembly in these regions, possibly by regulating the F-BAR protein Cdc15 [60,61]. As a result of this, while this Tea1/Tea4/Pom1 complex is not required for viability in normal cells, it becomes essential for cells in which the Mid1 pathway is also compromised [61].

1.8.2. Ring formation

After the arrival of Mid1p, the nodes gradually mature into cytokinesis nodes by accumulating a number of key ring proteins. The first components to arrive after Mid1p are the myosin essential light chain Cdc4 and the IQ domain-containing GTPase activating protein (IQGAP) Rng2 [49,62]. Rng2 is necessary for the subsequent recruitment of the myosin-II heavy chain and regulatory light chain, Myo2 and Rlc1, respectively, and later acts as the connection between Mid1p and the ring [62,63]. Mid1 then recruits the F-BAR (membrane binding domain) protein Cdc15, before node maturation is completed by the arrival of the formin Cdc12 [49], recruited by both Cdc15 and the Rng2-Myo2 module [62]. As well as being the last to arrive, Cdc12 is also the least abundant node protein, with each node thought to only contain an average of one Cdc12 dimer [64,65].

After the arrival of Cdc12, it is thought that the nodes condense into a ring through a mechanism called search, capture, pull and release (SCPR) [34]. According to this model, once the nodes have fully matured, Cdc12 begins nucleating actin filaments in random directions from each node. If these filaments pass within a certain distance of another node, they can be captured by the myosin in the second node. The myosin then

walks along the captured filament, towards the filament's barbed end, which is anchored in the first node by Cdc12. This will cause the two nodes to move towards each other, and across the entire network this process will lead to an overall condensation of the nodes (Figure 1.3) [34,50]. Crucially, captured and un-captured filaments are also stochastically severed (the 'release' step) by the cofilin Adf1, to allow for the nucleation of new filaments: both experiments and computer modelling show that without this step the nodes aggregate into clumps, rather than forming a uniform ring [34,66]. It is thought that the continuous removal of existing connections between nodes, and the formation of new connections, helps to ensure uniform node condensation by counteracting the effect of local density variations, which would otherwise lead to node clumping in regions of higher density [67].

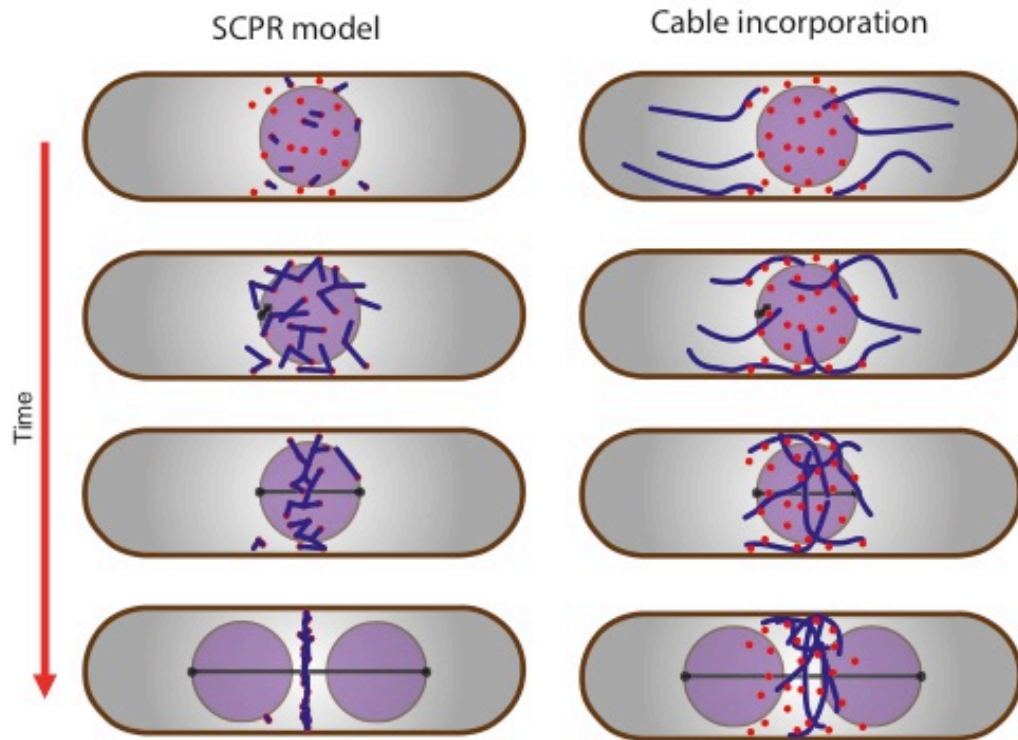


Figure 1.3. Mechanisms of actomyosin ring assembly in *S. pombe*.

Diagram of the two main pathways of ring formation in WT cells, depicting the SCPR mechanism, and the incorporation of nonmedially nucleated actin cables (red spots are nodes, blue lines are actin cables, and black line is the mitotic spindle. Adapted from Cheffings, *et al*, 2016).

It has also been observed that actin cables, which are nucleated away from the cell middle by Cdc12 ‘speckles’ (individual dimers) [68] can be transported to the site of ring formation (Figure 1.3) [69]. These can then incorporate directly into the contractile ring, although cofilin-dependent disassembly sometimes takes place beforehand, severing the filaments as they reach the cell middle [69]. In most cases, accumulation of actin cables at the cell middle seems to precede the arrival of Cdc12 to the nodes [69]. In a minority of cases, de novo nucleation of filaments by the nodal Cdc12 commenced before the incorporation of non-medially-nucleated cables [69], suggesting that both mechanisms operate during cytokinesis in WT cells, offering a level of redundancy that helps to reinforce the mechanisms of ring formation. However, there is no evidence that non-medially-nucleated cables are able to reliably form a contractile ring in the absence of de novo nucleation [70]. Instead, it has been suggested that these cables play a role in helping to form a compact

actin ring [71]. This mechanism of pre-existing actin cables being transported to the division site is reminiscent of ring formation in metazoan cells [72,73], indicating that the behaviour in *S. pombe* might reflect a less robust ancestral mechanism that was subsequently fine-tuned in metazoan cells.

1.8.3. Ring dwell/maturation phase

The process of ring formation is usually completed about 10 - 20 minutes before the end of anaphase [49]. Therefore, once the ring has been formed it does not start to contract immediately, but instead remains at the cell middle, and waits for the end of anaphase, at which point contraction is triggered by activation of the SIN pathway (see section 1.8.4) [59].

During this dwell time, a number of proteins enter and exit the ring. Notably, Mid1 exits the ring, with Cdc15 taking over its role of membrane anchoring [74], while the non-essential type II myosin Myp2 and the F-BAR domain containing protein Imp2 enter the ring [49,75]. Additionally, the paxillin-related protein Pxl1 and C2 domain containing protein Fic1 join the ring [75,76], and help to stabilise it by linking ring components to the SH3 domains of Cdc15 and Imp2 [75]. Directly adjacent to the ring, the anillin-like protein Mid2 and four species of septin proteins polymerise to form a double ring that flanks the AMR, and which remains until after ring contraction is finished [77,78].

1.8.4. Ring contraction

After the AMR has formed, and anaphase is completed, the ring must contract centripetally inwards, in order to physically divide the mother cell. In *S. pombe*, the signal to initiate ring contraction emanates from the spindle pole bodies (SPBs, the yeast equivalent of the centrosomes), from a cascade of protein kinases known as the Septation initiation network (SIN) pathway [59,79]. Without proper SIN signalling, ring contraction

does not occur, although rings are still able to form [58,59,80]. Conversely, when SIN activity is artificially induced, this leads to ring assembly (through a Mid1-independent pathway [59]) and contraction during any phase of the cell cycle, even interphase [81,82]. Despite the importance of SIN signalling for maintenance and contraction of the AMR, the exact protein targets for many of these processes remain unknown [82].

One important ring protein that is regulated by SIN signalling is the FCH (Fer and CIP4 homolgy) and BAR (Bin1 Amphiphysin Rvs161) (F-BAR) and SH3 domain containing protein Cdc15 [83,84]. Before ring formation, it exists in a hyperphosphorylated state, however as mitosis progresses it becomes progressively dephosphorylated [83,85,86]. At the end of anaphase, and directly before the onset of ring contraction, Cdc15 is completely dephosphorylated, which is believed to 'open up' the protein, allowing its SH3 domains to interact with other ring proteins, and enabling Cdc15 to act as a scaffold [83]. Cdc15 dephosphorylation is believed to be a result of Clp1 phosphatase activity [86], which is the fission yeast homolog of the Cdc14 phosphatase, and is a downstream component of the SIN pathway [74,86]. In *clp1Δ* cells, Cdc15 remains partially phosphorylated at the onset of ring contraction, which only leads to minor cytokinesis defects, but also predisposes the cells to negative genetic interactions with other mutations that affect ring contraction [80].

Because *S. pombe* is a fungus, and its cells are surrounded by a cell wall, ring contraction must also be accompanied by the synthesis of new cell wall material between the two daughter cells [32,87]. This process is referred to as septation, and requires the localisation of a number of septum synthesis proteins to the division site, which is also dependent on SIN signalling [88]. When septation is blocked, the AMR is unable to contract, as can be seen from conditional mutants of the primary septum synthesis protein Bgs1 [32]. When fully formed AMRs are disassembled, e.g. by treating cells with drugs that block actin polymerisation, then septation does not occur in a robust manner, leading to cytokinesis

failure in the majority of cases [89,90]. Therefore, both ring contraction and septation are necessary processes for successful completion of cytokinesis in *S. pombe*, with each unable to occur in the absence of the other.

1.8.5. Ring disassembly

The process of ring disassembly is concurrent with the process of ring contraction, as it has been shown that the volume of AMRs decrease during contraction, in proportion to the decrease in their circumference [45,91]. Therefore, the amount of actin contained in the ring must decrease as the ring contracts, possibly through the shortening of individual filaments, or the loss of entire filaments.

Recent work in *S. pombe*, and its close relative *Schizosaccharomyces japonicus*, provides support for the latter idea, as in contracting rings in these cells it was observed that bundles consisting of actin and other ring proteins were expelled from the ring [92]. This appeared to be dependent on the curvature of the ring, as bundles were only expelled after the ring had contracted to a certain size, suggesting that this is a mechanical mechanism of disassembly, rather than specifically depending on the activity of, for example, actin severing proteins [92].

This mechanism only functions during the later stages of ring contraction, therefore there must also be mechanisms that work in the earlier stages. A major candidate for this is the actin depolymerising factor (ADF)/cofilin Adf1, which is the principal actin severing protein in *S. pombe* [93]. However, proper Adf1 activity is necessary for AMR formation, which makes it difficult to probe the affect of its inactivation/absence during ring contraction [66,93]. To date, relatively little work has been performed in this area, and how this disassembly is controlled to ensure that it does not happen too quickly or too slowly remains unknown.

1.9. Major components of the contracting actomyosin ring

Below we discuss some of the important classes of proteins that are present in the AMR, and the roles that these are thought to play during ring contraction.

1.9.1. Tropomyosin

We have already discussed the presence of actin filaments in the AMR, including estimations of the number of filaments and their length (section 1.7.3). However, one important actin-binding protein that we haven't mentioned yet is tropomyosin, a dimeric α -helical coiled-coil protein that binds along actin filaments, and stabilises them against severing and disassembly [94]. Tropomyosin also regulates the binding of other actin binding proteins, particularly myosin motor proteins [95–98]. In *S. pombe*, tropomyosin is encoded by the *cdc8* gene [99], and Cdc8 has previously been shown through *in vitro* experiments to regulate the processivity of bound myosin molecules [95–98]. *cdc8* is an essential gene in *S. pombe*, and when it is absent or inactive actin cables and the AMR rapidly fall apart, and cells become multinucleate [48].

1.9.2. Myosin motor proteins

There are three myosin species present in the contracting ring: Myo2, Myp2, and Myo51 [100]. Only the type II myosin Myo2 is essential [100], and it arrives at the division site before the appearance of actin filaments [49], as it binds into the nodes, rather than binding directly to actin filaments [101]. Myo2 is believed to form dimers [102], and it was previously determined that there are ~ 3000 molecules of Myo2 in the ring [64], corresponding to 10 dimers being present in each of the ~ 150 nodes [65]. There is evidence to suggest that, after ring formation is completed, the node structures persist in the fully formed ring [65]. Myo2 binding into the nodes/ring is dependent on its C-terminal tail

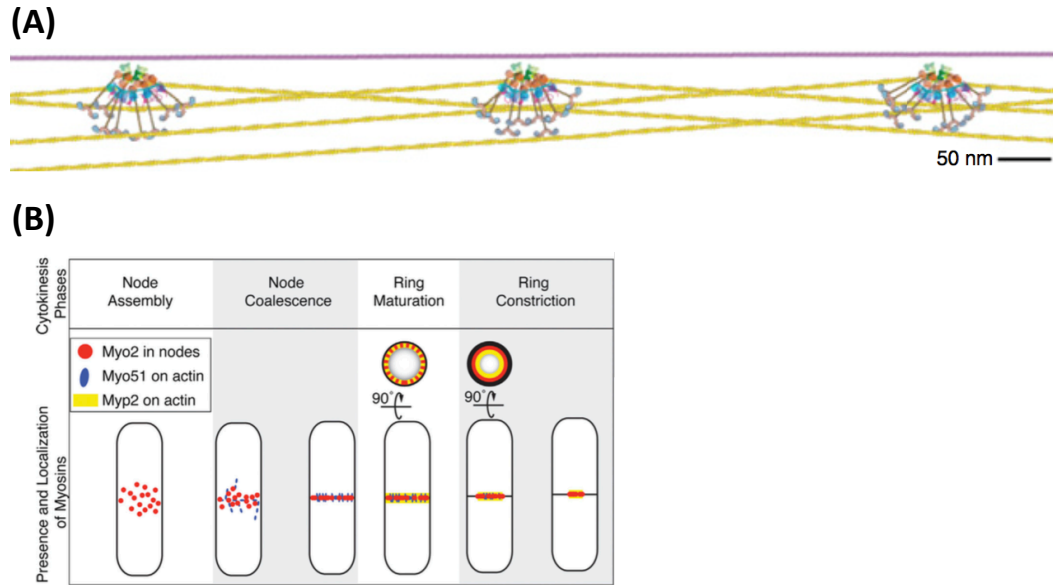


Figure 1.4: Localisation of myosins to the AMR

- (A) Diagram of proposed structure of cytokinesis nodes, where the head domains of Myo2 point outwards in a 'bouquet' arrangement, so that they are optimally organised to interact with nearby actin filaments. Adapted from Laplante, *et al*, 2016 [65].
- (B) Diagram illustrating the times as which the various myosin species localise to the AMR throughout cytokinesis. Adapted from Laplante, *et al*, 2015 [100].

region, with its N-terminal head domains believed to be pointed outwards in a bouquet-like arrangement, presumably so that they are organised in the optimal manner to interact with the actin filaments (Figure 1.4A) [62,65,103]. In the absence of active Myo2, the nodes are unable to form a ring, and the cell fails to go through cytokinesis [51].

The next myosin to appear in the ring is the type V myosin Myo51 (Figure 1.4B) [71,104]. This myosin is non-essential, and is believed to help with ring formation, specifically by helping to transport the nonmedially nucleated actin cables into the ring [69,71]. It is not believed to play a major role in ring contraction, although it is present in the contracting ring [71,100]. Its absence results in an increase in the time taken for ring formation, and leads to improper orientation of the nonmedially nucleated cables, but does not have much of an effect on the contraction rate [71,100].

The final myosin to localise to the ring is the non-essential type II myosin Myp2¹ [49,105]. This arrives in the ring directly before the onset of ring contraction (Figure 1.4B) [49], and unlike Myo2, its localisation to the ring is actin dependent, as it disappears from rings that are treated with Latrunculin A (Lat A), a drug which blocks actin polymerisation and leads to the disintegration of the ring [105]. Its absence has no effect on ring formation, as would be expected [100], however ring contraction is slowed in these strains [100], although this effect was found to be reduced at higher temperatures [106]. The exact role that Myp2 plays in ring contraction is not known. The tertiary and quaternary structure of the protein is also unknown, although it has been reported that, *in vitro*, the Myp2 tail region folds back on itself, preventing dimerisation or oligomerisation in the absence of other proteins [102]. More recently, through the use of fluorescently tagged Myp2, puncta of Myp2 fluorescence were observed in AMRs, suggesting that Myp2 forms oligomeric clusters *in vivo*, potentially through the binding of additional proteins to the C-terminal tail domain of the protein [105].

1.9.3. Actin nucleators

The primary actin nucleator in the *S. pombe* AMR is the formin Cdc12 [47]. This binds into the nodes during ring formation [68], and is the last main protein to arrive before the nodes begin to nucleate actin filaments, and subsequently condense to form a ring [49]. It was determined that there are around 300 molecules of Cdc12 in the ring, which work as dimers [64]. Therefore, there is an average of one Cdc12 dimer in each node, suggesting that each node nucleates a single filament [65]. Cdc12 is also believed to be responsible for the nonmedially nucleated actin cables that also contribute to ring formation, from its localisation in speckles that are seen away from the cell middle during mitosis/cytokinesis [68,69].

¹ *myp2* is non-essential in cells grown in rich media, however it becomes essential for cells grown at low temperatures (~ 18°C) and under specific nutritional conditions [102].

We have previously discussed how For3, the formin responsible for nucleating the interphase actin cables, also localises to the ring during cytokinesis. However, because it is believed to only play a minor role in the AMR, in our subsequent discussions on the roles of formins during cytokinesis, we will focus exclusively on Cdc12, and ignore the role of For3.

1.9.4. Actin crosslinkers

The *S. pombe* AMR also contains a number of dedicated actin crosslinking proteins. The most important of these for the process of ring formation are the α -actinin Ain1 and the fimbrin Fim1 [107]. Both were observed to localise to the AMR, however Fim1 was also observed in actin patches [107]. Neither protein is essential under normal growth conditions, however the absence of both proteins has a synthetic lethal affect, which causes ring formation to fail [107,108]. This makes it difficult to study their effect on ring contraction, so we do not know if they are also necessary for successful ring contraction.

It is also likely that the clusters of myosin molecules that are believed to be present in the ring (e.g. clusters of Myo2 in nodes, and clusters of Myp2) could also play a role in actin crosslinking [65,71,105], as it was previously found that Myo2 has both motor dependent and independent roles in ring formation [51].

1.9.5. Membrane anchors

When the AMR contracts, it needs to be able to pull on the plasma membrane to drive its invagination. Therefore, it is also important to ensure that the contracting ring is properly anchored to the membrane, so that it can transmit its contractile force to the membrane and the septum. Since there is some evidence to indicate that the nodes persist during ring contraction, it is likely that these act as the main membrane anchors [65]. Within the nodes, Cdc15 is likely the principle membrane

anchoring protein during ring contraction [74,109], whilst Myo2 and Rng2, which contain actin binding domains, are likely to link to the actin filaments, facilitating connections from the membrane to actin [51,63]. Cdc12 may also play a role if the filaments that it polymerises incorporate into the ring whilst remaining bound to the Cdc12 dimer at their barbed ends.

1.9.6. Actin severing/disassembly proteins

The final class of ring proteins we will discuss are those responsible for the disassembly and/or severing of actin filaments. The removal of old actin filaments contributes to the turnover of actin within the ring, and as we shall see in the following section, this is believed to be necessary for the generation of persistent contractility within AMRs.

The major protein responsible for this in *S. pombe* is the ADF/cofilin Adf1 [93]. In budding yeast, other proteins like Twinfilin and Cyclase activating protein have also been found to contribute to the overall disassembly of actin filaments [110,111]. Since both of these proteins are also present in fission yeast it is likely that they also contribute to actin disassembly and turnover within this organism. However, not much is known specifically about the fission yeast homologs of these proteins, due to a lack of research activity focused on them (for example, compare the lists of available literature for *twf1* at pombase.org and yeastgenome.org), so this discussion, and the experimental results documented in this thesis, will solely focus on the role of Adf1.

The protein Adf1 in *S. pombe* is referred to as both an ADF and a cofilin, however in higher eukaryotes these are actually separate, but closely related, proteins [112,113]. Mammals contain three forms of these proteins: ADF, cofilin-1, and cofilin-2, with cofilin-1 being the major form in non-muscle tissues, and cofilin-2 the major form in muscle [113]. Cofilin-1 is the most extensively studied of these proteins, as it is embryonically lethal, whereas deletion of ADF is non-lethal, and deletion

of cofilin-2 causes death after birth, due to severe muscle deficiencies [112].

Despite the similarities in their functions, *S. pombe* Adf1 and *H. sapiens* ADF/cofilin proteins have very different amino acid sequences, with only ~36 % amino acid identity between Adf1 and cofilin-1 (BLAST search), which is much lower than the 70-80% identity between the different human isoforms [112]. Additionally, there are also differences in the protein secondary structures between the two organisms, and in combination these results would suggest that studies investigating the effects of mutations in the yeast protein would have little carry-over to its effect in the human homologs. However, both the *S. pombe* and *H. sapiens* ADF/cofilin proteins do contain a single actin-depolymerising factor homology domain, or ADF-H.

Adf1 is an essential protein, and its absence or inactivity causes ring formation to fail, as actin filament severing is necessary for the SCPR mechanism to function properly [34,66,93]. Because of this, it is not known whether its activity is also needed during ring contraction, although based on our discussion in the next section it is likely to play an important role.

Adf1 is believed to bind cooperatively to actin filaments [114], and to alter their mechanical properties, such as their bending and torsional flexibilities, with cofilactin (regions of an actin filament where cofilin binding is saturated) filaments being more flexible in both instances [115,116]. Additionally, cofilactin has an increased twist (~25%) compared to bare actin [117], and it is thought that the induction of this extra twist is what allows cofilin to bind cooperatively to actin filaments [114].

From *in vitro* experiments, it has been shown that partially decorated actin filaments undergo severing at the boundaries between bare actin and cofilactin, which is thought to be because the different mechanical properties of the two neighbouring regions leads to the build up of mechanical stress at the actin-cofilactin boundary [118,119]. This model would imply that fully decorated (and bare) filaments will

experience fewer severing events than partially decorated filaments, and *in vitro* experiments also confirmed that this was the case [118]. However, in separate work, it was found that fully decorated actin filaments underwent depolymerisation from both ends, and it was shown that cofilin can also cause barbed-end capping proteins to unbind, which further promotes depolymerisation [120]. Therefore, it is likely that Adf1 in *S. pombe* is able to both sever and depolymerise actin filaments *in vivo*, although the relative contribution of each of these remains unknown.

1.10. Possible mechanisms of actomyosin ring contractility

In order for the AMR to contract, the actin filaments and myosin within the ring must interact in such a way that the overlap between pairs of filaments is increased, leading to a global decrease in the circumference of the ring. However, in a randomly organised bundle of actin filaments and myosin clusters, there should be an equal number of locally contractile and extensile configurations, which would lead to no overall shortening of the bundle (Figure 1.5A) [1]. Additionally, a number of mathematical models predict that myosin clusters have the ability to sort actin filaments within a bundle based on their polarity, and to then concentrate at the locations of filament barbed ends [121–123]. In terms of persistent contractility, this behaviour is counterproductive, as actomyosin interactions are at their most contractile when myosin clusters are biased towards the pointed ends of filaments, similar to a muscle sarcomere [1]. Therefore, in order for contractility to arise within an AMR there must be additional properties of the ring that help to overcome the equilibrium between locally contractile and extensile arrangements, and the susceptibility of actin filaments to polarity-based sorting.

This area has been the subject of extensive research, including mathematical modelling, and a number of potential models have been put forward. It has been proposed that if myosin clusters linger at the barbed ends of actin filaments then this could lead to local contractility

between pairs of parallel filaments [124]. However, no evidence for this mechanism has been found, and it would arguably lead to a corresponding increase in extensile arrangements between antiparallel filaments, which could cancel out the increased contractility of parallel filaments (Figure 1.5B) [1].

Another model proposed that *in vitro* actomyosin bundles contract when, in the presence of both fast and slow moving myosin clusters, or in the presence of actin crosslinkers, regions of contractile and extensile stress build up within actin filaments [125]. Regions that experience extensile stress would only stretch a small amount, whereas regions that are under compression would buckle, leading to apparent shortening of the filament, and biasing the actomyosin bundle towards contractility (Figure 1.5C) [125]. Additionally, previous work also suggests that myosin clusters should be able to generate the forces necessary to buckle an actin filament [126].

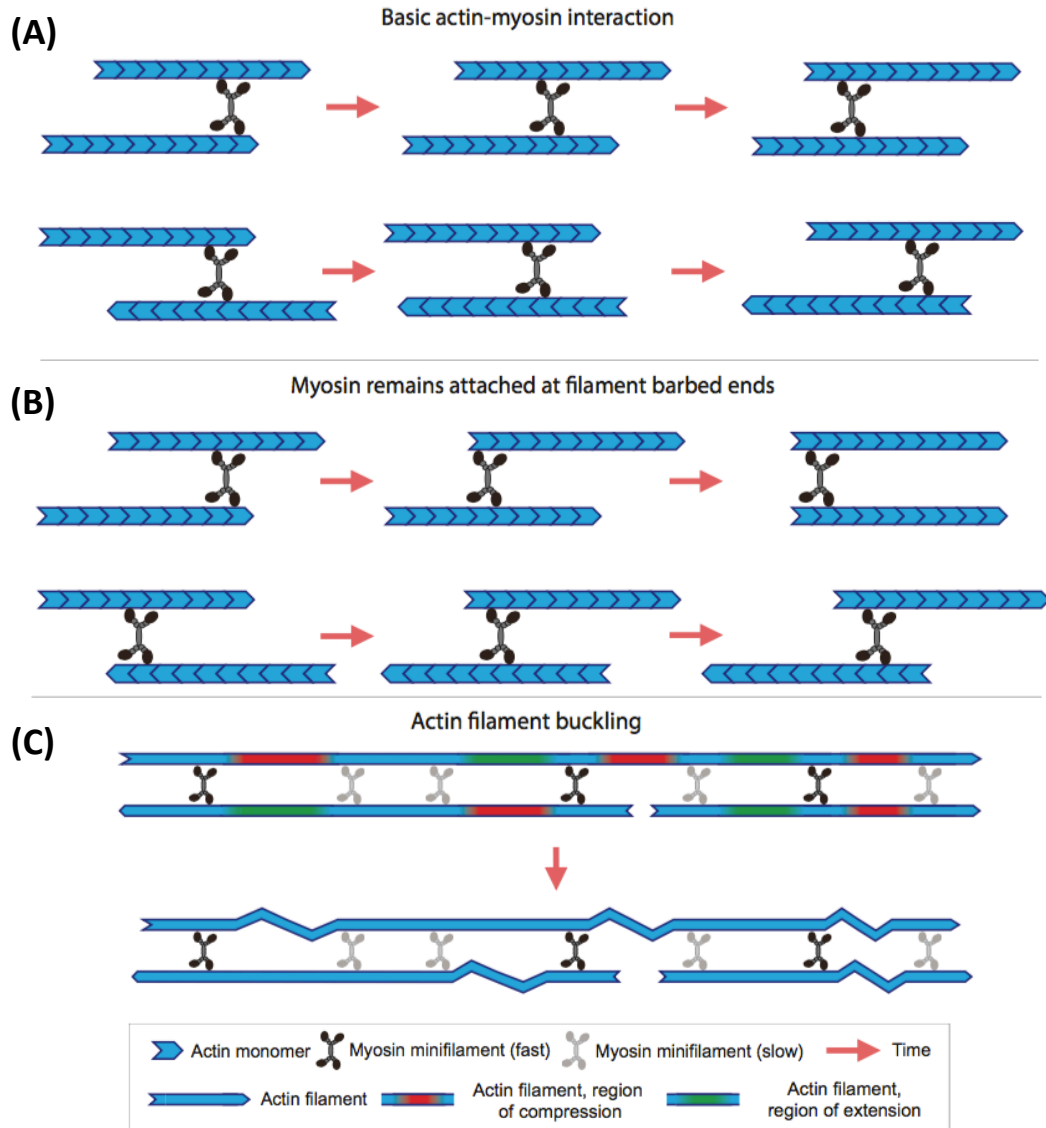


Figure 1.5: Mechanisms of actomyosin contractility (*in vitro*).

In A - C, the top-left actin filament has its barbed end orientated towards the left, (pointed end is orientated towards the right).

- (A) Interactions between a myosin cluster and a pair of antiparallel filaments should lead to an equal number of extensile and contractile configurations. No relative motion is induced between pairs of parallel filaments.
- (B) If myosin clusters linger at the barbed end of actin filaments, this could induce net contraction between parallel filaments, however this would also likely lead to greater expansion between antiparallel filaments.
- (C) If the myosin clusters have a range of velocities, then this could generate regions of contractile and extensile stress in an actin filament. The different behaviour of filaments under extensile and contractile forces (elastic stretching and buckling, respectively) can then lead to contractility.

Illustrations adapted from Cheffings, *et al*, 2016 [1].

However, it is not clear whether actin buckling can lead to sustained contraction, as experiments performed with linear actomyosin bundles showed a limited amount of contractility [125]. In experiments where the bundles were arranged into a ring shape, the bundle was able to contract fully [127], although it is not definite that these rings were employing/relying solely on this mechanism. Additionally, the actin filaments used in these experiments, and the filament lengths used in the corresponding simulations/mathematical modelling, were much longer than the filament lengths measured in the AMRs of a range of cells [45,46,128,129]. Furthermore, actin filaments are known to have persistence lengths of around 15 μm [130], meaning that filaments that are around two orders of magnitude shorter than this (e.g. in metazoan and amoeboid AMRs [128,129]) will likely behave as stiff rods, and will not bend appreciably. Because of this, and the fact that multiple myosin motors and/or crosslinkers must be bound to each filament for this mechanism to work, it seems unlikely that this mechanism would work with the shorter filaments that are present in AMRs.

More recent work has focused on the role of turnover within the AMR. In *S. pombe*, many of the ring proteins have been observed to turn over rapidly during contraction [37,131]. Additionally, treatment of contracting rings with Lat A is known to cause ring disassembly, implying that actin filaments also undergo turnover [37]. Actin filaments are thus continuously being nucleated and disassembled during ring contraction, with nucleation believed to be due to the formin Cdc12, whilst disassembly and removal of filaments is thought to be due to the action of the cofilin Adf1, and formin turnover.

Using these results, a number of models have proposed that turnover within the AMR is necessary for generating persistent contractility [35,123,132,133]. Stachowiak, *et al* [35], proposed a model where formins nucleate actin filaments in the ring, whilst anchoring their barbed ends to the cell membrane. This means that only the pointed ends of filaments are available for interaction with myosin clusters, ensuring that the filaments are organised so that contractile arrangements of

antiparallel filaments predominate (Figure 1.6A). Thus, the force of myosin pulling actin filaments together against the viscous drag of the formins in the membrane generates tension in the ring. While ring contraction could not actually be simulated because of the geometry used to set up the model, ring tension could be estimated for various ring circumferences, and was found to agree with the tensions measured from ring-dependent membrane furrowing in *S. pombe* spheroplasts (cells that have been separated from their cell wall) [35]. Moreover, when component turnover was turned off partway through a simulation, the simulated rings rapidly lost their tension, and the myosin clusters clustered together, presumably at the locations of actin filament barbed ends [35].

This model made the assumption that, in the contracting ring, Myo2 was localised in separate structures from the formin dimers. More recent data, using super-resolution microscopy, indicates that the nodes which are present during ring formation actually persist throughout ring contraction [65], which strongly suggests that the formin dimers and myosin clusters are actually localised together in the contracting ring. This is a different ring architecture to that used in the previously discussed simulations, however subsequent modelling work has shown that this architecture does also lead to the generation of contractile forces [132].

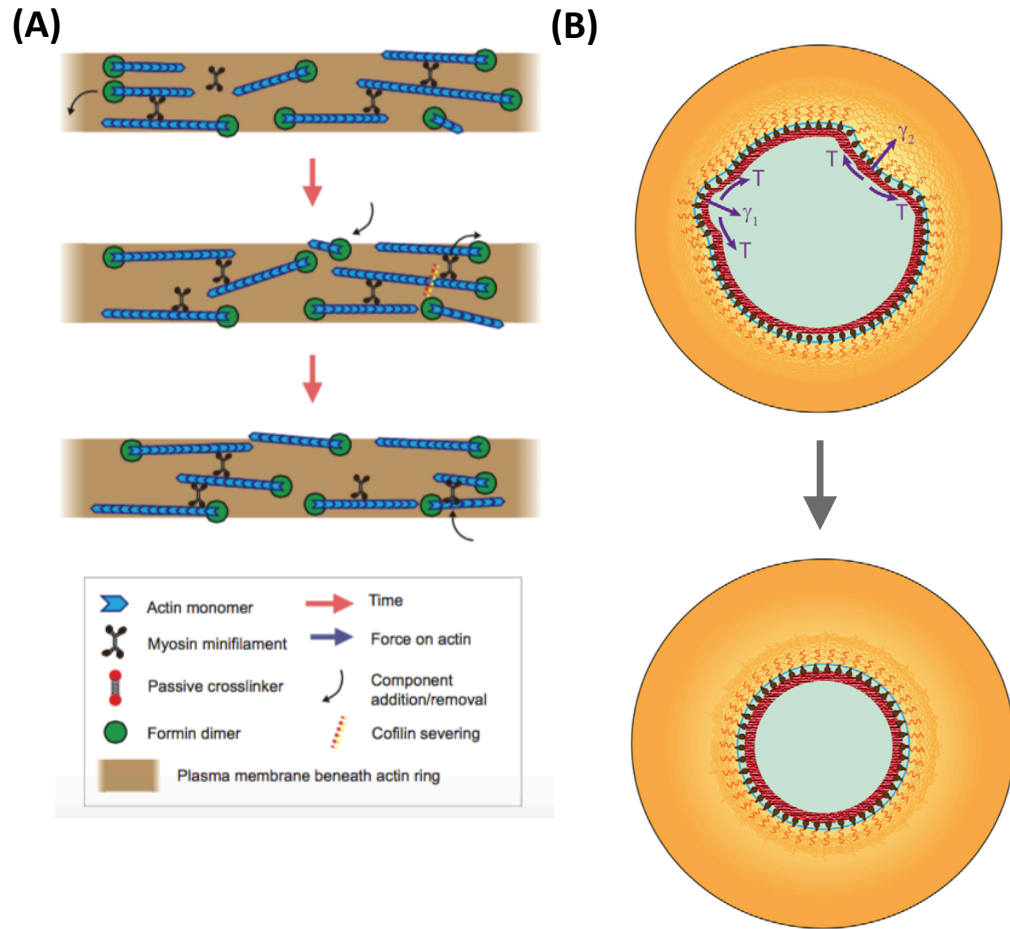


Figure 1.6: Mechanisms of actomyosin ring contraction, and its coordination with septation in *S. pombe*.

- (A) The dynamic nature of ring proteins could lead to contractility, as the continuous removal and polymerisation of actin filaments, and the continuous unbinding and binding of myosin clusters, means that myosins tend to interact with the pointed ends of actin filaments, leading to a predominance of contractile configurations. Adapted from Cheffings, *et al*, 2016.
- (B) Tension in the AMR is thought to regulate septum growth, as in regions where growth has lagged behind this leads to an inwards force which assists septum synthesis (γ_1), while in regions where septum growth has overtaken the other regions, this leads an outwards force which inhibits septum synthesis (γ_2). Diagram shows a cross-sectional view of a ring (red) with tension T , linked to the ingressing septum (orange). Adapted from Thiyagarjan, *et al*, 2015.

1.11. Interplay between actomyosin ring contraction and septation

AMR contractility is only half of the picture in *S. pombe* cytokinesis, as the cell also needs to build a new cell wall between the two daughter cells, a

process which occurs concomitantly with ring contraction [87]. This process is referred to as septation, and when it is blocked the AMR cannot contract [32]. The absence of the AMR has a more complicated effect on septation: The initial localisation of Bgs1, the primary septum synthesis protein, is dependent on the presence of the actomyosin ring, so in its absence Bgs1 does not localise correctly [88]. If the ring is disassembled after the initiation of ring contraction (e.g. by Lat A treatment), then it is possible for septation to continue, and to apparently complete successfully [89]. However, a closer look indicates that this is not the case, as the final hole left in the septum¹ is often highly deformed from its usual circular shape [90]. This is important, because cytokinesis is not truly completed until this hole has been closed, a process which is dependent on the endosomal sorting complex required for transport, or ESCRT, machinery in metazoan cells, whereas the exact machinery responsible for this remains unknown in fungi. If the final hole has an irregular shape, then it will be difficult for this hole to be properly closed, and this can lead to the subsequent death of the daughter cells during abscission. Therefore, although septation can progress in the absence of an AMR, it cannot produce a complete division septum, which means that the daughter cells will likely be inviable.

This result implies an additional role of the AMR during cytokinesis: As well as providing the force to pull the membrane inwards (concomitantly with septation), it also regulates septum synthesis to ensure that this occurs uniformly across the entire septum edge [90,134]. This idea is supported by experiments showing that septa in *myo2*-E1 and *cdc12*-112 (temperature sensitive mutants of *myo2* and *cdc12*, respectively) cells also appear to be highly distorted [90], suggesting that the regulation of septation does not just depend on the presence of the ring, but also on its ability to generate tension (Figure 1.6B).

¹ Because the contractile ring can only contract to a finite size, and the septum synthesis machinery will also be of a finite size, there will still be a small hole in the septum after ring contraction and septation have been completed.

This idea was explored further in a subsequent paper, where mathematical modelling of septation in *S. pombe* cells showed that the presence of a tension-generating ring helped to iron out any irregularities in the stochastic process of septum synthesis [134]. This is because the ring tension would inhibit septum growth in regions that had ingressed further than the rest of the septum, and promote septum growth in regions that were lagging behind [134] (Figure 1.6B). Simulations also demonstrated that this mechanism worked for a range of ring tension values, indicating a level of robustness which helps to ensure that septation can be properly completed even when AMR contractility is moderately perturbed [134]. This model relies on the assumption that the rate at which the primary septum is synthesised by Bgs1 is mechanoregulated by the force exerted on these from the AMR, which remains untested. However, it was observed that septa ingressed more slowly after the disassembly of the AMR, which is in agreement with this mechanism, since there is no longer a contractile ring to exert force on the Bgs1 molecules [90].

1.12. Aims, significance, and layout of this thesis

It is known that many components of the AMR undergo rapid turnover, and we have previously discussed how a number of computational models posit that this dynamism is necessary for the generation of contractile tension within AMRs. However, experiments where turnover is perturbed during AMR contraction have been scarce. Recent work in *S. japonicus* found that actin stabilisation during AMR contraction could rescue the effect of Lat A treatment [135], which prevents the polymerisation of new F-actin and causes the ring to disintegrate. From this it was proposed that one role of turnover is to help maintain actin filament homeostasis in the ring, therefore when the entry of new actin into the ring is blocked this homeostasis can be synthetically maintained by also blocking its disassembly and removal from the ring [135].

In *S. pombe*, actin turnover is believed to be regulated primarily by the ADF/cofilin Adf1. Previous work has focused on its role in ring formation, where actin severing is believed to work as an error-correction mechanism during the coalescence of precursor nodes into a uniform ring. However, for this study we wished to investigate the role of Adf1, and more generally to investigate the effect of reducing actin turnover, during ring contraction. From this, our initial objectives were:

- Use mutant alleles of *adf1* with reduced actin severing rates to see if reduced actin turnover has any noticeable effect on AMR contraction in the fission yeast *S. pombe*, and to thoroughly quantify any effect that may be present
- Additionally, attempt to perform pharmacological experiments using the actin stabilising drug jasplakinolide, as a secondary method to reduce actin dynamics during AMR contraction, and to see what affect this has on ring contraction

From these experiments, we found that contracting rings in these *adf1*-mutant cells displayed a ring peeling phenotype, where bundles of actin and myosin peeled off from one side of the ring, and were pulled in to the other. After characterising this phenotype, we then identified an additional objective for this work:

- Build a mathematical model of the fission yeast ring, with the goal of being able to reproduce this ring peeling phenotype in our model, in order to understand its origins

The results of this work should help us to refine our understanding of the role of actin turnover during ring contraction, and the effect that perturbing actin turnover has on an AMRs ability to generate tension.

As an additional project, we worked with another member of the lab to help them properly analyse data from fluorescence recovery after photobleaching (FRAP) experiments, in order to measure the

mobile/immobile fractions of various ring proteins, and to see how these vary with the age of the ring. To do so, we modelled the process of fluorescence recovery in FRAP experiments, and from this we developed a method of measuring the mobile fractions of ring proteins in *S. pombe*, which takes account of the limited pool of unbleached protein that is available in a small cell such as *S. pombe*. Measuring the mobility of ring proteins, and how their mobility changes throughout cytokinesis, will improve our understanding of how these proteins function in the ring, and opens up new ways of investigating their perturbation, by quantifying how their mobility, and the mobility of associated proteins, are affected.

The thesis layout is as follows: In the first results section (section 3, page 57), the results of all experimental work investigating the effect of perturbed actin turnover on AMR contraction are documented. The subsequent section (page 105) details all of the mathematical modelling and simulations of the AMR: an overview of the initial model is given first, followed by the results of the simulations that were performed, which is then followed by an in-depth mathematical description of the original model, and the subsequent modifications that were made, along with lists of the parameter values that were used in the simulations. In the final results chapter (section 5, page 176), the mathematical modelling of the process of FRAP recovery is shown, and the results that were obtained based on this mathematical modelling are also presented.

2. Materials and methods

2.1. Fission yeast strains

Fission yeast strains used in this thesis are listed in Table 2.1.

Table 2.1: Fission yeast strains used in this thesis.

Strain (MBY)	Genotype	Source
101	<i>ade6-210 ura4-D18 leu1-32 h-</i>	Lab collection (L.C.)
104	<i>ade6-216 ura4-D18 leu1-32 h+</i>	L.C.
151	<i>myo2-E1 ura4-D18 leu1-32 h-</i>	L.C.
192	<i>ura4-D18 leu1-32 h-</i>	L.C.
389	<i>nda3-KM311 ura4-D18 h-</i>	L.C.
625	<i>cyk3-GFP::ura4+ h-</i>	L.C.
737	<i>imp2::ura4+ ade6-216 ura4-D18 leu1-32 h+</i>	L.C.
2331	<i>cdc15-GFP::KanMX6 h-</i>	L.C.
3953	<i>pxl1::Ura4+ ura4-D18 leu1-32 h+</i>	L.C.
4010	<i>pxl1-GFP::ura4+ h+</i>	L.C.
4163	<i>rgf3-YFP::KanMX6 h-</i>	L.C.
4678	<i>adf1-1::ura4+ ade6-210 ura4-D18 leu1-32 h-</i>	L.C.
5180	<i>rlc1-tdtomato::NatMX6 ade6-M210 leu1-32 ura4-D18 h-</i>	L.C.
6656	<i>pAct1-Lifeact-GFP::leu1+ h-</i>	L.C.
7154	<i>myo51::ura4+ ura4-D18 leu1-32 ade6-210 h+</i>	L.C.
7967	<i>KanMX6::Pmyo2-GFP-myo2 ade6-M210 leu1-32 ura4-D18</i>	L.C.
10083	<i>myp2::NatMX6 ade6-210 ura4-D18 leu1-32 h+</i>	L.C.
10122	<i>(S. japonicus) rlc1-GFP::KanMX6</i>	L.C.
10126	<i>cdc15ΔSH3-GFP::KanMX6 ura4-D18 leu1-32 h+</i>	K. Gould
10127	<i>imp2ΔSH3::HphMX6 ura4-D18 leu1-32</i>	K. Gould
10146	<i>nda3-KM311 rlc1-tdtomato::NatMX6 h+</i>	L.C.
10149	<i>cdc15ΔSH3-GFP::KanMX6 rlc1-tdtomato::NatMX6</i>	L.C.
10174	<i>caf5::bsdR pap1Δ pmd1Δ mfs1Δ bfr1Δ dnf2Δ erg5::ura4+ h90 (7mdr)</i>	S. Kawashima
10177	<i>cdc12-mNeonGreen::KanMX6 h-</i>	K. Gould

10229	<i>myo2</i> -mApple::HphMX6 h-	L.C.
10262	<i>rlc1</i> -mNeonGreen::HphMX6 <i>leu1</i> -32 <i>ura4</i> -D18 h-	This study
10400	<i>blt1</i> -mCherry::NatMX6 h-	L.C.
10738	<i>adf1</i> -M3::KanMX6 <i>leu1</i> -32 <i>ura4</i> -D18 <i>his3</i> -D1 <i>ade6</i> -m216 h-	T. Pollard
10739	<i>adf1</i> -M2::KanMX6 <i>leu1</i> -32 <i>ura4</i> -D18 <i>his3</i> -D1 <i>ade6</i> -m216 h-	T. Pollard
10742	(<i>S. japonicus</i>) <i>myo2</i> -mNeonGreen::HphMX6	L.C.
10762	<i>adf1</i> -M3::KanMX6 <i>rlc1</i> -mNeonGreen::HphNT1 h+	This study
10763	<i>adf1</i> -M2::KanMX6 <i>rlc1</i> -mNeonGreen::HphNT1 h-	This study
10918	<i>rlc1</i> -mNeonGreen::HphMX6 <i>adf1</i> -M3::KanMX6 <i>myo2</i> ::NatMX6	This study
10919	<i>rlc1</i> -mNeonGreen::HphMX6 <i>adf1</i> -M2::KanMX6 <i>myo2</i> ::NatMX6	This study
10923	<i>adf1</i> -M3::KanMX6 <i>rlc1</i> -tdtomato::NatMX6 <i>cdc12</i> -mNG::KanMX6	This study
10991	KanMX6::Pmyo2-GFP- <i>myo2</i> <i>myo2</i> -mApple::HphMX6 <i>adf1</i> -M3::KanMX6	This study
10993	<i>rlc1</i> -tdtomato::NatMX6 <i>adf1</i> -1::ura4+ <i>nda3</i> -KM311	This study
11080	<i>caf5</i> ::bsdR <i>pap1Δ</i> <i>pmd1Δ</i> <i>mfs1Δ</i> <i>bfr1Δ</i> <i>dnf2Δ</i> <i>erg5</i> ::ura4+ <i>rlc1</i> -mNeonGreen::HphMX6 h90	This study
11086	<i>adf1</i> -M3::KanMX6 <i>Pact1</i> -Lifeact-GFP::leu1+	This study
11093	<i>myo2</i> -mNeonGreen::HphMX6 h+	This study
11170	<i>myo51</i> -mNeonGreen::HphMX6 h+	This study
11201	<i>rng2</i> -GFP::ura4+ h+	This study
11220	<i>adf1</i> -M3::KanMX6 <i>myo2</i> ::NatMX6 <i>Pact1</i> -Lifeact-GFP::leu1+	This study
11225	<i>ain1</i> -mNeonGreen::HphMX6 h+	This study
11232	<i>adf1</i> -M3::KanMX6 <i>myo2</i> -mNeonGreen::HphNT1	This study
11233	<i>adf1</i> -M3::KanMX6 <i>rlc1</i> -tdtomato::NatMX6 h+	This study
11250	<i>myo2</i> -R694C-3mYFP-3HA::HphNT1	M. Takaine
11258	<i>adf1</i> -M3::KanMX6 <i>rlc1</i> -tdtomato::NatMX6 <i>ain1</i> -mNeonGreen::HphMX6	This study
11259	<i>adf1</i> -M3::KanMX6 <i>rlc1</i> -tdtomato::NatMX6 <i>cdc15</i> -GFP::KanMX6	This study
11278	<i>adf1</i> -M3::KanMX6 <i>rlc1</i> -tdtomato::NatMX6 <i>rng2</i> -GFP::ura4+	This study
11280	<i>adf1</i> -M3::KanMX6 <i>rlc1</i> -tdtomato::NatMX6 <i>pxl1</i> -GFP::ura4+	This study

11282	<i>adf1</i> -M3::KanMX6 <i>rlc1</i> -tdtomato::NatMX6 <i>myo2</i> -R694C-3mYFP-3HA::HphNT1	This study
11318	<i>myo51</i> -mNeonGreen::HphMX6 <i>rlc1</i> -tdtomato::NatMX6 <i>adf1</i> -M3::KanMX6	This study
11429	<i>rlc1</i> -tdtomato::NatMX6 <i>myo2</i> ::NatMX6 <i>adf1</i> -1::ura4+ <i>nda3</i> -KM311	This study
11543	KanMX6::Pmyo2-GFP-Myo2 <i>adf1</i> -1::ura4+ <i>nda3</i> -KM311	This study
11544	<i>myo2</i> -mNeonGreen::HphMX6 <i>adf1</i> -1::ura4+ <i>nda3</i> -KM311	This study
11592	<i>rlc1</i> -tdtomato::NatMX6 <i>Pact1</i> -LAGFP::leu1+	This study
11647	<i>Pap1</i> ::HphNT1 <i>his3</i> -D1 <i>leu1</i> -32 <i>ura4</i> -D18 <i>ade6</i> -216	Jim Karagiannis
11667	<i>rlc1</i> -tdtomato::NatMX6 <i>adf1</i> -M3::KanMX6 <i>pap1</i> ::HphNT1	This study
11679	<i>adf1</i> -M3::KanMX6 <i>rlc1</i> -tdtomato::NatMX6 <i>Pact1</i> -LAGFP::leu1+	This study
11742	<i>adf1</i> -M3::KanMX6 <i>rlc1</i> -mNeonGreen::HphMX6 <i>blt1</i> -mCherry::NatMX6	This study
11743	<i>adf1</i> -M3::KanMX6 <i>rlc1</i> -tdtomato::NatMX6 <i>rgf3</i> -YFP::KanMX6	This study
11744	<i>adf1</i> -M3::KanMX6 <i>rlc1</i> -tdtomato::NatMX6 <i>cyk3</i> -GFP::ura4+	This study
11759	<i>adf1</i> -M3::KanMX6 <i>rlc1</i> -tdtomato::NatMX6 <i>myo2</i> -E1	This study
11770	<i>adf1</i> -M3::KanMX6 <i>Pact1</i> -LifeAct-GFP::leu1+ <i>myo51</i> ::ura4+	This study
11891	<i>adf1</i> -M3::KanMX6 <i>imp2ΔSH3</i> ::HphMX6	This study
11943	<i>adf1</i> -M3::KanMX6 <i>imp2ΔSH3</i> ::HphMX6 <i>rlc1</i> -tdtomato::NatMX6	This study
11944	<i>adf1</i> -M3::KanMX6 <i>Pact1</i> -LifeAct-GFP::leu1+ <i>myo2</i> -E1	This study
11945	<i>imp2</i> -mNeonGreen::HphMX6	This study
11948	<i>adf1</i> -M3::KanMX6 <i>cdc15ΔSH3</i> -GFP::KanMX6	This study
12107	<i>adf1</i> -M3::KanMX6 <i>cdc15ΔSH3</i> GFP::KanMX6 <i>rlc1</i> -tdtomato::NatMX6	This study
12182	<i>imp2ΔSH3</i> ::HphMX6 <i>rlc1</i> -tdtomato::NatMX6	This study
12183	<i>imp2</i> -mNeonGreen::HphMX6 <i>rlc1</i> -tdtomato::NatMX6	This study
12184	pDual::Padh81- <i>imp2</i> -mNeonGreen::leu1+	This study
12256	pDual::Padh81- <i>imp2</i> -mNeonGreen::leu1+ <i>Pimp2</i> - <i>imp2</i> -mNeonGreen::HphMX6	This study
12257	pDual::Padh81- <i>imp2</i> -mNeonGreen::leu1+ <i>adf1</i> -M3::KanMX6 <i>rlc1</i> -tdtomato::NatMX6	This study

2.2. Media used, culturing, and strain saving

Fission yeast cells (i.e. both *S. pombe* and *S. japonicus* strains) were grown on yeast extract with adenine (YEA, 5 g/l yeast extract, 30 g/l glucose, and 225 mg/l adenine). For experiments, cells were taken from -80°C storage and plated on YEA agarose plates, and grown at 24°C for 2 – 3 days. The cells were then used to inoculate the appropriate liquid medium, and grown at 24°C, until the cells reached an optical density (OD) of 0.2 – 0.5, at which point the cells were ready to be used. For strains where it is necessary for the temperature to be changed partway through the culturing process (e.g. for heat-sensitive or cold-sensitive mutants), a programmable shaker was used, so that the temperature could be changed automatically at the appropriate time. Cultures were diluted beforehand if necessary to ensure that they would not grow to an OD higher than 0.5. For long-term storage, strains were frozen at -80°C in YEA + 15% glycerol medium.

2.3. Drugs used

To stabilise the F-actin cytoskeleton, the drug Jasplakinolide (Sigma Aldrich) was used at the specified concentrations. For treatment, cells were grown to the appropriate density, and then 10 mL of culture was concentrated by centrifugation, and a volume of 50 or 100 µL cells was removed, to which the Jasplakinolide was added to produce the desired final concentration (for control experiments, Dimethyl sulfoxide [DMSO] was added instead). The mixture was shaken, and then approximately 20 µL of cells were imaged immediately using the cell suspension method (section 2.7.4).

To attempt to increase actin severing, we used the actin severing drug Swinholide A (Sigma Aldrich). As before, cells were grown to an appropriate density, before centrifuging 10 mL of culture to concentrate. 50 or 100 µL volume of cells were removed, to which Swinholide A was added to produce the desired final concentration (for control

experiments, DMSO was added instead). The mixture was shaken, and then approximately 20 μ L of cells were imaged immediately using cell suspension method (section 2.7.4).

2.4. Yeast genetics (classic and molecular)

2.4.1. Strain construction *via* mating

To create an *S. pombe* strain that is a combination of two pre-existing strains, cells from the two original strains with opposite mating types (h+ and h-) were plated on Extra Low Nitrogen (ELN) mating plates. The nutrient starvation causes cells of opposite mating types to mate and undergo sporulation to form tetrads. Once plated, the cells were kept at 24°C for 3 days, at which point either tetrad dissection or free spore analysis was performed to isolate the desired strain.

After the relevant method had been applied, the tetrads were grown on their plates at either 24°C for approx. 1 week, or 30°C for 4 days if none of the strains involved were temperature sensitive (TS). Then, colonies were replica plated onto the required selection plates, and/or placed at the appropriate temperature, and were grown for 1 to 2 days, at which point the appropriate colonies were selected, and if necessary their phenotype was checked via microscopy.

2.4.2. Tetrad dissection

Tetrad dissection allows the user to place the individual spores of a tetrad at specific positions on an agarose plate. These positions correspond to the points on a square grid, and enable the user to easily identify if the desired strain is present. This method is also useful if the desired strain contains two mutations/tags, etc. which both have the same marker.

To perform tetrad analysis, a small pinhead of sporulated cells from an ELN plate was suspended in 100 μ l of double distilled water

(ddH₂O). 2 µL of the cell suspension was placed at each end of one side of a YEA plate, streaked across the side of the plate using an inoculation loop, and then placed in a 30°C incubator for 5 – 10 mins to dry out the plate. Then the tetrads were dissected using a Singer Micromanipulator (MSM-Series 300, SINGER INSTRUMENT CO. LTD).

When mating cells containing LifeAct-GFP (LAGFP) with cells containing the *adf1*-M3 mutation, we found that we could not obtain any *adf1*-M3 LAGFP colonies when plating on normal YEA plates, so we instead used YEA + 1.2 M Sorbitol plates, as this is known to reduce the severity of some phenotypes. Once the colonies had grown on YEA + 1.2 M Sorbitol plates, the cells were subsequently able to grow normally on plates without Sorbitol, suggesting that the combination of *adf1*-M3 and LAGFP causes lethal defects in the sporulation process, but does not cause significant problems for normal cells.

2.4.3. Free spore analysis

For very simple crosses (e.g. very few insertions/deletions in the strains involved, everything has different markers), free spore analysis was performed to generate the desired strains. After 3 days on ELN plates, a large pinhead of sporulated cells was suspended in 990 µL ddH₂O with 10 µL Glusulase (PerkinElmer), which acts to digest the outer layer of the tetrads (the asci). This suspension was left overnight, and diluted 1000x with ddH₂O. The diluted suspension was plated onto multiple YEA plates, with 200 µl of suspension per plate, to enable colonies from individual spores to be discernible.

2.4.4. Strain construction *via* transformation of fission yeast cells

To transform fission yeast cells, a 50 mL culture of YEA was inoculated with the strain to be transformed, and grown overnight at 30°C (if the strain was TS, the culture was inoculated at an earlier time and allowed to grow for longer at 24°C). The next day, once the cells reached a slightly higher OD than is normally used (0.3 – 0.6), the cells were spun down,

washed in water, and then resuspended in 0.5 ml 1x LiAcTe solution (1 mL 10x TE, 1 mL 1 M lithium acetate, 8 mL sterile water to make 10 mL of solution).

For each transformation, 100 μ L of cell suspension was mixed with 240 μ L PEG 40 % LiAcTe (8 ml 50 % PEG 3350/4000, 1 mL 10x TE and 1 mL 1 M lithium acetate to make 10 mL), 4 μ L of single stranded carrier herring sperm DNA (Sigma Aldrich), and approximately 100 ng of transforming DNA, with a separate water control also performed.

The mixture was vortexed, and transferred to 30°C shaker for 1 hour, before heat shocking in a water bath at 42°C for 10 minutes. The cells were spun down and resuspended in 1 ml YEA, and then placed in the 30°C shaker for 3 hrs. Finally, the cells were plated onto pre-dried selective plates, with approximately 250 μ L of suspension per plate, and placed at 30°C (24°C if TS) for 4 days (~ 1 week), by which point colonies should appear.

In order to ensure correct integration of the transformation DNA, and the absence of additional insertions/mutations elsewhere in the genome, transformed cells were mated with WT cells using tetrad dissection, and the resulting colonies were checked to ensure there was the expected distribution of genotypes, i.e. that 2 out of the 4 spores from each tetrad contained the transformation DNA, and the other two were WT. The appropriate colonies were then plated and saved for future use.

2.4.5. C-terminal tagging of proteins with fluorophores from Pfa6A vectors

In order to tag *S. pombe* proteins at their C-terminus with the fluorophores contained in the vector Pfa6A, we first amplified two 250 bp regions of the gene of interest, directly before and after the gene's stop codon (making sure not to include the stop codon). To do this we utilised a pair of forward and reverse primers specific for each region in the gene of interest. Additionally, the reverse primer for the region before the stop codon also contained the sequence

GGGGATCCGTCGACCTGCAGCGTACGA at its 5' end, and the forward primer for the region after the stop codon contained the sequence GTTTAAACGAGCTCGAATTCATCGAT at its 5' end. These two additional sequences provide homology to specific regions in the Pfa6A vector, which allows for the subsequent PCR amplification of the desired fluorophore + marker from the vector. The final product of this PCR reaction contains the fluorophore, followed by its marker, with 250 bp of homology at each end for the region of insertion. This fragment was then transformed into the desired cells (normally WT), which were then plated on the appropriate selection plates, and fluorescence was confirmed using spinning disk microscopy.

2.4.6. Yeast genomic DNA purification

To purify fission yeast genomic DNA, 5 mL of cell culture was inoculated overnight. In the morning, the cells were spun down, washed in E-buffer (50 mM Sodium citrate and 100 mM Sodium phosphate), then spun down and resuspended in 5 mL of E-buffer with 1.2 M sorbitol.

0.038 g of lysing enzyme (Sigma) was added to the suspension, which was then incubated at 36°C for 1.5 hrs at 80 rpm. Then, 30 µl of zymolyase (G-Biosciences, 1.5 units/µL) was added, and the mixture was incubated for a further 1.5 hrs at 36°C and 80 rpm. Beta-mercaptoethanol was then added at a final concentration of 1 % (5 µL of 1 M stock), and further incubated for 30 mins at 36°C, 80 rpm.

The cells were then spun down gently at 450 relative centrifugal force (RCF) for 2 mins, and then resuspended in 0.5 mL 1x TE, + 50 µL 10% SDS and 10 µL of 20 mg/mL proteinase k (Invitrogen) and placed at 65°C for 30 mins, and then placed on ice for 10 mins. 200 µL of 5 M KAc (potassium acetate) solution was added, and the mixture was placed on ice for another 30 mins. Mixture was spun down at maximum speed for 30 minutes, the supernatant was recovered, and the DNA was precipitated by the addition of 500 – 800 µL of isopropanol. The mixture was again spun down at maximum speed for 10 minutes, and washed

twice with 70 % ethanol. After the final wash, the DNA was spun down again, the supernatant was removed and the DNA was air dried, before resuspending in 50 μ L ddH₂O and storing at 4°C.

2.5. Molecular cloning

2.5.1. PCR

All PCR was performed on a Biometra TRIO Thermocycler.

2.5.2. PCR from genomic DNA

To amplify sections of genomic DNA, the following protocol was used:

6.4 μ L of 10 μ M forwards primer, 6.4 μ L of 10 μ M reverse primer, 10 μ L PCR buffer No. 1 10x stock (500 mM Tris-HCl (pH 9.2), 160 mM (NH₄)₂SO₄ and 17.5 mM Mg Cl₂), 2 μ L of purified genomic DNA (although this amount could be varied to increase yield when necessary), 3.5 μ L of 10 mM dNTPs, 1 μ L Taq/Vent polymerase mixture (NEB, Ratio of 2:1) and 70.5 μ L of ddH₂O for a final volume of 100 μ L. The PCR program used was: 94°C for 2 mins, 94°C for 20 s, 52°C for 30 s, 68°C for 1 min 30 s (or roughly 50 s/kb to be amplified), cycling back to step 2 for 30 times, before a final step at 68°C for 7 mins, and holding at 16°C.

As the amount of genomic DNA obtained from a gDNA purification can be quite variable, we often performed a couple of simultaneous PCR reactions, using 1 μ L and 0.5 μ L of gDNA instead, and replacing the lost volume with an equivalent amount of ddH₂O.

2.5.3. Restriction digestion and ligation

All restriction digestions and ligations were performed using enzymes from NEB, and protocols as indicated on the NEB website. All ligations were performed using T4 DNA ligase and its appropriate buffer.

2.5.4. Purification of PCR product

All PCR reactions were ran out on 1 % agarose gels, from which the appropriate band was excised using a razor blade. The DNA was then purified using a QIAquick Gel Extraction kit (QIAGEN).

2.5.5. Plasmid extraction

To purify plasmid DNA from *E. coli*, cells containing the desired plasmid were grown overnight in 5 mL LB medium supplemented with ampicillin in a 36°C shaker. The next day, plasmid DNA was purified using a QIAprep Spin Miniprep Kit (QIAGEN).

2.5.6. Transforming *E. coli* cells

E. coli strain DH5 α (from lab stock, prepared by technician) was used for transforming. An appropriate amount of plasmid DNA was added to 100 μ L competent cells for 5 minutes, and cells were then heat shocked at 42°C for 1 minute, after which they were returned to ice for 2 minutes. 1 mL of LB broth was added to the cells, and they were incubated at 36°C for 30 – 60 minutes, before spinning down, removing 1 mL of supernatant, resuspending, and then plating on an LB-Ampicillin plate. A control transformation was always included. Plates were incubated at 36°C overnight, and were checked the next day for colony formation.

2.5.7. Creation of fission yeast strain with extra copy of *imp2*

In order to generate fission yeast strains containing two copies of the *imp2* gene, we decided to use the pDual expression vector system (empty vector from Dr Matsuyama [136], modified by other lab members to include mNeonGreen (mNG) tag, taken from pFa6A-mNeonGreen-KanMX6 plasmid in our collection), and to express the extra copy of *imp2* under the Adh81 promoter (Padh promoter sequence was taken from

pUC119 vectors [137], and inserted into modified pDual vector by other lab members).

Firstly, in order to insert *imp2* into the pDual vector, we cloned the gene from *S. pombe* cDNA (from lab stock), using forward and reverse primers for the beginning and end of the gene, respectively, making sure to exclude the stop codon. The forward primer also contained the sequence cgctagcgtcgacaggcctg at its 5' end, while the reverse primer contained the sequence ccttgccactaccctctag at its 5' end, which are homology sequences for specific regions in the pDual vector. In order to minimise errors in the cloning, we used Phusion polymerase, as this has a lower error rate than Taq/Vent mixture. PCR mixture used was: 10 µL of 5x Phusion HF Buffer, 1 µL of 10 mM dNTPs, 2.5 µL of 10 µM forward and reverse primers, 1 µL of cDNA, 0.5 µL of Phusion polymerase, and ddH₂O up to a final volume of 50 µL per reaction. The PCR program used was: 98°C for 30s, 98°C for 10s, 55°C for 1 minute, and then 72°C for 90s, cycling back to step 2 for a total of 35 repeats. Finally, the mixture was kept at 72°C for 10 minutes, before cooling and then running out on a gel.

The pDual vector was then linearised with BamH1 restriction enzyme, and the *imp2* clone was fused into the linearised vector using Gibson assembly (mixture consists of 2 parts of 2x NEBuilder HiFi DNA assembly mastermix (NEB), 1 part insert, and 1 part vector, usually to a total volume of 2 µL and is then incubated at 50°C for 1 hour before transforming into *E. coli*).

The final plasmid was pDual-*Padh81-imp2-mNG::leu*, and after sequencing to ensure that the cloned *imp2* had been correctly inserted, the plasmid was digested with Not1 enzyme, and then the larger fragment was purified and used to transform WT *S. pombe* cells, in order to insert an extra copy of *imp2* at the *leu1* locus.

2.6. Yeast cell biology methods

2.6.1. Cell cycle synchronisation

2.6.1.1. *cdc25-22* strains (G2 – M phase block)

Strains with the *cdc25-22* TS mutation are blocked at the G2 – M phase transition when shifted to their restrictive temperature (they also continue to increase in length during this time). Using a programmable shaker if necessary, a cell culture grown at the permissive temperature is shifted to 36°C for 3 – 3.5 hours to initiate the block. Cells will then enter M phase and begin to form an AMR about 30 – 45 minutes after being returned to the permissive temperature.

2.6.1.2. *nda3-KM311* strains (Metaphase block)

nda3-KM311 is a cold-sensitive (CS) mutation in the beta tubulin gene which prevents the formation of microtubules when at the restrictive temperature of 18°C. This precludes the formation of the mitotic spindle in mitotic cells, so that chromosome segregation does not occur. Importantly for this research, *nda3-KM311* cells form a complete AMR, which does not begin to contract until the cells are returned to their permissive temperature (24°C or higher).

To initiate the block, cells grown at the permissive temperature are shifted to 18°C until > 50% of cells have an AMR, which normally occurs after 6 – 8 hrs. After returning to their permissive temperature, *nda3-KM311* cells will quickly form a mitotic spindle and undergo karyokinesis within 5 minutes, after which ring constriction will quickly follow.

2.6.1.3. *cps1-191* strains (Cytokinetic block)

Fission yeast strains with the *cps1-191* genotype contain a mutation in the *bgs1* gene, which is responsible for synthesis of the primary septum during ring constriction. Cells with this mutation cannot form a primary septum when shifted to 36°C, meaning that ring contraction does not

occur. To initiate the block cells are shifted to 36°C for 3 hrs before imaging. When returned to the permissive temperature of 24°C, cells will initiate ring constriction within a few minutes, or alternatively they can be kept at 36°C in order to block cytokinesis indefinitely.

2.6.2. Fission Yeast Spheroplasting

Spheroplasts are cells that have been separated from their cell wall, causing them to adopt a spherical shape. They form normal looking AMRs, which slide along the inner surface of the membrane. Due to the change in cell shape, these rings are normally much larger than those in normal cells, and can be orientated in any direction, and both of these differences can be advantageous in certain situations.

To prepare spheroplasts, fission yeast cells are grown in YEA media up to an OD of approx. 0.5 in 20 mL. Using a *cdc25-22* strain, and blocking the cells at 36°C for 3 – 3.5 hrs beforehand will result in larger spheroplasts (and larger rings), although this is not necessary. Cells are then spun down in a falcon tube at 1900 RCF for 2 minutes, washed once with E-buffer (50 mM Sodium citrate, 100 mM Sodium phosphate), spun down and resuspended in 5 mL E-buffer with 1.2 M sorbitol.

To enzymatically digest the cell wall, 0.025g lysing enzyme (Sigma) is added to the cells, which are incubated at 80 rpm for 1 hr 30 mins, with the falcon tube laid flat on its side, at either 24°C or 36°C if using *cdc25-22* cells. Then, 25 µL of zymolyase (G-biosciences, 1.5 units/µL) was added, and the mixture was incubated for a further hour at the same temperature and rpm as before.

After this time, spheroplast formation is monitored via bench top microscopy, imaging the cells without a cover slip. When the cell wall appears sufficiently weakened, usually after ~1 hour, cells were spun down at 450 RCF for 2 mins, washed in E-buffer with 0.6 M sorbitol, then spun down and resuspended in 10 mL culturing medium (minimal medium + 0.8 M sorbitol + supplements). 50 µL of 2-Deoxy-D-glucose (Sigma Aldrich) at a concentration of 164.16 mg/mL was added, to

prevent cell wall regrowth, and the mixture was placed at 24°C, 80 rpm, with the falcon tube laid on its side.

After 3 hrs, we began to check the spheroplasts for ring formation using fluorescence microscopy, imaging the spheroplasts on a rectangular coverslip. When a majority of the spheroplasts had formed rings, the spheroplasts were imaged using the cell suspension method, detailed later.

2.6.3. Cell fixation and staining with Calcofluor white and DAPI

For cell-fixation, 5 mL of mid-log phase culture was centrifuged at 900 RCF for 3 minutes, and then washed with 1× phosphate-buffered saline (PBS). Cells were resuspended in 0.5 mL 1x PBS + 0.5 mL of 8% paraformaldehyde, and fixed on a shaker at 24°C for 12 minutes. The fixed cells were then washed once with PBS, and resuspended in 100 µL PBS. For permeabilisation, 100 µL of PBS + 1% Triton X-100 was added to 100 µL of fixed cells, and after 2 minutes the cells were washed twice with PBS, and resuspended in 25 µL PBS. For staining with calcofluor white (CW) and 4', 6-diamidino-2-phenylindole (DAPI), 10 µL of the final cell mixture was taken, and mixed with 10 µL of DAPI (2 µg/mL), and 2 µL CW at 500× dilution. For staining with just CW, cells were fixed but not permeabilised. After the final stage of fixation, cells were resuspended in 25 µL of PBS, and then 2 µL CW at 500× dilution was added to 10 µL of cells. For imaging fixed cells, these were placed on bare microscope slides, and then sealed under a coverslip using VALAP (section 2.7.3).

2.7. Microscopy and data analysis

2.7.1. Spinning disk microscopy

Spinning disk images were obtained using either one of two Andor Revolution XD microscopes. Both are equipped with Nikon Eclipse Ti

inverted microscopes, and Nikon Plan Apo Lambda 100x/1.45-NA oil-immersion lenses. Both microscopes were equipped with an Andor iXon Ultra EMCCD camera. Images were acquired using the Andor IQ3 software, at either 80 nm/pixel for the single camera microscope, or 69 nm/pixel for the TuCam system. Three laser lines at wavelengths of 405, 488, and 561 nm were used for excitation.

The following images were taken at a resolution of 69 nm: Figure 3.2B, 3.2C, 3.5B (*adf1-1* only), 3.5C - E, 3.5G - I, 3.6E, 3.6F, 3.7A (Rng2 only), 3.7B, 3.7C (Myo51 only), 3.9A, 3.9B, 3.10A, 3.12 (all), 3.13D and 5.1D. All other images were obtained at a resolution of 80 nm.

2.7.2. FRAP procedure (for experiments performed by Anton Kamnev)

FRAP experiments were performed on the TuCam system, at a resolution of 69 nm, using an Andor FRAPPA bleaching unit. Fluorophores were photobleached using a 455 nm laser line. A bleaching region of interest (ROI) was drawn as a 1 μ m line crossing one of the sides of the AMR in parallel to the longitudinal axis of the cell. Two laser lines of 488 nm and 561 nm wavelengths were used for excitation. Imaging software Fiji was used to process the images. To minimize bleaching of cytoplasmic recovery pool and damage to cell, the conditions for bleaching duration and laser power were tuned to achieve full bleaching of the fluorophore within selected ROI using minimum amount of laser power.

Three frames of prebleached images were acquired before photobleaching, followed immediately by time-lapse acquisition of images. Bleaching was completed in a mean of ~50–200 ms depending on the number of bleaching ROIs. For FRAP recovery curve quantification, a single z-slice at the middle plane of the cell was acquired every 0.3~1 sec (depending on fluorophore intensity) for a total duration of 2~3 min. For imaging induced bleaching control cells 20~30 cell per experiment were imaged in identical conditions with 4~5 FRAP ROIs drawn at random positions at least 2 μ m away from the cells with AMRs.

2.7.3. Agarose slide preparation

For imaging intact (i.e. not spheroplasts) and unsynchronised cells, sealed agarose pads were used. The agarose pads were made of YEA + 2% agarose placed on the concave side of a concave glass slide. 1 μ L of cells (concentrated from 1 mL by centrifugation at 450 RCF for 2 minutes) was placed on the agarose, a coverslip was placed on top, and then the edges were sealed with VALAP sealant (equal weight mixture of petroleum jelly, lanolin and paraffin, heated together on a hot plate and then mixed together and aliquoted into smaller containers). This method was used for the majority of image acquisitions, and was used for all the images we acquired, except for the instances described below.

2.7.4. Imaging using the cell suspension method

In certain cases, the agarose slide imaging method is not appropriate, e.g. for spheroplasts, which would not be able to maintain their shape, or for cells blocked with *nda3-km311* or *cps1-191* mutations, where the preparation of agarose slides would take too long, and when you wish to treat the cells with certain drugs. In these instances, cells were imaged in a cell suspension system, using μ -Slide 8 well glass bottom slides (ibidi). 1 mL of cell culture was concentrated by centrifugation at 450 RCF for 2 minutes, and then 10 – 20 μ L of cells were placed in one well of the 8 well slide. A PCR membrane was placed over the top of the well, in order to prevent evaporation of the growth media, which would cause unwanted motion of the cells.

2.7.5. Imaging using the CellASIC microfluidic system

For imaging *cps1-191* cells at 36°C, we utilised the CellASIC microfluidic platform (Merck Millipore). This system uses a range of specially made plates for different organisms which, when combined with the microfluidic pump, allows the user to keep cells stationary for long

periods of time at high temperatures, while constantly flowing through fresh medium, to ensure the cells remain healthy.

Using specialised Y04C yeast plates (Merck Millipore), approximately 100 μ L of cell suspension was added to the plate, and extra media to the necessary chambers. Cells were flowed into the imaging chamber (5 PSI for 5 seconds is sufficient), and then the media was flowed through at 5 PSI for approximately five minutes to wash out any unstable cells. Finally, media was perfused through indefinitely at a lower PSI, and the acquisition of time-lapse images was initiated.

2.7.6. Image Acquisition

3D spinning disk time-lapse images of cells were generally collected with a z spacing of 0.3 μ m over a range of 6 μ m for *S. pombe* cells, and 7.5 μ m for *S. japonicus* cells, with a time-step of 20s, 30s, or 1 minute, unless otherwise specified. For single time-point images, higher laser powers were used to provide increased signal for later quantification, while for time-lapse movies, the intensity was chosen to minimise photobleaching without compromising the measured signal. For imaging spheroplasts, a z-spacing of 0.5 μ m was used, over a range of \sim 10 μ m, with a typical timestep of 1 minute.

2.7.7. Image processing and quantification

All image processing and manual quantification was performed using the FIJI package of ImageJ (<https://fiji.sc>). Semi-automated quantification was carried out using custom-written FIJI (ImageJ) macros.

In cases where cells did not remain stationary over the course of the acquisition process, the plugin 'Correct 3D drift' was used to reduce this drift (Plugins/Registration/Correct 3D Drift). If necessary, further drift correction was carried out manually on 3D time-lapse images, by following moving cells with a ROI, duplicating the images at each time point, and then concatenating the images together. Rotational motion in

the x-y plane was also corrected in a similar manner, by rotating duplicated images at each time point to match their initial orientation.

All images were background subtracted (Process/Subtract Background), except for those used for intensity quantification/measurements. To generate face-on views of the AMRs, images were first rotated so that the rings were parallel to either the x or y axes. Then, a ROI was drawn around the ring (containing the ring at all time points), and this region was duplicated. A perpendicular view was then generated using the 'Reslice...' command (Image/Stack/Reslice...), using an output spacing of 0.1 or 0.15 μm , and the resulting image was then maximum-intensity projected to produce a single plane image/timelapse. Any observed movement that had not already been corrected for (e.g. in the z direction) was then corrected for as described previously.

Kymographs of contracting rings were generated from z-stack images, using a rectangular ROI drawn in the central plane of the ring, with the exception of pairs of kymographs showing two perpendicular views (e.g. Figure 3.5B and Figure 3.5C, page 70), which were both generated from face-on views of contracting rings, using two rectangular ROIs that were perpendicular to each other. The pixels inside these ROIs were duplicated, and kymographs were generated from the 'Make Montage...' function (Image/Stack/Make Montage...).

To create the false colour images in Figure 3.6, the source images were converted to 8-bit, the 'brgbcmyw' LUT (lookup table) was used, and the intensity calibration bars in these images were inserted using the 'Calibration Bar...' function (Analyze/Tools/Calibration Bar...).

To generate the segmented images in Figure 3.11, images of CW stained cells were converted into a binary image using the 'Threshold...' function (Image/Adjust/Threshold...) with the 'Yen' automated threshold. This binary mask was multiplied with the original image to produce an image only containing the high intensity pixels in the septum. Face-on views were then generated as described above. To view the cell wall signal in the images, an ROI was drawn around the cell in a region

adjacent to the septum. This ROI was duplicated (Image/Duplicate...), resliced, and then the resultant image was sum intensity projected to produce a strong cell wall signal. Background subtraction was applied to this image, and then the septum and cell wall images were combined to produce the images shown in Figure 3.11 (page 85).

2.7.8. Measuring contraction rate of actomyosin rings

Contraction rates were measured using raw 3D time-lapse images in cells expressing fluorescently tagged Rlc1. The diameter of the ring was measured from the distance between the spots of rlc1 fluorescence in the middle plane of the ring, at time-spacings of 1 minute. The diameter was plotted against time, and a straight line was fitted to the portion of the data representing contraction. The contraction rate was the gradient of this line, multiplied by π to get the rate of change of the ring circumference.

2.7.9. Measuring shortening rates of peeling bundles

The shortening rates of peeling bundles were measured from face-on time-lapse images of the ring. For each quantifiable peeling event (i.e. sufficient signal), a polygon ROI was drawn across the peeling bundle, and across the remaining ring circumference. This was repeated for each time step during each peeling event (i.e. every 20 or 30 s), and the measured perimeters were plotted against time. A straight line was fitted to data, and the gradient of this line was taken to be the bundle-shortening rate.

For bundles that had snapped, and were being reeled in at one end, the length of the bundle was measured from its anchor point in the ring, using a segmented line. As before, the measured lengths were plotted against time, and the gradient of a straight line fit was taken to be the shortening rate.

2.7.10. Measuring the timing of the first peeling event

For determining the time of the onset of ring contraction, the ring diameter was measured as before, except the period before ring contraction was now also included. Diameters were converted to circumferences, and scatter plots of circumference vs. time were made in Excel, from which the approximate time at which ring contraction begins was observed. To determine the initial ring circumference (C_0), the average circumference at times before ring contraction onset were measured, and a straight line ($y = m \times t + c$) was fitted to the contraction data at times later than the approximate onset of ring contraction. Then, y was set equal to C_0 in the equation of the straight line, and the corresponding value of t was found, which was set as the time of the onset of ring contraction. The time of the first peeling event was observed from face-on movies, and then the time relative to the onset of ring contraction was calculated by subtracting this time from the previously calculated time of the onset of ring contraction.

2.7.11. Comparing LifeAct density in contracting actomyosin rings

One of the problems with measuring the actin intensity in contracting AMRs is that there are many additional structures, such as actin patches and actin cables, which are directly adjacent to the ring, and which are difficult to exclude when trying to measure ring fluorescence. To try and account for this, we used a method where, as well as an actin label being present in the cell, a second ring protein was also fluorescently tagged. Then, the signal from the second ring protein was used to segment out the ring, while excluding the signal from nearby patches and cables as much as possible.

To compare the amount of actin in rings in WT and *adf1*-M3 cells, we used LAGFP under the *act1* (*S. pombe* actin gene) promoter as a marker for actin, in conjunction with Rlc1-tdtomato (tdT) to segment out

the AMR. For each strain, single timepoint z-stack images of live cells were obtained, using the DIC, mCherry and GFP channels, for approximately 100 cells containing AMRs at various stages of contraction. Using a custom imageJ script, we then performed semi-automated analysis on the collected images in order to measure the ring diameter and cell diameter (to provide an estimation for the degree of contraction), and to segment out the LAGFP fluorescence from the ring, and subsequently measure the total amount of LAGFP fluorescence in the ring. More details on this are provided in Figure 3.13 (page 92).

2.7.12. Measuring myosin-II fluorescence signal in actomyosin rings

To compare the amount of type-II myosin (Myo2 and Myp2) in rings in WT and *adf1*-M3 cells we used a similar method to that employed when comparing the amount of actin localised in the ring. We took single timepoint z-stack images of either WT or *adf1*-M3 cells containing GFP-Myo2 and Myp2-mApple, using the DIC, mCherry and GFP channels, for approximately 45 cells containing AMRs at various stages of contraction. The difference between the cell diameter and ring diameter was used to estimate how much the ring had contracted already. To measure the fluorescence from the ring, we used sum-intensity projections of the fluorescence images, and drew an ROI around the Myo2 fluorescence, and used this region to measure the fluorescence signal from the Myo2 and the Myp2. More details about this can be seen in Figure 3.13 (page 92).

2.7.13. Fitting of Gaussian mixture models to histograms of peeling event times

Fitting of Gaussian mixture models (GMMs) to our datasets was performed using the 'fitgmdist' function in MATLAB. A GMM is fitted directly to the data, rather than to the histogram, so the optimal GMM is

independent of the appearance of the histogram. Custom MATLAB scripts were used to generate models with between 1 and 5 components (i.e. number of individual Gaussians), and select which of these produced the best fit, based on which model had the lowest Akaike information criteria (AIC) value. We also calculated the Akaike weights/probabilities for each model, using the formula

$$w_i(AIC) = \frac{\exp\{-0.5 \cdot (AIC_i - \min(AIC))\}}{\sum_{i=1}^N \exp\{-0.5 \cdot (AIC_i - \min(AIC))\}},$$

where w_i is the probability for the i^{th} model, AIC_i is the AIC value for the i^{th} model, $\min(AIC)$ is the minimum AIC value from all the models, and N is the number of models [138].

2.7.14. Statistical analysis

For comparison of medians, the Mann-Whitney U-test was used. For comparison of two linear regression models, analysis of covariance (ANCOVA) was used. All statistical analysis was performed using MATLAB_R2016b (MathWorks, https://uk.mathworks.com/products/new_products/release2016b.html).

3. Experimental results and discussion

3.1. Investigating the effect of reduced actin turnover in contracting actomyosin rings

The role of actin turnover in ring formation has been well documented [34,66], whilst a number of mathematical models have highlighted its potential importance for the process of ring contraction [35,123,132,133]. We therefore decided to investigate the effect of reducing actin dynamics during ring contraction in the fission yeast *S. pombe*. To do so, we first utilised two mutants of the *S. pombe* actin severing protein ADF/cofilin, Adf1-M2 and Adf1-M3, which have previously been shown to have reduced actin binding affinities and severing rates [66]. Initially, we measured what affect these mutants had on the ring contraction rate, and we found that there was no difference between the WT and *adf1*-M3 cells, whilst there was a significant, but nonetheless small, difference between WT and *adf1*-M2 cells (Figure 3.1A). This contrasts slightly with previous observations, where no difference was observed between the ring contraction rates in WT, *adf1*-M2, and *adf1*-M3 cells [66].

While performing the quantification of the contraction rates in *adf1* mutant cells, we observed patches of Rlc1 fluorescence that were within the ring plane, but did not seem to be attached to the ring. Producing face-on views of the rings in these cells showed that bundles of myosin, and presumably actin, were peeling off from one side of the ring, and moving across to the other side of the ring (Figure 3.1B, Figure 3.1C). This phenotype was not seen in *adf1*⁺ cells (Figure 3.1D). We decided to call this phenotype ‘ring peeling’, and when an actomyosin bundle peeled off from the ring we called this a ‘peeling event’.

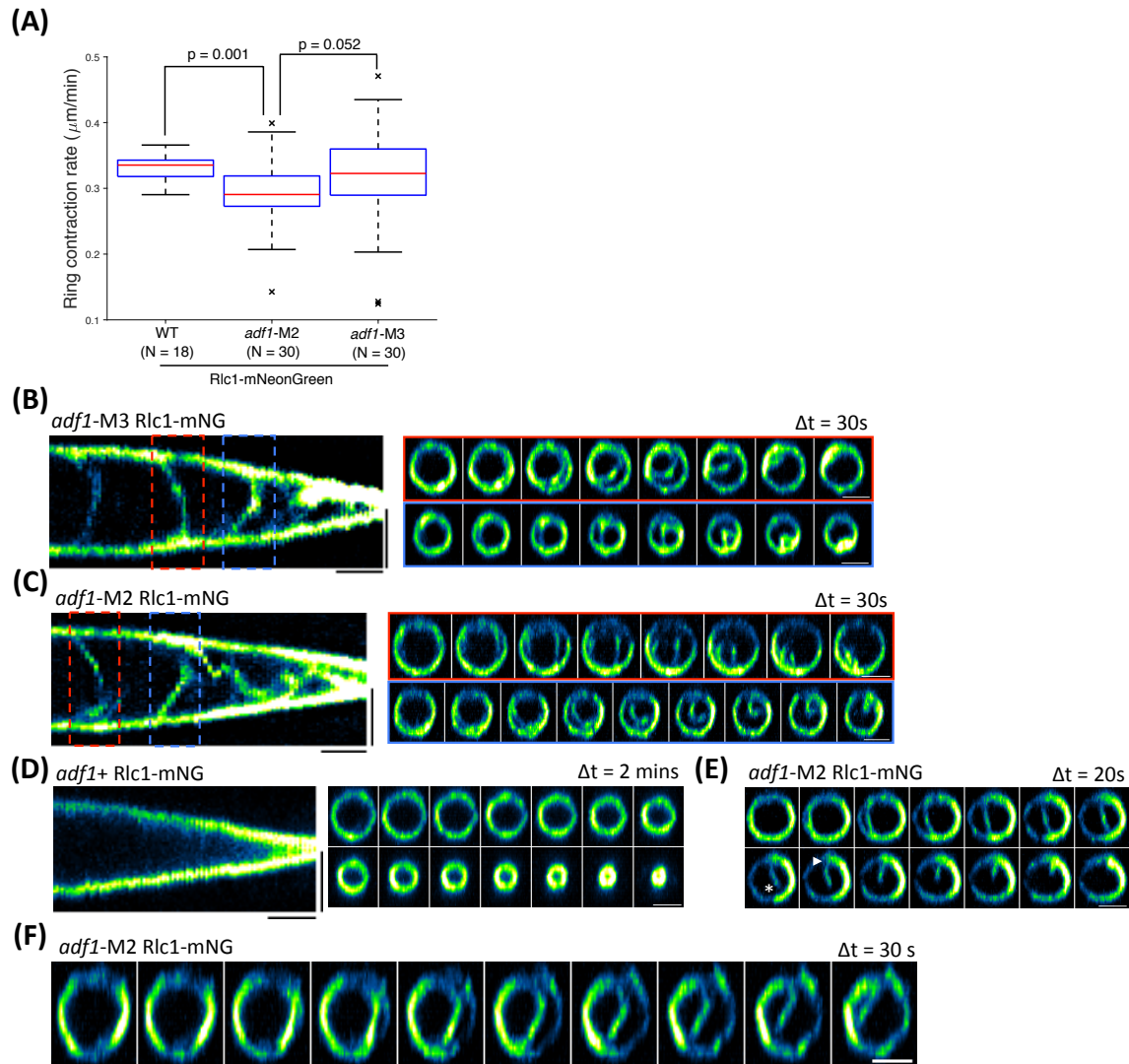


Figure 3.1: Contracting rings in *adf1*-M2 and *adf1*-M3 cells display a ring peeling phenotype.

- (A) Boxplots for the rate of change of circumference of rings in WT, *adf1*-M2, and *adf1*-M3 cells. p-values are calculated from the Mann-Whitney U-test.
 - (B) Kymograph and montages of a contracting ring in an *adf1*-M3 Rlc1-mNG cell. Two separate peeling events are shown in the montages.
 - (C) Kymograph and montages of a contracting ring in an *adf1*-M2 Rlc1-mNG cell. Two separate peeling events are shown in the montages.
 - (D) Kymograph and montage of a contracting ring in a WT (*adf1*+) cell (control experiment for B and C).
 - (E) Montage of a peeling event where the peeled bundle snaps at one end (asterisk), and is then reeled in to the main ring at its remaining attachment point (arrowhead).
 - (F) Montage of a peeling event in an *adf1*-M2 cell, where the ring has a kink on its right side. When a peeling event occurs at this location, the kink is also present on the peeling bundle, and remains as the bundle moves across the ring.
- All scale bars in montages are $2\text{ }\mu\text{m}$. Scale bars in kymographs are $2\text{ }\mu\text{m}$ and 5 minutes.

By making kymographs of contracting rings in the *adf1*-M2 and *adf1*-M3 cells, it can be seen that there appear to be 3-4 discrete peeling events per ring contraction, and that the ring peeling seems to begin shortly before ring contraction is initiated (Figure 3.1B and Figure 3.1C). Looking at face-on time-lapse images of peeling events also indicated that subsequent peeling events initiate from the opposite side of the ring relative to the previous event (Figure 3.1B and Figure 3.1C). Additionally, it was possible for us to observe a couple of sub-phenotypes of the ring peeling: Most of the time, the peeling actomyosin bundle would travel from one side of the ring across to the opposite side (Figure 3.1B and Figure 3.1C). However, sometimes the bundle would snap partway across the ring, at one of its attachment points, and would then be reeled in to the ring through its remaining attachment point (Figure 3.1E). We refer to this as ‘snapping-and-reeling’, whilst we refer to peeling bundles that do not snap as ‘unbroken peeling’.

Finally, we also observed an interesting peeling event in an *adf1*-M2 cell, where a small kink in the right hand side of the ring is also present in a peeling bundle which originates from this location (Figure 3.1F). This kink persists in the peeled bundle as it moves across the ring, suggesting that peeling bundles are not under significant amounts of tension, although this is the only example that we were able to find of such behaviour.

3.2. Ring peeling is not an artefact of defective ring formation

Because Adf1 function is also important for ring formation [66,93], it was possible that the ring peeling that we observed could be the result of a problem during ring formation, rather than because of reduced actin turnover during ring contraction. To rule this out, we used a strain containing the TS *adf1*-1 mutation, in conjunction with the CS tubulin mutation *nda3*-KM311, which causes cells to be blocked in metaphase when placed at low temperatures. Thus, by blocking cells in metaphase at

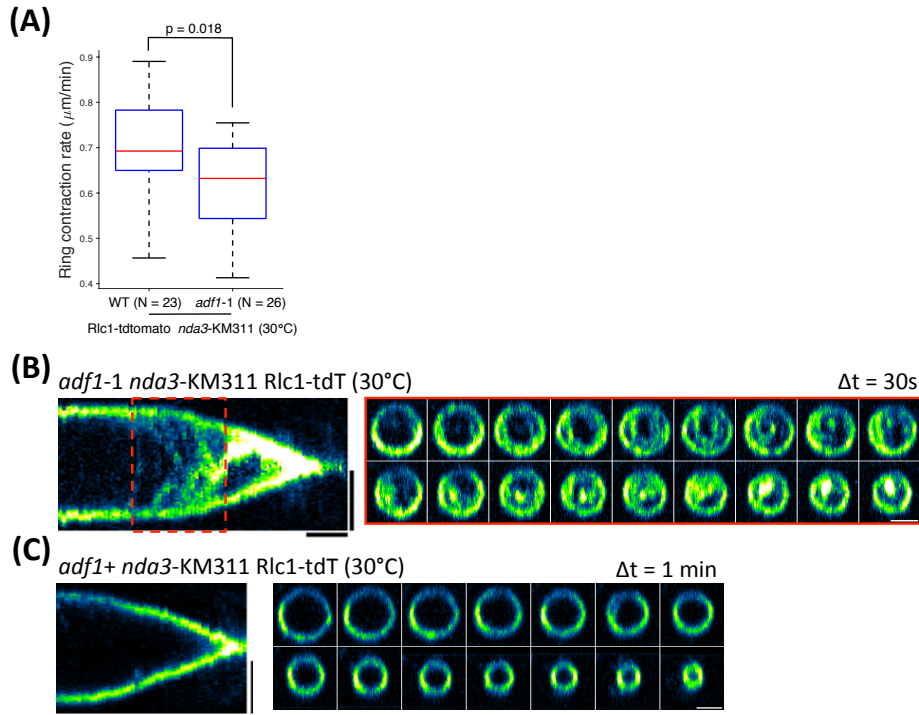


Figure 3.2: Rings in *adf1-1* cells also display a ring peeling phenotype.

- (A) Boxplots for rate of change of circumference for rings in *adf1-1* and WT cells. p-value is calculated from the Mann-Whitney U test.
- (B) Kymograph and montage of a contracting ring in an *adf1-1* cell at 30°C, with continuous peeling events visible in the montage.
- (C) Kymograph and montage of a contracting ring in an *adf1+* cell at 30°C (control experiment for B)

All scale bars in montages are 2 μ m. Scale bars in kymographs are 2 μ m and 5 minutes.

18°C, and then shifting to the restrictive temperature of *adf1-1*, we were able to generate AMRs that were formed with normal Adf1 function, but experienced impaired Adf1 function during contraction.

Shifting metaphase-arrested cells to 36°C caused the rings to fall apart, even in the WT control cells (possibly due to the rapid temperature change), however, when we instead shifted cells to the semi-restrictive temperature of 30°C the rings remained intact. By measuring the contraction rates, we found a significant decrease for rings in *adf1-1* cells at 30°C when compared to control cells (Figure 3.2A). From face-on movies of contracting rings in *adf1-1* cells we observed ring peeling (Figure 3.2B), which was much less noticeable in control cells (Figure 3.2C, see quantification in section 3.3). The observed peeling seemed to be more continuous than that observed in *adf1-M2* and *adf1-*

M3 cells, which meant it was not feasible to identify individual peeling events, and their location relative to the preceding event, however we were still able to see that ring peeling also appears to begin shortly before the onset of ring contraction in this strain (Figure 3.2B).

3.3. Quantification of the ring peeling phenotype

In order to gain a better understanding of the ring peeling phenotype, and to confirm some of our earlier qualitative observations, we next decided to perform quantitative analysis of contracting rings in these cells. We started by analysing the percentage of rings displaying the peeling phenotype in *adf1*-M2, *adf1*-M3, and *adf1*-1 cells, and in the corresponding control cells, whilst also measuring the relative proportion of each sub-phenotype (Figure 3.3A). In the WT control for the *adf1*-M2 and *adf1*-M3 cells, we observed a small proportion of rings displaying some snapping-and-reeling. However, these bundles only peeled off a short way before snapping (Figure 3.3B), so were not as noticeable as in *adf1* mutants, and the majority of AMRs did not show any peeling behaviour (Figure 3.3A). By contrast, in *adf1*-M2 and *adf1*-M3 cells, nearly 100% of AMRs displayed some form of peeling, the most common type being unbroken peeling, with some snapping-and-reeling events observed, and a small amount of AMRs displaying continuous peeling (Figure 3.3A), like that observed in *adf1*-1 cells.

In the *adf1*⁺ control for the *adf1*-1 cells, we detected a relatively high proportion of AMRs undergoing snapping-and-reeling events (Figure 3.3A, 48% of rings displayed some form of peeling). However, similar to what we observed in the control cells for the *adf1*-M2 and *adf1*-M3 strains, these bundles only peeled off a short distance before snapping and being reeled in (similar to Figure 3.3B), so they were not as readily visible as the events in *adf1*-1 cells. In the *adf1*-1 cells, we found that almost 100% of AMRs displayed a peeling phenotype, the most common of which was continuous peeling (Figure 3.3A).

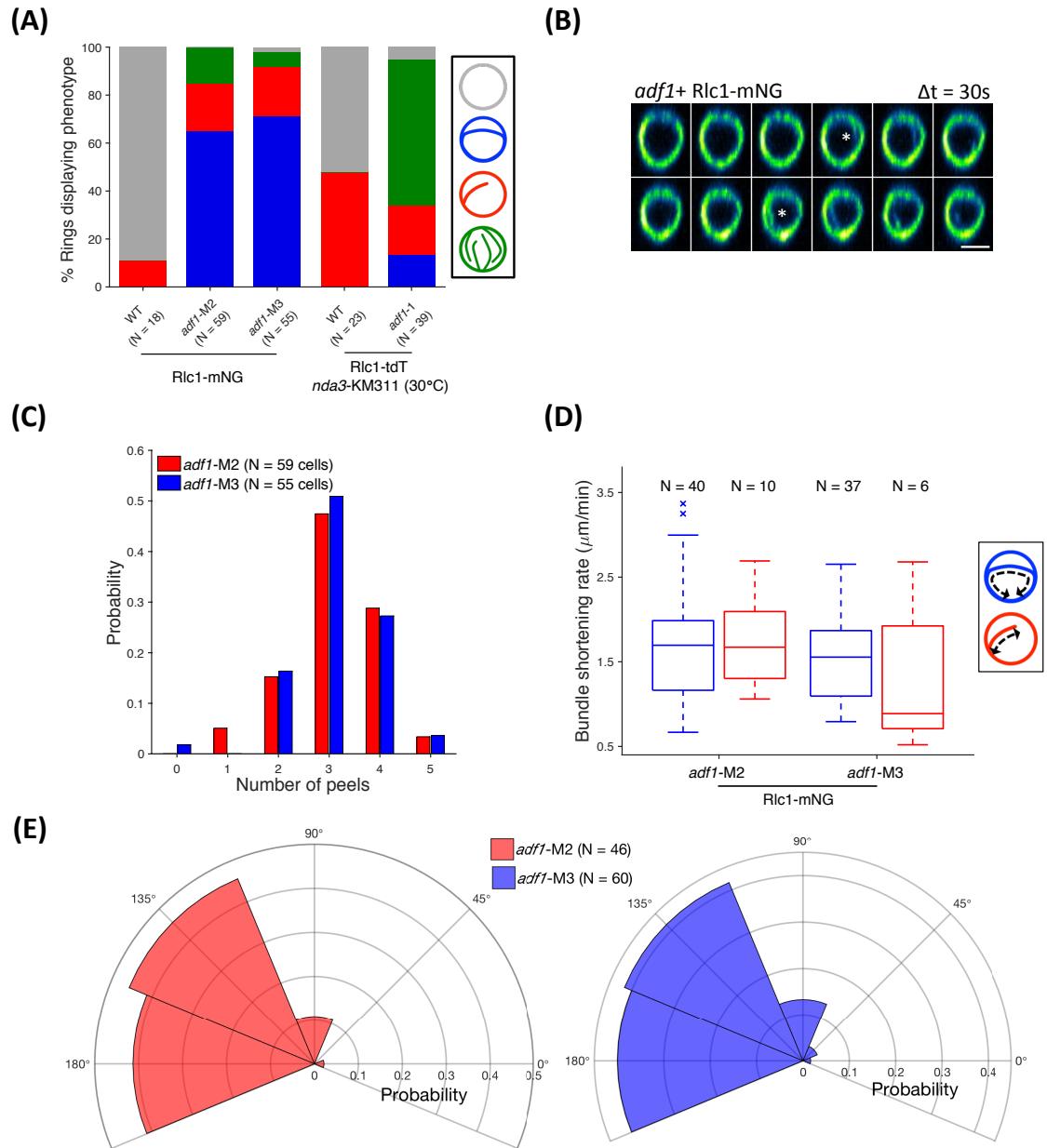


Figure 3.3: Initial quantification of ring peeling phenotype.

- (A) Quantification of the relative proportions of each sub-phenotype observed in each strain. The colour coding of the bars represents the different sub-phenotypes (no phenotype - grey, unbroken peeling - blue, snapping and reeling in - red, and continuous/non-discrete peeling - green), as depicted in the figure legend.
- (B) Representative montage of minor peeling events observed in a small subset of *adf1*+ cells – Asterisks mark these events, all images taken from the same ring. Scale bar is 2 microns.
- (C) Histograms of the number of peeling events (only unbroken peeling and snapping and reeling events) observed per ring contraction for *adf1*-M2 and *adf1*-M3 strains.
- (D) Measurement of the shortening rate of peeling bundles in *adf1*-M2 and *adf1*-M3 cells. Data for unbroken peeling and snapping-and-reeling sub-phenotypes are shown separately, as denoted in the figure legend. No significant differences were observed when comparing sub-phenotypes within a single strain, or when comparing the same sub-phenotype across both strains, determined by using the Mann-Whitney U test.
- (E) Polar histogram plots of the location of peeling events (only unbroken peeling and snapping and reeling events), relative to the preceding event, for *adf1*-M2 and *adf1*-M3 cells. Radial axis denotes the probability of observing a peeling event at a given angle, relative to the previous event, which was defined as occurring at 0°.

We subsequently measured the number of peeling events in *adf1*-M2 and *adf1*-M3 cells, and by plotting histograms we found that most rings in these cells display an average of 3 peeling events, with 4 events also being relatively common (Figure 3.3C). It is possible that more peeling events do occur in the final stages of ring contraction, but we cannot detect these due to the small size of the ring at these times. We did not perform this quantification on rings in *adf1*-1 cells, as the prevalence of continuous peeling phenotype in this strain made it difficult to count individual peeling events.

Next, we measured the shortening rate of peeling bundles in *adf1*-M2 and *adf1*-M3 cells. We divided our quantification between bundles that underwent normal peeling, and those that displayed snapping-and-reeling events. From our data, we observed no significant differences between bundle shortening rates, both when comparing sub-phenotypes within the same strain, or comparing the same sub-phenotypes between strains (Figure 3.3D). In *adf1*-M3 cells, the shortening rate of snapping-and-reeling bundles does appear to be lower than that for the normal peeling bundles, however the number of data points for this sub-phenotype is quite low, and the interquartile range and total range of the data does appear similar to that in the rings displaying unbroken peeling. Overall, the peeling/reeling bundles shortened at an approximately 6-fold faster rate than the rate of ring contraction in WT or *adf1*-M3 cells (Figure 3.1A, Figure 3.3D). However, this was still roughly an order of magnitude slower than the contraction rates observed in isolated rings, which contract in the absence of membrane ingression and septation at speeds which approach the load-free velocity of type II myosin [95,139,140].

We also plotted polar histograms to investigate if there was any relationship between the locations of subsequent peeling events, as appeared to be the case from our qualitative observations (Figure 3.1B, Figure 3.1C). In peeling rings where we could observe at least two consecutive peeling events (unbroken peels and snapping and reeling

events only), we measured the angular separation between the peeling locations of these events. From this analysis, we found that around 80 – 90 % of peeling events in *adf1*-M2 and *adf1*-M3 cells started from the opposite side of the ring relative to the previous event (Figure 3.3E).

3.4. Timing of peeling events relative to the onset of ring contraction

We next decided to investigate the time at which ring peeling starts. From our kymographs, it seemed to be the case that peeling started around 5-10 minutes before the onset of ring contraction. We analysed this more closely, by collecting 4D images of *adf1*-M2, *adf1*-M3, and *adf1*-1 cells, and selecting cells where ring contraction did not initiate until at least 20 minutes after the start of the image acquisition, to try and ensure we were observing the first peeling event(s)¹. In all three *adf1* mutants, the first peeling event(s) occurred at a median time of around 5 minutes before ring contraction began (Figure 3.4A), confirming our earlier qualitative observations. Whilst we did observe one peeling event occurring as early as ~30 mins before ring contraction onset, this was a very faint and minor event, not too dissimilar to those we sometimes observed in WT cells (similar to Figure 3.3B).

To investigate if subsequent peeling events also displayed distinct timing behaviour, we measured the timing of the first three peeling events in *adf1*-M2 and *adf1*-M3 cells. If the peeling times were completely random, then we would expect the data to exhibit a roughly flat distribution. Instead, we observed that the histograms for both strains showed three main peaks (Figure 3.4B), indicating that ring peeling events occur at predictable times. To prove this, we fitted a GMM to each dataset (excluding outlier events occurring at times of < -15 minutes), comparing models with between one and five components (i.e. number of individual Gaussians), and using the AIC to determine the optimum

¹ We are saying 'event(s)' because in *adf1*-1 cells it is very difficult to identify an individual peeling event, so in these cells it is not necessarily correct to say that we have identified the first event, but rather that we have identified the time at which the peeling events begin.

model. For both strains, we found that a 3-component model was the *best* fit, with the 3-component model for peeling events in *adf1*-M2 (*adf1*-M3) cells being 20 (3) times more likely than the next most probable model. Specifically, we obtained probabilities for models containing 1 – 5 components of 0.0045, 0.0365, 0.91, 0.0441, and 0.0048 for *adf1*-M2 cells, and 0.0001, 0.1284, 0.6469, 0.2099, and 0.0148 for *adf1*-M3 cells, respectively. Additionally, the 3-component model probability density functions reproduced the patterns evident in the histograms, suggesting that they are a *good* fit (Figure 3.4B).

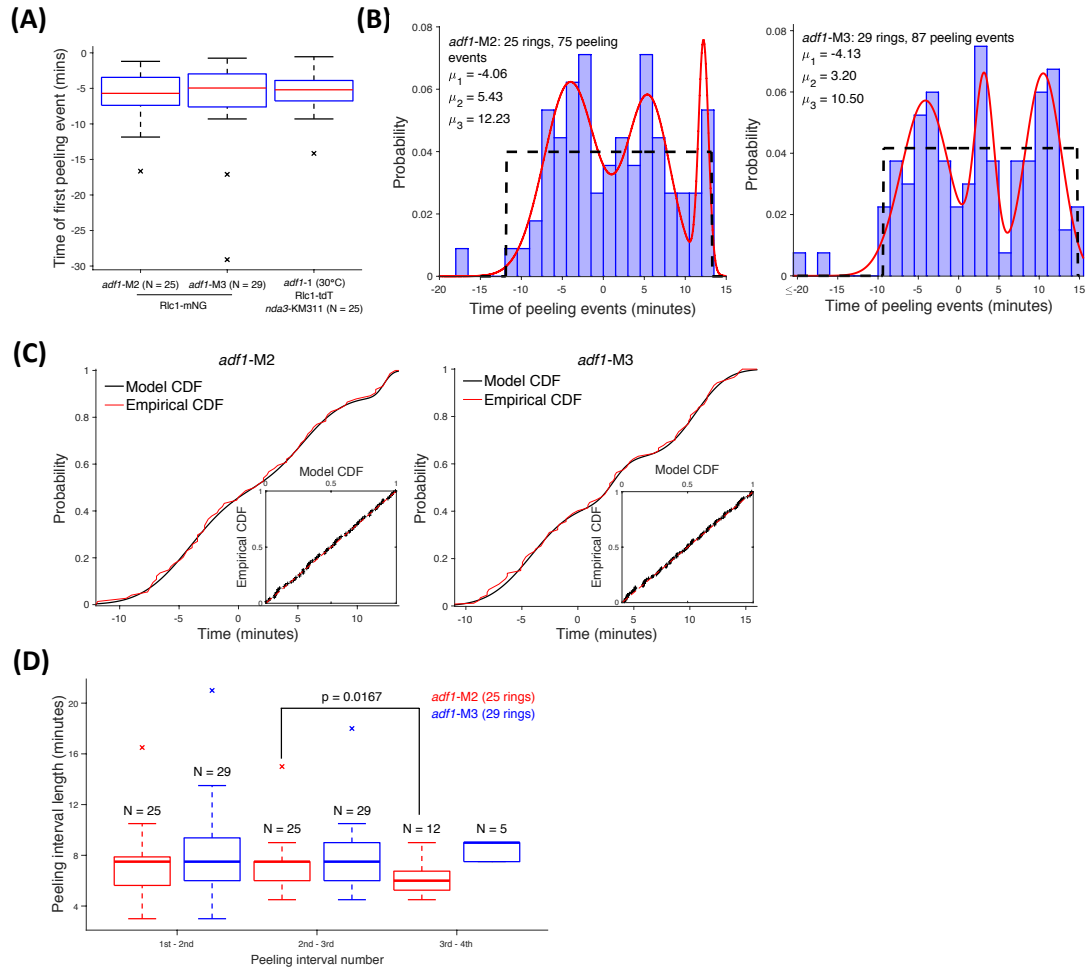


Figure 3.4: Quantification of the timing of peeling events

All data used in this figure came from cells where ring contraction did not start until at least 20 minutes after the start of image acquisition. We only used data from from *adf1*-M2 and *adf1*-M3 cells where we observed at least three peeling events (only unbroken peeling and snapping-and-reeling events).

- Quantification of the time of the 1st peeling event(s), measured relative to the onset of ring contraction, in *adf1*-M2, *adf1*-M3, and *adf1*-1 cells.
- Histograms of the times at which the first three peeling events occur in *adf1*-M2 and *adf1*-M3 cells, measured relative to the onset of ring contraction. The PDF of the optimal 3-component GMM is overlaid (red line), and the centres of the three Gaussian components are listed on the graph. The PDF of a uniform distribution (black dashed line) is also included. All analysis excluded outlier events occurring at times < -15 minutes.
- Plots of the CDF from our 3-component GMMs, overlaid with the empirical CDF measured from our data, showing goodness-of-fit for the model. Inserts show P-P plots, to further support the goodness of fit between the model and the data.
- Boxplots showing the time intervals between different peeling events for *adf1*-M2 and *adf1*-M3 rings. p-values for significant differences are shown on the graph, determined from the Mann-Whitney U test (comparisons were only made within the same strain).

We also investigated the distribution of peeling events, by comparing our datasets to uniform distributions (Figure 3.4B), for which the lower and upper endpoints were determined by the minimum and maximum values in our datasets (again, excluding outlier events at times of less than -15 minutes). The Kolmogorov-Smirnov (KS) test is commonly used in this situation, however in this instance we decided that this was not the optimum test to use. This is because the KS test is not very powerful when comparing datasets where the empirical CDFs cross each other multiple times [141], which is the case when our data is compared to a uniform distribution (Figure 3.4B). Instead, we decided to use the Anderson-Darling (AD) test, as this does not have the previously discussed drawback [141]. From this, we obtained p-values of < 0.001 for both the *adf1*-M2 and *adf1*-M3 datasets, indicating that a uniform distribution does not provide a good fit the distributions of the timing of peeling events.

We also wished to make a direct comparison between our uniform distribution fits, and our GMM fits to the data. However, it was not possible to calculate AIC values for the uniform distribution fit, as the fitting procedure for this distribution is not the same as for more complex distributions (i.e. Normal, Poisson, etc.) in MATLAB, with the fit only relying on the minimum and maximum values in the dataset. Similarly, it was not possible use the AD test with our GMM fits, because it is necessary to compare the AD test statistic to a list of critical values, which are only available for certain standard distributions (currently the Normal, Lognormal, Extreme value, Exponential and Weibull distributions in MATLAB). Therefore, even though it is not the ideal test to use in this circumstance, we performed χ^2 goodness of fit tests to try and get some measure of whether the uniform distributions or the GMMs provided a better fit to our datasets. For the *adf1*-M3 data, we obtained p-values of 8401 and 0.9455 for the uniform distribution and GMM fitting, respectively, indicating that the GMM may be a better fit to the data. However, for the *adf1*-M2 data, we obtained p-values of 0.8940 and 0.5239 for the uniform distribution and GMM, respectively, which would

suggest that the uniform distribution is actually a better fit to the data in this circumstance. However, because there are a large number of parameters (9) in our 3-component GMMs, we needed to use a relatively large number of bins for our data, which meant that the number of observed peeling events per bin was much lower than is optimal for the χ^2 test (approximately 8 and 6 peeling events per bin for the *adf1*-M3 and *adf1*-M2 datasets, respectively). Therefore, this limits how meaningful the results of these tests are, and makes it difficult to firmly conclude whether a uniform distribution or a GMM is a better fit to the data, when trying to take account of the increased complexity of the GMMs.

Because the appearance of a histogram varies with the binning used, we also plotted the model cumulative density functions (CDFs) alongside the empirical CDFs of the data. We did this because the empirical CDF does not utilise binning, so its appearance is completely determined by the data. These plots showed excellent agreement between the model and the data (Figure 3.4C), and making P-P plots (model CDF vs. empirical CDF) further reinforced this (Figure 3.4C, inserts). Overall, this analysis indicates that peeling events are not completely stochastic, but instead occur in a sequence and at predictable times relative to the onset of ring contraction.

We next decided to quantify the time intervals between different peeling events, which we predicted would decrease as the ring contracts, since as the ring gets smaller peeling bundles will have a shorter distance to travel until they reach the other side of the ring. Plotting this data for *adf1*-M2 and *adf1*-M3 cells showed that there was no observable difference in the time interval between the 1st and 2nd events and the interval between the 2nd and 3rd events (Figure 3.4D). In the *adf1*-M3 cells we did not observe many rings which underwent 4 peeling events, so although we did observe an increase for the time interval between the 3rd and 4th events, this difference was not significant. We saw more rings with 4 peeling events in the *adf1*-M2 strain, and the interval between the 3rd and 4th peeling events was found to have decreased by a significant

amount, although only when compared to the previous interval (Figure 3.4D).

3.5. Dependence of ring peeling on the individual myosin species in the ring

We previously observed that ring peeling seemed to start around 5 minutes before the onset of ring contraction (Figure 3.4A). This is roughly the same time that Myp2, the non-essential type-II myosin in *S. pombe*, localises to the contractile ring [49]. We therefore wondered whether Myp2 plays a role in the ring peeling that we have observed in *adf1* mutants.

To investigate, we imaged *adf1*-M3 *myp2* Δ and *adf1*-1 *myp2* Δ double mutants, using Rlc1 as a ring marker as before. In these strains, the ring peeling phenotype could not be observed, as shown using kymographs constructed from two perpendicular views of the ring (Figure 3.5A and Figure 3.5B, *adf1*-M3: 18 rings with no peeling, *adf1*-1: 11 rings with no peeling and 1 ring with 1 minor peeling event, similar to Figure 3.3B). This seemed to indicate that Myp2 contributes to ring peeling.

As Rlc1 is a light chain for both myosin II heavy chains, Myo2 and Myp2, we decided to also use *adf1* mutant strains where the type-II myosins were directly tagged. When using cells expressing *GFP-myo2* we also observed no ring peeling (Figure 3.5C), as would be expected from our previous observation with *myp2* Δ cells. However, when using cells expressing *myp2-mNG*, we saw ring peeling in both *adf1*-M3 (Figure 3.5D) and *adf1*-1 (Figure 3.5E) cells, with the majority of the Myp2 being pulled off of the main ring on the peeling bundle (Figure 3.5D). Tagging both proteins with different fluorophores in *adf1*-M3 cells further confirmed that Myp2, but not Myo2, was detected in peeling bundles (Figure 3.5F).

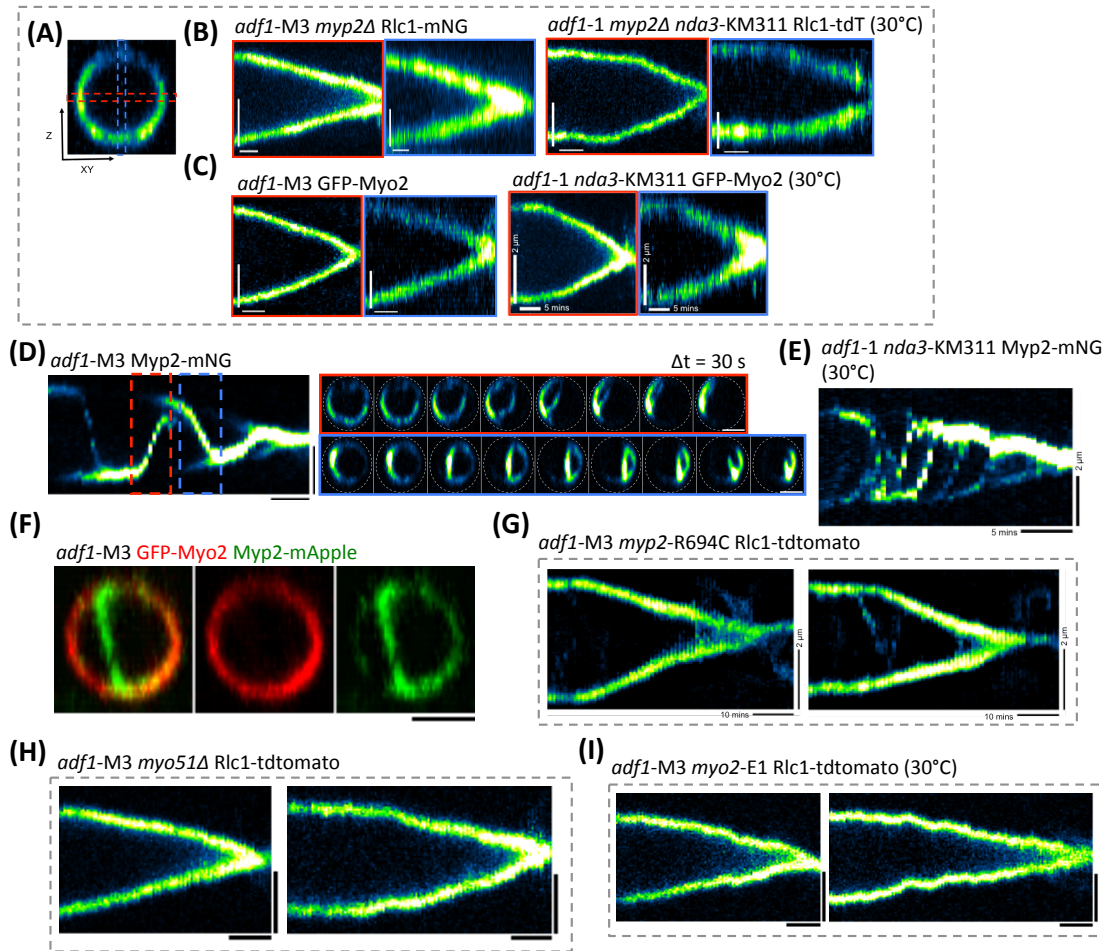


Figure 3.5: Ring peeling depends on three Myosin species.

- (A) To demonstrate the absence of ring peeling, kymographs of two perpendicular directions were created for contracting rings. Image shows the colour coding used for this section of the figure.
- (B) Kymographs from two perpendicular views of contracting rings in *adf1*-M3 *myp2*Δ and *adf1*-1 *myp2*Δ cells, using Rlc1 as a ring marker.
- (C) Kymographs from two perpendicular views of contracting rings in *adf1*-M3 and *adf1*-1 cells, when fluorescently tagged Myo2 is used as a ring marker.
- (D) Kymograph and montages of a contracting ring in an *adf1*-M3 cell, where Myp2 has been fluorescently tagged. Two separate peeling events are shown in the montages.
- (E) Kymograph of ring contraction in an *adf1*-1 cell, where Myp2 has been fluorescently tagged.
- (F) Single timepoint image of a peeling ring in an *adf1*-M3 cell, where both Myo2 and Myp2 have been fluorescently tagged.
- (G) Kymographs of contracting rings in *adf1*-M3 *myp2*-R694C cells, where a noticeable reduction in the number of peeling events is observed.
- (H) Kymographs of contracting rings in *adf1*-M3 *myo51*Δ cells, where ring peeling now appears to be completely absent.
- (I) Kymographs of contracting rings in *adf1*-M3 *myo2*-E1 cells at 30°C, where ring peeling also appears to be absent.

Scale bars in montages are 2 μm. Scale bars in kymographs are 2 μm and 5 minutes, except in G, where they are 2 μm and 10 minutes.

We were curious about which aspect of Myp2 function is responsible for the peeling bundles: Is it simply needed to act as a crosslinker, or is its motor function important as well? To test this, we used a *myp2* mutant, R694C, which maintains normal actin binding properties, but is unable to translocate actin filaments [105,142]. Creating an *adf1*-M3 *myp2*-R694C double mutant, and using Rlc1-tdT as a ring marker, we observed a distinct reduction in the number of observed peeling events, with only occasional, and weak, peeling events observed during cytokinesis in some cells (Figure 3.5G, 4 rings with no peeling, 11 rings with one or two peeling events, no rings with more than two peeling events). This would suggest that Myp2 motor function contributes to ring peeling, but that Myp2 crosslinking of actin bundles also plays a role, as we still see more peeling events than were observed in the *adf1*-M3 *myp2Δ* cells. However, a simpler explanation is that the same amount of ring peeling occurs in the *myp2Δ* and the *myp2*-R694C cells, but we do not see them in the *myp2Δ* cells because only Myo2 is fluorescently tagged in these cells, and it does not localise to the peeling bundles. We shall discuss this further in section 3.6.

As a control experiment, we decided to see if deleting *myo51* also had an effect on ring peeling in *adf1*-M3 cells. As Myo51 is thought to mainly function during AMR formation we expected its absence would have very little effect [71,100,106]. However, to our surprise, we observed an almost complete abrogation of the peeling phenotype (Figure 3.5H, 15 rings with no peeling, 1 ring with minor peeling, similar to Figure 3.3B), as observed in the *myp2Δ* cells. Sequencing confirmed that both the *myo51Δ* and *adf1*-M3 mutations were present in these cells.

Subsequently, we checked if Myo2, the only other myosin in the ring, also plays a role. It is not possible to delete *myo2*, as it is an essential gene, however there is a TS allele available, *myo2*-E1, which has been shown to be unable to bind and translocate actin filaments *in vitro* [51,139]. At the restrictive temperature of 36°C *myo2*-E1 cells are unable to form an AMR, so in order to allow rings to form we instead used the semi-restrictive temperature of 30°C, and in these cells we again

observed an almost complete absence of ring peeling (Figure 3.5I, 13 rings with no peeling, 2 rings with minor peeling, similar to Figure 3.3B).

3.6. Imaging ring peeling using the actin marker LifeAct

We have observed that *adf1*-M3 cells that also contain *myp2Δ*, *myo51Δ*, or *myo2*-E1 mutations do not display a ring peeling phenotype when using Rlc1 as a ring marker. However, it is still possible that ring peeling is occurring, and we are unable to observe it because of an absence of fluorescently tagged proteins on the peeling bundles. In order to determine whether this was the case, we decided to image these double mutants again, but this time using LAGFP (expressed under the *act1* promoter) as a ring marker, as this binds directly to cellular actin [69,143].

We first decided to qualitatively compare how the *adf1*-M3 mutation affects the distribution of actin throughout the cell. Comparing WT and *adf1*-M3 cells at different cell cycle stages, we observed an apparent increase in the number of actin patches in *adf1*-M3 cells, and the actin patches also appeared to have an increased fluorescence intensity (Figure 3.6A). Similarly, the fluorescence signal from the cytoplasm (representing both unbound and G-actin-bound LifeAct) also appeared to be reduced in *adf1*-M3 cells, suggesting that a greater proportion of the total cellular actin is contained in F-actin structures. Comparison of the LAGFP signal from the AMR was difficult to carry out, due to the extra actin patches in the *adf1*-M3 cells obscuring the signal from the ring (Figure 3.6A).

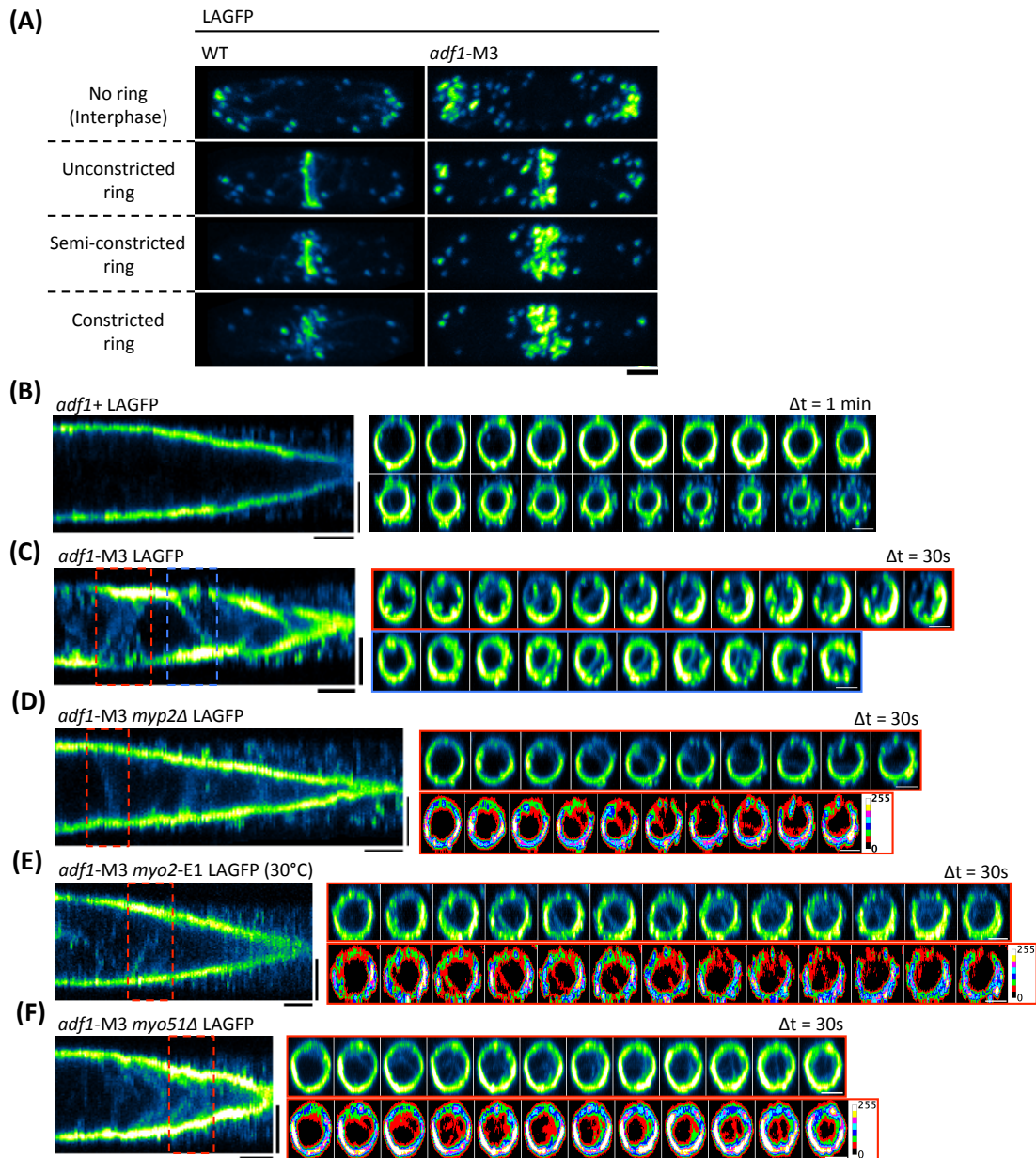


Figure 3.6: Ring peeling depends on three myosin species II.

- (A) Single timepoint images of WT and *adf1*-M3 cells expressing LAGFP, obtained at different points in the cell cycle, and highlighting the different distribution of F-actin between strains (intensities are roughly comparable between images).
- (B) Kymograph and montage of a constricting ring in a WT cell expressing LAGFP.
- (C) Kymograph and montage of a constricting ring in an *adf1*-M3 cell expressing LAGFP.
- (D) Kymograph and montage of a constricting ring in an *adf1*-M3 *myo2* Δ cell expressing LAGFP. Corresponding false colour images are shown in the montage to make faint peeling events more visible.
- (E) Kymograph and montage of a constricting ring in an *adf1*-M3 *myo2*-E1 cell expressing LAGFP. Corresponding false colour images are shown in the montage to make faint peeling events more visible.
- (F) Kymograph and montage of a constricting ring in an *adf1*-M3 *myo51* Δ cell expressing LAGFP. Corresponding false colour images are shown in the montage to make faint peeling events more visible.

Scale bars for montages and single timepoint images are 2 μm . Scale bars in kymographs are 2 μm and 5 minutes.

Next, we focused specifically on contracting rings, making kymographs in order to see if ring peeling could be observed. In WT cells, no ring peeling was observed, as would be expected (Figure 3.6B). In kymographs of *adf1*-M3 cells, peeling bundles were clearly visible (Figure 3.6C), and it appeared that there was a higher number of peeling events during ring contraction than compared to *adf1*-M3 cells imaged using Rlc1 as a ring marker, suggesting that there are some peeling bundles which do not contain Myp2.

We then investigated whether peeling bundles could be seen in *adf1*-M3 cells containing some of the previously used myosin mutations. Imaging *adf1*-M3 *myp2Δ* cells, we were able to detect peeling actomyosin bundles in contracting rings (Figure 3.6D). However, the frequency of these peeling events, and the intensity of actin on the bundles, was qualitatively much less than what was observed in *adf1*-M3 *myp2+* cells. This result would suggest that, while Myp2 is not essential for ring peeling to occur, it still plays a very important role, perhaps acting as a crosslinker within the peeling bundle, and/or providing the force to cause the bundles to peel off.

We obtained similar results when imaging *adf1*-M3 *myo2*-E1 cells at 30°C, with only occasional and faint peeling events being visible (Figure 3.6E). In *adf1*-M3 *myo51Δ* cells we also observed that peeling bundles appeared to be fainter, however the frequency of peeling events also appeared to be much higher (Figure 3.6F), somewhat resembling the continuous peeling we observed in *adf1*-1 cells (Figure 3.2B). We did attempt to make an *adf1*-M3 *myp2Δ myo51Δ* LAGFP strain, to see what affect the triple mutation would have on ring peeling, however we were not able to do so, as the strain would lose its LAGFP by the time we imaged it. Nonetheless, these experiments have shown that the peeling of myosin-containing bundles depended, to a large extent, on the activity of all three ring-localised myosins, although only Myp2 and Myo51 were clearly visualised as part of the peeling bundles (see below).

3.7. Localisation of other ring proteins in peeling rings

Currently, we have already seen how Rlc1, Myo2, Myp2, and actin localise in peeling rings, so we decided to also investigate the localisation of other ring proteins in peeling rings. A previous study found that contractile ring proteins seem to localise into three different layers within the ring: the proximal layer, which is closest to the membrane, an intermediate layer, and a distal layer, which includes actin [103]. We therefore decided to investigate whether the localisation of contractile ring proteins in peeling rings is dependent on which of the three layers the protein binds to. In order to see if the proteins localised to peeling bundles, we created strains where Rlc1 was also tagged. Because many of the proteins we were investigating localise to the AMR at quite low densities [64], we took single timepoint images with high laser intensities, rather than making timelapse movies as was previously done.

For the proximal layer, we have already seen that Myo2 does not localise to peeling bundles (Figure 3.5C), so we decided to also investigate the F-BAR protein Cdc15, the IQGAP Rng2, and the formin Cdc12. As for Myo2, we also observed no fluorescence from these proteins on peeling bundles (Figure 3.7A), with the possible exception of Cdc12, where for some rings it was possible to observe a very faint fluorescence signal on the peeling bundles.

For intermediate layer proteins, we decided to image the paxillin-like protein Pxl1, the actin filament anchoring protein Cyk3, the RhoGEF Rgf3, and the ubiquitin domain-like protein Blt1. Similarly to proteins in the proximal layer, none of the intermediate layer proteins showed any fluorescence on the peeling bundles (Figure 3.7B), however the fluorescence signal for Rgf3 was very low, so for this protein it is difficult to draw any conclusions.

Finally, we investigated proteins that localise to the distal layer. We have already seen that Myp2 and actin are important components of the peeling bundles, so we also sought to investigate the type-V myosin Myo51, the α -actinin Ain1, and the fimbrin Fim1. For Myo51, we

observed protein localisation on the peeling bundles, although a large amount of the protein remains in the main ring, unlike Myp2 (Figure 3.7C). We found that the *adf1-M3 ain1-mNG* strain appeared to be synthetically sick, which made it difficult to observe contractile rings, although we did manage to observe one ring with a peeling bundle, which showed some Ain1 localisation (Figure 3.7C). It has previously been observed that Adf1-M3 and Ain1 Δ have a synthetically sick genetic interaction [66], which would suggest that tagging Ain1 at its C-terminus significantly reduces the protein's functionality. Finally, we were unable to create a strain containing *adf1-M3* and *fim1-GFP*, again possibly due to a synthetic interaction between the two genes. Furthermore, looking closely at the fluorescence in the *fim1-GFP* strain, it was difficult to discern specific AMR localisation, despite previous papers suggesting that it does localise to the AMR [103]. Overall, these results suggest that only proteins that localise in the actin/distal layer of the ring can be observed in peeling bundles, whilst proteins in the intermediate and proximal layers remain in the main ring.

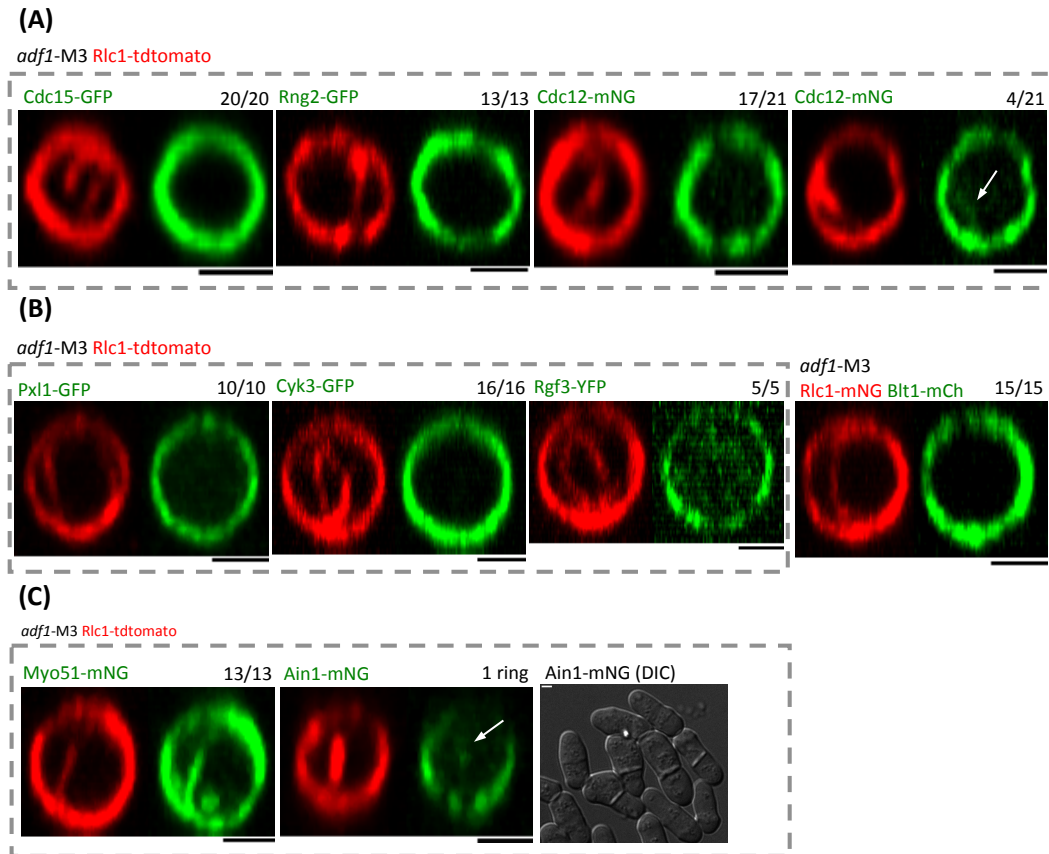


Figure 3.7: Protein localisation within peeling rings.

Fractions above images indicate the number of rings displaying the localisation shown, out of the total number of peeling rings observed.

- (A) Dual colour single timepoint images of rings in *adf1-M3* cells coexpressing fluorescently tagged Rlc1, and fluorescently tagged ring proteins from the proximal ring layer. No localisation of these proteins to peeling bundles is observed, with the possible exception of Cdc12.
- (B) Similar to A, except we are investigating proteins which localise to the intermediate layer of the ring. Again, no localisation to peeling bundles is observed, although some proteins were very faint.
- (C) Similar to A, except we are investigating proteins which localise to the distal/actin layer of the ring. We found that these proteins (and also Myp2) can be seen in peeling bundles. Cells containing *adf1-M3* Ain1-mNG were quite sick, so it was difficult to find rings with peeling bundles.

Scale bars in images are 2 µm.

3.8. Model of ring peeling in *adf1* mutant cells

Because previous work has shown that actin turnover is necessary for the stable generation of tension in AMRs [35,123,132,133], we hypothesised that reduced actin turnover might lead to an imbalance of tension along the ring, with regions of higher tension and regions of lower tension existing in the AMR. Regions of higher tension would then

experience a greater inwards force compared to other regions of the ring, which could then lead to the actin filaments in that region being peeled away from the ring (Figure 3.8A).

From this basic working model of ring peeling, we made two testable predictions about the ring's behaviour: Firstly, we hypothesised that the *adf1* mutant strains would be sensitive to further mutations that affect the anchoring of the AMR to the membrane/division septum, as this would make it easier for ring peeling to occur (Figure 3.8A). Secondly, because it has been suggested that ring tension regulates septum growth [90,134], we also hypothesised that if rings in *adf1* mutant cells have less uniform tension, then this could lead to asymmetric septum growth, and septation defects within *adf1* mutant cells.

3.9. Genetic interaction between *adf1*-M3 and mutations that partially compromise ring anchoring

To test our first prediction, we initially looked for potential genetic interactions between *adf1*-M3 and *pxl1Δ* cells, as Pxl1 has been shown to play a role in anchoring the ring to the membrane/septum, by linking ring components to the SH3 domains of Cdc15 and Imp2 [75]. Additionally, Pxl1 only arrives in the ring towards the end of anaphase [76], so any observed interaction should be entirely due to the effect of *pxl1Δ* on AMR contraction. Following tetrad dissection, we found that the presumed double mutants were inviable, indicating a synthetic lethal interaction (Figure 3.8B). We also found that deletion of the full-length *imp2* produced a lethal interaction with *adf1*-M3 (Figure 3.8B).

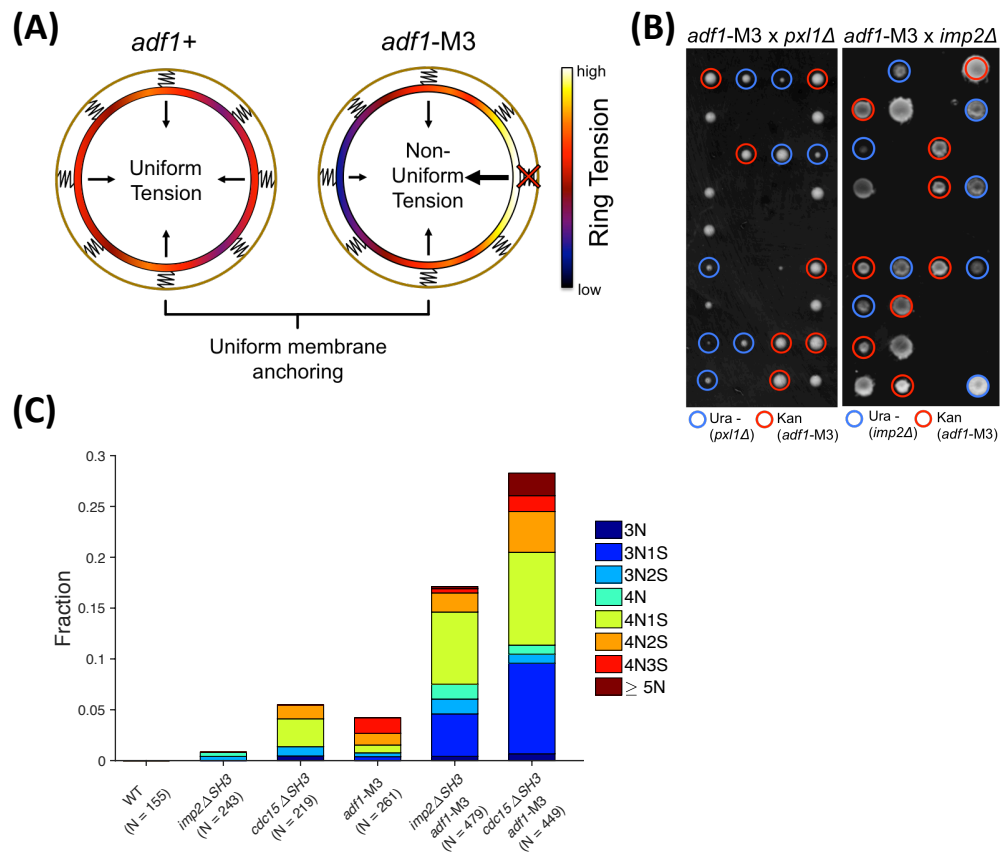


Figure 3.8: Genetic interaction between *adf1-M3* and *pxl1Δ/ΔSH3* mutations.

- (A) Diagram showing the cross-section of an *S. pombe* cell, with an AMR that is linked to the membrane via uniformly distributed linkers. We propose that in WT cells ring tension is uniformly distributed around the ring, while in *adf1-M3* cells the tension is non-uniform, which leads to regions of high tension, and causes actomyosin bundles to peel away from the ring.
- (B) Dissected tetrads of *adf1-M3* cells crossed with *pxl1Δ* and *imp2Δ*, showing that both of these double mutants are synthetically lethal (18 tetrads dissected for each cross).
- (C) Septum phenotype analysis from CW and DAPI staining of *adf1-M3 ΔSH3* double-mutant cells, showing that the strains are synthetically sick, with *adf1-M3 cdc15ΔSH3* cells having the most severe phenotype. Analysis only included cells with at least 2 nuclei. Data for cells with only 2 nuclei are not shown. Colour coding in legend denotes number of nuclei ('N') and number of septa ('S') that were visible in the cells.

As a next step, we decided to see if there was a similar interaction between *adf1-M3* cells and strains where the SH3 region of either *imp2* or *cdc15* was deleted. These strains were not synthetically lethal, but by fixing and staining with CW and DAPI, and counting the number of septa and nuclei in cells with ≥ 2 nuclei, we were able to show that they were

synthetically sick (Figure 3.8C). Whilst this would appear to further support our prediction that *adf1* mutant cells are sensitive to additional mutations that affect AMR anchoring, it is possible that this may not be due to an interaction between the proteins in question, but simply because increasing the number of defective proteins causes a deterioration in the overall health of the cell. Previous work looking for genetic interaction with the *adf1-1* allele found that many of the crosses did not display a synthetic effect, even when *adf1-1* was combined with mutations in genes encoding ring components such as Rng2, Cdc8 and Cdc12 [93], although from the paper it is not clear if this was determined based on more than just qualitative observations. Therefore, we can conclude that it is likely that *adf1* mutants are sensitive to further mutations that partially compromise ring anchoring, in support of our model of ring peeling. However, in order to be certain, it would be useful to perform further crosses of *adf1*-M3 cells with a selection of control mutants, that do not affect ring anchoring (or further perturb actin turnover), to check that these do not lead to an additive effect similar to what have observed with the $\Delta SH3$ mutants.

We decided to have a closer look at the effect that the *adf1*-M3 $\Delta SH3$ double-mutants had on the ring peeling phenotype, by using Rlc1-tdT as a ring marker. Because of the reduced number of connections between the actin filaments and membrane-bound proteins, we expected to see a greater number of peeling events, and to potentially see some ‘catastrophic’ peeling events which would cause the ring to fall apart. However, when we imaged the *adf1*-M3 *imp2* $\Delta SH3$ cells, ring peeling seemed to occur at the same frequency as in the *adf1*-M3 single mutant, and the only difference we could observe was a slower contraction rate of the AMR (Figure 3.9A). Whilst we did not observe any catastrophic peeling events, in one cell we noticed that the AMR did break apart during contraction.

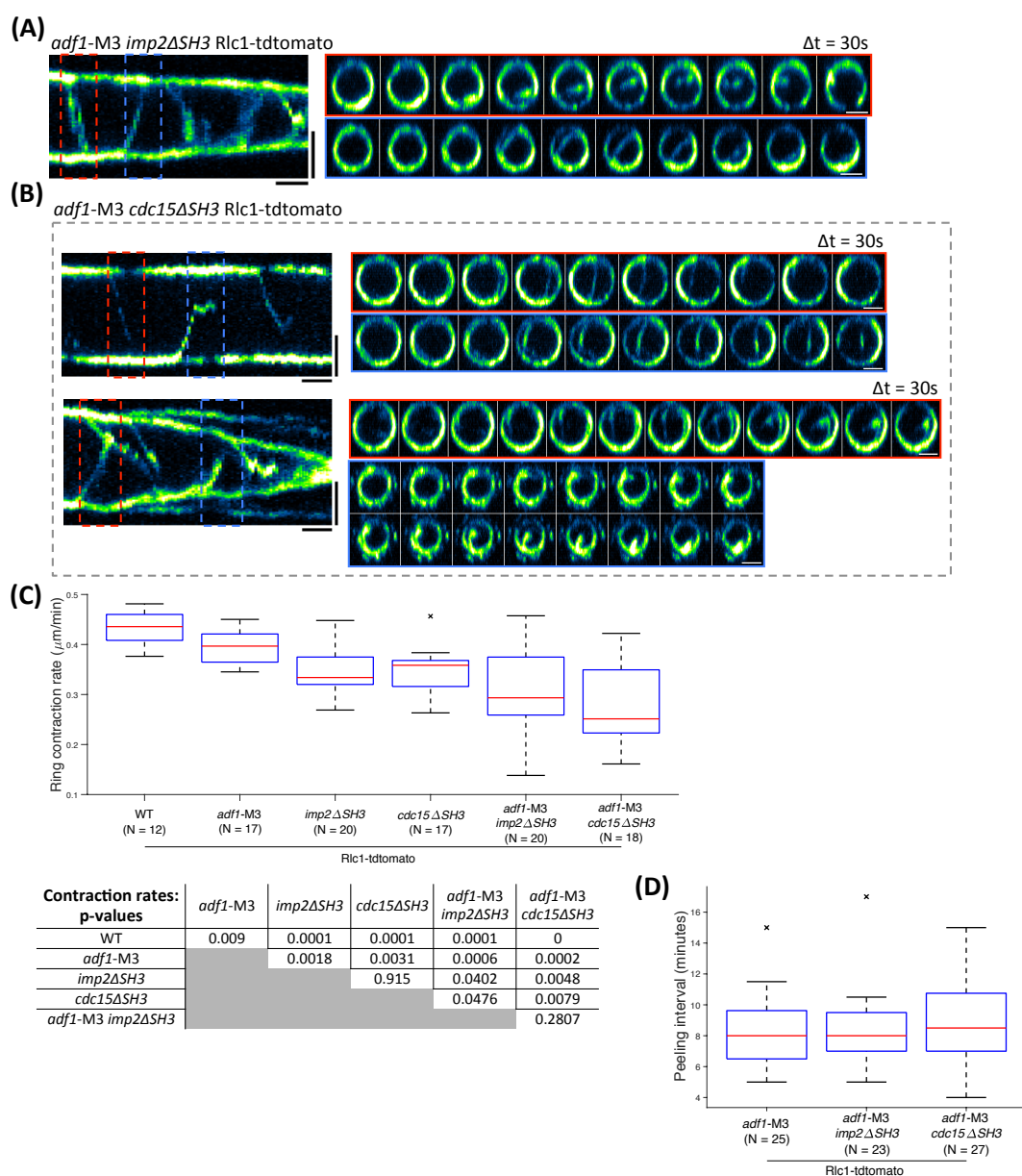


Figure 3.9: Examining ring contraction in *adf1-M3 Δ SH3* cells.

- (A) Kymograph and montages of an *adf1-M3 imp2 Δ SH3* ring undergoing slower contraction.
- (B) Kymographs and montages of two *adf1-M3 cdc15 Δ SH3* rings at different stages of cytokinesis.
- (C) Quantification of the ring contraction rates in WT, *adf1-M3*, Δ SH3 single mutant and *adf1-M3 Δ SH3* double mutant cells. P-values are shown in the table below, determined from the Mann-Whitney U test.
- (D) Quantification of the time interval between peeling events in *adf1-M3*, *adf1-M3 imp2 Δ SH3*, and *adf1-M3 cdc15 Δ SH3* rings. No significant differences are measured between the strains, determined from the Mann-Whitney U test.
- All scale bars in montages are 2 μm . Scale bars in kymographs are 2 μm and 5 minutes.

For the *adf1*-M3 *cdc15* Δ *SH3* cells, we also observed an apparent reduction in the ring contraction rate (Figure 3.9B). As before, we also observed some rings which appeared to break during contraction, and we also saw one ring which did not initiate contraction throughout the entire image collection time. Additionally, while discreet peeling events could still be observed in this strain, they appeared to be messier than in the *adf1*-M3 *imp2* Δ *SH3* strain, with Rlc1 fluorescence rarely subtending the entire arc of the peeling bundle (Figure 3.9B).

It was previously observed that *cdc15* Δ *SH3* rings contracted at a slower rate [75], so we also quantified the contraction rate of our double mutants, to see if the reduced contraction speed was purely due to the Δ *SH3* mutations, or because there was an additive affect with the *adf1*-M3 mutation. We found that, whilst the median contraction rate of Δ *SH3* single mutants was reduced compared with WT, the median contraction rate of the double mutants was reduced even further (Figure 3.9C). Additionally, we also observed a significant difference between the contraction rates of WT and *adf1*-M3 cells (Figure 3.9C), in contrast to our previous results where we did not detect a difference between the two strains (Figure 3.1A). In this experiment we were using Rlc1-tdT as a ring marker, whereas previously we were using Rlc1-mNG, which provides a potential explanation for this discrepancy, as Rlc1-tdT may exacerbate the *adf1*-M3 phenotype, and/or Rlc1-mNG may somewhat suppress the phenotype.

In order to further quantify the effect of these double mutants, we also measured the time interval between peeling events. The median time interval increased slightly between *adf1*-M3 and *adf1*-M3 *imp2* Δ *SH3* cells, and between the *imp2* Δ *SH3* and *cdc15* Δ *SH3* double mutants (Figure 3.9D), however this difference was not significant, suggesting that the peeling frequency is not drastically affected in these strains.

Overall, whilst we did find that *adf1*-M3 cells display synthetically sick/lethal interactions with strains where ring anchoring is compromised, these cells did not display the phenotypes we expected, such as an increased frequency of peeling events. However, we did

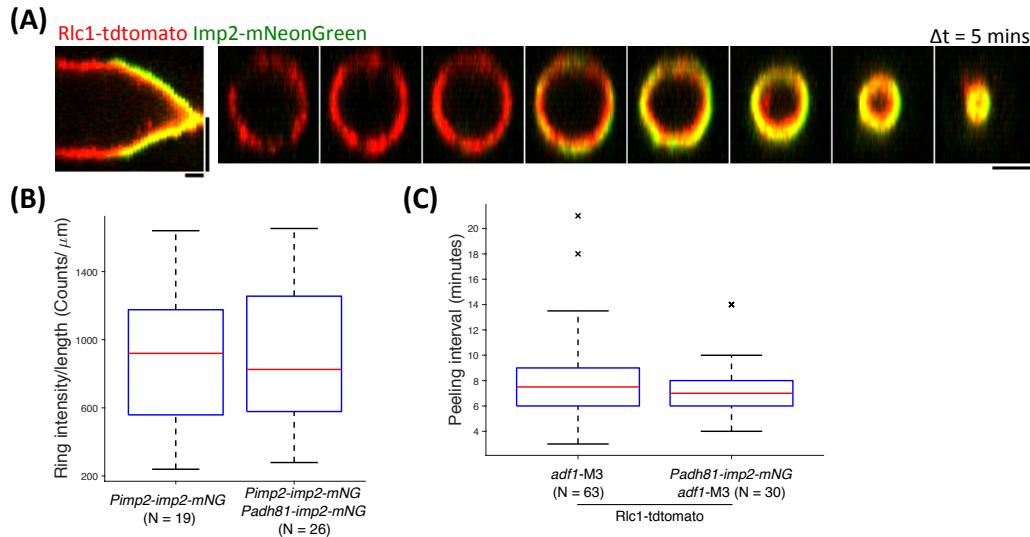


Figure 3.10: Attempting to rescue the peeling phenotype by increasing membrane anchoring of the ring.

- (A) Kymograph and montage showing the time that Imp2 localises to the ring.
 (B) Comparison of the amount of Imp2 localised to the ring between cells with a single copy of the *imp2* gene, and cells with two copies.
 (C) Comparison of the time interval between peeling events in *adf1-M3* cells where there is a single copy of *imp2*, and where there are two copies.

All scale bars in montages are 2 μm . Scale bars in kymographs are 2 μm and 5 minutes.

observe some rings that seemed to fall apart during contraction, and the combined effect of the double mutants lead to a reduced ring contraction rate, indicative of an additive effect during cytokinesis.

3.10. Attempting to rescue the peeling phenotype by increasing membrane anchoring of the ring

Because *adf1-M3* cells were sensitive to mutations that compromised membrane anchoring of the ring, we wondered if we could rescue the ring peeling phenotype by increasing the membrane anchoring. We decided to try and achieve this by inserting an extra copy of *imp2*, under the *Padh81* promoter [136,137], into the *S. pombe* genome. By imaging cells expressing *rlc1-tdT* and *imp2-mNG*, we found that Imp2 only localises to the AMR directly before the onset of ring contraction (Figure 3.10A), so having extra Imp2 in the cell should not adversely affect ring formation.

After inserting the 2nd copy of *imp2* into the genome, we checked to see if this led to an increased amount of Imp2 localising to the AMR. By imaging cells with uncontracted rings, and measuring the ring fluorescence/ring circumference, we found that there was no increase in the amount of ring-localised Imp2 after inserting an extra copy into the genome (Figure 3.10B), indicating that the rescue was unlikely to be successful. As expected, when we imaged *adf1*-M3 *Padh81-imp2-mNG* cells the peeling phenotype appeared to be unaffected, and when measuring the intervals between peeling events, we observed no difference between *adf1*-M3 and *adf1*-M3 *Padh81-imp2-mNG* cells (Figure 3.10C).

3.11. Effect of *adf1* mutations on septation

Based on our working model of ring peeling (Figure 3.8A), our second prediction was that *adf1* mutant cells would display septation defects, due to the hypothesised imbalance of tension around the ring. To test for this, we performed CW staining on WT, *adf1*-M2 and *adf1*-M3 cells, and quantified the different septa morphologies that we observed, performing separate analysis for fully-septated and partially-septated cells. For the fully septated cells, we saw only flat, hemispherical, or wavy septa in control cells. We reasoned that the wavy septa could be the result of non-uniform septum deposition, and therefore an indicator of non-uniform ring tension. By quantifying the relative proportion of each morphology, we found that the majority of WT cells displayed either hemispherical or flat septa, with a minority showing wavy septa (Figure 3.11A). In *adf1*-M2 and *adf1*-M3 cells, we saw a greater proportion of wavy septa compared to the control cells, and we also observed a number of cells that had either failed septation and undergone branching, displayed a misplaced hemispherical septum, or cells where the septum was particularly bright and messy, and it was difficult to determine a specific morphology (Figure 3.11A).

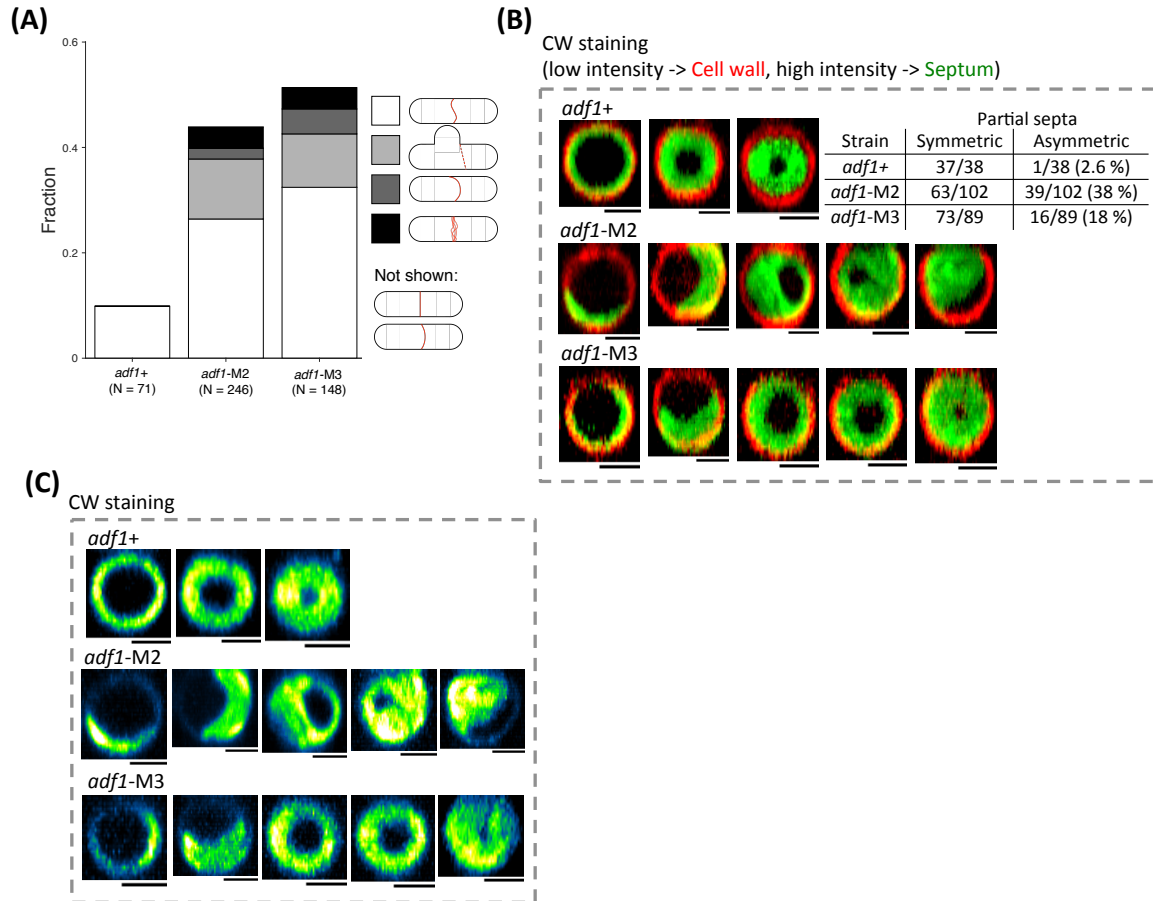


Figure 3.11: Effect of *adf1* mutants on septation.

- (A) Quantification of septum morphology in fully septated WT, *adf1-M2* and *adf1-M3* cells, from CW staining of fixed cells. Septa were categorised as being straight, hemispherical (data for these two not shown), wavy (white), branched and failed septation (light grey), misplaced hemispherical (dark grey), or bright and improperly organised (black).
- (B) Representative images of symmetric septa in WT cells, and asymmetric septa in *adf1-M2* and *adf1-M3* cells, from CW staining of fixed cells. Images have been segmented into low and high intensity regions, to represent the outer cell wall and the division septum, respectively. Table shows analysis of partially septated cells, showing the proportion of which appeared symmetric or asymmetric.
- (C) Corresponding non-segmented images for those shown in (B), showing CW staining of septa in WT, *adf1-M2*, and *adf1-M3* cells.
- Scale bars in single timepoint images are 2 μ m.

Next, we analysed the partially-septated cells, by looking for evidence of asymmetric septum deposition. We did so by visually examining the partially septated cells in our images, and looking for cells where bright CW staining (indicating deposition of septum material) was only visible partway around the cell circumference, or where septation was almost complete and the remaining hole in the septum was radially displaced from the centre of the division plane (Figure 3.11B and Figure

3.11C). In WT cells we only observed 1/38 (2.6 %) partially-septated cells with asymmetric septum deposition. By contrast, in *adf1*-M3 cells we found that 16/89 (18 %) cells displayed asymmetric septum deposition, whilst in *adf1*-M2 cells this increased to 39/102 (38 %) of the partially septated cells (Figure 3.11B).

The observation that more *adf1*-M2 cells display asymmetric septum deposition than *adf1*-M3 cells makes sense, as *adf1*-M2 is the more severe of the two mutants, so it would presumably have the greater effect on ring tension during AMR contraction [66]. Whilst we did not quantify the degree of asymmetry, qualitative observations would also suggest that the partial septa in *adf1*-M2 cells were more asymmetric than those in *adf1*-M3 cells, especially when comparing cells at the later stages of septation (Figure 3.11B and Figure 3.11C). However, this raises the questions of why we observe slightly more aberrant septa in *adf1*-M3 cells when quantifying the fully septated cells (Figure 3.11A). Perhaps it is the case that a greater portion of the septa in *adf1*-M2 cells are so asymmetric that they are unable to successfully complete septation [134], which reduces the number of aberrant septa we observe when quantifying fully septated cells, and increases the portion of partially septated cells that are observed to be asymmetric.

As this data indicates that septum synthesis is defective in *adf1* mutant cells, this also supports our working model that reduced actin turnover during AMR contraction leads to a non-uniform tension distribution around the ring, which then causes ring peeling to occur at regions of increased tension (Figure 3.8A).

3.12. Attempting to recreate and rescue the ring peeling phenotype through drug treatment of cells

Having observed and investigated our ring peeling phenotype, we wondered if this phenotype could be recreated by treating WT cells containing fully formed rings with the actin stabilising drug Jasplakinolide. *S. pombe* is known to be relatively impermeable to a

number of drugs, including Jasplakinolide, so to account for this problem, we used a strain of *S. pombe* where the 7 multi-drug-resistance genes have been deleted (7mdr strain) [144], which was found to make the cells more susceptible to drug treatments. However, when using the 7mdr strain, with Rlc1-mNG as a ring marker, and treating cells with various concentrations of Jasplakinolide, we found that ring contraction was blocked for concentrations greater than 50 μ M, or appeared to be unaffected when using concentrations below this value (data not shown). DMSO control treatments produced no detectable affect.

We also attempted to perform these experiments on spheroplasts of 7mdr Rlc1-mNeonGreen cells. Similarly to before, we observed that at a concentration of 25 μ M or higher, ring contraction was blocked, whilst at concentrations of 10 μ M or less the rings would slide across the membrane as in WT cells. Some rings, when treated with lower concentrations of Jasplakinolide, did seem to display some minor peeling events (Figure 3.12A). However, examples of this could also be seen in DMSO controls, and in spheroplasts that had undergone no special treatment (Figure 3.12B), meaning that this was not a specific effect of the Jasplakinolide treatment. Interestingly, in both the Jasplakinolide treated and untreated spheroplasts, we saw that the rings would sometimes fall apart shortly after a peeling event occurred (Figure 3.12A and Figure 3.12B), suggesting that the altered cellular geometry, and/or the absence of a division septum, makes AMR contraction in spheroplasts less robust, and more prone to failure.

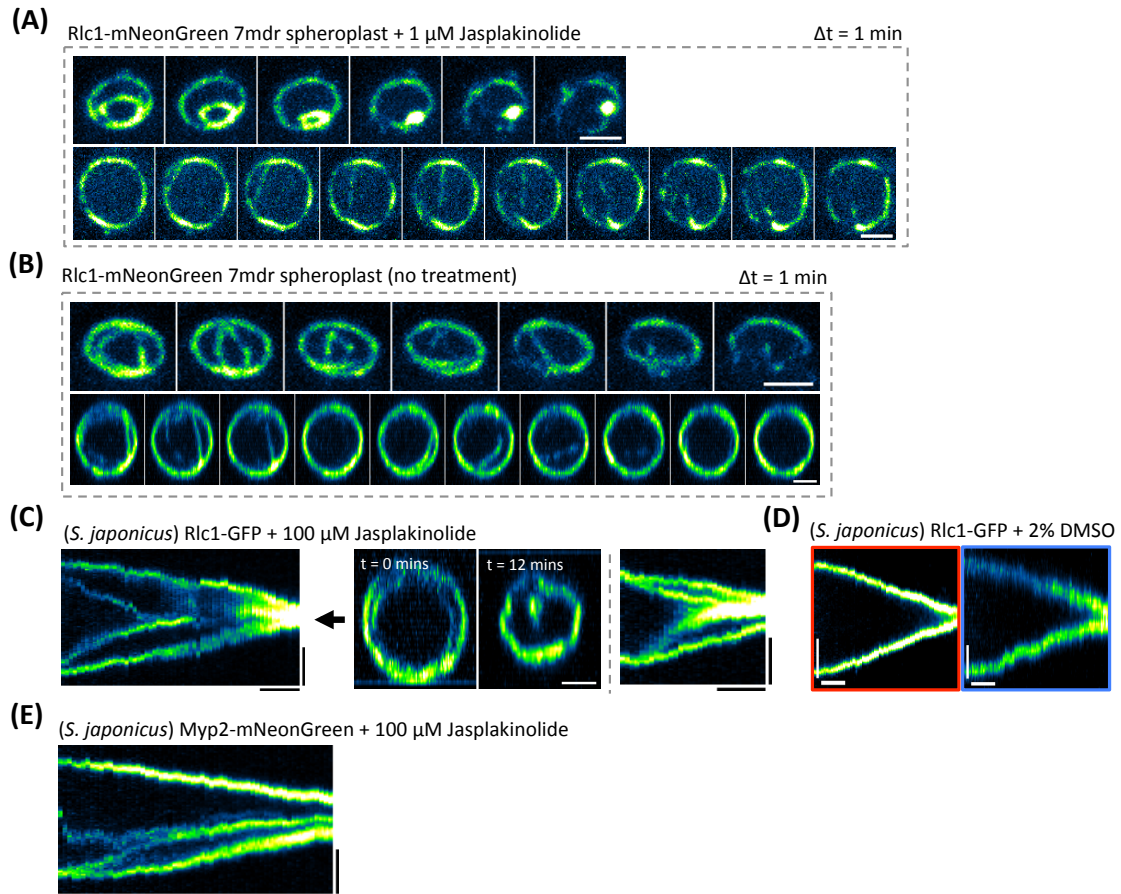


Figure 3.12: Drug treatment of fission yeast cells to recreate the phenotype.

- (A) Montages of contracting rings in 7mdr spheroplasts treated with 1 μ M Jasplakinolide, which display minor ring peeling events.
 - (B) Montages of contracting rings in 7mdr spheroplasts that underwent no special treatment, but still display minor ring peeling events.
 - (C) Two example kymographs of ring contraction in *S. japonicus* cells expressing Rlc1-GFP that have been treated with 100 μ M Jasplakinolide. Additionally, a short montage is shown for the first kymograph, demonstrating the distortion in the main ring as ring contraction progresses.
 - (D) Kymographs of two perpendicular views of a contracting ring in an *S. Japonicus* cell expressing Rlc1-GFP, treated with DMSO (control for experiment in C).
 - (E) Kymograph of ring contraction in an *S. japonicus* cell expressing Myp2-mNeonGreen, which has been treated with 100 μ M Jasplakinolide.
- Scale bars in montages are 2 μ m. Scale bars in kymographs are 2 μ m and 5 mins.

Subsequently, we wondered if it would be possible to recreate the phenotype using the fission yeast *S. Japonicus*, which is a very close relative of *S. pombe*, and is known to be more amenable when it comes to pharmacological studies [135,145]. We treated cells expressing *rlc1-GFP* with 100 μ M of Jasplakinolide, and found that in cells containing contracting AMRs we could observe bundles of Rlc1 peeling away from

the main ring (Figure 3.12C). However, the behaviour of these bundles was different to that observed in *S. pombe* *adf1*-M3 cells, as only one main peeling event was observed, after which the peeled bundle remained in the centre of the ring as a loose aggregate, until the main ring contracted inwards towards it. Additionally, defects in the contraction of the main ring were often observed, with the ring losing its circularity and becoming kinked as contraction progressed (Figure 3.12C). 50 μ M Jasplakinolide treatment only caused a few minor peeling events, and rings in DMSO controls showed no peeling, or cytokinesis defects (Figure 3.12D).

As in *S. pombe*, Rlc1 is a light chain for both of the myosin II heavy chains, Myo2 and Myp2, in *S. Japonicus*. We therefore decided to repeat the drug treatment experiments in strains where Myo2 and Myp2 were separately tagged. Using Myp2-mNG as a ring marker, we again observed a single peeling event upon treatment with 100 μ M Jasplakinolide (Figure 3.12E). Compared to the peeling observed in *S. pombe* cells with *adf1* mutations, a larger proportion of the Myp2 appeared to remain in the main ring after the peeling event (Figure 3.12E). We attempted to perform a similar experiment using mNG-Myo2 as the ring marker, however the fluorescence signal from this strain was very low (data not shown), making it difficult to observe whether the Myo2 stayed on the membrane, as would be expected from the results in *S. pombe*.

As a final drug treatment experiment, we wondered if the ring peeling phenotype in *S. pombe* *adf1*-M3 cells could be rescued by treating with a drug that severs actin filaments, such as Swinholide A [146,147]. We initially attempted to perform the rescue on *adf1*-M3 cells, with Rlc1 used as a ring marker. Swinholide A was used at concentrations of 10 and 20 μ M, however we observed no difference in the behaviour of rings when comparing to DMSO control cells (data not shown).

Again, we wondered if the drug was able to enter the cell, and remain in the cell without being pumped out by the efflux pumps. Using the 7mdr strain that we used before was not feasible, because when performing a genetic cross, the presence of so many mutations/deletions

means that the chance of any given spore containing all of these mutations, in addition to the mutations/deletions/insertions in the second strain is incredibly low, meaning that an unfeasibly large number of spores would need to be analysed in order to find the desired strain (i.e. 7mdr *adf1*-M3 *rlc1*-mNG/tdT).

Instead, we decided to use a strain containing the *pap1* Δ mutation. *pap1* is a regulator of a number of efflux pumps in *S. pombe*, such as Bfr1, Pmd1 and Caf5, and loss of function, or deletion of the gene, makes the cells more sensitive to various drug treatments [148]. We therefore performed Swinholide A treatment on *adf1*-M3 *pap1* Δ cells. Treating with 5 μ M of the drug, we observed that a large number of rings fell apart (data not shown), particularly those in the late stages of assembly or the early stages of contraction, which we did not see in the DMSO treatment. This made it difficult to observe whether the drug had an effect on the cells, although in rings that were already at the later stages of contraction we still saw peeling events. We did not perform further experiments with lower concentrations of Swinholide A due to time constraints.

3.13. Effect of the *adf1*-M3 mutation on the amount of myosin and actin in the ring

Reduced actin severing appeared to lead to an increase in the proportion of cellular actin that was in the form of F-actin, rather than G-actin (Figure 3.6A). However, it was difficult to observe if this also led to an increase in the amount of actin contained in the ring. Whilst it might be logical to assume that this is the case, it is also possible that the reduction in the amount of actin in the G-actin pool, and the large increase in the number of actin patches (Figure 3.6A), plus the increase in their intensity and lifetime [149], might lead to there actually being less actin in the AMRs of *adf1*-M3 cells.

If it is the case that the amount of actin in the AMR is altered, then it is possible that the amounts of other proteins in the ring might also be affected in *adf1*-M3 cells. We decided to investigate this, by measuring

the amount of Myo2 and Myp2 in the AMR in WT and *adf1*-M3 cells, and then comparing the amount of actin in the rings, by using LAGFP as an actin marker, and using fluorescence from Rlc1-tdT to segment out the portion of the LifeAct signal that is from the AMR [150].

Because the amount/concentration of various ring proteins in *S. pombe* has been shown to change during AMR contraction [64], we decided to quantify the amount of protein in the ring as a function of time. However, in order to avoid having to make timelapse movies to observe the onset of contraction, which would then require taking account of imaging-induced photobleaching, we instead took single timepoint images, and used the ring's size as a measure of how far through contraction it had progressed (Figure 3.13A). This takes advantage of the relatively constant contraction rate of the AMR in *S. pombe*, in order to assume that the reduction in ring size is proportional to the length of time that the ring has been contracting for [37]. To calculate this 'contraction index', we measured the ring diameter, and divided this by the cell diameter, measured from DIC images. We then subtracted this value from 1 to obtain the contraction index, which is ~0 for uncontracted rings, and approaches a value of 1 for rings that have fully contracted (Figure 3.13A).

To measure the amount of Myo2 and Myp2 in the ring, we made sum intensity projections of 3D images, and drew ROIs around the region of Myo2 fluorescence. This region was used to measure both the total Myo2 and Myp2 fluorescence, and then these values were divided by the circumference of the ring, as we found this produced a linear relationship when plotted against the contraction index, which made it easier to compare between the two strains (Figure 3.13B).

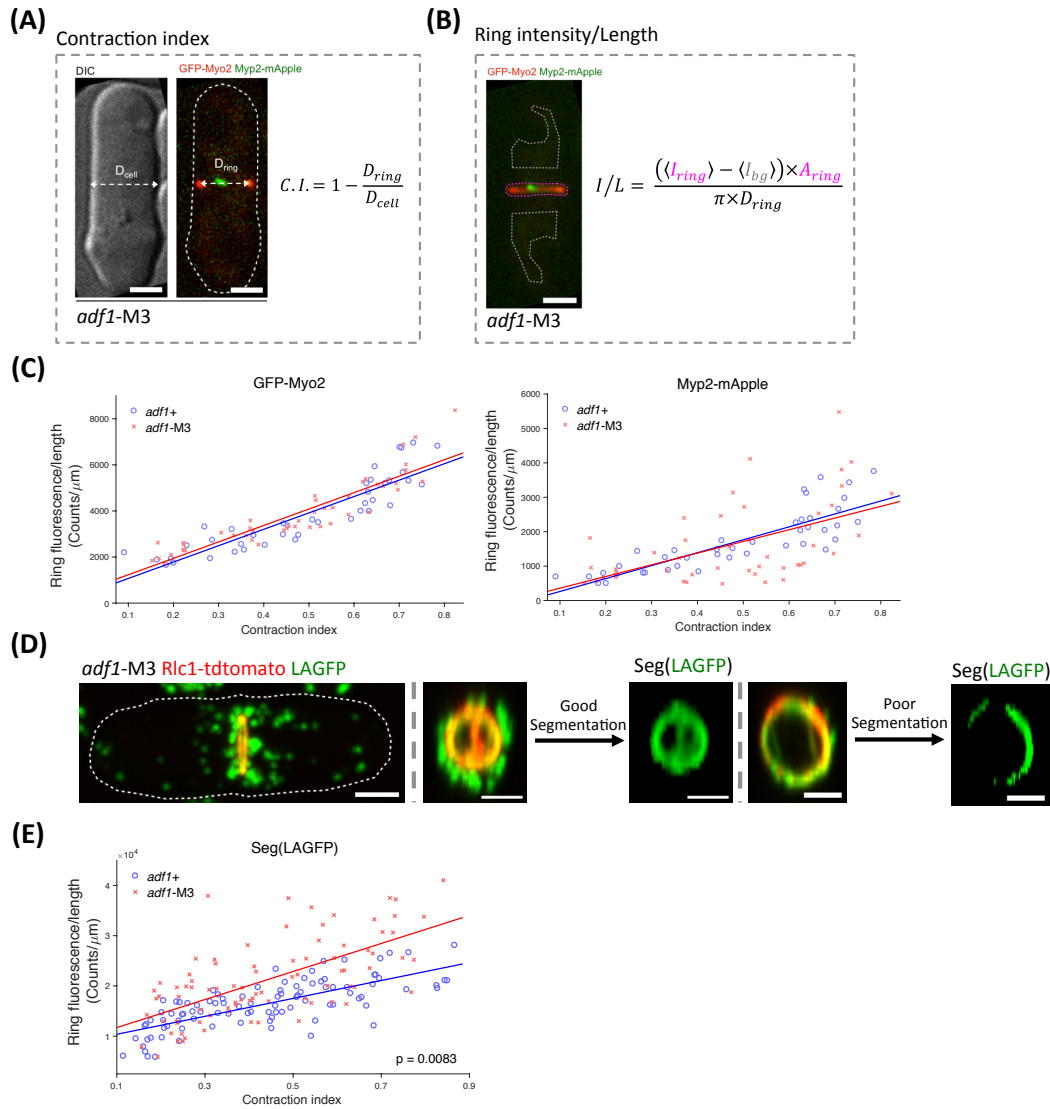


Figure 3.13: Effect of Adf1-M3 on protein levels in contracting rings.

- (A) Diagram depicting how the contraction index (C.I.) was measured, to provide an approximate measure for the time after the onset of ring contraction.
- (B) Diagram depicting how the fluorescence intensity was measured from rings, including normalisation from background (bg) measurements.
- (C) Plots comparing ring fluorescence/length vs. C.I. for cells containing both GFP-Myo2 and Myp2-mApple, in *adf1+* and *adf1-M3* backgrounds. No statistical difference was measured in the intensity of either protein in the ring across both strains (determined from ANCOVA).
- (D) Rlc1-tdtomato fluorescence was used to segment out the ring fluorescence from LAGFP in *adf1+* and *adf1-M3* cells. In some cases, this produced a good segmentation (1st example), however sometimes only part of the LifeAct signal from the ring was segmented out (2nd example), which were referred to as poorly segmented rings. Rings that were determined to be poorly segmented (in both sets of cells) were excluded from subsequent analysis.
- (E) Plot comparing ring fluorescence/length vs. C.I. for the segmented LAGFP signal in *adf1+* and *adf1-M3* cells. Comparison of the two datasets shows a statistically significant difference between them (determined from ANCOVA), with the linear fits to both datasets having the same y-intercept, but different slopes, meaning that rings in *adf1-M3* cells appearing to retain more actin as ring contraction progresses.
- Scale bars in single timepoint images are 2 μ m.

As the localisation of Myo2 to the AMR is independent of actin, we expected there to be no difference in the amount of ring fluorescence between the two strains, and we indeed found this to be the case (Figure 3.13C). Myp2 localisation to the AMR, on the other hand, is dependent on actin, so presumably any difference in the amount of ring-localised Myp2 between the strains would be indicative of a difference in the amount of actin in the ring. Once again, we saw no difference between the two strains (Figure 3.13C), suggesting that the amount of F-actin in the AMR is not altered by the *adf1*-M3 mutation, although the variability in the amount of Myp2 in the ring appeared to be greater in the *adf1*-M3 cells.

Next, we tried to compare the amount of actin in the AMR in WT and *adf1*-M3 cells. We used LAGFP as an actin marker, and Rlc1-tdT to segment out the portion of the LAGFP in the ring (Figure 3.13D), in order to exclude the fluorescence signal from the nearby actin patches (Figure 3.6A), which would be difficult to exclude using the same method we employed earlier (Figure 3.13B) [149,150]. We found that some rings were well segmented by this process, however some were not (Figure 3.13D), with large segments of the ring not being included in the final image. We found examples of this poor segmentation in both WT and *adf1*-M3 strains.

When we included this poorly segmented data in our analysis, we did not observe a difference between the WT and *adf1*-M3 cells. However, when we excluded the poorly segmented rings from the dataset (excluding rings where more than a quarter of the ring's circumference was not visible in the segmented image), we were able to detect a difference in the amount of ring-localised LAGFP (Figure 3.13E). It seems that uncontracted rings in both strains contain roughly the same density of LAGFP, while as the rings contract the *adf1*-M3 cells accumulate a greater density of LAGFP in their rings (Figure 3.13E).

However, because we are using an actin binding protein as an actin marker, rather than directly tagging actin itself (because fluorescently tagged actin does not incorporate into formin-nucleated actin filaments [64]), we must be cautious about the conclusions we

draw from results obtained using LAGFP. Because cellular LifeAct exists in equilibrium between an unbound state, a G-actin bound state, and an F-actin bound state [143], changes in the ratio of F-actin/G-actin within the cell will only lead to a proportional change in the amount of F-actin-bound LifeAct within a very small range. Considering the magnitude of the apparent change in the proportion of F-actin/G-actin between WT and *adf1*-M3 cells (Figure 3.6A), it seems unlikely that this difference would fall within this small range, therefore it would be unwise to use our measurements of ring-localised LAGFP signal to draw any firm conclusions about the effect of the *adf1*-M3 mutation on the amount of actin contained in the AMR. Using the previously measured dissociation constants of LifeAct binding to both G- and F-actin [143], we performed a simple back-of-the-envelope calculation which suggested that using LAGFP would overestimate changes in the ratio of F-actin/G-actin, assuming that $[F\text{-actin}] \leq [G\text{-actin}]$ within the cell (see section 8.1).

3.14. Blocking ring contraction in *adf1*-M3 cells

We previously observed that contracting rings in *adf1*-M2 and *adf1*-M3 cells only display 3 – 4 peeling events per ring contraction (Figure 3.3C). However, as the ring is decreasing in size, it is possible that there could be more ring peeling events, which cannot be seen because the ring is too small. There is also the question of whether ring peeling could carry on indefinitely if ring contraction is slowed down, or stopped entirely, in an *adf1*-M3 cell. We already saw in *adf1*-M3 $\Delta SH3$ double-mutants that, although ring contraction was slowed down, the time interval between peeling events was unaffected (Figure 3.9D), suggesting that ring peeling is able to persist indefinitely in a ring where contraction has been completely blocked.

To test this, we created a double mutant strain containing *adf1*-M3 and *cps1*-191. *cps1*-191 is a TS mutation of the primary septum synthesis protein Bgs1, which blocks ring contraction at 36°C (*bgs1* is an essential gene, so it is not possible to create a deletion mutant in haploid

S. pombe cells). Cells containing both mutations, with Rlc1-mNG as a ring marker, were blocked at 36°C for three hours, before imaging. In these cells, we observed a large aggregate of Rlc1 material in the centre of the ring, with only a few faint bundles of actomyosin peeling off from the main ring to join this aggregate (Figure 3.14A). As would be expected, the Rlc1 aggregate, and faint peeling bundles, are not present in cells that also have their *myp2* gene deleted (Figure 3.14B).

However, as a control experiment we also imaged *adf1*-M3 *bgs1*⁺ cells at 36°C, to see if the observed phenotype was a result of imaging the cells at 36°C, rather than from blocking septation. Unfortunately, this seemed to be the case, with the ring peeling behaviour of *adf1*-M3 *bgs1*⁺ cells at 36°C more closely resembling that of the *adf1*-M3 *cps1*-191 cells at 36°C (Figure 3.14C), rather than the behaviour of *adf1*-M3 *bgs1*⁺ cells at 25°C (Figure 3.1B).

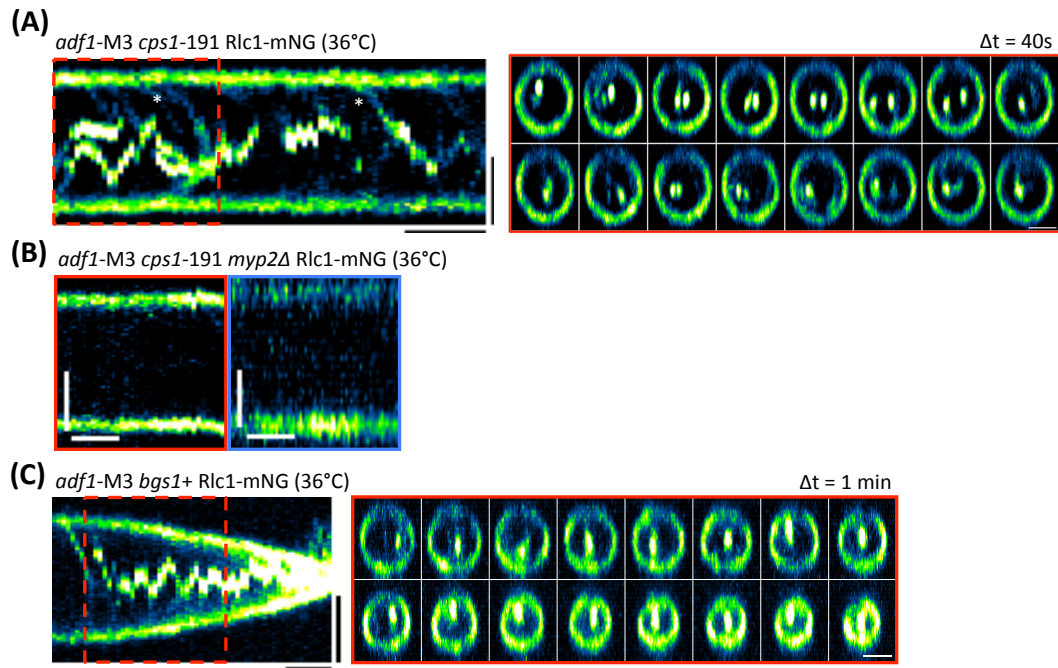


Figure 3.14: Effect of blocking ring constriction in Adf1-M3 cells.

- (A) Kymograph and montage of peeling behaviour in rings in *adf1-M3 cps1-191* cells which have been blocked at 36°C. Faint actomyosin bundles (asterisks) can be observed peeling off towards an actomyosin aggregate in the middle of the ring.
- (B) Kymographs of *adf1-M3 cps1-191 myp2Δ* rings, made from two perpendicular views of the ring (as indicated in Figure 3.5A) showing the absence of an actomyosin aggregate in the middle of the ring.
- (C) Kymograph and montage of ring contraction in *adf1-M3 bgs1+* cell at 36°C, which also shows the presence of the actomyosin aggregate seen in rings in *adf1-M3 cps1-191* cells.

Scale bars in montages/single images are 2 μm . Scale bars in kymographs are 2 μm and 5 minutes.

3.15. Discussion

3.15.1. Why do we observe different ring peeling behaviour with different mutants/treatments?

We set out to investigate the effect of reducing actin turnover during fission yeast cytokinesis. To do so we employed a number of previously characterised mutants of the *S. pombe* actin severing protein Adf1 [66,93], whilst also attempting to use Jasplakinolide treatment of WT fission yeast cells to stabilise actin in contracting rings. From our experiments, we saw that contracting rings in *S. pombe adf1* mutant cells

displayed a peeling phenotype (Figure 3.1B, Figure 3.1C, Figure 3.2B). This phenotype was dynamic, with multiple peeling events occurring during cytokinesis, and in *adf1*-M2 and *adf1*-M3 cells the peeling bundles moved in a back-and-forth manner across the AMR (Figure 3.3E). When we treated *S. Japonicus* cells with Jasplakinolide, we also saw the peeling of actomyosin bundles away from the ring (Figure 3.12C). However this was a much more static phenotype, with only a single peeling event occurring directly after treatment with the drug, and with the peeled bundle remaining in the centre of the ring until the main ring contracted inwards to meet it.

This difference can perhaps be explained by the observation that peeling occurs across almost the entire circumference of the ring in *S. japonicus* (Figure 3.12C), whereas in *S. pombe* the peeling originates only from a small arc of the ring (Figure 3.1B, Figure 3.1C). This might mean that, in *S. pombe*, once the bundle is peeled off it is able to be pulled in to the opposite side of the ring through its attachment points, whilst because the bundles in *S. japonicus* peel off from everywhere it is not left with any attachment points to the ring, so the bundle cannot be reeled in. However, the question then becomes why there is a difference in the peeling locations between the two organisms. Perhaps there are some unknown structural differences between the AMRs in each organism, or perhaps Adf1 has an unknown additional role and/or Jasplakinolide has an unknown additional effect, which causes this difference in behaviour.

Then there is also the question of why the peeling phenotype of rings in *adf1*-M2 and *adf1*-M3 cells is different to what we observed in *adf1*-1 cells. It is probably unlikely that this is due to differing degrees of severity of these mutations, since the *adf1*-M2 mutation induced a similar relative change in the ring contraction rate compared to the *adf1*-1 mutation at 30°C (Figure 3.1A, Figure 3.2A), potentially indicating that these alleles are similar with regards to their severity. Whilst the Adf1-M2 and Adf1-M3 proteins have been biochemically characterised [66], this has not been carried out for Adf1-1 [93]. Therefore, we do not know whether the phenotype of the *adf1*-1 mutation is caused by a reduced F-

actin binding affinity, a reduced actin severing rate, a mixture of both, or by some other factor. Since the Adf1-M2 and Adf1-M3 proteins were found to have reduced actin binding and actin severing [66], it is possible that the Adf1-1 protein may only experience a reduction in one of these, which could then affect the exact nature of the observed peeling phenotype. We shall discuss this further in the next section.

Going further, one may also wonder why the ring peeling phenotypes in *adf1*-M2 and *adf1*-M3 cells are so similar, even though they are completely different mutations in the *adf1* gene. Both Adf1-M2 and Adf1-M3 were previously found to have reduced actin binding and actin severing, and their behaviour only differed in the degree to which these properties were reduced [66]. This is despite the fact that the *adf1*-M2 mutations are located on the opposite side of the protein to the *adf1*-M3 mutations, which are found in the actin-binding domain [66]. How these two sets of mutations lead to the same qualitative effects will be difficult to answer without, for example, performing molecular dynamics or protein folding simulations to investigate their allosteric effect. However, the fact that these two mutations produce the same qualitative effects on the properties of the protein would suggest that the subsequent phenotypes would also be similar.

3.15.2. What is the cause of ring peeling in *adf1* mutant cells?

We hypothesised that the initial peeling-off of a bundle is caused by a circumferential tension imbalance in the AMR (Figure 3.8A). This idea was inspired by recent work performed in *Drosophila* embryos, examining the role of actin dynamics during gastrulation [151]. In this study, the authors targeted Profilin, Cofilin, and Cyclase-associated protein (all of which are involved in the turnover of actin), and also injected cells with latrunculin A (actin monomer sequestering drug) and phalloidin (actin disassembly inhibitor), in order to probe the effects of reduced actin turnover. The authors found that when actin turnover was reduced the balance of tension along the apical surface was lost, and

epithelial cells would often become stretched and distorted, and subsequently some of the embryos even failed to form a ventral furrow during apical constriction [151].

When trying to find a possible explanation for our peeling phenotype, we realised a similar model would also provide an explanation for our observations in *S. pombe*: If reduced turnover of actin leads to tension imbalance around the ring, then some regions will experience a higher inwards force [134], and these regions may undergo peeling. We do not know whether a non-uniform distribution of tension is a common feature of contractile actomyosin systems when actin turnover has been reduced. The importance of actin turnover for the generation of tension and contractility has only been realised as a result of theoretical studies [1], so it seems likely that further theoretical work would be the best way to determine the effect of reduced actin turnover within an AMR, and whether this leads to tension heterogeneity.

It has also been hypothesised that ADF/Cofilin proteins are able to regulate actomyosin assembly and contractility, not just by severing and/or depolymerising actin filaments, but by also competing with myosin II for actin binding sites [152]. The authors of this study used ADF/cofilin from a range of organisms (human, chick, *Xenopus*, *Drosophila*, *acanthamoeba*, starfish and yeast – presumably *S. cerevisiae*) to perform F-actin cosedimentation along with myosin S1 fragments. By doing so, they found that the molar ratio of actin-bound myosin S1 to F-actin decreased as the concentration of ADF/cofilin increased, indicating that the ADF/cofilin is able to competitively inhibit binding of myosin II to F-actin. If this is also the case for Adf1 in *S. pombe*, then this would further support our model, as it was found that Adf1-M2 and Adf1-M3 have reduced actin binding affinity, which would create more actin binding sites for myosin II in the ring, and therefore increase ring tension. If the overall ring tension is higher, in addition to there being an imbalance of tension around the ring, then this would further increase the propensity for ring peeling to occur in *adf1*-M2 and *adf1*-M3 cells.

Additionally, this may provide a potential explanation for the differences in phenotypes observed between *adf1-M2/adf1-M3* cells and *adf1-1* cells: Adf1-M2 and Adf1-M3 were previously biochemically characterised and found to have reduced binding to actin filaments [66], while Adf1-1 has not undergone such characterisation. It is possible that Adf1-1 displays more normal binding kinetics to actin filaments, and only struggles with severing/depolymerisation, for example. If this is the case, then Adf1-1 would still compete with myosin II for actin binding sites, unlike Adf1-M2 and Adf1-M3, meaning that the overall ring tension would not be increased, which would then affect the exact behaviour of the peeling bundles (Figure 3.1B, Figure 3.1C, Figure 3.2B).

Our model of tension imbalance does not answer the question of how a peeled bundle subsequently moves across the ring after it has peeled off: Does the peeling bundle itself contract, or is it reeled in through its attachment points (which also move around the ring)? Our observation of a bundle that peels off from a part of the ring with a noticeable kink would support the second idea, as the kink is also present in the peeling bundle, which suggests that the central region of the bundle is not contracting or under tension (Figure 3.1F). This implies that peeling bundles are reeled in at their attachment points, with the shortening of the peeled bundle pulling the attachment points along passively. Quantification of the shortening rate of peeling bundles shows that there does not appear to be a difference between the unbroken peels and the reeling-in of the snapped bundles (Figure 3.3D), which further suggests that the tension stored within a peeled bundle is negligible.

In this case, it would seem likely that Myo2, which remains in the ring during peeling events, would be the motor responsible for the reeling-in at the attachment points, while Myp2 and Myo51 may mostly play a role in crosslinking the peeling bundle. However, this does not explain why the absence of *either* Myp2 *or* Myo51 causes ring peeling to disappear (Figure 3.5B, Figure 3.5H), as the other protein would still be present and able to crosslink the peeling bundle. This is especially puzzling for the *myo51* deletion, as Myo51 is only thought to play a minor

role in AMR contraction [71,100,106], and there are estimated to be 5× fewer molecules of Myo51 in the ring than there are of Myp2, at least in WT cells [64,71].

Nonetheless, the requirement that all three myosins are present does explain why peeling does not start until the final myosin, Myp2, arrives in the ring (Figure 3.4A). The back-and-forth wave-train nature of ring peeling can also be explained by the observation that most of the Myp2 is pulled off the ring on the peeling bundle (Figure 3.5D), and ends up located on the opposite side of the ring. There, it would generate tension heterogeneity, and subsequently initiate the next peeling event at the site of maximum Myp2 density, possibly by crosslinking the inner side of the AMR, causing a fracture to form between different layers of the ring [100,103].

Based on this, and our observation that peeling bundles shorten at a constant rate (Figure 3.3D), this would suggest that the time interval between successive peeling events gets shorter as the AMR contracts. We attempted to see if this was the case, however our results were inconclusive (Figure 3.4D). It is possible that for the first few peeling events the ring has not contracted enough in order to noticeably shorten the interval between these events, and we did not observe many cells undergoing four peeling events, so it was difficult to draw conclusions about what happens when the ring is at a smaller size, particularly for *adf1*-M3 cells (Figure 3.4D).

3.15.3. Perturbing actin turnover in other organisms

It may also be pertinent to ask what happens in the AMRs of other organisms/model systems when actin turnover is perturbed. In the budding yeast *S. cerevisiae* actin turnover is not required *per se*, as shown by the observation that AMRs are relatively unaffected by treatment with Latrunculin A [153]. However disassembly of actin filaments is required, and when this is blocked or reduced (e.g. through Jasplakinolide

treatment or the use of cofilin mutants) then AMR contraction is attenuated [153].

In fission yeast *S. pombe* it is possible to isolate AMRs through the permeabilisation of spheroplasts [140]. These isolated rings contract in an ATP and Myosin dependent manner, and without turnover of actin and other ring components [140]. Ring contraction in isolated *S. pombe* rings is also significantly faster than in cells [140]. While it goes against current knowledge that these rings are able to contract without actin turnover, it seems likely that they rely on different mechanisms which are not available to rings in cells, and which do not require turnover.

On the other hand, AMRs in *S. japonicus* cells were also found to be able to contract in the apparent absence of any turnover (both assembly and disassembly), as cells that were treated with both Jasplakinolide and latrunculin A were able to contract, albeit at a slightly reduced rate, whereas rings in cells just treated with latrunculin A would fall apart into clusters [135]. From this, it was proposed that one role of turnover is to help maintain actin filament homeostasis in the ring, and when the entry of new actin into the ring is blocked this homeostasis can be synthetically maintained by also blocking its disassembly and removal from the ring [135]. How this idea fits into our wider understanding of the role of turnover in AMR contraction remains to be seen, and more work is required to see whether similar behaviour can be found in other organisms.

In the *C. elegans* embryo, it was found that treating embryos with Latrunculin A (after permeabilisation, by treatment with RNAi for *perm-1*) prevented furrow ingression [28,154]. While we found a number of additional papers that document the presence of actin turnover in AMRs [155–161], we could not find any further examples of experiments where actin turnover was perturbed in the AMRs of higher eukaryotes. This is perhaps due to the fact that we have only recently begun to appreciate the importance of actin turnover for ensuring tension generation and contractility within AMRs [1]. This could also be because of the increased difficulty in performing these experiments, due to the more complex

nature of these cells, and the subsequent complication of only compromising protein function at one specific time and location, without also affecting other aspects of the cell. Hopefully, now that the role of turnover during ring contraction is starting to become better understood, there will be more experiments to investigate the effect of perturbing actin turnover during actomyosin contraction.

If reduced actin turnover in the AMRs of amoeboid and metazoan cells also leads to tension heterogeneity in the ring, what phenotype might we expect to observe (under the assumption that our hypothesis in Figure 3.8A is correct)? Ring contraction is known to generally be much faster in these cells than it is in fission yeast (~5 minutes vs. 20 minutes, and from a larger initial ring circumference), as the ring contraction speed in fission yeast is limited by the rate of septum deposition [28,158,162,163]. Therefore, rather than observing peeling events from regions of higher tension, we might instead observe asymmetric ring contraction, with the regions of higher tension ingressing faster than the regions of lower tension. Then, in organisms/cell types where AMR contraction usually occurs in a symmetric manner, we might instead find that the final hole between the two daughter cells is radially misplaced from the centre of the division plane.

In summary, we have found that fission yeast cells expressing hypomorphic alleles of the actin severing protein Adf1 display a ring peeling phenotype during ring contraction. This phenotype is dynamic, and peeling events occur at predictable times. Additionally, peeling appears to be dependent on the presence of all three of the *S. pombe* myosins that localise to the AMR. These *adf1* mutant cells are sensitive to further mutations that compromise membrane anchoring of the ring, and they also display septum defects. In combination, these two sets of results support a model where ring peeling is caused by increased tension heterogeneity around the circumference of the AMR. Attempts to synthetically recreate and rescue the phenotype in *S. pombe* cells were unsuccessful, however we were able to observe a similar phenotype in *S.*

japonicus cells by treating them with the actin stabilising drug Jasplakinolide.

4. Ring modelling results and discussion

To gain a better understanding of the mechanisms causing ring peeling, we attempted to build a mathematical model of an AMR, in the hope of recreating the phenotype *in silico*. We adapted an existing mathematical model, which successfully simulated the behaviour of the contracting AMR in *S. pombe* [35]. However, due to recent experimental results suggesting a subtly different ring structure [65], in addition to the limitations of the original model with regards to recreating the ring peeling phenotype (i.e. 2-dimensional flat geometry, no Myp2 clusters), it was clear that the model would need to undergo some modification before it was appropriate for the desired task. Specifically, we made the model 3-dimensional, with the goal of utilising a cylindrical geometry rather than the flat geometry of [35], and we placed the myosin clusters and formin dimers into the same ‘node’ structures, as new evidence suggests that these persist from ring formation until the end of ring contraction [65]. Then, we made the interactions between myosin clusters and actin filaments more realistic, by better accounting for the limited number of Myo2 molecules within each node, and we also included Myp2 clusters in the model.

Here we provide a non-mathematical overview of the original model, and the subsequent modifications that we made to the model, whilst discussing the results that we obtained from each modification. Full mathematical details of this model and subsequent modifications can be found in section 4.7, along with full lists of the parameter values used for simulations with each of these models.

4.1. Description of the original model

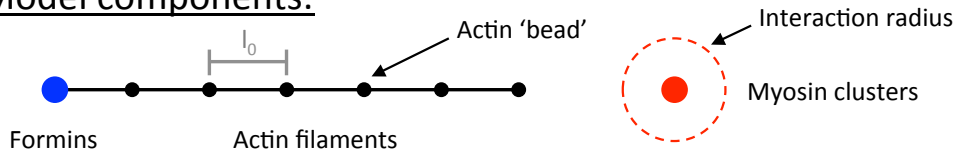
The model that we adapted was originally used to measure tension in a simulated AMR, and to see if this value reflected the tension measured in

fission yeast spheroplasts [35]. In this model, the ring is laid out flat on a 2D surface, which represents the inner surface of the plasma membrane, and has periodic boundary conditions at each end to maintain its topology (i.e. entities in the simulation which exit the ring at one end will re-enter the ring at the other end). The ring had a length of 10 μm , and a width of 0.2 μm . The model consisted of separate myosin clusters (representative of Myo2 in the *S. pombe* ring) and formin dimers, both of which would bind randomly within the area of the ring, and also unbind randomly, and formin dimers that were bound in the ring would nucleate and polymerise actin filaments in a random direction (Figure 4.1).

Actin filaments were modelled as semi-flexible polymers: Essentially, in order to calculate the forces on actin filaments, they were discretised into subunits or ‘beads’, which were separated by a distance of l_{act}^0 (0.1 μm). Within a filament, a spring force¹ between neighbouring beads was responsible for maintaining this spacing, while a bending force (calculated from the spatial derivative of each filament’s bending energy) was applied to try and restore bent filaments to a straight configuration (Figure 4.1), assuming a persistence length of 10 μm [130].

¹ A spring force, or spring interaction, is where the force experienced by an object is proportional to its displacement from some equilibrium position, and this force acts to return the object to this equilibrium position, e.g. like a stretched (compressed) spring that wants to contract (expand) to return to its original length. This is also called a Hookean interaction/force.

Model components:

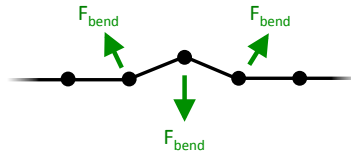


Intra-filament forces:

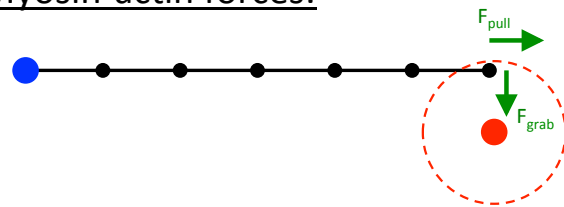
- Spring forces



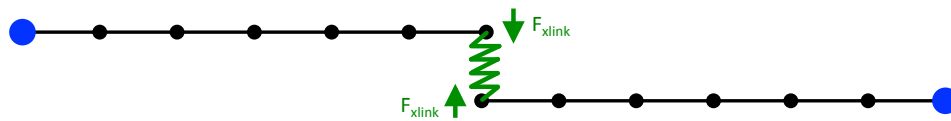
- Bending forces



Myosin-actin forces:



Actin crosslinking forces:



Myosin excluded volume forces:

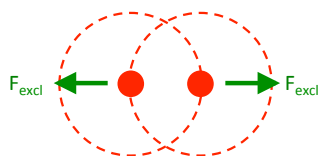


Figure 4.1: Diagram of components and forces in original ring model.

Diagram showing the individual components from the original ring model in Stachowick, *et al* [35], how these components interact with each other, and the different forces generated from these interactions. The model consists of formin dimers, which nucleate actin filaments, and myosin clusters. Actin filaments experience intra-filament elastic and bending forces, and inter-filament crosslinking forces. Myosin clusters interact with actin filaments, exerting 'pulling' and 'grabbing' forces, and also exert excluded volume forces on other nearby myosin clusters.

Additionally, beads in actin filaments could also interact with myosin clusters, and if a bead came within the capture distance ($0.1 \mu\text{m}$) of a myosin cluster then a connection was formed between the pair. Myosin clusters exerted two forces on actin beads: a 'pulling' force, and a

‘grabbing’ force (Figure 4.1). The pulling force is the simplest, and corresponds to myosin-induced translocation of the actin filament. This is modelled as a constant force of 4 pN, which is parallel to the filament’s local direction, and points towards the filament’s pointed end (Figure 4.1). The simplification that the pulling force has a constant magnitude relies on the assumption that the relative velocity between the cluster and the actin filament is much smaller than the load-free velocity of the myosin. Due to the high drag coefficients of the myosin clusters and formin dimers (1.3 and 1.9 nN s/ μ m, respectively, against a pulling force of 4 pN), this is arguably a valid assumption to make in these simulations.

The grabbing force represents the binding interaction between a myosin head and an actin filament. This was modelled as a spring force between the cluster centre and the bead, with an equilibrium length of zero, and which acts perpendicular to the actin filament (so that it neither assists nor hinders the pulling interaction), pulling the bead towards the cluster’s centre (Figure 4.1). Each pulling and grabbing interaction also produces an equal and opposite force on the myosin cluster, due to Newton’s third law of motion. When the distance between a myosin cluster and an actin filament increased beyond the capture radius, that connection was removed.

Finally, actin beads can also experience crosslinking forces between other nearby actin beads that aren’t part of the same filament, which represents crosslinking by proteins such as α -actinin or fimbrin (Figure 4.1). Again, this is modelled as a spring interaction between pairs of nearby beads, with an interaction distance of 0.05 μ m and an equilibrium length of 0.03 μ m. Similar to the myosin-actin forces, if the distance between two crosslinked beads becomes greater than the interaction distance, the connection between those beads is removed. However, unlike the myosin-actin forces, these interactions are dynamic, with crosslinking interactions between nearby actin beads being formed with a rate per length of k_{on}^x , and unbinding with a rate of k_{off}^x .

The simulation did not include specific formin entities, and instead the actin filament barbed ends were treated as formins, by giving

them a much greater drag coefficient than the other actin beads, caused by their binding to the membrane. Furthermore, because the barbed end subunit represents the formin dimer on the filament, myosin-actin and actin-actin crosslinking interactions could not be formed with the barbed end subunits of simulated actin filaments.

Excluded volume interactions between actin filaments were not included, due to the small diameter of an actin filament (5 – 9 nm) relative to the width of the ring. Similarly, the formin dimers/barbed ends were also considered to be small enough to ignore excluded volume interactions. Excluded volume interactions were included for the myosin clusters, which were described using a repulsive spring interaction between any pair of myosin clusters that came closer than a threshold distance $d_{myo} = 50$ nm (Figure 4.1).

As the myosin clusters could interact with multiple actin filaments, it was necessary to include in the model a method of regulating these interactions, to ensure that unphysical behaviour did not emerge (e.g. a myosin cluster being able to exert a finite force on an infinite number of filaments). This was controlled by the parameter '*maxInt*' (maximum interactions), which determines the number of actin filaments that a single myosin cluster can interact with before the force it exerts on each filament becomes reduced. When the number of filaments a cluster interacts with is less than the value of *maxInt* (set to 10 in the original simulation), then the cluster exerts 4 pN of pulling force on each filament. When the number of filaments a cluster interacts with is greater than *maxInt*, then the force exerted on each filament is equal to $4 \times \text{maxInt} / n_{fil}$ pN, where n_{fil} is the number of filaments that the cluster interacts with. This is only applied to the pulling forces from each cluster, and not to the grabbing forces. We discuss the implications of this later, in section 4.4.

The simulated ring is dynamic, with components unbinding from the ring, and new components binding into the ring. Formin dimers/filament barbed ends and myosin clusters bind into the ring at a random location, with probabilities per timestep of $r_{for} \times L \times \Delta t$ and

$r_{myo} \times L \times \Delta t$, respectively. Here, r_{for} and r_{myo} are binding rates/length for formin dimers and myosin clusters, respectively, L is the ring length, and Δt is the simulation timestep. The values of r_{for} and r_{myo} are given by $r_{for} = \rho_{for} k_{off}^{for}$ and $r_{myo} = \rho_{myo} k_{off}^{myo}$, where ρ_{for} and ρ_{myo} are the average linear densities of formin dimers and myosin clusters in the ring, respectively, and k_{off}^{for} and k_{off}^{myo} are the formin and myosin cluster unbinding rates, respectively, which lead to unbinding probabilities per timestep of $k_{off}^{for} \times \Delta t$ and $k_{off}^{myo} \times \Delta t$, respectively. Between pairs of nearby actin beads, crosslinking interactions are formed with a probability of $k_{on}^x \times l_{act}^0 \times \Delta t$, with k_{on}^x being a binding rate per length, and are broken at a rate of $k_{off}^x \times \Delta t$.

Newly bound formins instantly nucleate a new actin filament in a random direction, modelled as a bead connected to the formin dimer/barbed end with a very short equilibrium length ($=v_{pol} \times \Delta t$, where v_{pol} is the actin polymerisation rate). Actin filaments were polymerised by increasing the rest length between the 1st and 2nd beads in a filament, until this reaches a threshold length of 0.12 μm , at which point a new bead was inserted between these beads, with an equilibrium distance from the barbed end of 0.02 μm , and of 0.1 μm to the next bead. This process of polymerisation was continued, with new beads being inserted between the 1st and 2nd beads of a filament every time that the equilibrium length of this connection exceeded 0.12 μm .

To mimic the effect of severing by the cofilin Adf1, actin filaments were severed with a probability of $r_{sev} \times l_{fil} \times \Delta t$, where r_{sev} is the severing rate per length for simulated filaments, and l_{fil} is the length of the actin filament. If a filament is severed, then the actual severing takes place at a randomly chosen point along the filament length, and any beads between the severing point and the filament's pointed end are removed from the simulation.

To model the unbinding of ring components, formin dimers/barbed ends and myosin clusters were removed from the simulation with probabilities of $k_{off}^{for} \times \Delta t$ and $k_{off}^{myo} \times \Delta t$, respectively. In

combination with the binding rates, these help to maintain a roughly constant number of formin dimers and Myo2 clusters in the ring. Additionally, when a formin dimer/barbed end unbinds from the ring, the filament that it nucleates is also removed from the ring, along with any interactions between the filament and other simulation components. A timestep of 5×10^{-5} s was used in the simulation, and at every timestep the forces on each of the components were calculated. These were summed to give the net force on each component, and then each component was moved by a distance of $F_{net} \times \Delta t / \gamma$, where F_{net} is the total force acting on a given component, and γ is the drag coefficient for that component.

Finding interactions between myosin clusters and actin filaments, crosslinking interactions between different actin filaments, and excluded volume interactions between myosin clusters, required checking the distances between all of the relevant components, which is a computationally expensive process. Additionally, simulating the processes of component turnover and actin severing requires the generation of large quantities of random numbers, which is also a computationally expensive process. Because ring components only move very small distances in a single timestep, it is not necessary to perform these calculations for every timestep of the simulation. Instead, these can be performed for a small subset of timesteps (e.g. every 200th timestep) with negligible errors, and with the relevant binding/unbinding/severing probabilities, etc., modified to account for this. This makes the simulation much more efficient, and if these timesteps are chosen correctly then this will not have any noticeable effect on the behaviour of the simulated ring, as these calculations are still being performed on timescales that are much less than the timescale over which the configuration of the simulated ring evolves (milliseconds vs. seconds/minutes).

Similarly, in terms of performing quantification of the simulation, and making images/movies of the simulated rings, it was not necessary to save the configuration of the ring at every timestep, as the ring does not evolve much over this time, and the size of the data files would be

prohibitively large. Therefore, the ring configuration was only saved for a small subset of timesteps, typically at intervals of 1 or 2s in the simulation.

A list of parameter values used in the original simulation is shown in Table 4.1, and a list of the temporal parameters used is shown in Table 4.2.

4.1.1. Extracting tension information from simulation data

In order to measure the total ring tension at a given timestep, we first measured the tension stored in all of the springs within the simulation (i.e. connections between adjacent actin beads, connections between crosslinked actin beads, grabbing interactions between myosin clusters/nodes and actin filaments, and excluded volume interactions between pairs of myosin clusters/nodes), and calculated the component of this tension that was parallel to the ring axis. For example, in an actin filament that was completely parallel to the ring axis, 100% of the tension in the filament would contribute to the overall ring tension, while in a filament that is perpendicular to the ring axis the tension stored in the filament would have no contribution. These tension values were then normalised by multiplying them with the ratio of the component of the spring's length along the ring axis to the total length of the ring (for an explanation of why this is necessary, see section 4.7.1.8). Repeating this process for all the springs within the simulation, and summing these values, gave us the value of the total ring tension, T , at a given timepoint in the simulation.

To investigate how much the tension varies along the length of our simulated rings, we made heatmaps of local ring tension along the ring length, across the entire time of the simulation. To do so, the ring length was divided into 60 bins. Then, the total tension within each of the bins was measured. This was carried out in a similar way to how the total ring tension was measured, except we only included actin filament segments within a given bin, and we normalised by the length of the bin,

rather than by the total ring length. To produce a heatmap, this process was repeated for every bin, and at each timepoint at which the ring configuration was saved, and the data was made into a heatmap using the 'imagesc' function in MATLAB.

To measure the standard deviation of ring tension along the length of the ring, we measured the tension in the individual bins as previously described, and then measured the standard deviation of these values. This was repeated for each timestep where the ring configuration was saved, and used to plot the standard deviation of the ring tension over time.

4.2. Modifying the ring structure and dimensionality

Since the publication of the original model, super-resolution microscopy of the *S. pombe* ring has provided strong evidence that the precursor nodes that are present during ring formation (approx. 140 of them) also persist throughout ring maturation and contraction [65]. Based on previous measurements of protein concentrations in the *S. pombe* ring, it is estimated there is an average of one formin Cdc12 dimer and ~ 10 Myo2 dimers per node [64,65]. Therefore, we first modified the model to reflect these observations, with formin and myosins both placed in the same node structures. The simulated rings contained an average of 150 nodes, the same as the number of formin dimers in the previous simulation, and this meant that each node nucleated a single actin filament. To model the presence of Myo2 in these nodes, they were also given the ability to capture and pull any nearby actin filaments. This was largely implemented in the same way as for the myosin clusters in the original model, with the exception that a node could not interact with the filament that it nucleates.

Nodes were given a drag coefficient of $1.5 \text{ nN s}/\mu\text{m}$, which is between the values used previously for the formin dimers and myosin clusters. A previous model, examining ring formation, used a node drag coefficient of $400 \text{ pN s}/\mu\text{m}$ [164], significantly less than was used in our

simulations, and in the original simulations using this model. However, in terms of the general behaviour of the ring, the precise value used should not matter too much, as long as it is high enough to limit myosin clusters to the low velocity/high force end of their F-v relationship, which allows us to assume that the magnitude of the pulling forces is a constant. We used the formin dimer unbinding rate as the unbinding rate for nodes in the simulation, and when a node unbinds from the ring the filament that it nucleates is also removed from the simulation. Pairs of nodes also experience excluded volume interactions when they get too close to each other, in the same manner as the myosin clusters in the original model, with the same parameter values used calculate the magnitude of this force.

Because we doubled the number of myosin-containing entities in the model, going from 75 Myo2 clusters in the original model to 150 nodes, in order to keep the total pulling force in this model consistent with the previous one, we needed to do the equivalent of halving the number of Myo2 molecules in each node. To do this, we reduced the value of *maxInt* from 10 down to 5.

Additionally, we increased the length of the ring from 10 μm to 12 μm (change in diameter from 3.2 μm to 3.8 μm), as it was previously observed that *adf1*-M2 and *adf1*-M3 cells have a slightly increased cell diameter when compared to WT cells [66]. Finally, we also decreased the ring width from 0.2 μm to 0.1 μm , to reflect the results of recent super resolution observations of the ring [92].

Next, the model was made to be 3-dimensional, by allowing for height (z coordinate) above the membrane (defined as the x - y plane, where $z = 0$), and we set the volume above the membrane, i.e. $z > 0$, as being inside the cell, while the volume below the membrane, i.e. $z < 0$, was defined as being outside of the cell. The nucleation angle of actin filaments above the membrane was set to 8° , as this was the angle that was previously measured for actin filaments during the process of ring formation [62]. The nucleation angle in the x - y plane was chosen randomly, as was the case in the 2D version of the model. The motion of

nodes was constrained to only take place in the x - y plane (i.e. no z motion), and for any actin filament beads with a z -coordinate below the membrane height, a constant force of 5 pN was exerted in the $+z$ direction, to account for the excluded volume below the membrane, and to try and return the actin beads to the 'allowed' volume in the simulation.

Simulations with this model produced the same basic behaviour as observed previously, with the nodes undergoing bidirectional motion, and with most actin filaments being successfully captured into the ring (Figure 4.2A, blue circles represent nodes, grey lines are actin filaments, and green circles are crosslinkers). However, the measured tension was reduced slightly, from 340 ± 57 pN to a value of 273 ± 22 pN (Figure 4.2B). This is most likely because our simulated ring had a length of 12 μm , rather than 10 μm , as was previously used. As we effectively kept the total amount of myosin in the ring the same (by halving the value of maxInt), this means there is a slightly lower linear density of myosin in our simulated ring, which would logically lead to a slightly lower ring tension in our simulations [35]. Changing the ring length from 10 μm to 12 μm will decrease the myosin density by a factor of 1.2, so correcting for this by multiplying our measured tension by 1.2 produces a value of 327 ± 26 pN, which is closer to the original value of 340 ± 57 pN (this assumes that the relationship between myosin density and ring tension is linear, at least over the range of values used here).

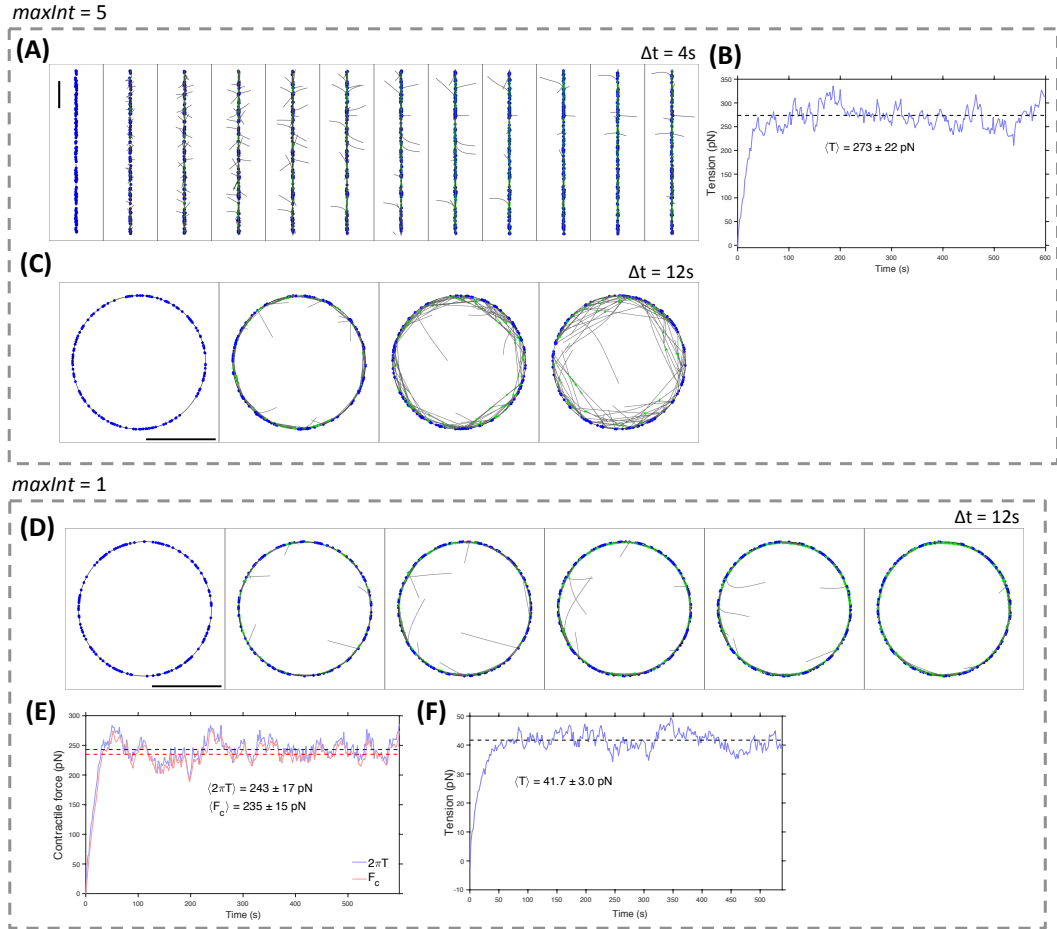


Figure 4.2: Making the model 3D, and utilising different geometries.

For A - C, all data shown is from simulations using a *maxInt* value of 5. All data in D - F is from simulations using *maxInt* = 1. All scale bars are 2 μm .

- (A) Montage of snapshots from a simulated 3D ring, using the same flat geometry that was used in simulations from the original model.
- (B) Ring tension vs. time for the simulated ring shown in A. The average tension is calculated from after 100 s of simulated time, until the end of the simulation.
- (C) Snapshots from a simulation using a 3D cylindrical geometry, with the same parameter values as the simulation shown in A.
- (D) Snapshots from another simulation using the cylindrical geometry, but with *maxInt* reduced to 1.
- (E) Contractile force vs. time for the simulation shown in D. The contractile force is measured using two methods, and the results of both of these are plotted.
- (F) Tension vs. time for a simulation using flat 3D geometry (images not shown), similar to A, but with *maxInt* = 1, as was used to successfully simulate rings with cylindrical geometry.

4.3. Altering the model geometry from flat to cylindrical

The model was next modified so that all the nodes in the simulation lie on the inner surface of a cylinder, with a radius of $R = 12/2\pi \mu\text{m}$, which represents the inner surface of the *S. pombe* plasma membrane. The attachments of the nodes to the membrane were modelled as Hookean springs, so that if the nodes are pulled away from the membrane, or pushed in towards it, they will experience a restoring force proportional to the distance that they have been displaced. This connection was given a high spring constant (i.e. high stiffness) in order to ensure that the extension or compression is always very small.

As before, an excluded volume interaction was included, except now this was applied to any beads in the actin filaments that moved to a radius greater than the radius of the cylinder (i.e. outside of the cytoplasmic volume). For these beads, a constant restoring force of 5 pN was applied towards the cylinder's axis, in order to push the actin beads back into the allowed volume.

It is important to note that, whilst the model now uses 3D cylindrical ring geometry, the simulated ring is still unable to contract, as the cylinder that it is attached to has a fixed radius. We have already discussed how, in *S. pombe* cells, the process of ring contraction is closely coupled to the process of septum synthesis, and how neither is able to occur without the other (section 1.11, page 30) [32,89]. Therefore, performing a realistic simulation that allows the ring to contract would also require modelling the process of septum synthesis, which would further increase the complexity of the model.

We performed simulations with this cylindrical model, using the same parameter values that were used for the simulations in our flat model. However, in our initial simulations we observed that many actin filaments did not remain against, or near, the membrane, but were pulled away (Figure 4.2C). Because the previous simulations used a flat geometry, this behaviour was not seen before, and we realised this was

most likely happening because the pulling force on the actin filaments was overcoming the grabbing forces that were holding them near the membrane. Comparison of our 3D cylindrical model to a similar 3D model (aimed at describing ring formation [164]) suggested that this was the case, as for their simulations a *maxInt* value of 3 was used for each node, with slightly less than half the number of nodes that we used in our simulations (and therefore roughly double the amount of Myo2 per node) [164].

We found that reducing the value of *maxInt* down to 1 was necessary in order to keep the majority of the filaments contained in the ring (Figure 4.2D). It would theoretically have been possible to increase the strength of the myosin grabbing forces, which keep actin filaments near the membrane. However, the way that myosin grabbing forces are implemented in this model arguably leads to them being overpowered already, as they do not experience the same decrease in force when interacting with multiple filaments that is applied to the pulling forces. We will discuss our attempts to resolve these issues in the next section of this chapter.

Additionally, from a basic consideration of the number of Myo2 molecules in each node, and from knowledge of the processivity of type II myosins, it can be argued that the myosin pulling forces in the simulation are also overpowered, hence we chose to reduce these rather than increase the strength of the grabbing forces. This is because, using the measured number of Myo2 molecules in the *S. pombe* AMR, and assuming there are 75 Myo2 clusters in the ring (as was the case in the original model), it can be calculated that there would be an average of around 40 Myo2 molecules in each cluster [64]. In the original model, these clusters could interact with up to 10 actin filaments at maximum force, which equates to 4 Myo2 molecules exerting a time-averaged force of 4 pN on each filament. Considering that type II myosins are known to be not particularly processive, with Myo2 previously measured to have a duty ratio of approximately 10% [95], then for 4 Myo2 molecules interacting with a single actin filament, a time-averaged force of 1.6 pN would be a

better estimate¹. Therefore, decreasing the value of *maxInt* in our simulations also makes sense based on considerations of the mechanochemical properties of type II myosins.

We wondered if increasing the amount of crosslinking in the ring would also help to prevent this single-filament peeling that was observed: On the one hand, if the actin filaments were more tightly crosslinked to each other, then this would mean that the pulling forces from the nodes would effectively be shared across multiple filaments, and therefore reduce the force on individual filaments. On the other hand, this would not increase the number of connections between actin filaments and the membrane, so it might not prevent the single-filament peeling from happening. We performed some simulations where we used a *maxInt* value of 5, and increased the crosslinker binding rate, however we found that this did not appear to make a difference to the amount of individual filaments peeling off of the ring. We shall discuss more about the effect that crosslinkers have on the simulation in section 4.8.3.

After reducing the value of *maxInt* in our simulations, and checking that this produced more WT-like behaviour (Figure 4.2D), we also decided to implement a new method to measure the ring tension: Previously, the ring tension was measured by summing all the tension in all the springs in the simulation, in the direction parallel to the ring (i.e. along the x-axis). As the direction parallel to ring was no longer constant, this method became more complicated to use in our cylindrical model. Instead, to measure the total contractile force the ring exerts on the inner surface of the cylinder, we summed the tension stored in the springs connecting the nodes to the membrane. It can be shown that this contractile force, F_c , is equal to 2π times the ring tension, T (i.e. $F_c = 2\pi T$)². Using both methods, and plotting $2\pi T$ and F_c as a function of time on the same graph, showed that both results are largely in agreement

¹ Assuming that the 4 Myo2 molecules exert 4 pN of force on a single actin filament 40% (10%×4) of the time, this leads to a time averaged force of 1.6 pN. This is a *very* simplistic approximation, which does not take account of, for example, multiple myosin heads binding at the same time.

² The equation for the Laplace pressure in 2D is $F_c/L = T/R$, where $L = 2\pi R$, and R is the radius of the ring. Rearranging, and substituting for L , give $F_c = 2\pi T$.

(Figure 4.2E). Using our 3D cylindrical ring model, with the reduced value of *maxInt*, the simulated ring produced a mean $2\pi \times$ tension of 243 ± 17 pN, and exerted a mean contractile force on the membrane/cell wall of 235 ± 15 pN.

Returning to our flat model, and again using the reduced value of *maxInt* in our simulations, we measured an average ring tension of 41.7 ± 3 pN (Figure 4.2F), which is more than a 5 \times reduction compared to the case with a *maxInt* value of 5 (Figure 4.2B). While this decrease in ring tension would be expected after reducing the value of *maxInt*, this means that the simulated ring tension is no longer in agreement with the experimentally measured value of 390 pN [35]. However, the reduction in the value of *maxInt* was necessary in order to keep actin filaments near the membrane in our cylindrical model, an issue which was not apparent when using the flat geometry. Therefore, there must be additional mechanisms which help to make the process of tension generation more efficient, or which increase the number of connections between the AMR and the membrane, and we will discuss some of these in section 4.8.2.

4.4. Making the myosin-actin interactions more realistic

As we previously mentioned, certain aspects of the way that the myosin in the nodes interacts with actin filaments in the simulation can be considered unrealistic. Primarily, there is no upper cap on the number of actin filaments that a single node can interact with, so it could hypothetically bind to an infinite number of actin filaments. This is less of an issue for the pulling forces, as these are reduced when a node interacts with multiple filaments, which means that in the limit where a node interacts with a large number of actin filaments, the pulling force on each filament would become very small. However, up until now, the grabbing forces are not reduced when interacting with multiple actin filaments, which means that a single node can exert a finite grabbing

force on a potentially infinite number of actin filaments, which is obviously unrealistic behaviour.

Additionally, when a node interacts with an actin filament in the simulation, the grabbing force acts to pull the filament down to a height of zero above the membrane. However, from the predicted node structure, based on super-resolution microscopy imaging [62,65,103], the myosin heads extend a distance of around 100 nm into the cytoplasm, implying that they would be unlikely to interact with a filament near to the membrane. This is an issue that we attempt to address later, and for now we will focus on resolving the problems with the number of grabbing interactions that a node can make.

We started by looking at the way nodes interact with multiple actin filaments, and we considered a few mechanisms that could be considered to be more realistic than those employed so far: Firstly, the nodes could still be allowed to interact with an unlimited number of filaments, but the grabbing force could also be reduced in a similar manner to the pulling force, so that as the number of filaments that a node interacts with increases, the grabbing force that each of those filaments experiences would decrease proportionally. Secondly, the number of filaments that a node can interact with could be capped at a maximum value – so *maxInt* would be redefined as the maximum number of filaments that a cluster could interact with. Within this second mechanism, there are further considerations to be made about its implementation: Firstly, the filaments that a myosin cluster interacts with can be chosen at random for every timestep where the myosin-actin interactions are recalculated (myosin timesteps, see section 4.1), which would limit the processivity of the myosin walking on actin filaments. Secondly, once a myosin cluster has found some actin filaments to interact with, it could walk along those filaments in a processive manner, and only unbind probabilistically, based on the average length of time that a myosin head is bound to an actin filament in its duty cycle, as measured from *in vitro* experiments [95].

After some experimentation, we decided to set an upper limit on how many actin filaments a node can interact with, with actin-myosin interactions being recalculated at every myosin timestep (i.e. no persistence of walking). We chose this because we realised that we could change the time between myosin timesteps to be roughly equal to the time that a myosin head remains bound to an actin filament [95]. Therefore it would be unnecessary to implement the more complicated model, where unbinding from an actin filament occurs with a certain probability for each myosin timestep. We also settled on using a *maxInt* value of 2, based on the measured duty ratio of ~10% for Myo2, and the estimation of 20 Myo2 molecules being present in each of the nodes [95].

Performing a simulation of a ring with these new myosin-actin interactions, and using the flat geometry, we noticed that the number of filaments that did not get captured in the ring was higher (Figure 4.3A) than we saw previously (Figure 4.2A), which we would expect since we have reduced the overall strength of the grabbing forces. The ring also produced a higher tension than before (Figure 4.3B, Figure 4.2F), which again would be expected as only the myosin pulling forces can contribute to ring tension, and in our improved model we have increased the maximum amount of pulling force that each node is capable of generating. The ring tension was still much less than the experimentally measured value, however [35].

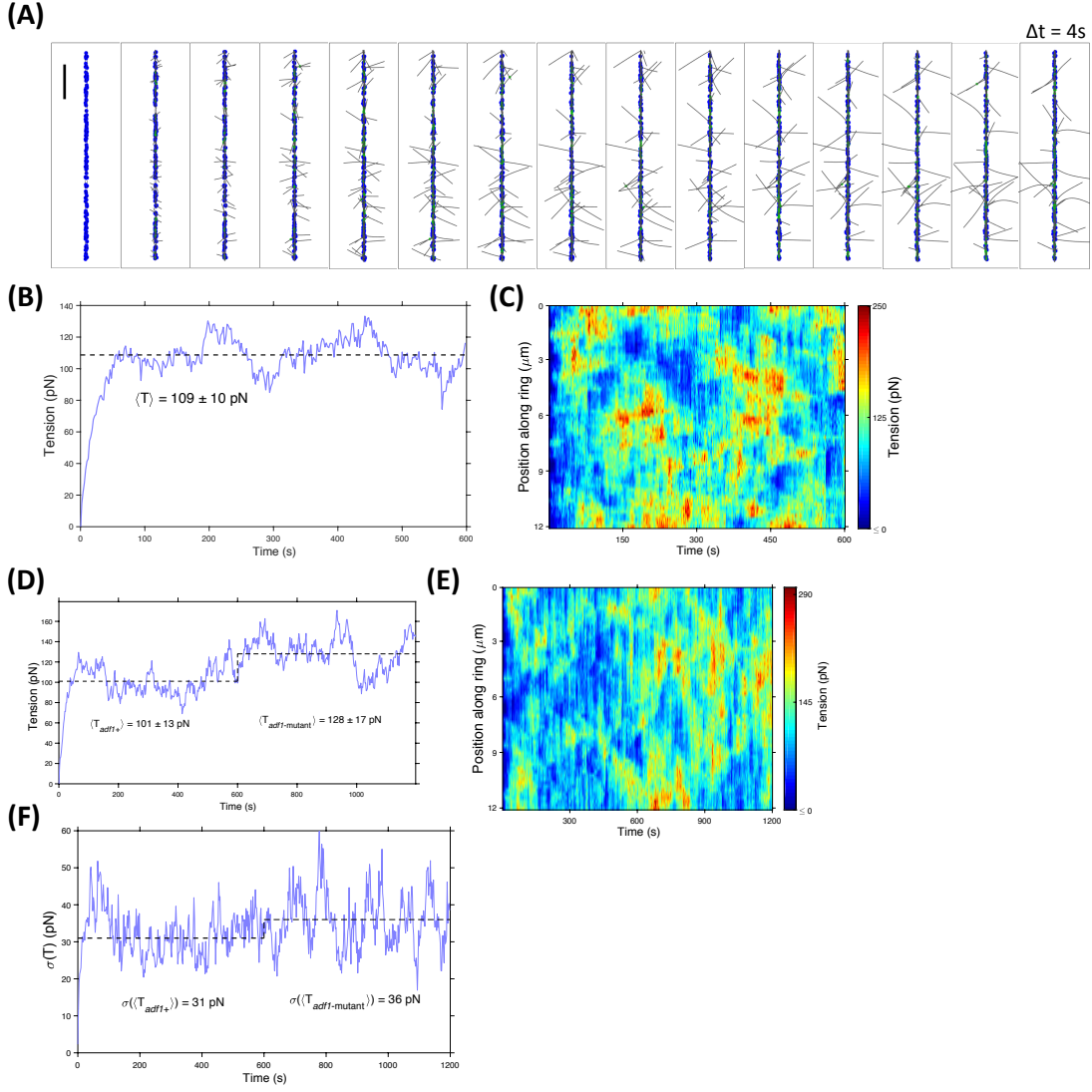


Figure 4.3: Modifying the myosin-actin interactions.

- (A) Montage of snapshots from 3D ring using flat geometry, with new actin-myosin interactions implemented. Scale bar is $2 \mu\text{m}$.
- (B) Ring tension vs. time for the simulation shown in A. The time-averaged tension is calculated by averaging the ring tension measured at all time-points after $t = 100\text{s}$ in the simulation.
- (C) Heat-map showing the tension along the simulated ring as a function of time.
- (D) Ring tension vs. time for a simulation where the actin severing rate is reduced by a factor of 2 at the 600s timepoint.
- (E) Heat map of ring tension for the same simulation data used in D.
- (F) Standard deviation of ring tension along the ring length, plotted vs. time, for the same simulation data used in D and E.

By limiting the total number of interactions between each node and the nearby actin filaments, we have effectively increased the strength of the pulling forces whilst decreasing the strength of the grabbing forces. Because of this, we realised that if we were to use this model of myosin-actin interactions in a simulation that employed cylindrical

geometry we would likely observe the same behaviour that we initially saw, where the grabbing forces were overpowered by the pulling forces, causing actin filaments to be pulled out of the ring (Figure 4.2C). Because of this, from this point onwards we only simulated the ring using the flat geometry, rather than the cylindrical geometry. Although we did not manage to overcome this problem, we will discuss ways that this could potentially be achieved in section 4.8.1.

Because we could no longer perform simulations using the cylindrical geometry, this meant we would not be able to observe peeling events in our simulations. Instead, we decided to look for other ways to see if perturbing actin severing could lead to ring peeling. We previously hypothesised that ring peeling could be caused by an imbalance of tension around the ring (Figure 3.8A), therefore we decided to try and make heatmaps showing the local tension in the ring, and to then see if reducing the actin severing rate would increase the circumferential variability in the ring tension.

We made a heatmap of our previous simulation, which showed that there was already some tension variability in the ring (Figure 4.3C). Next, we performed a simulation where the actin-severing rate is reduced twofold partway through the simulation, to try and mimic the effect of our *adf1* mutants. Doing so led to an increase in the total ring tension after the severing rate was reduced (Figure 4.3D). This was also visible from the heatmap of the ring tension (Figure 4.3E), and it seemed that the circumferential variability in the tension might also have increased. Measuring the standard deviation in the ring tension at each timepoint also showed that this was the case (Figure 4.3F), however the magnitude of the increase was not particularly large (only about 16% of the original value), suggesting that it would not be sufficient to cause peeling in these rings.

4.5. Adding in Myp2 clusters to the ring model

Next, we decided to introduce clusters of Myp2 into the simulation, as we previously found that the presence of both membrane-bound and non-membrane-bound myosin species was necessary to observe ring peeling in cells (Figure 3.5, Figure 3.6, pages 70 and 73). In terms of their interactions with actin filaments, these were modelled in a similar way as the Myo2 clusters in the nodes, as they were able to interact with a maximum of 2 nearby actin filaments, exerting pulling and grabbing forces on them. However, unlike the nodes, the Myp2 clusters did not experience a binding interaction with the membrane (i.e. they were not held at a height of zero above the membrane), as their localisation to the ring is actin dependent [105]. This had two main effects on how we modelled the Myp2 clusters.

Firstly, we gave the Myp2 clusters a much lower drag coefficient than the nodes, to reflect the reduced drag of the cytoplasm vs. the membrane. This in turn had the effect of allowing Myp2 clusters to move at faster velocities than the nodes, which meant that it was now necessary calculate the pulling forces using a force-velocity relationship (F-v, assumed to be linear) [123,132]. Because the nodes have very high drag coefficients, they will always move at speeds much slower than their load free velocity of $\sim 0.35 \mu\text{m/s}$ [95,139], which means that they will always be at the low velocity/high force end of the F-v relationship. Thus, assuming that they exerted their maximum possible force (the stall force) was a valid simplification for the model. However this assumption is not valid for the Myp2 clusters, which meant that it was necessary to utilise a F-v relationship.

Secondly, because the Myp2 clusters bound directly to actin filaments, rather than to the membrane, like the nodes, we needed a new method to allow Myp2 clusters to bind into the ring. We achieved this using a 'docking' mechanism, where we initially placed the Myp2 cluster at a random point along the ring (the x-axis), and at a randomly chosen position in the y-z plane, so that the Myp2 cluster lay on the arc of a

semicircle, centred on the ring, with a radius of r_{dock} . Then, we gradually moved the Myp2 cluster inwards towards the ring, with a step size of $dock_step$, until the Myp2 cluster was able to find an interaction with at least one actin filament, or until the cluster reached a final distance of r_{dock_final} from the ring axis, although the vast majority of Myp2 clusters did find an actin filament to interact with by this point. During this process, the main ring simulation was paused, and when the docking procedure was completed the ring simulation was allowed to continue. We chose this mechanism, rather than just randomly placing the Myp2 clusters somewhere in the volume of the ring, because we believed that this would be more representative of the way that Myp2 actually binds into the ring, in an actin dependent manner.

In the absence of any available published data on Myp2 turnover, Myp2 clusters were given the same binding kinetics as the nodes, with the same unbinding rate ($k_{off}^{myp} = k_{off}^{node}$), and a binding rate of $r_{myp} = \rho_{myp} k_{off}^{myp}$ to maintain the density of Myp2 clusters at around an average value of $\rho_{myp} = 100/L$. This value was based on measurements indicating that the total amount of Myp2 in the ring is 2/3 the amount of Myo2, and assuming that there are also 20 molecules of Myp2 in each Myp2 cluster [64].

Additionally, Myp2 clusters were subjected to excluded volume forces. A Myp2 cluster experienced excluded volume interactions with other Myp2 clusters, with nodes, and with the membrane when it moved to a height of $z < 0$. These forces were all implemented as previously described for other ring components.

We first performed a simulation where the ring was simulated for 600s without any Myp2 clusters being present. Then, we added in the 100 clusters of Myp2, before allowing the simulation to run for another 600s in the presence of Myp2 (Figure 4.4A, red circles are Myp2 clusters). We chose to add in all the clusters to the ring at once, rather than allowing them to start binding into the ring with their usual binding rate. This is because the latter option would have increased the length of time for which we needed to run the simulation, in order to wait for

~100 Myp2 clusters to bind into the ring (a process that would take around 2 minutes of simulated time to complete).

Adding in the Myp2 clusters only had a small effect on the total ring tension (Figure 4.4B). From a histogram of the Myp2 cluster speeds, we can see that most of the clusters move at speeds of much less than their maximum of $0.35 \mu\text{m/s}$ (Figure 4.4C), which means that they are exerting forces on the actin filaments that are relatively close to their stall force of 4 pN. Therefore, it is somewhat surprising that the increase in ring tension is so small. However, tension generation in an AMR is not just a function of the myosin density in the ring, but is also dependent on the distribution of the myosin clusters along the actin filaments, with biasing towards the pointed end of actin filaments being optimum for tension generation [1,35]. Therefore, it is likely that the Myp2 clusters are less biased towards the pointed ends of actin filaments, or spend less time there than the nodes, due to their lower drag coefficient/higher walking speeds.

Next, we performed a simulation where actin severing was reduced twofold after the addition of Myp2 into the ring (and after allowing time for the ring to equilibrate in the presence of the Myp2). Myp2 clusters were added into the ring after 120s, and then the severing was reduced at a time of 480s. Once again, we observed an increase in the ring tension after reducing the severing rate (Figure 4.4D), which was larger than the difference we observed in simulations without Myp2 (Figure 4.3D). This also led to an increase of the standard deviation of the tension (Figure 4.4E). Furthermore, when examining the corresponding heatmap, and looking at the region after the severing was reduced, we saw that there appeared to be a greater distinction between the regions of high tension, and the regions of medium or low tension (Figure 4.4F), which in a cylindrical geometry could potentially lead to the peeling away of actomyosin bundles.

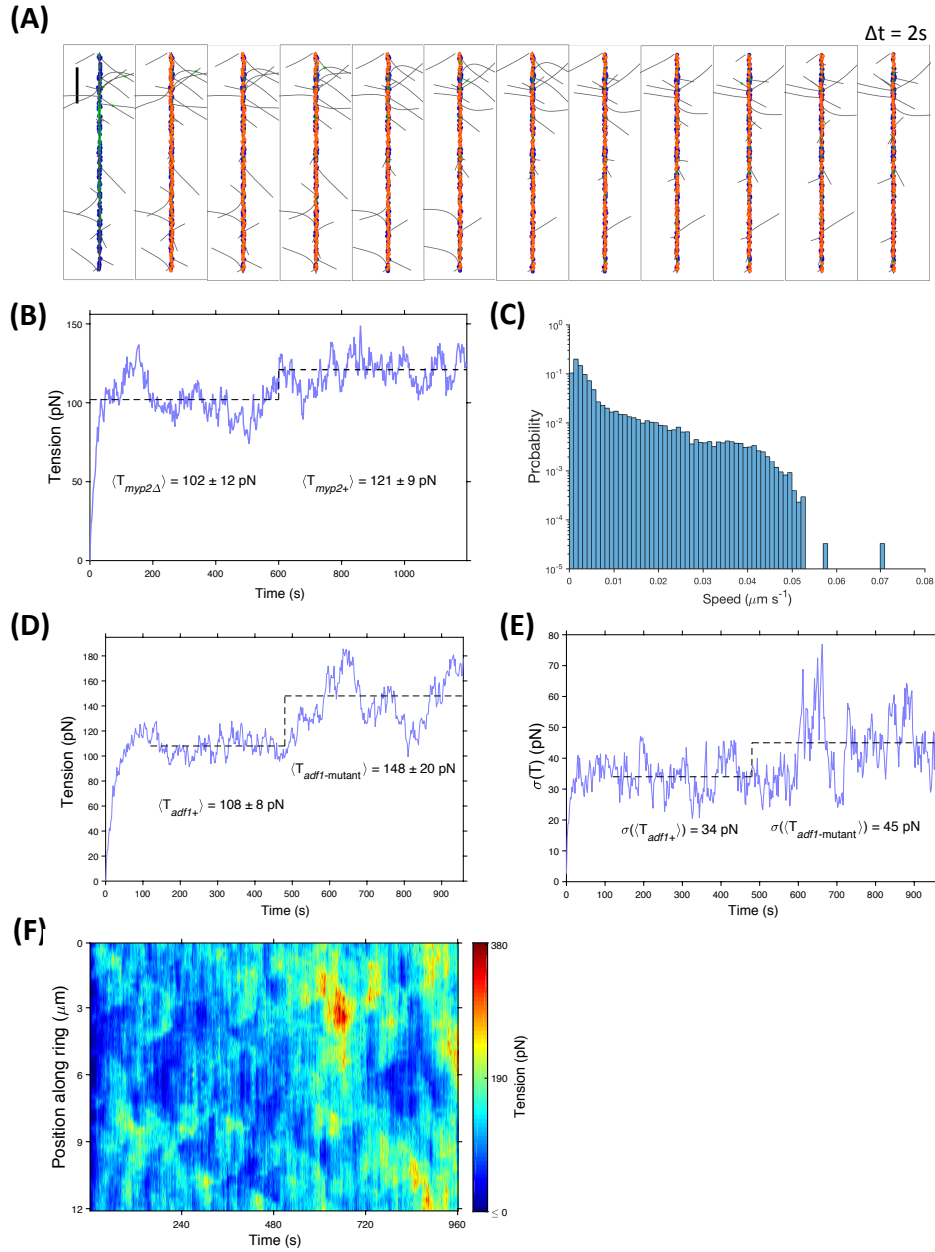


Figure 4.4: Adding in Myp2 clusters.

- (A) Montage of snapshots from a simulation of a 3D ring using flat geometry, starting at the timestep before Myp2 clusters are added in to the simulation. Scale bar is 2 μm .
- (B) Ring tension vs. time for the simulation data shown in A. The time-averaged tension before the addition of Myp2 clusters is calculated by averaging the ring tension measured at all timepoints after $t = 100 \text{ s}$, up until the addition of Myp2. The time-averaged tension after the addition of Myp2 clusters is calculated by averaging the ring tension measured at all timepoints from 100 s after the addition of Myp2 clusters, until the end of the simulation.
- (C) Histogram of Myp2 velocities from the simulation data used in A and B. The maximum speed of Myp2 in the F-V relationship is $0.35 \mu\text{m/s}$.
- (D) Ring tension vs. time for a simulation with Myp2 clusters (added in at $t = 120 \text{ s}$) where the severing dynamics are reduced at $t = 480 \text{ s}$.
- (E) Standard deviation of ring tension along the ring length, as a function of time, for the same simulation data as shown in D.
- (F) Heat map of ring tension vs. time for the same simulation data used in D and E.

4.6. Attempting to more accurately model the structure of the nodes

For our next goal, we sought to more accurately model the structure of the nodes, trying to take account of the individual pairs of Myo2 heads within the nodes. So far, we have modelled the nodes as single points, where if one of the actin beads comes within a certain capture distance of a node, then an interaction can potentially be formed with that bead (Figure 4.5A). However, by modelling the individual pairs of Myo2 heads, we hoped to better reproduce the behaviour of the *S. pombe* AMR, without having to rely on parameters such as *maxInt*, whose values are somewhat open to interpretation, and can be modified to suit the goals of the simulation that is currently being performed (see section 4.3, [35,108,164])

We decided to explicitly simulate individual pairs of myosin heads within each myosin cluster/node (i.e. assuming the Myo2 molecules work as dimers). Then, rather than having a single, relatively large interaction volume for each node (Figure 4.5A), we would instead utilise a set of smaller interaction volumes, centred on each of the individual pairs of Myo2 heads (hereafter referred to as just ‘heads’). This required us to consider the set of forces that would be needed to produce the desired behaviour, and we shall document these below.

Firstly, because each of the Myo2 heads would have a smaller interaction volume, it would be necessary for the heads to explore the available space around the node, in order to search for actin filaments. To achieve this, we applied randomly generated forces to each of the heads, to mimic the behaviour of thermal diffusion/brownian motion (Figure 4.5B) [165]. Calculation of these forces required the estimation of a drag coefficient for the heads, which we calculated using Stoke’s law for an idealised sphere¹, assuming a radius of 7 nm for a single myosin head

¹ Stoke’s law states that $\gamma = 6\pi\eta R$, where γ is the drag coefficient, η is the dynamic viscosity of the surrounding fluid (assuming $\eta = 350\eta_{water} = 0.301 \text{ Pa s}$ [108]), and R is the radius of the spherical object.

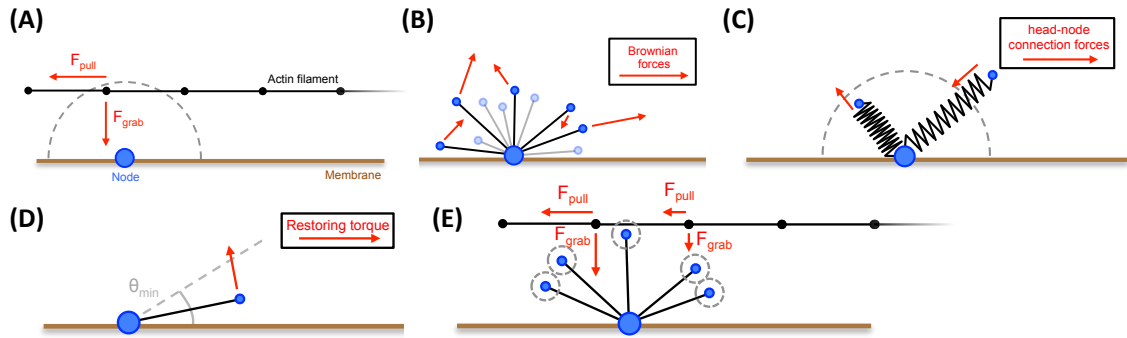


Figure 4.5: Modelling individual myosin heads within clusters.

- (A) Schematic of old model of myosin clusters/nodes, and how they interact with actin filaments that come within the capture radius (grey dashed semicircle).
- (B) Diagram of new model of myosin clusters within nodes. Ten individual 'head' domains (representing Myo2 dimers) are attached to the centre of the node, and undergo diffusive/brownian motion, modelled with randomly generated forces.
- (C) Diagram of spring-connection forces between node centre and head domains. Nodes and heads are connected by a Hookean interaction, which pulls them together if they get too far apart, and pushes them away if they get too close (equilibrium distance shown by grey semicircle, = 80 nm).
- (D) Diagram of how the restoring torque keeps heads above the membrane. If the angle between the head-node connection and membrane decreases below a value θ_{\min} , then the head experiences a restoring torque to push it back into the optimum region for interacting with actin filaments. The direction of this force is perpendicular to the node-head connection, and points towards the line perpendicular to the membrane surface at the centre of the node.
- (E) Diagram of how the new Myo2 clusters in nodes interact with actin filaments. The individual heads each have a small radius of interaction around them (dashed grey circles). When one of these comes into contact with a segment of an actin filament, pulling and grabbing forces are exerted on the beads at either end of the segment, with the division of the forces determined by where on the segment the head is closest to. Equal and opposite forces are exerted on the bound head, due to Newton's third law of motion.

[166]. The value that we obtained from Stoke's law was then multiplied by 2, to account for the pair of Myo2 heads in each 'head' in the model.

On their own, the brownian forces would lead to the diffusion of the heads away from their nodes. Therefore, we next needed to include additional forces that constrained this diffusive motion to occur over a hemisphere that was centred on the node. In order to maintain the distance between the node centre and a head that is attached to that node, we included a spring interaction between these two entities. This pulled the node centre and head together if they moved too far away from each other, and pushed them away if they became too close (Figure 4.5C). Then, in order to keep the heads in the allowed volume (i.e. $z > 0$), and in the optimum region for interacting with actin filaments (i.e. away

from the membrane surface), we applied a restoring torque to heads when the angle defined by the head, the node centre, and the membrane, fell below a threshold value (Figure 4.5D). This force had a constant magnitude of τ , and was directed perpendicular to the line between the node and the head, and towards the line perpendicular to the membrane surface at the centre of the node, in order to push the heads away from the membrane (see section 8.1 for more detail). As a final addition, we also included an excluded volume interaction for any heads that moved below the membrane at $z = 0$, by exerting a constant force of 5 pN in the + z direction on these heads.

Having ensured that the heads would be able to explore the hemisphere around the node, in order to search for actin filaments, we next needed to consider how the heads would interact with actin filaments. Rather than having a single interaction volume centred on the node, like before, we now used a set of smaller interaction volumes (radius of 15 nm) centred on each of the heads in the node (Figure 4.5E). However, this introduced another problem, as up until now the myosin clusters only interacted with the beads in the actin filaments, which are spaced 100 nm apart, and if we are using an interaction radius of 15 nm around each head, then the chance that a head will be able to interact with a given filament is very small. This is because even if part of a filament segment (i.e. the section between 2 neighbouring beads) passes within this distance of a head, it is still unlikely that the head will be near enough to one of the beads at each end of the segment, in order to interact with it (Figure 4.5E).

One solution to this would be to decrease the spacing between actin beads. However, whilst this would be simple to implement, it would drastically slow down the speed of simulations by increasing ~ 10 fold the number of actin beads within the simulation. Instead, rather than just measuring the distances between a head and the beads, we decided to implement a method where we first identify which actin filament segment was closest to a given head. Then, we measured the distance between the head and the nearest point of this segment. If this distance

was less than the capture radius of 15 nm around the head, then an interaction was formed, with the pulling and grabbing forces being divided between the beads at either end of the segment¹, and with the larger portion of the force being exerted on the bead that is nearest to the head (Figure 4.5E).

Finally, we also introduced an approximation of the myosin ATPase cycle for each Myo2 head. Unbound heads can exist in a state where they are either unavailable or available to bind to actin filaments. An available head will bind with certainty to a single actin filament that comes within the interaction volume of that head. In this bound state, heads exert pulling and grabbing forces on the actin filament, as before. The pulling force from a single head has a total magnitude of 4 pN, and is directed towards the filament pointed end, whilst the grabbing force is proportional to the distance between the head and the nearest point of the actin segment (maximum magnitude of ~ 1.7 pN), and is directed perpendicular to the filament and towards the head. Heads will remain in their bound state for a length of time determined by the duty ratio of Myo2 and the length of the ATPase cycle [95], and after this time has passed a head will unbind from an actin filament, and enter the unavailable state. The rate constant for the transition from unavailable to available was chosen so that, at any given time, there is likely to be 2 heads per cluster bound to nearby actin filaments, under the assumption that when a head becomes available it is very quickly able to find an actin filament to interact with.

In order to test this new model of myosin clusters/nodes, we first built a toy model containing a single actin filament with a fixed barbed end position, and a single Myo2 cluster, the centre of which was given the same drag coefficient as the nodes in our previous simulations, and which would pull itself along the actin filament (Figure 4.6A). If the

¹ If the distance between a pair of beads is defined as being 1 unit length, and if a myosin head binds to a point that is a distance λ away from the first bead, and $1 - \lambda$ away from the second bead, then the pulling and grabbing forces exerted on the 1st bead will be equal to $(1 - \lambda)$ multiplied by the total forces, while the forces exerted on the 2nd bead will be equal to λ multiplied by the total forces.

system behaved as expected, then we should see that the Myo2 cluster moves along the actin filament with a roughly constant velocity, corresponding to a time-averaged pulling force of 4 pN¹.

Simulations of this toy model indicated that that this was indeed the case. We observed that the cluster moved along the actin filament with a roughly constant velocity (Figure 4.6A, Figure 4.6B), and plotting a histogram of the number of bound heads at each timestep showed that most of the time there was only one head bound (Figure 4.6C). Measuring the time-averaged force exerted on the filament by the cluster, we found that this was around 4.7 pN, indicating that a mean of ~ 1.2 heads were bound to the filament at any given time (Figure 4.6D). From our histogram, we can see that there were quite a few instances where two or more heads are bound to a filament, which appeared to be mostly balanced out by the number of instances where no heads were bound to an actin filament, therefore this behaviour is quite self consistent. Overall, it seems that the toy model has produced the behaviour that would be expected, indicating that our model of the myosin clusters is realistic.

¹ During ring formation in fission yeast spheroplasts, it was estimated that nodes pull on actin filaments with a time-averaged force of ≈ 4 pN [35]. Therefore, for our model to be considered accurate, it is important that this behaviour is reproduced.

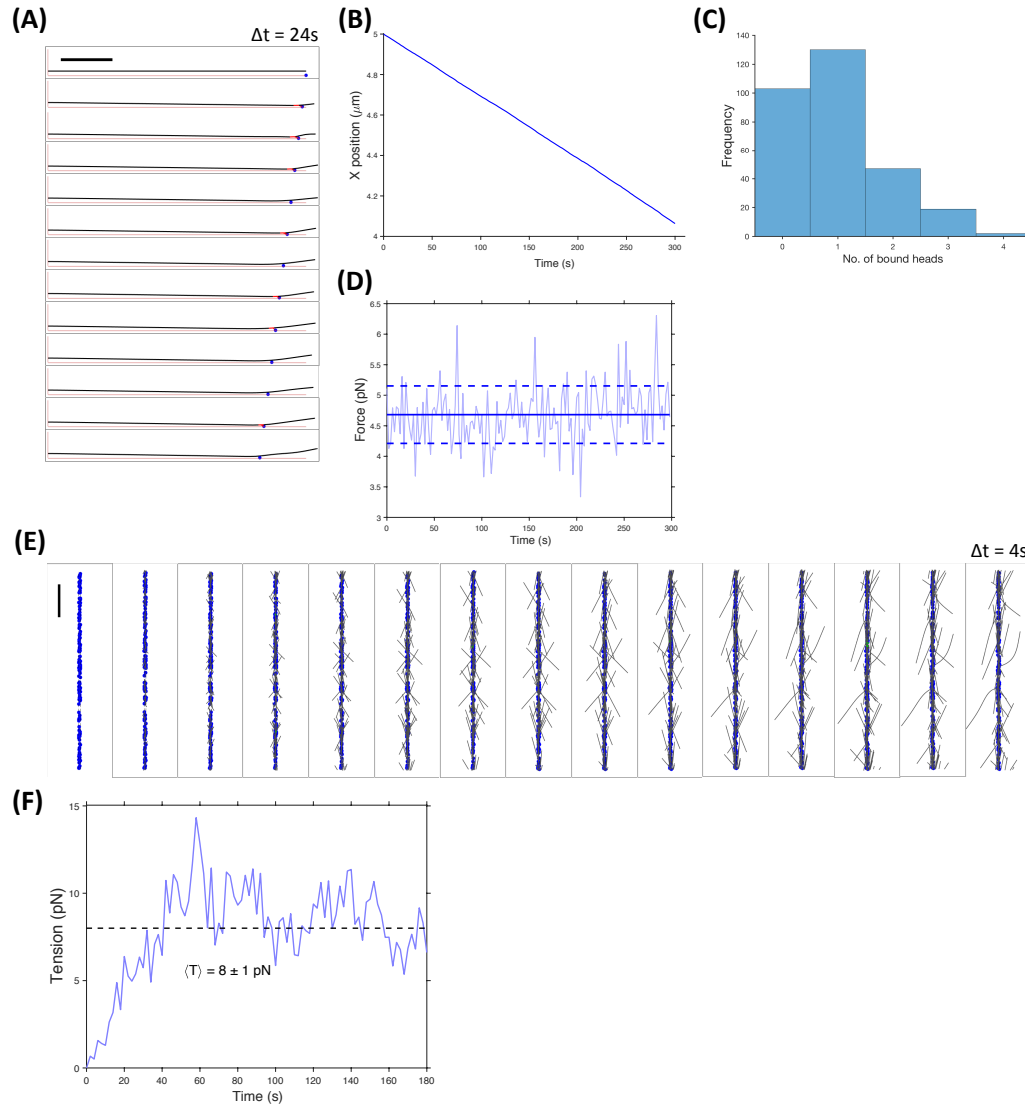


Figure 4.6: testing and implementing new model of myosin clusters.

- (A) Montage of snapshots from a simulation of a toy model with a single actin filament interacting with a single myosin cluster. Actin filament segments in red highlight which sections of the filament are interacting with the myosin heads in the cluster. Scale bar is 1 μm .
- (B) Graph of the cluster position vs. time.
- (C) Histogram of the number of myosin heads bound to the actin filament at a given time.
- (D) Plot of the force experienced by the myosin cluster vs. time. The full line indicates the time-averaged (mean) force experienced by the cluster, while the dashed lines indicate \pm the standard deviation about the mean.
- (E) Montage of snapshots from a simulated ring where the new model of the myosin clusters within the nodes is implemented. Scale bar is 2 μm .
- (F) Ring tensions vs. time for the data shown in E. The time-averaged tension is calculated from all data points after $t = 100\text{s}$.

We then implemented this model of the node structure into our full model of the ring, using the flat geometry. We initially found that actin filaments nucleated from the nodes were not captured in the ring, most likely due to their nucleation angle being lower than the threshold

angle that we set for the myosin heads. To try and counter this, we biased the nucleation direction of actin filaments to be along the direction of the ring. This resulted in some improvement to the capture of actin filaments, however this was still much worse than in any of our previous models (Figure 4.6E). Furthermore, measuring the tension in the ring showed that this was significantly reduced when compared to the tension produced in our previous simulations (Figure 4.6F). This suggests that the Myo2 heads are struggling to find actin filaments to interact with, most likely because the geometry of the system was not as idealised as that employed in our toy model (i.e. the sole actin filament in the toy model was placed an optimal height above the membrane, and was parallel to the membrane). Due to time constraints in the project we were unable to pursue this further.

4.7. Mathematical description of ring modelling, and lists of ring parameters

A full mathematical description of the original model, its modifications, and the parameters that were used for simulations can be found below. We also describe how ring properties were extracted from the simulation data, and used to quantify the results from our simulations. All simulations, and their subsequent analysis, were performed in MATLAB_R2016b.

4.7.1. The original model:

4.7.1.1. Forces and velocities

At a given time in the simulation, there are N actin filament subunits ('beads'), and M myosin clusters. The barbed end of each filament is assumed to be attached to a formin dimer, and is given a drag coefficient γ_{for} , which is much greater than the actin bead drag coefficient γ_{bead} . The total force acting on the i^{th} actin bead is

$$\mathbf{F}_i^{tot,act} = \mathbf{f}_i^{spr} + \mathbf{f}_i^{bend} + \mathbf{f}_i^x + \mathbf{f}_i^{pull} + \mathbf{f}_i^{grab}, \quad (4.1)$$

where $\mathbf{F}_i^{tot,act}$ is the total force on the i^{th} actin bead, \mathbf{f}_i^{spr} is the force from the spring connection to adjacent beads in the filament, \mathbf{f}_i^{bend} is the bending force which acts to try and keep actin filaments straight, \mathbf{f}_i^x is from crosslinking interactions with actin beads in other filaments, and \mathbf{f}_i^{pull} and \mathbf{f}_i^{grab} are the total pulling and grabbing forces, respectively, from myosin clusters interacting with the i^{th} actin bead.

The total force acting on the j^{th} myosin cluster is given by

$$\mathbf{F}_j^{tot,myo} = \mathbf{f}_j^{pull,myo} + \mathbf{f}_j^{grab,myo} + \mathbf{f}_j^{excl}, \quad (4.2)$$

where $\mathbf{F}_j^{tot,myo}$ is the total force on the j^{th} myosin cluster, $\mathbf{f}_j^{pull,myo}$ and $\mathbf{f}_j^{grab,myo}$ are the Newton's 3rd law pair forces for the pulling and grabbing forces, respectively, that the j^{th} myosin cluster exerts on actin filaments, and \mathbf{f}_j^{excl} is the excluded volume force from interactions between the j^{th} myosin cluster and other nearby clusters.

The forces on each actin bead and myosin cluster are calculated at every simulation timestep, and are used to update the position of the simulation components using the forward Euler method:

$$\mathbf{r}_i^{act}(t + \Delta t) = \mathbf{r}_i^{act}(t) + \frac{\mathbf{F}_i^{tot,act}}{\gamma_i} \cdot \Delta t, \quad (4.3)$$

$$\mathbf{r}_j^{myo}(t + \Delta t) = \mathbf{r}_j^{myo}(t) + \frac{\mathbf{F}_j^{tot,myo}}{\gamma_{myo}} \cdot \Delta t. \quad (4.4)$$

Here, t is the current time in the simulation, Δt is the simulation timestep, γ_i is equal to γ_{for} if the i^{th} actin bead is a barbed end, and is equal to γ_{bead} otherwise (because the barbed ends are the formin dimers, which are bound to the membrane, therefore experiencing a higher drag), and γ_{myo} is the myosin cluster drag coefficient. Additionally, \mathbf{r}_i^{act} and \mathbf{r}_j^{myo} are position vectors for the i^{th} actin bead and

the j^{th} myosin cluster, respectively, and because the model is 2-dimensional, they each contain two elements, an x and a y coordinate.

4.7.1.2. Actin filament springs

The force on the i^{th} actin bead from its spring connections to neighbouring actin beads is given by

$$\mathbf{f}_i^{spr} = -\sum_j k_{act} (|\mathbf{r}_i^{act} - \mathbf{r}_j^{act}| - l_{act}^0) \cdot \frac{\mathbf{r}_i^{act} - \mathbf{r}_j^{act}}{|\mathbf{r}_i^{act} - \mathbf{r}_j^{act}|} \quad (4.5)$$

where the sum is over the neighbouring beads, $j = i + 1, i - 1$ ($j = i + 1$ for filament barbed ends, and $j = i - 1$ for filament pointed ends), k_{act} is the stiffness of the spring connection, and l_{act}^0 is the equilibrium distance between neighbouring actin beads.

4.7.1.3. Actin bending forces

The bending force on the i^{th} actin bead is given by

$$\mathbf{f}_i^{bend} = -\frac{\partial}{\partial \mathbf{r}_i^{act}} \left[\frac{\kappa}{l_{act}^0} \sum_{j=1}^{N-2} (1 - \hat{\mathbf{t}}_{j+1} \cdot \hat{\mathbf{t}}_j) \right], \quad (4.6)$$

where κ is the actin filament bending modulus, and $\hat{\mathbf{t}}_j$ is the unit vector parallel to spring j ($\hat{\mathbf{t}}_j = (\mathbf{r}_{j+1}^{act} - \mathbf{r}_j^{act}) / |\mathbf{r}_{j+1}^{act} - \mathbf{r}_j^{act}|$). The quantity in the square bracket is the total bending energy of the filament containing the i^{th} actin bead, and its spatial derivative is used to find the bending force on each actin bead (the exact form of this is shown in Gauger and Stark, 2006 [167]).

4.7.1.4. Actin crosslinking forces

Crosslinking forces between nearby actin beads (separation < 50 nm) on different filaments are modelled as a spring interaction between the pair of beads, given by the formula

$$\mathbf{f}_i^x = -\sum_j k_x (|\mathbf{r}_i^{act} - \mathbf{r}_j^{act}| - r_x^0) \frac{\mathbf{r}_i^{act} - \mathbf{r}_j^{act}}{|\mathbf{r}_i^{act} - \mathbf{r}_j^{act}|}, \quad (4.7)$$

where k_x is the spring constant for the crosslinking interaction, r_x^0 is the equilibrium length of the spring, and the sum is over all actin subunits j that are linked to actin subunit i by crosslinking interactions. Because, in the simulation, the filament barbed ends acted as the formin dimers, crosslinking interactions were only allowed to form between non-barbed end actin subunits.

4.7.1.5. Myosin II pulling

The pulling force exerted on the i^{th} actin bead from all the myosin clusters that it interacts with is given by

$$\mathbf{f}_i^{pull} = n_i^{myo} f_{myo} \hat{\mathbf{t}}_{i-1}, \quad (4.8)$$

where f_{myo} is the force that a cluster exerts on a single actin filament, and n_i^{myo} is the effective number of myosin clusters interacting with the i^{th} bead. The purpose of n_i^{myo} is to take account of the behaviour of myosin clusters when they interact with multiple actin filaments: When a myosin cluster interacts with a number of actin filaments greater than a certain threshold value, called *maxInt*, the pulling force that the cluster exerts on each filament is reduced (section 4.1). To take account of this when calculating the total myosin pulling force on a single actin bead, the term n_i^{myo} is used, which is calculated as $n_i^{myo} = \sum_j \alpha_j$, where the sum is over the myosin clusters j that interact with the i^{th} actin bead, and $\alpha_j = 1$ if cluster j interacts with $n_j^{int} \leq \text{maxInt}$ actin filaments, or $\alpha_j = \text{maxInt} /$

n_j^{int} when $n_j^{int} > \maxInt$ (n_j^{int} is the number of actin filaments that myosin cluster j interacts with).

For each myosin cluster, each pulling interaction also produces an equal and opposite force on the myosin cluster, the total on cluster j being $\mathbf{f}_j^{pull,myo}$, from Newton's third law of motion. Additionally, interactions between myosin clusters and the barbed ends of filaments were not allowed, as the barbed ends are the formin dimers in the simulation. Because the characteristic velocity (force divided by drag coefficient) of the myosin clusters and formin dimers is much smaller than the previously measured load-free actin gliding velocities of Myo2 [95,139], we assumed that the pulling forces were independent of the relative motion of the myosin clusters and actin filaments.

4.7.1.6. Myosin II grabbing

As well as exerting pulling forces, myosin II clusters also exert grabbing forces on actin beads, which draws them in to the centre of the cluster. This binding is modelled as a spring interaction with an equilibrium length of zero, and the grabbing force on the i^{th} actin bead is given by

$$\mathbf{f}_i^{grab} = -\sum_j k_{grab} \left[(\mathbf{r}_i^{act} - \mathbf{r}_j^{myo}) - ((\mathbf{r}_i^{act} - \mathbf{r}_j^{myo}) \cdot \hat{\mathbf{t}}_i) \hat{\mathbf{t}}_i \right], \quad (4.9)$$

where k_{grab} is the spring constant for the grabbing interaction, and the sum is over all the myosin clusters j that are within a distance of r_{myo} from the i^{th} actin bead. The second term in the square brackets is to calculate the component of $\mathbf{r}_i^{act} - \mathbf{r}_j^{myo}$ that is parallel to the actin filament, and then subtract off this component so that the final grabbing force only acts perpendicular to the filament.

For each myosin cluster, the grabbing interaction also produces an equal and opposite force on the myosin cluster, the total on cluster j being $\mathbf{f}_j^{grab,myo}$, again from Newton's third law of motion. Similarly, grabbing interactions between myosin clusters and the barbed ends of

filaments were not allowed, as the barbed ends are the formin dimers in the simulations.

4.7.1.7. Myosin cluster excluded volume forces

When a pair of myosin clusters comes within a distance d_{myo} of each other, they experience an excluded volume repulsion force. The force on the i^{th} myosin cluster is given by

$$\mathbf{f}_i^{excl} = -\sum_j k_{myo}^{excl} (|\mathbf{r}_i^{myo} - \mathbf{r}_j^{myo}| - d_{myo}) \frac{\mathbf{r}_i^{myo} - \mathbf{r}_j^{myo}}{|\mathbf{r}_i^{myo} - \mathbf{r}_j^{myo}|}, \quad (4.10)$$

where k_{myo}^{excl} is the spring constant for repulsion, and the sum is over all myosin clusters j that are within a distance d_{myo} of the i^{th} cluster. The value of k_{myo}^{excl} was chosen to be very large, in order to approximate a hard sphere interaction between clusters.

4.7.1.8. Measuring ring tension in the simulated rings

The ring tension at a given timestep in simulated rings was calculated using the formula

$$T = \sum_{i=1}^{N_{spring}} \frac{\cos^2(\theta_i^{spring}) T_i^{spring} l_i^{spring}}{L}, \quad (4.11)$$

where the sum is over all the springs in the simulation, θ_i^{spring} is the angle between the i^{th} spring and the ring axis (along the x direction), T_i^{spring} is the tension stored in the i^{th} spring, l_i^{spring} is the length of the i^{th} spring, and L is the length of the simulated ring.

The expression inside the sum in equation 2.11 can be broken down as the product of two quantities: The first is given by $\cos(\theta_i^{spring}) T_i^{spring}$, which is the component of the tension in the i^{th} spring that is parallel to the ring axis, and is present because only this component of the i^{th} spring's tension will contribute to the total ring

tension. The second quantity is given by $\cos(\theta_i^{spring}) l_i^{spring} / L$, which is the component of the i^{th} spring's length parallel to the ring axis, divided by the length of the ring. This second quantity appears because it is necessary to normalise the tension stored in each filament relative to the length of the ring: For example, if a ring consists of a single filament with a length of L , that is oriented parallel to the ring axis and placed under a tension T , then the total tension in the ring would be T . If that filament is cut in half, and both of the subsequent filaments are also placed under a tension of T , then the total tension in the ring should still be T , because the compressive force in the membrane underneath the filaments (caused by the tension in the filaments) has not been increased by cutting a single filament into two shorter filaments.

4.7.1.9. Parameter values in the original model

All the parameter values used in the original version of the model are listed in Table 4.1. All the values shown are taken from Stachowiack, *et al*, 2014 [35].

Table 4.1: List of parameter values used in the original simulation.

Parameter	Meaning	Value
d	Ring binding zone width	$0.2 \mu\text{m}$
L	Ring length	$10 \mu\text{m}$
γ_{for}	Formin drag coefficient	$1.9 \text{ nN s}/\mu\text{m}$
γ_{bead}	Actin bead drag coefficient	$0.2 \text{ pN s}/\mu\text{m}$
γ_{myo}	Myosin cluster drag coefficient	$1.3 \text{ nN s}/\mu\text{m}$
ρ_{for}	Mean formin dimer linear density	$150/L \mu\text{m}^{-1}$
ρ_{myo}	Mean Myosin cluster linear density	$75/L \mu\text{m}^{-1}$
k_{off}^{for}	Formin unbinding rate	0.023 s^{-1}
k_{off}^{myo}	Myosin cluster unbinding rate	0.026 s^{-1}
v_{pol}	Formin-mediated actin polymerisation rate	70 nm/s
l_{act}^0	Equilibrium length between actin beads	$0.1 \mu\text{m}$
k_{act}	Actin filament stretching spring constant	$1000 \text{ pN}/\mu\text{m}$
l_p	Actin filament persistence length	$10 \mu\text{m}$

κ	Actin filament bending modulus	$K_b T l_p$, 0.0414 pN μm^2
k_{off}^x	Actin crosslinker unbinding rate	3.3 s ⁻¹
k_{on}^x	Actin crosslinker binding rate	1 $\mu\text{m}^{-1}\text{s}^{-1}$
k_x	Actin crosslinking spring stiffness	25 pN/ μm
r_x^0	Actin crosslinking spring rest length	30 nm
r_x^{bind}	Threshold distance for crosslinking interaction	50 nm
r_{myo}	Myosin cluster capture radius	100 nm
f_{myo}	Myosin cluster pulling force/filament	4 pN
$maxInt$	Maximum number of filaments that a myosin cluster can interact with at full force	10
k_{grab}	Spring constant for grabbing interaction	5 pN/ μm
d_{myo}	Myosin cluster excluded volume distance	50 nm
k_{myo}^{excl}	Myosin excluded volume spring constant	1000 pN/ μm
r_{sev}	Cofilin mediated actin filament severing rate	0.03 $\mu\text{m}^{-1}\text{s}^{-1}$

Simulations were performed with a timestep of $5 \times 10^{-5}\text{s}$, equating to 20,000 timesteps per second of simulated time. However, there were a number of aspects of the simulation that were computationally expensive, and did not necessarily need to be performed at every single timestep. These are: searching for crosslinking interactions between actin filaments, searching for interactions between myosin clusters and actin filaments, and simulating the turnover of ring components, through the severing of actin filaments and the unbinding and binding of formin dimers and myosin clusters.

In order to increase the simulation efficiency, these aspects of the simulation were only performed for a small subset of the total number of simulation timesteps, with the corresponding binding/unbinding probabilities, etc., modified to reflect this. The parameters relating to this process are shown in Table 4.2, and are the same as was used in Stachowick, *et al*, 2014 [35].

Table 4.2: List of temporal parameters used in the original model.

Parameter	Meaning	Value
-----------	---------	-------

Δt	Simulation timestep	5×10^{-5} s, or 20,000 steps/s
t_x	Time between updating crosslinking interactions	0.015s, or every 300 timesteps
t_{sev}	Time between calculating turnover of simulation components, and severing of actin filaments	0.1s, or every 2000 timesteps
t_{myo}	Time between updating myosin-actin interactions	0.01s, or every 200 timesteps
t_{save}	Time between saving ring data for quantification and making movies of the simulation	1s

From the parameters listed in Table 4.2, we can use the myosin pulling force f_{myo} and the formin drag coefficient γ_{for} (see Table 4.1, because $\gamma_{for} \gg \gamma_{bead}$, we can ignore the drag from actin beads in a filament) to estimate how far ring components will move over these times. In a single timestep, a formin dimer will move on the order of 10^{-7} μm in a single timestep, a distance of $\sim 10^{-5}$ μm between both crosslinking and myosin timesteps, and $\sim 10^{-4}$ μm between severing/turnover timesteps. In reality, a single actin filament will likely be pulled by multiple myosin clusters. However those myosin clusters are also likely to interact with multiple actin filaments (average of around 20 filaments in the ring cross-section), which will reduce the force that they exert on individual filaments, and that means that these are likely to be reasonable order-of-magnitude estimates of the displacement of ring components over these times. For myosin and crosslinking timesteps, the distances moved are both much less than the corresponding interaction distances (r_x^{bind} and r_{myo} , see Table 4.1), so only recalculating these interactions every t_{myo} and t_x seconds, respectively, is unlikely to affect the behaviour of the simulated ring.

With regards to severing, a filament of average length (~ 1 μm) will have a probability of being severed over a time Δt of $\sim 10^{-6}$. Over a time of t_{sev} , this becomes $\sim 10^{-3}$, which is still $\ll 1$. Similarly, the probability of a myosin cluster or formin dimer unbinding over a time of t_{sev} is $\sim 10^{-3}$, again $\ll 1$. Therefore, only allowing filament severing and

component turnover to occur every t_{sev} seconds should also not have a noticeable effect on the simulated ring behaviour.

Additionally, it was not necessary to save ring data (for quantification and making movies of the simulation) at every timestep, so this data was only saved every t_{save} seconds in the simulation.

Modifications to the model:

Most modifications applied to the model build on the previous modifications, so we will describe each of these in sequence.

4.7.2. Combining myosin clusters and formin dimers into nodes

Instead of having separate myosin clusters and formin dimers, we combined them into the same ‘node’ structure. Like the formin dimers, each node nucleated a single filament, and like the myosin clusters, each node was able to grab and pull nearby actin filaments, with the exception of the filament that it nucleated. When new nodes bound into the ring, they immediately nucleated a new filament, and when a node unbound from the ring its filament also was removed. The equations for calculating pulling and grabbing forces were slightly modified to reflect this new ring organisation, with the pulling and grabbing forces on the i^{th} actin bead changing to

$$\mathbf{f}_i^{pull} = n_i^{node} f_{myo} \hat{\mathbf{t}}_{i-1}, \quad (4.12)$$

and

$$\mathbf{f}_i^{grab} = -\sum_j k_{grab} \left[(\mathbf{r}_i^{act} - \mathbf{r}_j^{act}) - ((\mathbf{r}_i^{act} - \mathbf{r}_j^{act}) \cdot \hat{\mathbf{t}}_i) \hat{\mathbf{t}}_i \right], \quad (4.13)$$

respectively. Here, n_i^{node} is similar to n_i^{myo} in equation 4.8, and is the effective number of nodes interacting with the i^{th} bead, $n_i^{node} = \sum_j \alpha_j$, where the sum is over the nodes j that interact with the i^{th} actin bead, and

$\alpha_j = 1$ if node j interacts with $n_j^{int} \leq \text{maxInt}$ actin filaments, or $\alpha_j = \text{maxInt}/n_j^{int}$ when $n_j^{int} > \text{maxInt}$. In equation 4.13, the sum is over nodes j that interact with the i^{th} bead (i.e. separation of less than r_{myo}).

Excluded volume interactions between nodes were calculated in a similar way as before, using the equation

$$\mathbf{f}_i^{\text{excl}} = -\sum_j k_{\text{node}}^{\text{excl}} (|\mathbf{r}_i^{\text{act}} - \mathbf{r}_j^{\text{act}}| - d_{\text{node}}) \frac{\mathbf{r}_i^{\text{act}} - \mathbf{r}_j^{\text{act}}}{|\mathbf{r}_i^{\text{act}} - \mathbf{r}_j^{\text{act}}|}, \quad (4.14)$$

where, in this case, i and j are the indices of beads that are at the barbed end of filaments, the sum is over the beads j which are within a distance d_{node} of the i^{th} bead, $k_{\text{node}}^{\text{excl}}$ is the spring constant of repulsion, and d_{node} is the excluded volume distance between nodes.

The equations for the total force on individual actin beads was modified as follows: If the i^{th} actin bead is not a barbed end, then the formula remains the same as equation 4.1, except with the pulling and grabbing forces were calculated from equations 4.12 and 4.13. However, if the i^{th} bead is a barbed end, then the formula becomes:

$$\mathbf{F}_i^{\text{tot,act}} = \mathbf{f}_i^{\text{spr}} + \mathbf{f}_i^{\text{bend}} + \mathbf{f}_i^{\text{pull,myo}} + \mathbf{f}_i^{\text{grab,myo}} + \mathbf{f}_i^{\text{excl}}, \quad (4.15)$$

where $\mathbf{f}_i^{\text{pull,myo}}$ and $\mathbf{f}_i^{\text{grab,myo}}$ are the Newton's 3rd law pair forces from the pulling and grabbing forces that the node exerts on other actin filaments, respectively, and $\mathbf{f}_i^{\text{excl}}$ is calculated using equation 4.14.

We did not perform any simulations with this model, and instead proceeded to make our next modification. Because of this, we will not list the new set of parameter values until the end of subsequent section.

4.7.3. Making the simulation 3D (still using flat geometry)

The next step was to make the model 3 dimensional. This was achieved by defining the membrane to be at a height of $z = 0$, and defining the volume of $z > 0$ as being inside the cell, and the volume of $z < 0$ as outside

of the cell, and therefore excluded. The calculation of forces and component velocities was mostly the same as in the previous model, as it was simply a case of changing all the vectors from having 2 components to having 3 components (i.e. x , y , and z). However, a few additional considerations needed to be made. Firstly, we included a membrane excluded volume force that is applied to actin beads that move below $z = 0$:

$$\mathbf{f}_i^{mem} = f_{mem} \hat{\mathbf{z}}, \quad (4.16)$$

where f_{mem} is the magnitude of the membrane excluded volume force, and $\hat{\mathbf{z}}$ is the unit vector pointing in the $+z$ direction. Secondly, for nodes, we only allowed motion within the x - y plane (i.e. no z motion). From these considerations, the equation for the total force acting on the i^{th} actin bead, in the case when it was not a barbed end, became

$$\mathbf{F}_i^{tot,act} = \mathbf{f}_i^{spr} + \mathbf{f}_i^{bend} + \mathbf{f}_i^x + \mathbf{f}_i^{pull} + \mathbf{f}_i^{grab} + \mathbf{f}_i^{mem}, \quad (4.17)$$

whilst for the case where the i^{th} bead was a barbed end, the equation for the total force became

$$\mathbf{F}_i^{tot,act} = (\mathbf{f}_i^{spr} + \mathbf{f}_i^{bend} + \mathbf{f}_i^{pull,myo} + \mathbf{f}_i^{grab,myo} + \mathbf{f}_i^{excl})_{xy}, \quad (4.18)$$

where $(\dots)_{xy}$ means that we only take the x and y components of whatever is within the brackets.

We also increased the ring length from $10 \mu\text{m}$ to $12 \mu\text{m}$ (change in diameter from ~ 3.2 to $\sim 3.8 \mu\text{m}$), as $10 \mu\text{m}$ is on the smaller end of measured ring circumferences, and it was also previously observed that *adf1*-M2 and *adf1*-M3 cells had slightly larger diameters than WT cells [66]. We also decreased the ring width from $0.2 \mu\text{m}$ to $0.1 \mu\text{m}$, to reflect more recent super resolution observations of the ring [92]. Neither of these modifications were expected to change the overall behaviour of the

simulated ring. The updated set of parameter values are shown in Table 4.3. Temporal parameters were the same as in Table 4.2.

Table 4.3: List of parameter values used in 3D flat geometry simulation with nodes. Parameters that are new, or modified from the previous iteration of the model, are shaded. (A) [92]. (B) [66]. (C) Value is halfway between values for myosin clusters and formin dimers in original model. (D) Same values as used for the formin dimers in the original model. (E) [62]. (F) Similar to values used previously [164]. (G) The same values as used for myosin clusters in the original simulations. (H) Because the number of myosin clusters was doubled (now localised in the nodes), we halved the value of *maxInt*.

Parameter	Meaning	Value
d	Ring binding zone width	0.1 μm (A)
L	Ring length	12 μm (B)
γ_{node}	Node drag coefficient	1.5 nN s/ μm (C)
γ_{bead}	Actin bead drag coefficient	0.2 pN s/ μm
ρ_{node}	Mean node linear density	150/L μm^{-1} (D)
k_{off}^{node}	Node unbinding rate	0.023 s $^{-1}$ (D)
v_{pol}	Formin-mediated actin polymerisation rate	70 nm/s
θ_{nuc}	Angle of filament nucleation above membrane	8° (E)
l_{act}^0	Equilibrium length between actin beads	0.1 μm
k_{act}	Actin filament stretching spring constant	1000 pN/ μm
l_p	Actin filament persistence length	10 μm
κ	Actin filament bending modulus	$K_b T l_p$, 0.0414 pN μm^2
f_{mem}	Magnitude of membrane exclusion force on actin beads	5 pN (F)
k_{off}^x	Actin crosslinker unbinding rate	3.3 s $^{-1}$
k_{on}^x	Actin crosslinker binding rate	1 $\mu\text{m}^{-1}\text{s}^{-1}$
k_x	Actin crosslinking spring stiffness	25 pN/ μm
r_x^0	Actin crosslinking spring rest length	30 nm
r_x^{bind}	Threshold distance for crosslinking interaction	50 nm
r_{myo}	Node capture radius	100 nm (G)
f_{myo}	Myosin cluster pulling force/filament	4 pN
$maxInt$	Maximum number of filaments that a node can interact with at full force	5 (later, 1) (H)
k_{grab}	Spring constant for grabbing interaction	5 pN/ μm

d_{node}	Node excluded volume distance	50 nm (G)
k_{node}^{excl}	Node excluded volume spring constant	1000 pN/ μ m (G)
r_{sev}	Cofilin mediated actin filament severing rate	$0.03 \mu\text{m}^{-1}\text{s}^{-1}$

4.7.4. Using a 3D cylindrical geometry

For the next step, rather than using a flat geometry with periodic boundary conditions, we used a cylindrical geometry, to reflect the morphology of the yeast cell, and to allow us to visualise ring peeling, if present, when actin severing is perturbed.

The ring was placed on the inner surface of a cylinder, representing the yeast membrane, with the area inside the cylinder representing the cytoplasm. The cylinder was oriented so that its long axis was along the z-direction, with the z-axis describing the axis of the cylinder, and with the ring placed in the x-y plane, i.e. at $z = 0$. Any actin beads that moved outside of the cytoplasmic region (i.e. $\sqrt{x^2 + y^2} > \text{cell radius}$) experienced an excluded volume force, given by the formula

$$\mathbf{f}_i^{mem} = -f_{mem}\hat{\mathbf{r}}, \quad (4.19)$$

where f_{mem} again determines the magnitude of the membrane excluded volume force, and $\hat{\mathbf{r}}$ is a unit vector that points in the radial direction in a cylindrical polar coordinate system (i.e. $\hat{\mathbf{r}} = (x\hat{\mathbf{x}} + y\hat{\mathbf{y}})/\sqrt{x^2 + y^2}$).

In addition, we introduced a binding force between nodes and the membrane, modelled as a Hookean spring with a rest length of zero, in order to stop the nodes from being pulled away from the membrane, or pushed into the excluded volume. This is calculated using

$$\mathbf{f}_i^{bind} = -k_{bind}(|\mathbf{r}_{i,xy}^{act}| - R_0) \frac{\mathbf{r}_{i,xy}^{act}}{|\mathbf{r}_{i,xy}^{act}|}, \quad (4.20)$$

where k_{bind} is the spring constant for the membrane-node interaction, R_0 is the cell radius, and $\mathbf{r}_{i,xy}^{act}$ is the vector of the x-y coordinates of the i^{th}

actin bead. This force replaces the condition in the previous iteration of the model that prevents any motion of nodes in the z-direction.

The equation for the total force acting on actin beads that are not barbed ends is the same as in equation 4.17, except equation 4.19 was used to calculate the excluded volume force from the membrane. The equation for the total force on nodes/barbed end beads is given by

$$\mathbf{F}_i^{tot,act} = \mathbf{f}_i^{spr} + \mathbf{f}_i^{bend} + \mathbf{f}_i^{pull,myo} + \mathbf{f}_i^{grab,myo} + \mathbf{f}_i^{excl} + \mathbf{f}_i^{bind}, \quad (4.21)$$

where \mathbf{f}_i^{bind} is given by equation 4.20. The parameter values used for this model are given in Table 4.4. Temporal parameters were the same as in Table 4.2. When using this model and the previous, flat version, we initially used *maxInt* values of 5, and then switched to using values of 1 (see section 4.3).

Table 4.4: List of parameter values used in 3D cylindrical geometry simulation with nodes. Parameters that are new, or modified from the previous iteration of the model are shaded. (A) [66]. (B) Chosen to be sufficiently large to only allow small extension of the membrane-node connection.

Parameter	Meaning	Value
d	Ring binding zone width	0.1 μm
$R0$	Cylinder radius	12/2 π μm (A)
γ_{node}	Node drag coefficient	1.5 nN s/ μm
γ_{bead}	Actin bead drag coefficient	0.2 pN s/ μm
ρ_{node}	Mean node linear density	150/L μm^{-1}
k_{off}^{node}	Node unbinding rate	0.023 s $^{-1}$
v_{pol}	Formin-mediated actin polymerisation rate	70 nm/s
θ_{nuc}	Angle of filament nucleation above membrane	8 $^\circ$
l_{act}^0	Equilibrium length between actin beads	0.1 μm
k_{act}	Actin filament stretching spring constant	1000 pN/ μm
l_p	Actin filament persistence length	10 μm
κ	Actin filament bending modulus	$K_b T l_p$, 0.0414 pN μm^2
f_{mem}	Magnitude of membrane exclusion force on actin beads	5 pN

k_{off}^x	Actin crosslinker unbinding rate	3.3 s ⁻¹
k_{on}^x	Actin crosslinker binding rate	1 μm ⁻¹ s ⁻¹
k_x	Actin crosslinking spring stiffness	25 pN/μm
r_x^0	Actin crosslinking spring rest length	30 nm
r_x^{bind}	Threshold distance for crosslinking interaction	50 nm
r_{myo}	Node capture radius	100 nm
f_{myo}	Myosin cluster pulling force/filament	4 pN
$maxInt$	Maximum number of filaments that a node can interact with at full force	5 (later, 1)
k_{bind}	Spring constant for interaction between node and membrane	1000 pN/μm (B)
k_{grab}	Spring constant for grabbing interaction	5 pN/μm
d_{node}	Node excluded volume distance	50 nm
k_{node}^{excl}	Node excluded volume spring constant	1000 pN/μm
r_{sev}	Cofilin mediated actin filament severing rate	0.03 μm ⁻¹ s ⁻¹

4.7.5. Making the myosin actin interactions more realistic

In order to make the interactions between myosin clusters and actin filaments more realistic, we limited the maximum number of interactions that could be made between the myosin clusters in the nodes and actin filaments in the ring. In a previous paper, it was found that Myo2 in *S. pombe* had an *in vitro* duty ratio of around 10% (average of 14% and 5.8%, values obtained from two different methods), and the length of its ATPase cycle was found to be around 0.2s [95]. If there are 20 Myo2 molecules per node, then an average of 2 heads should be bound to actin filaments at a given time, with a binding lifetime of around 0.02s (t_{on}). Therefore, we redefined $maxInt$ to be the maximum number of interactions a node can make with actin filaments, and we set this value to 2 (so one node could exert a pulling force of f_{myo} on two filaments). Then, we set $t_{myo} = 0.02s$, which was a slightly larger value than previously used (Table 4.2). However, as this was roughly equal to t_{on} , this meant that we could simply recalculate the node-actin interactions at every myosin timestep, under the assumption that the previous set of interactions had finished their power stroke and unbound from their

filaments, and that a new set of myosin heads would be available to bind. Thus, we expected this model to reproduce the time-averaged characteristics of myosin cluster interactions with actin filaments. When more than two filaments were available to interact with a given node, the two filaments that the node interacts with were chosen randomly. We performed simulations with this node model using a flat geometry, for the reasons discussed in section 4.4.

Grabbing interactions between nodes and actin beads were still calculated using equation 4.13. The pulling forces on the i^{th} actin bead were similarly calculated using 4.12 as before, except we redefined n_i^{node} to simply be the number of nodes interacting with the i^{th} bead, since the maximum number of interactions was now capped, so we did not have to worry about reducing the pulling forces from nodes that interacted with multiple actin filaments. Thus, the forces on actin beads were still calculated using equations 4.17 and 4.18, but with the previously mentioned modifications.

With this model, we also performed simulations where actin severing was reduced, to mimic the effect of cofilin mutants. After allowing the simulation to run for a certain length of time (long enough to reach steady state and measure the ring tension), the severing rate was multiplied by the parameter r_{mutant} , with $r_{\text{mutant}} \leq 1$, to reduce the severing rate in the simulation from that point onwards.

The updated set of parameters used for this model are shown in Table 4.5, and the updated temporal parameters are shown in Table 4.6.

Table 4.5: List of parameter values used in 3D flat geometry simulation with more realistic node-actin interactions. Parameters that are new, or modified from the previous iteration of the model, are shaded. (A) Based on the estimated number of Myo2 molecules per node [64,65], and measurements of the Myo2 duty ratio [95]. (B) We do not know the degree to which actin severing in *adf1*-M3 cells is reduced, therefore we chose to reduce the severing rate by 50%, to get a qualitative idea of its effect.

Parameter	Meaning	Value
d	Ring binding zone width	0.1 μm

L	Ring length	12 μm
γ_{node}	Node drag coefficient	1.5 nN s/ μm
γ_{bead}	Actin bead drag coefficient	0.2 pN s/ μm
ρ_{node}	Mean node linear density	150/ L μm^{-1}
k_{off}^{node}	Node unbinding rate	0.023 s^{-1}
v_{pol}	Formin-mediated actin polymerisation rate	70 nm/s
θ_{nuc}	Angle of filament nucleation above membrane	8°
l_{act}^0	Equilibrium length between actin beads	0.1 μm
k_{act}	Actin filament stretching spring constant	1000 pN/ μm
l_p	Actin filament persistence length	10 μm
κ	Actin filament bending modulus	$K_b T l_p$, 0.0414 pN μm^2
f_{mem}	Magnitude of membrane exclusion force on actin beads	5 pN
k_{off}^x	Actin crosslinker unbinding rate	3.3 s^{-1}
k_{on}^x	Actin crosslinker binding rate	1 $\mu\text{m}^{-1}\text{s}^{-1}$
k_x	Actin crosslinking spring stiffness	25 pN/ μm
r_x^0	Actin crosslinking spring rest length	30 nm
r_x^{bind}	Threshold distance for crosslinking interaction	50 nm
r_{myo}	Node capture radius	100 nm
f_{myo}	Myosin cluster pulling force/filament	4 pN
$maxInt$	Maximum number of filaments that a node can interact with	2 (A)
k_{grab}	Spring constant for grabbing interaction	5 pN/ μm
d_{node}	Node excluded volume distance	50 nm
k_{node}^{excl}	Node excluded volume spring constant	1000 pN/ μm
r_{sev}	Cofilin mediated actin filament severing rate	0.03 $\mu\text{m}^{-1}\text{s}^{-1}$
r_{mutant}	Number to multiply r_{sev} by to reduce the actin severing rate partway through the simulation	0.5 (B)

Table 4.6: List of temporal parameters used in the ring model where node-actin interactions were made to be more realistic. New or modified parameters are shaded. (A) Chosen to be roughly the same as the measured length of the Myo2 duty cycle [95]. (B) It was not necessary to save simulation output every 1s, so we increased this to 2s. (C) Chosen to allow us sufficient simulation time before and after altering the severing rate (e.g. to measure ring tension).

Parameter	Meaning	Value
Δt	Simulation timestep	5×10^{-5} s, or 20,000 steps/s
t_x	Time between updating crosslinking interactions	0.015s, or every 300 timesteps
t_{sev}	Time between calculating turnover of simulation components, and severing of actin filaments	0.1s, or every 2000 timesteps
t_{myo}	Time between updating myosin-actin interactions	0.02s, or every 400 timesteps (A)
t_{save}	Time between saving ring data for quantification and making movies of the simulation	2s (B)
t_{mutant}	Time at which actin severing rate was altered, to mimic the effect of <i>adf1</i> mutants	600s (C)

4.7.6. Generating heatmaps of ring tension

Because we wished to investigate how ring tension varies locally within the ring, we generated heatmaps of ring tension to visualise this property. We did so by first dividing the ring length into 60 individual bins. Then, we measured the tension stored in the actin filament segments within each of these bins, with the tension stored in the i^{th} bin given by

$$T_i = \sum_{j=1}^{N_{spring,i}} \frac{\cos^2(\theta_j^{spring}) T_j^{spring} l_j^{spring}}{L_{bin}}, \quad (4.22)$$

where the sum is over the actin beads j located within the i^{th} bin (the total number of which is $N_{spring,i}$), and L_{bin} is the length of the individual bins. We only measured the tension stored in actin filament springs, and

not any of the other springs in the simulation, because it was previously found that the tension stored in actin filaments accounted for > 99% of the tension within simulated rings [35], which we also found to be the case in our earlier simulations. This same method was used after we included Myp2 clusters in our model.

4.7.7. Including Myp2 clusters in the ring simulation

Our next step was to include Myp2 clusters in the simulation. These were modelled as non-membrane bound myosin clusters, with the same $maxInt$ and t_{on} properties of Myo2 in the nodes, and the ability to exert grabbing and pulling forces on actin beads. Because these structures were not membrane bound, their drag coefficient was reduced by a factor of 10 compared to the node drag coefficient. This allowed the Myp2 clusters to travel at greater speeds than the Myo2 clusters in the original model, which meant it was necessary to employ a Force-velocity (F-v) relationship in order to calculate the amount of pulling force these exerted on actin filaments [123].

For our simulations including Myp2 clusters, the pulling and grabbing forces on actin beads were modified to also include components from the Myp2 clusters. Thus, the pulling force on the i^{th} actin bead becomes

$$\mathbf{f}_i^{pull} = \left(n_i^{node} + \sum_j \left(1 - \frac{v_{i,j}}{v_{myp}} \right) \right) f_{myo} \hat{\mathbf{t}}_{i-1}, \quad (4.23)$$

where the second term in the main bracket describes the contribution from Myp2 clusters, assuming a linear force-velocity relationship. Here, the sum is over the Myp2 clusters j that interact with the i^{th} bead, $v_{i,j}$ is the relative velocity between the j^{th} Myp2 cluster and the i^{th} bead (orientated along the direction parallel to the filament), and v_{myp} is the load-free velocity of the Myp2, which we assumed to be the same as Myo2 [95]. Here, we have assumed that the maximum force exerted by the Myp2 molecules is the same as the Myo2 molecules. Previous

comparisons between these two motor proteins found that the differences in their biological functions were conferred by their tail domains, rather than their head domains, indicating that this is probably a reasonable approximation to make [102].

Similarly, grabbing forces on actin beads were also modified to include interactions with Myp2 clusters as well, with the formula for the grabbing forces becoming

$$\begin{aligned} \mathbf{f}_i^{grab} = & -\sum_j k_{grab} \left[(\mathbf{r}_i^{act} - \mathbf{r}_j^{act}) - \left((\mathbf{r}_i^{act} - \mathbf{r}_j^{act}) \cdot \hat{\mathbf{t}}_i \right) \hat{\mathbf{t}}_i \right] - \sum_k k_{grab} \left[(\mathbf{r}_i^{act} - \right. \\ & \left. \mathbf{r}_k^{myp}) - \left((\mathbf{r}_i^{act} - \mathbf{r}_k^{myp}) \cdot \hat{\mathbf{t}}_i \right) \hat{\mathbf{t}}_i \right]. \end{aligned} \quad (4.24)$$

Here, the second sum is over the Myp2 clusters k that interact with the i^{th} bead, and \mathbf{r}_k^{myp} is the position vector of the k^{th} Myp2 cluster.

We also included excluded volume forces between pairs of Myp2 clusters, and between Myp2 clusters and nodes. These were calculated in a similar manner as before, assuming a repulsive spring force for any entities that came within a certain threshold distance of each other. We assumed this threshold distance was the same for the Myp2 clusters as it was for the nodes. Additionally, Myp2 clusters with $z < 0$ also experienced a membrane exclusion force, in the same manner as equation 4.16.

Based on this, the forces experienced by non-barbed-end actin beads were the same as in equation 4.17, except the grabbing and pulling forces were now calculated using equations 4.23 and 4.24, respectively, to include the contributions from Myp2 clusters. Additionally, the forces exerted on filament barbed ends were also the same as in equation 4.18, except the excluded volume force now included interactions between nodes and Myp2 clusters. The total force experienced by the k^{th} Myp2 clusters was

$$\mathbf{F}_k^{tot,myp} = \mathbf{f}_k^{pull,myp} + \mathbf{f}_k^{grab,myp} + \mathbf{f}_k^{excl,myp} + \mathbf{f}_k^{mem,myp}. \quad (4.25)$$

Here, $\mathbf{F}_k^{tot, myp}$ is the total force exerted on the k^{th} cluster, $\mathbf{f}_k^{pull, myp}$ and $\mathbf{f}_k^{grab, myp}$ are the Newton's 3rd law pair forces for the pulling and grabbing forces, respectively, that the k^{th} Myp2 cluster exerts on actin filaments, $\mathbf{f}_k^{excl, myp}$ is the total excluded volume force between the k^{th} cluster and both other Myp2 clusters and nodes, and $\mathbf{f}_k^{mem, myp}$ is the excluded volume force between the k^{th} Myp2 cluster and the membrane.

The updated set of parameter values used for this model are shown in Table 4.7. Temporal parameters used for this model are shown in Table 4.8. These parameters were mostly the same as those in Table 4.6, with the exception that we also included a parameter to set the time at which we added the Myp2 clusters into the simulation, t_{myp} . If we were performing a simulation where we did not alter the severing, then t_{myp} had a value of 600s, however if the simulation included alteration of the severing rate, then t_{myp} was set to the earlier time of 120s, in order to not make the simulation time prohibitively long.

Table 4.7: List of parameter values used in 3D flat geometry simulation with after the inclusion of Myp2 clusters. Parameters that are new, or modified from the previous iteration of the model, are shaded. (A) Chosen to be an order of magnitude lower than the node drag coefficient. (B) Based on the measured number of Myp2 molecules in the ring [64], and assuming that there are the same number of Myp2 molecules per cluster as for Myo2 in the nodes. (C) The same values as used for the nodes. (D) [95]. (E) Chosen to be sufficiently far away from the ring that there is unlikely to be any actin filaments nearby. (F) Close enough to the ring axis so that a Myp2-actin interaction is likely to be formed soon. (G) Chosen to be less than r_{myo} , so that the docking will stop once a single Myp2-actin interaction is found.

Parameter	Meaning	Value
d	Ring binding zone width	0.1 μm
L	Ring length	12 μm
γ_{node}	Node drag coefficient	1.5 nN s/ μm
γ_{bead}	Actin bead drag coefficient	0.2 pN s/ μm
γ_{myp}	Myp2 cluster drag coefficient	150 pN s/ μm (A)
ρ_{node}	Mean node linear density	150/L μm^{-1}
ρ_{myp}	Mean Myp2 cluster linear density	100/L μm^{-1} (B)

k_{off}^{node}	Node unbinding rate	0.023 s ⁻¹
k_{off}^{mvp}	Myp2 cluster unbinding rate	0.023 s ⁻¹ (C)
v_{mvp}	Myp2 load-free velocity	0.35 µm/s (D)
r_{dock}	Initial distance that new Myp2 clusters are placed from the ring/x-axis, when initiating the docking procedure	0.3 µm (E)
r_{dock_final}	Distance from ring axis at which to finish docking procedure if no Myp2-actin connections are formed	0.075 µm (F)
$dock_step$	Size of individual steps in docking procedure	0.02 µm (G)
v_{pol}	Formin-mediated actin polymerisation rate	70 nm/s
θ_{nuc}	Angle of filament nucleation above membrane	8°
l_{act}^0	Equilibrium length between actin beads	0.1 µm
k_{act}	Actin filament stretching spring constant	1000 pN/µm
l_p	Actin filament persistence length	10 µm
κ	Actin filament bending modulus	$K_b T l_p$, 0.0414 pN µm ²
f_{mem}	Magnitude of membrane exclusion force on actin beads	5 pN
k_{off}^x	Actin crosslinker unbinding rate	3.3 s ⁻¹
k_{on}^x	Actin crosslinker binding rate	1 µm ⁻¹ s ⁻¹
k_x	Actin crosslinking spring stiffness	25 pN/µm
r_x^0	Actin crosslinking spring rest length	30 nm
r_x^{bind}	Threshold distance for crosslinking interaction	50 nm
r_{myo}	Node and Myp2 capture radius	100 nm (C)
f_{myo}	Myosin cluster (nodes and Myp2) pulling force/filament	4 pN
$maxInt$	Maximum number of filaments that a node or Myp2 cluster can interact with	2 (C)
k_{grab}	Spring constant for grabbing interaction	5 pN/µm
d_{node}	Node and Myp2 cluster excluded volume distance	50 nm (C)
k_{node}^{excl}	Node and Myp2 cluster excluded volume spring constant	1000 pN/µm (C)
r_{sev}	Cofilin mediated actin filament severing rate	0.03 µm ⁻¹ s ⁻¹
r_{mutant}	Number to multiply r_{sev} by to reduce the actin severing rate partway through the simulation	0.5

Table 4.8: List of temporal parameters used in the ring model where Myp2 clusters were included. New or modified parameters are shaded.

(A) Chosen to allow sufficient simulation time before and after altering the severing rate (e.g. to measure ring tension). (B) Chosen to allow sufficient simulation time before and after adding in the Myp2 clusters, if the severing is not altered, or to allow sufficient time before and after altering the severing in the presence of Myp2.

Parameter	Meaning	Value
Δt	Simulation timestep	5×10^{-5} s, or 20,000 steps/s
t_x	Time between updating crosslinking interactions	0.015s, or every 300 timesteps
t_{sev}	Time between calculating turnover of simulation components, and severing of actin filaments	0.1s, or every 2000 timesteps
t_{myo}	Time between updating myosin-actin interactions	0.02s, or every 400 timesteps
t_{save}	Time between saving ring data for quantification and making movies of the simulation	2s
t_{mutant}	Time at which actin severing rate was altered (only in some simulations), to mimic the effect of <i>adf1</i> mutants	480s (A)
t_{myp}	Time at which Myp2 clusters are added into the simulation	600s, or 120s if the severing rate will be subsequently reduced (B)

4.7.8. Modelling the node structure with increased resolution

We attempted to improve the accuracy of our model of the nodes in the simulation, by simulating pairs of Myo2 head domains, and allowing each of these to interact with nearby actin filaments. As there are an estimated 20 Myo2 molecules in each node, we simulated 10 ‘heads’ for each node. Modelling this new node structure in a way that produced the desired behaviour required the implementation of a set of forces on the head domains.

We define \mathbf{r}_i^{head} as being the position vector of the i^{th} head within our simulation. However, it is also useful for us to define the local position of a given head, relative to its node. This is calculated by

$$\mathbf{r}_i^{head,local} = \mathbf{r}_i^{head} - \mathbf{r}_j^{act}, \quad (4.26)$$

where $\mathbf{r}_i^{head,local}$ is the position of the i^{th} head, relative to the position of the centre of its node, which is the j^{th} actin bead in the simulation.

In order to allow the heads to explore the available space around the node centre, and search for actin filaments to interact with, we applied a randomly generated force to each of the heads, which mimicked the behaviour of thermal diffusion/brownian motion. This is given by

$$\mathbf{f}_i^{brown} = \sqrt{\frac{2k_B T \gamma_{head}}{\Delta t}} \cdot \mathbf{rand}_N, \quad (4.27)$$

where \mathbf{f}_i^{brown} is the brownian force on the i^{th} head, γ_{head} is the drag coefficient of the head domains, and \mathbf{rand}_N is a three-component vector of normally distributed random numbers [165].

In order to stop the heads from moving away from their node, we applied a spring interaction between the node and the head, representative of stretching and compression of the Myo2 tail domain. For the i^{th} head, this is given by

$$\mathbf{f}_i^{tail} = -k_{tail} (|\mathbf{r}_i^{head,local}| - l_{myo}) \frac{\mathbf{r}_i^{head,local}}{|\mathbf{r}_i^{head,local}|}, \quad (4.28)$$

where k_{tail} is the spring constant of the Myo2 tail, and l_{myo} is the equilibrium length between the node centre and the head.

\mathbf{f}_i^{tail} will act to keep the head domains a distance l_{myo} from the node centre, however it will not prevent them from moving below the membrane at $z = 0$. Additionally, we ideally need to apply a force that will

keep the Myo2 heads away from the membrane surface, so that they will spend more time in the region where they are likely to find actin filaments to interact with. We achieved this by exerting a restoring torque on head domains that moved too close to the membrane (Figure 4.5D), given by the formula

$$\mathbf{f}_i^{torque} = -\tau \hat{\boldsymbol{\theta}}_i^{local}, \quad (4.29)$$

where \mathbf{f}_i^{torque} is the restoring force exerted on the i^{th} head, τ is the magnitude of the restoring torque, and $\hat{\boldsymbol{\theta}}_i^{local}$ is a unit vector in the polar direction in a spherical coordinate system that is centred on the node which the i^{th} head is bound to. This unit vector is calculated using the formula

$$\hat{\boldsymbol{\theta}}_i^{local} = \frac{\begin{bmatrix} \mathbf{r}_{i,x}^{head,local} \cdot \mathbf{r}_{i,z}^{head,local}, \\ \mathbf{r}_{i,y}^{head,local} \cdot \mathbf{r}_{i,z}^{head,local}, \\ -(\mathbf{r}_{i,x}^{head,local})^2 - (\mathbf{r}_{i,y}^{head,local})^2 \end{bmatrix}}{\left(|\mathbf{r}_i^{head,local}| \cdot \sqrt{(\mathbf{r}_{i,x}^{head,local})^2 + (\mathbf{r}_{i,y}^{head,local})^2} \right)}, \quad (4.30)$$

where $\mathbf{r}_{i,x}^{head,local}$ is the x component of $\mathbf{r}_i^{head,local}$. Equation 4.30 is the unit vector conversion formula for calculating $\hat{\boldsymbol{\theta}}$ in a spherical polar coordinate system, based on a set of Cartesian position coordinates. In addition to the restoring torque, we also included a membrane exclusion force, \mathbf{f}^{mem} , on any heads that have $z < 0$, in the same manner as equation 4.16.

Thus, with equations 4.16 and 4.27 – 4.30, we have defined the necessary forces to allow the head domains to explore the available space around their nodes, in search of actin filaments to interact with. However, it is now necessary to redefine how the myosin heads search for actin beads to interact with, because the smaller interaction radius around each myosin head, compared to the previously used interaction

radius around the nodes, meant that it would be difficult to find connections between myosin heads and actin beads (Figure 4.5E).

Rather than searching for actin beads within a given distance of a head domain, we first found the actin bead that was closest to the myosin head, and then checked which of the two neighbouring actin beads was closest to the myosin head. Then, we measured the shortest distance between the myosin head and the segment between these two neighbouring actin beads, and if this value was less than the interaction radius of the head, a connection was formed between the head and that filament.

The vector from the closest point on an actin filament segment to the i^{th} head domain is given by the equation

$$\mathbf{r}_i^{grab} = (\mathbf{r}_i^{head} - \mathbf{r}_j^{act}) - \lambda_i(\mathbf{r}_{j+1}^{act} - \mathbf{r}_j^{act}), \quad (4.31)$$

where \mathbf{r}_i^{grab} is the vector from the closest point on the segment to the head, the j^{th} actin bead is the bead connected to the segment that is nearest to the filament barbed end, and λ_i is given by

$$\lambda_i = (\mathbf{r}_i^{head} - \mathbf{r}_j^{act}) \cdot \hat{\mathbf{t}}_j / |\mathbf{r}_i^{head} - \mathbf{r}_j^{act}|. \quad (4.32)$$

λ_i is a number between 0 and 1, which denotes how far along the actin filament segment the closest point to the i^{th} myosin head is located (i.e. $\lambda_i \rightarrow 0$ corresponds to the head being closest to the j^{th} actin bead, while $\lambda_i = 0.5$ corresponds to the nearest point being exactly half way along the segment). Then, the distance between the i^{th} myosin head and the closest point of an actin filament segment is simply given by the magnitude of equation 4.31, $|\mathbf{r}_i^{grab}|$, and if this value is less than $r_{myo} = 15$ nm, a connection will be formed between the i^{th} myosin head, and the actin filament segment between beads j and $j + 1$.

Because the brownian motion of the heads may cause them to move to distances slightly beyond the capture radius of the head, we

introduced a distinct breaking radius, $r_{myo_Break} = 25$ nm, where the connection between a filament segment and a head would only be severed if the distance between them became greater than this value. This helped to ensure that connections between heads and filament segments weren't prematurely removed because of small fluctuations in distance caused by the brownian forces exerted on the heads.

Now that we have identified which filament segments the i^{th} myosin head interacts with, we are able to calculate the grabbing and pulling forces that are exerted on the actin filament. Rather than exerting these forces on a single actin bead as before, they are now divided between the beads at either end of the nearest actin filament segment, with the exact division determined by the value of λ_i . On the j^{th} actin bead (defined the same as in equation 4.31), the total pulling force due to all interacting myosin heads, i , that interact with the segment between the j^{th} and the $j+1^{th}$ bead is

$$\mathbf{f}_j^{pull} = f_{myo} \hat{\mathbf{t}}_j \sum_i (1 - \lambda_i), \quad (4.33)$$

whilst the corresponding total pulling force on the $j+1^{th}$ bead is

$$\mathbf{f}_{j+1,i}^{pull} = f_{myo} \hat{\mathbf{t}}_j \sum_i \lambda_i. \quad (4.34)$$

Similarly, the total grabbing force on the j^{th} actin bead due to all interacting myosin heads, i , that interact with the segment between the j^{th} and the $j+1^{th}$ bead is given by

$$\mathbf{f}_{j,i}^{grab} = k_{grab} \sum_i \mathbf{r}_i^{grab} (1 - \lambda_i), \quad (4.35)$$

whilst the corresponding total grabbing force on the $j+1^{th}$ bead is

$$\mathbf{f}_{j+1,i}^{grab} = k_{grab} \sum_i \mathbf{r}_i^{grab} \lambda_i. \quad (4.36)$$

From these, we write the total pulling force on the j^{th} actin bead as

$$\mathbf{f}_j^{pull} = f_{myo}(\hat{\mathbf{t}}_j \sum_i (1 - \lambda_i) + \hat{\mathbf{t}}_{j-1} \sum_k \lambda_k), \quad (4.37)$$

where the first sum is over the myosin heads i that interact with the segment towards the pointed end, relative to bead j , whilst the second sum is over the myosin heads k that interact with the segment towards the barbed end, relative to bead j . Similarly, the total grabbing force on the j^{th} actin bead is

$$\mathbf{f}_j^{grab} = k_{grab}(\sum_i \mathbf{r}_i^{grab} (1 - \lambda_i) + \sum_k \mathbf{r}_k^{grab} \lambda_k), \quad (4.38)$$

where again, the first sum is over the myosin heads i that interact with the neighbouring segment in the direction of the pointed end, while the second sum is over the myosin heads k that interact with the neighbouring segment towards the barbed end direction.

We are now able to write the equations for the total forces exerted on each of the ring components. For non-barbed end actin beads, this is the same as in equation 4.17, except the pulling and grabbing forces are calculated using equations 4.37 and 4.38, respectively. For the i^{th} myosin head, the total force is

$$\mathbf{F}_i^{tot,head} = \mathbf{f}_i^{brown} + \mathbf{f}_i^{tail} + \mathbf{f}_i^{torque} + \mathbf{f}_i^{mem} + \mathbf{f}_i^{pull,head} + \mathbf{f}_i^{grab,head}, \quad (4.39)$$

where $\mathbf{f}_i^{pull,head}$ and $\mathbf{f}_i^{grab,head}$ are the Newton's 3rd law pair forces for the pulling and grabbing forces, respectively, that the i^{th} myosin head exerts on an actin filament. The total force exerted on the barbed-end bead (the i^{th} bead) of an actin filament is given by

$$\mathbf{F}_i^{tot,act} = (\mathbf{f}_i^{spr} + \mathbf{f}_i^{bend} + \mathbf{f}_i^{excl} + \mathbf{f}_i^{tail,node})_{xy}, \quad (4.40)$$

where $f_i^{tail,node}$ is the total of the Newton's 3rd law pair force for all the tail stretching forces from the myosin heads within that node.

One final aspect that we introduced was an approximation of the myosin ATPase cycle for the individual heads within nodes. We created three possible states in which myosin heads could exist: unavailable (for binding), available (for binding), and bound. Unavailable heads are not able to bind nearby actin filaments, and transition into the available state with a rate of $r_{available}$. Available heads will bind with certainty to the nearest actin filament segment if the distance constraint is satisfied. Bound heads will remain bound, and exert pulling and grabbing forces, for a time t_{bound} , after which the head will unbind and re-enter the unavailable state. $r_{available}$ and t_{bound} were chosen based on previously measured properties of the Myo2 ATPase cycle, and accounting for the fact that each of the 10 heads within a node is meant to correspond to a Myo2 dimer [168].

In simulations using this model, we did not get to the point where we could include Myp2 clusters, and investigate the effects of reduced actin severing. Therefore, we will not discuss, for example, how our new model of the Myo2 clusters within nodes can be adapted to also model the Myp2 clusters.

The list of parameters used when simulating this model of the ring is given in Table 4.9. The temporal parameters used in these simulations are given in Table 4.10.

Table 4.9: List of parameter values used for simulations where we attempted to account for the node microstructure. Parameters that are new or modified from previous versions of the model are shaded. See discussion directly below the table for explanation of why these parameter values were used.

Parameter	Meaning	Value
d	Ring binding zone width	0.1 μm
L	Ring length	12 μm
γ_{node}	Node drag coefficient	1.5 nN s/ μm
γ_{bead}	Actin bead drag coefficient	0.2 pN s/ μm

γ_{head}	Myosin head drag coefficient	0.079 pN s/ μ m (assuming radius = 7 nm)
ρ_{node}	Mean node linear density	150/L μ m ⁻¹
n_{head}	Number of heads per node	10
k_{off}^{node}	Node unbinding rate	0.023 s ⁻¹
t_{cycle}	Length of Myo2 ATPase cycle	0.2 s
t_{bound}	Length of time for which a head binds to an actin filament	0.038
$r_{available}$	Rate of transition from unavailable to available state	6.173 s ⁻¹
v_{pol}	Formin-mediated actin polymerisation rate	70 nm/s
θ_{nuc}	Angle of filament nucleation above membrane	8°
l_{act}^0	Equilibrium length between actin beads	0.1 μ m
k_{act}	Actin filament stretching spring constant	1000 pN/ μ m
l_p	Actin filament persistence length	10 μ m
κ	Actin filament bending modulus	$K_b T l_p$, 0.0414 pN μ m ²
f_{mem}	Magnitude of membrane exclusion force on actin beads	5 pN
k_{off}^x	Actin crosslinker unbinding rate	3.3 s ⁻¹
k_{on}^x	Actin crosslinker binding rate	1 μ m ⁻¹ s ⁻¹
k_x	Actin crosslinking spring stiffness	25 pN/ μ m
r_x^0	Actin crosslinking spring rest length	30 nm
r_x^{bind}	Threshold distance for crosslinking interaction	50 nm
l_{myo}	Equilibrium distance from node centre to head domains	80 nm
k_{tail}	Spring constant for myosin tail stretching	2500 pN/ μ m
r_{myo}	Myosin head capture radius	15 nm
r_{myo_Break}	Breaking distance for head-filament interactions	25 nm
f_{myo}	Myosin cluster (nodes and Myp2) pulling force/filament	4 pN
τ	Magnitude of restoring torque on heads	10 pN
k_{grab}	Spring constant for grabbing interaction	66.7 pN/ μ m
d_{node}	Node excluded volume distance	50 nm
k_{node}^{excl}	Node excluded volume spring constant	1000 pN/ μ m

We estimated γ_{head} by estimating the radius of a myosin head as being 7 nm [166], using Stoke's law to calculate the drag coefficient for a sphere with this radius ($\gamma = 6\pi\eta R$, R is the radius), and then multiplying this drag coefficient by 2, to account for each simulated head corresponding to 2 Myo2 heads (a dimer). For this calculation, we assumed that the cytoplasmic viscosity had a value of $\eta = 350\eta_{water} = 0.301 \text{ Pa s}$, the value which was previously used in estimating the drag coefficient of the actin beads [108]. n_{head} was calculated based on the measured number of Myo2 dimers in the ring, divided by the average number of nodes in the simulation [64].

We took the value of t_{cycle} from previous *in vitro* measurements of the enzymatic properties of Myo2 [95]. When calculating the times that a head spends in the unavailable and bound states, we needed to take account of the fact that each head in the simulation represents a Myo2 dimer. We did so by increasing the duty ratio, rather than increasing the rate constant $r_{available}$, as this second option would increase the frequency with which we needed to update the states of the head domains (see Table 4.10), and both options would still lead to a given head in the simulation spending the same overall amount of time in the bound state.

The duty ratio of Myo2 was previously measured to be $\sim 10\%$, i.e. the probability that a Myo2 head is bound to an actin filament at a given time is 0.1 [95]. We calculated an effective duty ratio for our simulated heads, by calculating the probability that at least one of the heads in a given Myo2 dimer was in the bound state ($= 2 \times p_{bound} \cdot p_{unbound} + (p_{bound})^2 = 0.19$). Multiplying this value by t_{cycle} gave a value of $t_{bound} = 0.038\text{s}$. Then, the rate at which heads in the unavailable state transition to available state was calculated as $r_{available} = 1/(t_{cycle} - t_{bound})$, under the assumption that once a head enters the available state it will find an actin filament to interact with on a timescale that is much less than t_{cycle} .

The value of l_{myo} was chosen based on previous work studying the localisation of proteins within cytokinesis nodes in *S. pombe*, including

the N- and C-terminal ends of Myo2 [62,103]. k_{tail} was chosen so that the myosin tail domain would be twice as stiff as an actin filament segment (i.e. $k_{tail} = 2 \times (l_{act}^0 \cdot k_{act}) / l_{myo}$). r_{myo} was chosen to be the same as in other models of the *S. pombe* ring, which took a similar approach to modelling the clusters of Myo2 [133], and r_{myo_Break} was chosen to be sufficiently larger than r_{myo} so as to not unnecessarily throw away myosin-actin connections because of thermal fluctuations in the position of the head domain. The value of τ was chosen to be sufficient to overcome thermal forces when pushing head domains away from the membrane, and k_{grab} was chosen so that the strength of the grabbing interaction remained a similar magnitude to before, despite the decrease in the equilibrium distance.

Table 4.10: List of temporal parameter values used in simulations where we attempted to account for the node microstructure. Parameters that are new or modified from previous versions of the model are shaded. See discussion directly below table for explanation of why these parameter values were used.

Parameter	Meaning	Value
Δt	Simulation timestep	5×10^{-5} s, or 20,000 steps/s
t_x	Time between updating crosslinking interactions	0.015s, or every 300 timesteps
t_{sev}	Time between calculating turnover of simulation components, and severing of actin filaments	0.1s, or every 2000 timesteps
t_{myo}	Time between updating head-actin interactions	0.01s, or every 200 timesteps
t_{head}	Time between updating the state of unavailable myosin heads	0.002, or every 40 timesteps
t_{save}	Time between saving ring data for quantification and making movies of the simulation	2s

We slightly decreased the value of t_{myo} , in order to decrease the likelihood that we ‘missed’ any potential connections, due to the relatively rapid diffusion of the head domains. t_{head} was chosen so that we

could avoid having to generate large amounts of random numbers every timestep, in order to determine if any head domains transition from the unavailable to available states, whilst still ensuring that the probability that this occurred within a time of t_{head} seconds was $\ll 1$.

4.8. Discussion

4.8.1. Weaknesses of the original model

As previously mentioned, the models that we developed here were adapted from a previously developed ring model, the goal of which was to reproduce experimentally measured values of ring tension *in silico*. An average ring tension of 390 ± 150 pN was measured from ring sliding in fission yeast spheroplasts, while the simulation produced a ring tension of 340 ± 57 pN [35]. However, we initially found some aspects of the model to be unrealistic, particularly with the way that individual myosin clusters/nodes interact with multiple actin filaments, and this calls into question the validity of the results previously obtained with this model.

Most importantly, we found that the value of the parameter *maxInt*, which controls how a myosin cluster/node interacts with multiple actin filaments, was vastly overestimated. In the original model, myosin clusters were assumed to contain 40 Myo2 molecules, and were given a *maxInt* value of 10, meaning that the authors were claiming that 4 Myo2 molecules were able to exert a time averaged force of 4 pN on an actin filament [35]. Type II myosins are known to be non-processive, making this behaviour unlikely [169]. Furthermore, when we implemented an equivalent description in our model (20 Myo2 molecules per node, *maxInt* set to 5) using a cylindrical geometry we found that large numbers of actin filaments peeled away from the ring as individual filaments (Figure 4.2C), and this was only resolved by reducing the value of *maxInt* to 1 (Figure 4.2D), so that the myosin pulling forces did not overpower the grabbing forces.

This would then suggest that a *maxInt* value of 2 or 3 would be more appropriate for the original simulations performed with this model, where there were 40 Myo2 molecules per cluster. These *maxInt* values correspond to 20 or ~ 13 Myo2 molecules per cluster, respectively, walking processively along a single actin filament. This would then reduce the tension generated by the model by a factor of ~ 5 or ~ 3 , respectively, leading to approximate values of ~ 68 pN or ~ 110 pN, respectively. This is significantly less than what was observed experimentally, suggesting that the mechanism of tension generation in this model is not sufficient to produce the experimentally measured values, and/or the experimentally measured value is over estimated. It is also possible that rings in spheroplasts are able to recruit myosin at a greater density than rings in cells, meaning that they have a higher tension. Better understanding of this discrepancy will require further experimental work, including more measurements of AMR tension in fission yeast, and further mathematical modelling.

We also argue that the myosin grabbing forces were implemented in an unrealistic manner. Unlike the pulling forces, which were reduced when a myosin cluster/node interacts with multiple actin filaments, the grabbing forces are not reduced, meaning that a single node or cluster can hypothetically exert a finite force on an infinite number of actin filaments [35]. We first attempted to correct this by limiting the number of interactions with actin filaments that are available for each node. We set this to 2, meaning that each node can only exert pulling and grabbing forces on 2 actin filaments (Figure 4.3A). However, this prevented us from using the 3D cylindrical geometry for our simulations, as the pulling forces would now overpower the grabbing forces and lead to actin filaments being pulled away from the membrane. This was a problem that was present in subsequent iterations of our model, and which we did not find a way to solve.

One possible, and somewhat realistic, solution to this problem would be to increase the number of entities that are able to grab actin filaments, but not exert pulling forces on them. For example, the node

protein Rng2 contains an actin binding calponin homology domain (CHD) [170,171], whilst unpublished research from our lab has shown that Pxl1, which interacts with the SH3 domains of Cdc15 and Imp2 [75], is also able to bind to tropomyosin, which provides another mechanism whereby actin filaments can be linked to the membrane. Therefore, it seems likely that there are proteins other than Myo2 that are able to bind to actin filaments and link them to the membrane.

A recent model of the fission yeast AMR in a 3D cylindrical geometry also attempted to model individual heads of Myo2 that interact with individual actin filaments, in a similar way to the later iteration of our model, except with even greater detail in the description of the myosin molecules [133]. The authors simulated a number of potential AMR structures, but in all of these the only linker between actin filaments and the membrane was the simulated Myo2 molecules, and despite this they did not see the peeling away of actin filaments that we would expect to see from our simulations. In these simulations, they use an actin bead friction coefficient 30 times greater than that used in previous simulations, including our own [133]. This value is used without justification, and additionally the beads in actin filaments are now placed only 5.5 nm apart, which gives a friction/length around 500 times greater than that used in previous simulations ($\sim 1000 \text{ pN s}/\mu\text{m}^2$ vs. $2 \text{ pN s}/\mu\text{m}^2$). This will significantly slow down the speed with which actin filaments move, since the pulling force exerted by the myosin molecules was the same as in our simulations, which could mean that filaments get disassembled by cofilin before they are able to be pulled out of the ring.

When we attempted to implement our own ring model where we explicitly include individual pairs of Myo2 heads, we found that very few actin filaments were captured and pulled on by the Myo2 heads, even when we biased the polymerisation direction of actin filaments to be parallel to the ring, and this led to a very low ring tension (Figure 4.6E, Figure 4.6F). This is despite our observation that this description of the myosin clusters/nodes worked quite well in a toy model (Figure 4.6A–Figure 4.6D). In the toy model, the actin filament was placed at an

optimum height above the cluster, which may have helped the simulations to work more smoothly than they otherwise should have. We hypothesised that, in the full ring model, where the actin filaments weren't optimally positioned to interact with the nodes, the diffusion of the heads was too fast, and myosin timesteps were not often enough, to enable successful capturing of actin filaments by the myosin heads. However, when we tried reducing the time between myosin timesteps this did not have an effect.

4.8.2. Evidence of ring peeling/tension heterogeneity in our simulations

Our original goal for this mathematical modelling work was to reproduce ring peeling *in silico*, from simulated rings where the actin turnover had been perturbed. Due to problems we identified with simulating rings in a cylindrical geometry, we were unable to do this, so we instead returned to our simulations using a flat geometry, and looked for evidence of tension heterogeneity around the ring, by making heatmaps of the ring tension over time. In all of our simulations, we found that reducing the severing rate lead to an increase in overall ring tension (Figure 4.3D, Figure 4.4B), possibly due to the increase in the amount of actin in the ring, which would increase the ease with which the Myo2 in the nodes could find actin filaments to interact with. In the absence of Myp2 this only lead to a small increase in the circumferential variability of the ring tension (Figure 4.3F), however when Myp2 was included in simulations we found that the variability increased a greater amount (Figure 4.4E).

This agrees with our experimental results, where we found that we needed both membrane-bound and non-membrane-bound myosin species in order to see ring peeling events (Figure 3.5, Figure 3.6), and these modelling results suggest that Myp2 helps to increase the tension heterogeneity in rings where turnover is reduced. However, the exact mechanism that could cause this is unknown. Further simulations could explore this by, for example, including Myp2 clusters that are unable to

generate pulling forces, to see if the Myp2 motor activity is necessary, or whether Myp2 acting as a crosslinker between filaments is sufficient.

4.8.3. Further limitations of the model, and potential future modifications

One limitation of our model, and that of Stachowiack, *et al* [35], is that when an actin filament is severed, the portion of the filament that is not attached to the node is removed from the simulation. This was also the case in other models that examined ring formation from precursor nodes [34,108,164]. Based on previous efforts to study the actin filaments in the ring using electron microscopy, it seems that it is very likely that the number of filaments in the ring is greater than the number of nodes [45,46,64,65], meaning that significant portion of the filaments in the ring must not be attached to a formin dimer in a node. We did not make any serious attempts to include non-formin-bound actin filaments, although we doubt that doing so would have fixed any of the issues that we faced, and it is likely something to investigate once a basic working model is achieved.

Our model, and previous models, assume that the formin-dependent polymerisation rate of actin filaments is constant [35,108,164]. However, recent theoretical and experimental results have indicated that polymerisation by Cdc12 is mechanoregulated by the tension in the actin filament that it nucleates, with Cdc12 dimers experiencing a tension-dependent reduction in their polymerisation rate [172,173]. When considering the SCPR pathway of ring formation, this mechanism makes intuitive sense, because if an actin filament has been captured and is being pulled in towards another node, then the continued polymerisation of that filament would work against the process of node condensation. To use an analogy, the myosin motor would essentially be trying to ascend a descending escalator, and although it may eventually manage to reach the top, it would have been much more efficient just to climb a set of static stairs, or, dropping the

analogy, to walk along a filament that isn't being continuously polymerised. The same argument could also be applied to ring contraction, since continued polymerisation of a filament that is being pulled on by a myosin will also act to decrease the tension in that filament, and therefore decrease the tension in the ring.

It was recently reported that the binding of ADF/cofilin to actin filaments is also tension regulated, with filaments that are under tension experiencing a reduction in ADF/cofilin binding [174]. This work was not carried out using *S. pombe* proteins, so we do not know whether this mechanism is also present in fission yeast, but it seems like this should be a fairly universal property of actin filaments and ADF/cofilin proteins. Again, this mechanism makes intuitive sense, since if a filament is under tension then it is likely contributing to the overall ring tension, so severing or disassembling that filament will then be counterproductive. On the other hand, a filament that is not under tension will not be contributing to ring tension, so it makes sense to disassemble the filament, so that the actin can be recycled, and boost the generation of new filaments that could contribute to ring tension.

Early in our work modifying the model, we found that making myosin-actin interactions more realistic caused the simulated ring tension to drop significantly below the value that was measured experimentally (Figure 4.2F, Figure 4.3B). Perhaps including these two mechanisms would allow the ring to generate tension in a more efficient manner, which would then restore the simulated ring tension back to the experimentally observed value.

One aspect of the model that we have not discussed much is the effect of the actin crosslinkers. In the original model, it was found that the absence of crosslinkers had little effect on the tension generated in the simulated rings [35]. One possible reason for this is that the spring constant used is quite low, leading to a maximum crosslinker force of 0.5 pN. Although this is the same as the maximum grabbing force from the Myo2 clusters, there was no limit on the number of grabbing interactions

that could be formed, whilst the number of crosslinking interactions between filaments is limited by their on and off rates.

The value of the crosslinker spring constant, k_x , was taken from published work investigating the bending stiffness of actin bundles crosslinked with different crosslinking proteins [175]. By isolating actin monomers and actin binding proteins inside emulsion droplets, and quantifying the transverse thermal fluctuations of the resulting rings that formed in these droplets, the authors were able to measure the shear stiffness of a number of actin binding proteins, utilising a theoretical description of their actin bundles. However, the shear stiffness is not the same as the extensional stiffness/spring constant [175], and the shear stiffness is likely to be around an order of magnitude smaller than the true extensional stiffness. Therefore, perhaps the inclusion of crosslinkers with a higher spring constant would have more of an effect on the total ring tension in the simulation.

Furthermore, the maximum distance of crosslinking interactions was 50 nm, however, crosslinking interactions could only be formed between actin beads, and these were spaced 100 nm apart within the filaments. Therefore, for two parallel filaments that are separated by a distance of less than 50 nm, it is still possible that the distance between beads on the neighbouring filaments will be greater than 50 nm, preventing the formation of crosslinking interactions. This behaviour is unrealistic, since in reality the actin filament binding sites for crosslinkers aren't spaced 100 nm apart. Because of this, a more realistic way to simulate the behaviour of actin crosslinkers might be to include specific actin-crosslinker entities in the simulation, and to allow these to diffuse through the ring volume. Then, these crosslinkers could be allowed to bind to actin filaments in a similar manner to the myosin heads in our final iteration of the model (Figure 4.5), by being able to bind to the segments between actin beads.

In summary, we attempted to modify a pre-existing model of the fission yeast AMR in order to see if we could observe ring peeling events *in*

silico. We first made the model 3 dimensional, and then modified it to use a cylindrical geometry. Doing so revealed issues with the myosin pulling and grabbing forces, which were not apparent from simulations using the flat geometry. We spent some time trying to fix these problems, by improving how we modelled the myosin-actin interactions, however we were unable to find a satisfactory way to do this which also allowed us to use the cylindrical geometry. We then attempted to look for evidence of tension heterogeneity in flat rings after reducing the filament severing rate, and when we included Myp2 clusters in our simulations we found some evidence that this was the case, however more work needs to be done to investigate this further. Subsequent efforts to make our model more realistic worked well when tested in 'toy' system with optimised geometry, but did not appear to work when used in our ring model.

5. Modelling FRAP recovery curves in the fission yeast ring

Note: This section describes work performed in collaboration with another lab member, with goal of better estimating mobile/immobile fractions of proteins from FRAP experiments in *S. pombe*. As such, this work is not directly related to the work previously documented in this thesis.

FRAP is a commonly used technique to investigate the turnover of fluorescently tagged proteins within a cell [176]. By using a laser to bleach a small population of the fluorophores, it is possible to subsequently observe the recovery of fluorescence intensity to the bleached region, and the time that this takes provides an indicator of how fast this turnover occurs, usually quantified as the time it takes for the fluorescence intensity to recover to half of its original value, $t_{1/2}$.

Additionally, it is also possible to identify whether some of the protein of interest exists in an immobile state, where it is not able to undergo turnover, and one can estimate the size of this fraction by measuring the difference between the pre-bleach intensity and the post-bleach plateaux in the intensity [176]. This relies on the assumption that only a very small portion of the fluorescent proteins within the cell are bleached, to ensure that enough unbleached protein remains in order to observe its true recovery behaviour. When this assumption is not valid, e.g. in cells with a very small cytoplasmic volume, then this will lead to incomplete fluorescence recovery, even for proteins that have a mobility of 100%, and to an overestimation of the immobile fraction.

FRAP has previously been used to study the dynamics of AMR proteins in a number of organisms, including fission yeast [37,84,86,135]. However, one limitation of these studies was that they did not differentiate between the turnover at different stages of cytokinesis. For example, in fission yeast the formed ring exists for

several minutes before contraction starts [49], and due to the relatively slow speed of ring constriction the ring may still appear to be the same size even several minutes after this point. If the dynamics of a ring protein differ before and immediately after the onset of ring contraction, this will not be detected if one is just looking at rings that appear to not have started contracting. Previously, SPB separation at the onset of anaphase was used as a zero-timepoint when investigating the timing of various cytokinetic events, such as the arrival/departure of various ring proteins, and the onset of ring contraction [49]. However, this method requires the user to observe SPB separation, which is not always feasible, particularly when the aim is to perform FRAP experiments on contracting AMRs.

Additionally, because fission yeast cells have very small cytoplasmic volumes, and because it is often the case for ring proteins that a large portion of its total cellular population is located in the AMR (e.g. greater than 40% for Myo2, Cdc15, Cdc12 and Rng2 [64]), it is very difficult to avoid bleaching a significant portion of the total pool of fluorescent proteins, which subsequently limits the total amount of recovery that can be observed. Therefore, conventional analysis will tend to lead to overestimation of the immobile fraction when studying ring proteins in *S. pombe*.

Another member of our lab was interested in investigating how protein turnover changes over the course of cytokinesis, with a particular interest in the F-BAR and SH3 domain protein Cdc15. In order to overcome the first problem mentioned above, they took advantage of the relative homogeneity in the diameter and length of dividing *S. pombe* cells (Figure 5.1A), and of the approximately linear rates of mitotic spindle extension and AMR contraction, to index different AMRs based on their age (Figure 5.1B): For cells going through anaphase, rings were indexed based on the length of the mitotic spindle in the cells (observed using strains with fluorescently tagged tubulin), while it was also observed that ring contraction initiation coincides with the breakdown of the mitotic spindle, which provided a reliable indicator for the end of

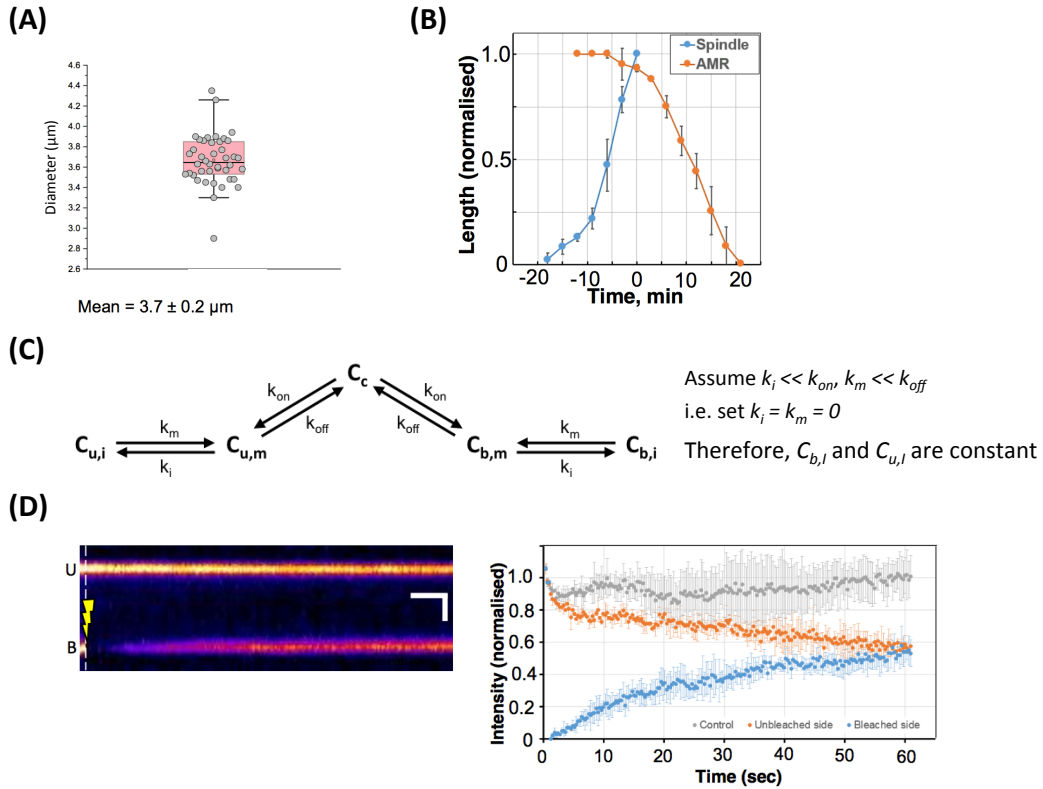


Figure 5.1: Preliminary experiments and considerations for analysis of FRAP experiments.

- (A) Plot of measured cell diameters in *S. pombe* cells (N = 41).
- (B) Plot of spindle length and AMR diameter (normalised to a maximum value of 1) over time, with $t = 0$ defined as the onset of ring contraction.
- (C) Schematic representation of our model for protein turnover within bleached AMRs. The protein of interest moves between cytoplasmic (C_c) and ring-bound populations in the mobile and immobile fractions of the bleached and unbleached portions of the ring ($C_{b,m}$ and $C_{b,i}$, and $C_{u,m}$ and $C_{u,i}$ respectively).
- (D) Bleaching profile of GFP-Myo2 fluorescence in an AMR, showing the changes in intensity in the bleached and unbleached portions of the ring, and in control cells where no bleaching was performed.

Data in B and D were obtained by Anton Kamnev. Images/graphs in A, B, and D, were produced by Anton Kamnev.

anaphase and the start of cytokinesis/septation (Figure 5.1B). Then, the age of contracting rings was calculated based on their diameters, compared to the average measured diameter of uncontracted rings (Figure 5.1A).

This provided a solution to the first problem listed above. However, the problem remained that a limited cytoplasmic pool of a given protein would make it difficult to determine its true mobile/immobile fraction, which was the primary interest of these

experiments. Therefore, we decided to see if there was a way that this problem could be solved using a mathematical modelling approach.

5.1. Mathematical modelling of FRAP recovery

In order to build our mathematical model, and derive a method of measuring the mobile fractions which takes account of the limited cytoplasmic pool of protein, we divided the cell into three different compartments: The portion of the ring which is bleached during the FRAP experiment, the portion which remains unbleached, and the cytoplasm. The two ring compartments were then each divided into two sub-compartments, representing the mobile (m) and immobile (i) fractions. We hypothesised that exchange between the ring and the cytoplasm could only occur through proteins that were in the mobile state, and not the immobile state (or, at the very least, that cytoplasmic exchange with the immobile fraction is much slower than with the mobile fraction). Additionally, we also hypothesised that exchange between the mobile and immobile fractions happens on much longer timescales than the exchange between the mobile portion of the ring protein with the cytoplasm¹. This behaviour is illustrated in Figure 5.1C.

From this basic model of protein dynamics during FRAP experiments, we subsequently wrote down a system of differential equations describing the concentration of the unbleached protein in each of the various ring compartments. To do so, we made a number of simplifying assumptions. Firstly, we assumed that the exchange between the mobile and immobile fractions was slow enough to be ignored on the timescale of the FRAP experiments (Figure 5.1C). We also ignored changes in cellular geometry, e.g. due to contraction of the AMR, as these would be negligible over the ~2 minute timescale of the experiment. Furthermore, we also assumed that the direct transport/diffusion of the

¹ Indeed, if exchange between the immobile fraction and the cytoplasm/mobile fraction did occur on experimentally relevant timescales, then it would not truly be an immobile fraction.

protein between the bleached and unbleached regions of the ring was negligible¹, and that diffusion in the cytoplasm was sufficiently fast that the cytoplasmic protein concentration could be assumed to be uniform². These last two assumptions enabled us to adopt an ODE (ordinary differential equation) based approach, which made solving the model much simpler than if we had decided to include the effects of diffusion, which would have necessitated a PDE (partial differential equation) based approach.

With these assumptions, we can write down a differential equation model that describes the exchange of unbleached fluorescently-tagged proteins between their various pools, as in Figure 5.1C:

$$\frac{dC_{u,i}}{dt} = \frac{dC_{b,i}}{dt} = 0, \quad (5.1)$$

$$\frac{dC_{u,m}}{dt} = k_{on}C_c - k_{off}C_{u,m}, \quad (5.2)$$

$$\frac{dC_{b,m}}{dt} = k_{on}C_c - k_{off}C_{b,m}, \quad (5.3)$$

$$\frac{dC_c}{dt} = [k_{off}(L_u C_{u,m} + L_b C_{b,m}) - k_{on}C_c(L_u + L_b)]/V. \quad (5.4)$$

Here, $C_{u,i}$ and $C_{u,m}$ ($C_{b,i}$ and $C_{b,m}$), are linear the densities along the AMR of unbleached protein in the non-bleached (bleached) portion of the ring, in the immobile and mobile fractions, respectively. C_c is the concentration of the protein in the cytoplasm, whilst k_{on} and k_{off} are the linear binding and unbinding rates of the protein to the ring. Finally, L_u and L_b are the arc lengths of the unbleached and bleached portions of the ring, respectively,

¹ For example, using the node drag coefficient and the myosin pulling force from section 4, node localised proteins should move with a characteristic velocity of around 3 nm/s, which over two minutes leads to a total distance travelled of less than 1 μ m.

² Calculating the diffusion coefficient of a protein with a 10 nm radius ($D = k_B T / \gamma$, where the drag coefficient is $\gamma = 6\pi\eta R$, where R is the protein radius, and η is the dynamic viscosity of the cytoplasm), we can estimate that this protein will diffuse a characteristic distance of $\sim 1 \mu$ m over a time of 2 seconds (estimated from $rmsd(t) = \sqrt{6Dt}$, the formula for the root-mean-square-deviation of a diffusing particle in 3-dimensions).

whilst V is the cytoplasmic volume of the cell. In this model recovery in the bleached portion of the ring corresponds to binding of cytoplasmic protein into the ring, and to reequilibration of the unbleached part due to exchange with the cytoplasm.

As equations 5.2 – 5.4 are a set of coupled 1st order differential equations, the solution can be found by first rewriting equations 5.2 – 5.4 in their matrix form

$$\frac{d}{dt} \bar{c} = \bar{Z} \bar{c}, \quad (5.5)$$

where \bar{c} is a column vector of $C_{u,m}$, $C_{b,m}$ and C_c , while \bar{Z} is a 3×3 matrix containing the coefficients in equations 5.2 - 5.4. Then, in order to solve equation 5.5 we can make the substitutions

$$\bar{c} = \bar{x} e^{\lambda t}, \quad (5.6)$$

$$\frac{d}{dt} \bar{c} = \lambda \bar{x} e^{\lambda t}. \quad (5.7)$$

Inserting these into equation 5.5, and rearranging, gives

$$(\bar{Z} - \lambda \bar{I}) \bar{x} e^{\lambda t} = \bar{0}, \quad (5.8)$$

where \bar{I} is the 3×3 identity matrix. Then, in order to find non-trivial solutions for our model, equation 5.8 must be solved to find its eigenvalues (λ) and corresponding eigenvectors (\bar{x}). This is achieved by solving the equation

$$\det(\bar{Z} - \lambda \bar{I}) = 0, \quad (5.9)$$

Doing so reveals that there are 2 non-zero eigenvalues, whilst the 3rd is zero because the total amount of a specific protein in the cell is conserved. The general solution is then given by:

$$C_{u,m} = A + B e^{-k_{off}t} + C e^{-(k_{off} + k_{on}(L_u+L_b)/V)t}, \quad (5.10)$$

$$C_{b,m} = A - B \frac{L_u}{L_b} e^{-k_{off}t} + C e^{-(k_{off} + k_{on}(L_u+L_b)/V)t}, \quad (5.11)$$

$$C_c = A \frac{k_{off}}{k_{on}} - C \frac{(L_u+L_b)}{V} e^{-(k_{off} + k_{on}(L_u+L_b)/V)t}. \quad (5.12)$$

Here, A , B and C are constants which are determined by the initial conditions of the model, and t is the time after the photobleaching.

Equations 5.10 and 5.11 describe the amount of ring-bound protein in the mobile fraction, However, in our experiments we are only able to measure the total amount of fluorescence from each portion of the ring. These are given by:

$$C_u = C_{u,i} + C_{u,m} = (1 - f_m)C_u(0) + C_{u,m}, \quad (5.13)$$

$$C_b = C_{b,i} + C_{b,m} = (1 - f_m)C_b(0) + C_{b,m}. \quad (5.14)$$

Here, C_u and C_b are the linear densities of the total amount (i.e. the sum of the mobile and immobile fractions) of unbleached protein in the unbleached and bleached regions of the ring, respectively, f_m is the mobile fraction of the protein in the ring (so $1 - f_m$ will be the immobile fraction), and $C_u(0)$ and $C_b(0)$ are the initial values of C_u and C_b immediately after photobleaching. We are able to write equations 5.13 and 5.14 in their final form because we have made the assumption that $C_{u,i}$ and $C_{b,i}$ do not change on the timescale of the FRAP experiment (Figure 5.1C), so the amount of unbleached protein in the immobile fraction should not change from the start of the experiment. By substituting equations 5.10 and 5.11 into equations 5.13 and 5.14, we obtain:

$$C_u = (1 - f_m)C_{ring,pre} + A + Be^{-k_{off}t} + Ce^{-(k_{off}+k_{on}(L_u+L_b)/V)t}, \quad (5.15)$$

$$C_b = A - B\frac{L_u}{L_b}e^{-k_{off}t} + Ce^{-(k_{off}+k_{on}(L_u+L_b)/V)t}. \quad (5.16)$$

For equation 5.15, we have assumed that the unbleached portion of the ring is not directly affected by the FRAP laser, and therefore $C_u(0) = C_{ring,pre}$, the linear fluorescence density in the ring directly before the photobleaching (Figure 5.1D). For equation 5.16, we have used the initial condition that $C_b(0) = 0$, i.e. that the bleached portion of the ring is completely bleached at the start of the FRAP experiment (and therefore, $C_{b,i} = 0$, Figure 5.1D). Thus, equations 5.12, 5.15 and 5.16 provide the general solutions for the density of the fluorescently-tagged protein located in the cytoplasm, unbleached portion of the ring, and bleached portion of the ring, respectively.

Finally, we used these equations to derive a method to measure f_m . As this only appears in one of the time-independent terms in equation 5.15, we can investigate the steady state form of our general solutions, i.e. when $t \rightarrow \infty$, which causes the terms multiplied by B and C to disappear. Then, subtracting the steady state form of equation 5.16 from the steady state form of equation 5.15, and rearranging for f_m , we find that

$$f_m = 1 - \frac{C_u(\infty) - C_b(\infty)}{C_{ring,pre}}. \quad (5.17)$$

This can be compared to the value that would be expected when there is a non-limiting cytoplasmic pool of unbleached protein,

$$f_m = C_b(\infty)/C_{ring,pre}, \quad (5.18)$$

and we can see that in the limit where $C_u(\infty) \rightarrow C_{ring,pre}$ (i.e. there is sufficient cytoplasmic pool so that the intensity of the unbleached

portion of the ring doesn't decrease) then equation 5.17 is reduced to equation 5.18, as we would expect. Therefore, in order to measure f_m , we only need to measure the steady state values of C_u and C_b , and the pre-bleach ring intensity $C_{ring,pre}$.

5.2. Estimating k_{off} and k_{on}

We found that it is relatively easy to measure the mobile/immobile fraction of a ring protein, whilst taking account of the limited pool of the protein within the cell. In fact, we found that it wasn't even necessary to calculate the values of the constants A , B , and C in equations 5.12, 5.15 and 5.16. However, if we wish to calculate the values of k_{off} and k_{on} as well, then we will need to calculate the value of these constants. We have already discussed the initial conditions for C_b and C_u , whilst the initial condition for C_c is

$$C_c(0) = (C_{tot} - L_u C_{ring,pre})/V, \quad (5.19)$$

where C_{tot} is the total amount of protein fluorescence in the cell directly after photobleaching. Using these three conditions, we can calculate the values of A , B and C .

At $t = 0$ the equations for C_u , C_b and C_c become

$$f_m C_{ring,pre} = A + B + C, \quad (5.20)$$

$$0 = A - B \frac{L_u}{L_b} + C, \quad (5.21)$$

$$C_c(0) = A \frac{k_{off}}{k_{on}} - C \frac{(L_u + L_b)}{V}. \quad (5.22)$$

By rearranging equation 5.20 to make C the subject, and substituting into equation 5.21, we find that

$$B = \frac{L_b f_m C_{ring,pre}}{L_u + L_b}. \quad (5.23)$$

Substituting equation 5.23 back into equation 5.20 allows us to find a relationship between C and A :

$$C = f_m C_{ring,pre} \left(\frac{L_u}{L_u + L_b} \right) - A. \quad (5.24)$$

Substituting equation 5.24 into equation 5.22, we find that

$$A = \frac{k_{on}}{k_{off}V + k_{on}(L_u + L_b)} \left(f_m L_u C_{ring,pre} + V C_c(0) \right), \quad (5.25)$$

and rearranging equation 5.24 to make A the subject, and then substituting into equation 5.22 again, we find

$$C = \frac{V}{k_{off}V + k_{on}(L_u + L_b)} \left(f_m k_{off} C_{ring,pre} \left(\frac{L_u}{L_u + L_b} \right) - k_{on} C_c(0) \right). \quad (5.26)$$

With A , B , and C now determined, it is hypothetically possible to estimate k_{on} and k_{off} (having first measured f_m using equation 5.17) by fitting equations 5.12, 5.15 and 5.16 to the recovery profiles of the three pools of the protein of interest. However, this requires prior measurement of V , L_u , L_b , and C_{tot} , which could introduce extra uncertainties into the process.

Instead, k_{off} can be measured with a similar approach to that used in the derivation of equation 5.17, except without using the steady state versions of the equations. Subtracting equation 5.16 from equation 5.15, and substituting in the value of B from equation 5.23 gives us

$$C_u - C_b = C_{ring,pre} (1 - f_m + f_m e^{-k_{off}t}). \quad (5.27)$$

Thus, by plotting the difference in the intensities between the unbleached and bleached regions of the ring, and fitting equation 5.27 to the data, it is possible to measure k_{off} without needing to measure V , L_u

and L_b for each cell. However, the process is complicated by the need to correct for imaging-induced photobleaching: During post-FRAP image collection, the fluorophores in the cell will gradually become photobleached, and the degree of photobleaching will increase over time. Therefore, in order to correct the measured values of C_u and C_b , it is necessary to apply a time-dependent bleach correction, and whilst this is possible to do, it is nonetheless a complicated procedure. This is not an issue when using equation 5.17 to find f_m , since you are only measuring the steady state fluorescence intensities, so it is only necessary to perform a single bleach correction. We also considered whether there was an optimal method to measure k_{on} , but we were unable to find a way to do this beyond fitting equations 5.12, 5.15 and 5.16 to the recovery curves.

The application of equation 5.27 was not pursued in the analysis of the experimental data, because of the previously discussed complications. Nonetheless, with more time to carry out the additional control experiments, and subsequent analysis, in order to perform the time-dependent bleach corrections, it would be feasible to use equation 5.27 to estimate both k_{off} and f_m simultaneously. This may possibly be more accurate than just using equation 5.17, as this requires waiting a relatively long time for the recovery profiles to reach a plateau, and on this timescale it is possible that exchange between the mobile and immobile fractions may not be negligible, which violates one of the assumptions used to derive the model (see equation 5.1). Instead, equation 5.27 could be fitted to the earlier portion of the recovery curve (e.g. before it has plateaued), to make it more likely that turnover between the mobile and immobile fractions remains negligible at that point in time.

5.3. Using the model to calculate the mobile fractions of various ring proteins

Having derived an equation to calculate values of mobile fractions which account for a limited cytoplasmic pool of available protein, FRAP experiments were performed with a range of fluorescently tagged ring proteins, and the results from these were used to calculate the age dependent mobile fractions. From comparing the calculated values using equations 5.17 ('Corrected') and 5.18 ('Raw'), it can be seen that the same qualitative behaviour was observed for most of these proteins (Figure 5.2A), with the possible exception of Cdc15, where a sudden drop in mobility before the onset of ring contraction is much more visible in the corrected data. Additionally, by calculating the corrected values of the mobile fraction we saw that a lot of the proteins that did not display much fluorescence recovery were actually almost 100% mobile, such as Ain1, Myo51 and Myo2.

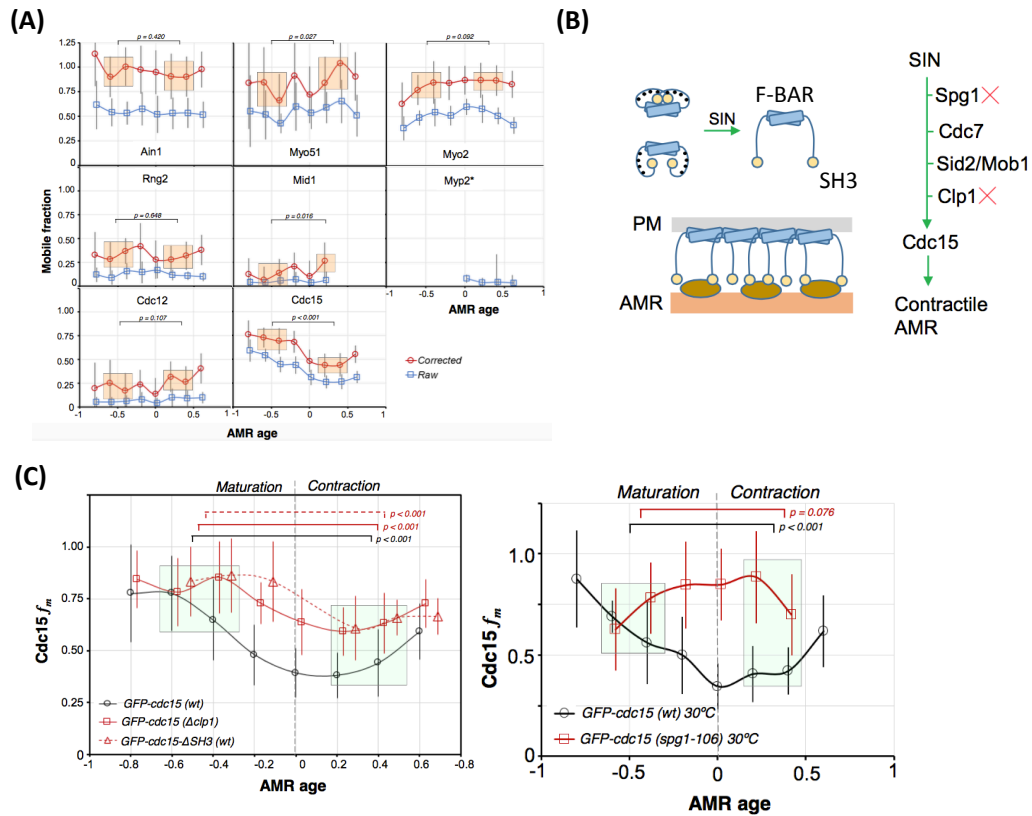


Figure 5.2: Investigating protein turnover within the ring, as a function of AMR age.

- (A) Plots of results from FRAP experiments, showing the mobile fractions for a range of ring proteins as a function of actomyosin ring age. Timescale of AMR age is relative, with -1 corresponding to SPB separation, 0 corresponding to spindle breakdown, and +1 corresponding to the full contraction of the ring. The 'raw' values (calculated from equation 5.18) and 'corrected' values (calculated from equation 5.17) are both shown. Corrected values are not shown for Myp2, as the fluorescence intensity appeared to increase on the unbleached side, which lead to negative values for the corrected mobile fraction.
- (B) Illustration of the effect of SIN signalling on the phosphorylation state of Cdc15 (shown as a dimer), and of the SIN signalling pathway that leads to this.
- (C) Graphs showing the effect of various SIN/Cdc15 mutants on the mobile fraction of Cdc15 within the ring.

All of the data presented in this figure was obtained by Anton Kamnev. All images and graphs in this figure were prepared by Anton Kamnev.

Most of the proteins tested here maintained a fairly constant mobility throughout cytokinesis, with the exception of Cdc15, which became less mobile directly before ring contraction began (Figure 5.2A). It is known that Cdc15 must be dephosphorylated before the onset of ring contraction, and that this is regulated by the SIN pathway (Figure 5.2B) [83,85,86], therefore the question of what happens to the Cdc15 mobility in a number of SIN/Cdc15 mutants was investigated. In cells

where the phosphatase Clp1 has been deleted, or where the SH3 domain of Cdc15 has been deleted, the decrease in Cdc15 mobility was much smaller, although still significant (Figure 5.2C). Furthermore, using the temperature sensitive *spg1-106* mutation, which is lethal at 32°C, the mobility of Cdc15 within the ring showed a markedly different profile from the WT control cells, with the protein displaying a much higher mobility for the majority of cytokinesis (Figure 5.2C).

5.4. Discussion

This data suggests that Cdc15's phosphorylation state controls its mobility within the ring, and that the failure to immobilise Cdc15 in these mutant strains could be the cause of their cytokinesis defects. Further experiments would be needed to confirm this. For example, if a Cdc15 mutant that maintains a high mobility, without its phosphorylation state being affected, could be produced, then this would provide a useful way to check whether Cdc15 immobilisation is necessary for normal cytokinesis to occur.

Using the corrected form of the mobile fraction that we have derived here had the largest effect on proteins that were highly mobile, and not particularly abundant within the ring (i.e. Ain1 and Myo51 in Figure 5.2A). The qualitative behaviour of the raw and corrected data are consistent with each other for most of the proteins. However, the exception to this is Cdc15, where the raw data is consistent with a linear decrease, until shortly after the onset of ring contraction (Figure 5.2A). Using the corrected values of the mobile fraction, it is demonstrated that there is a sudden drop in the mobility at the onset of ring contraction, rather than a gradual decrease.

6. Conclusions, and future directions

In this thesis, we have identified and characterised a ring peeling phenotype that can be observed during ring contraction in fission yeast cells when actin turnover has been reduced. We hypothesised that this was caused by an increase in tension heterogeneity in the ring when turnover was decreased, with peeling events occurring at regions of increased tension. Further experiments supported this, by confirming a number of predictions that were based on this model.

The work presented in this thesis raises a number of questions, which can be answered by further experiments. Firstly, we can ask whether turnover is actually reduced in the AMRs of *adf1*-mutant cells? We would expect this to be the case, however it would still be a worthwhile experiment to perform, in order to make certain that the rings are behaving as we think they are. A simple way to do this would be to treat cells with Latrunculin A, which blocks actin polymerisation, and to measure the kinetics of actin depolymerisation, to see if this is slower in the *adf1* mutant cells. This could be monitored by either performing the experiment on cells expressing LAGFP, or by taking population based approach, by fixing and staining cells for actin at regular intervals after the addition of Latrunculin A, and counting the proportion of cells at each stage that still contain F-actin structures.

We could also take our septum analysis experiments further, by repeating them for *adf1-1 nda3*-KM311 cells at a range of temperatures, e.g. 25°C, 30°C, and 33°C, and see if the number of septum defects in fully septated cells, and asymmetric septa in partially septated cells, increases with the temperature. For the partially septated cells, we could also quantify the degree of asymmetry in these septa, in order to confirm that the septa become more asymmetric as the Adf1-1 becomes more inactivated.

Because of our hypothesis that peeling is caused by tension heterogeneity, we can also ask whether there is an increase in the density of proteins like myosin and actin in the region of the ring where a peeling event occurs, directly before the peeling event. This can already be seen in some of our images, however these only indicate that Myp2 is heterogeneously localised around the ring, so more experiments would need to be performed to examine Myo2 and actin. Myo2 would be relatively easy to investigate, however actin would be more complicated, as we would need to segment the rings (like in Figure 3.13D) in order to properly visualise the actin. From these images, we could then see how the density of the protein varies around the ring, and whether this correlates with the locations of peeling events.

Previously, we discussed possible reasons why the peeling phenotype in *adf1-1* cells is different from the phenotype in *adf1-M2* and *adf1-M3* cells, and we hypothesised that this could be due to differences in the way that the function of these proteins is affected (e.g. Adf1-1 could have normal actin binding rates, but severely reduced severing rates, whereas Adf1-M2 and Adf1-M3 have reduced binding and severing rates). Therefore, it would be worthwhile to biochemically characterise the Adf1-1 mutant, to see how its behaviour differs from the Adf1-M2 and Adf1-M3 proteins, and to see if this can explain the differences in the peeling phenotypes between these strains.

As a final question, we could ask whether recreating the *adf1-M2* and *adf1-M3* mutations in *S. japonicus* also leads to ring peeling behaviour, and if so, does this peeling behaviour resemble the peeling observed in *S. pombe adf1-M2* and *adf1-M3* cells, or does it resemble the peeling in Jasplakinolide treated *S. japonicus* cells? Additionally, if the peeling phenotype is present in these cells, it would also be much easier to conduct pharmacological experiments on these mutants, e.g. to see if Swinholide A (actin severing drug) could rescue the effect of the Adf1-M2 and Adf1-M3 mutants. Comparison of the sequence of the Adf1 protein in *S. pombe* and *S. japonicus* shows a sequence identity of 88% with no gaps, and this includes the residues that are mutated in the Adf1-M2 and Adf1-

M3 proteins, suggesting that this approach could be successful. However, it would also be necessary to perform biochemical analysis of the mutant protein, in order to ensure that they behave as expected.

It is also worth considering what mathematical modelling work could be performed in the future. This work is complicated by the fact that we do not currently understand how the *S. pombe* AMR generates tension, and while a number of ideas have been proposed, none of these are without their problems. The first major model proposed that the continuous binding of formin-containing nodes into the ring, and the subsequent polymerisation of actin filaments from these nodes, caused a bias towards contractile actin-myosin configurations [35,132]. However, this model assumes that all the actin filaments in the ring are bound into a node via their barbed end attachment to a formin dimer, and as we have previously discussed there are also issues with how they model the interactions between the actin filaments and the myosin clusters (see section 4.4).

Furthermore, recent experiments using 3D electron cryotomography did not detect the presence of nodes in the contracting *S. pombe* AMR [46], and subsequent modelling suggested that a 'nodeless' model could also lead to the generation of contractile forces [133]. Unfortunately, there are also problems with this model: We have already discussed how the actin filaments here were given much higher drag coefficients than in previous models (see section 4.8.1), and there is also the issue that the rate constants used for the myosin ATPase cycle in their simulations lead to a duty ratio of ~ 0.7 , which is much greater than the values normally observed for type II myosins [95,169]. Additionally, the model also included the presence of bipolar tetrameric myosin molecules, presumably meant to be representative of Myp2, however there is no evidence that Myp2 forms bipolar oligomers, and the limited amount of available data suggests that it is unable to do so, because its tail domain appears to fold back on itself [102]. The paper's authors are careful to point out that there are a number of aspects of this model that remain unproven, and that the results they present are meant more as an

exploration of possible ring architectures, rather than as a definitive conclusion about the AMR architecture in *S. pombe*. However, until more experimental evidence becomes available, the results of this paper will have to be treated with caution.

Since we do not understand how AMRs generate tension, this makes it difficult to subsequently investigate the effect of reduced actin turnover on contracting AMRs. We could take the opposite approach, by attempting to build a number of AMR models, and comparing how they are affected by reduced actin turnover, however this would be a substantial amount of work, and would not necessarily reveal the mechanisms behind the contractility of the ring, or the mechanisms that lead to ring peeling [177]. Therefore, while obtaining a mathematical model of the contracting fission yeast AMR that reproduces the ring peeling phenotype remains an attractive goal, at this point in time it is perhaps also an unfeasible goal.

7. Bibliography

1. Cheffings, T.H., Burroughs, N.J., Balasubramanian, M.K. (2016). Actomyosin Ring Formation and Tension Generation in Eukaryotic Cytokinesis. *Curr. Biol.* 26, r719–37.
2. Lutkenhaus, J., Pichoff, S., Du, S. (2012). Bacterial cytokinesis: From Z ring to divisome. *Cytoskeleton.* 69, 778–90.
3. Green, A.R., Paluch, E., Oegema, K. (2012). Cytokinesis in animal cells. *Annu. Rev. Cell Dev. Biol.* 28, 29–58.
4. Balasubramanian, M.K., Srinivasan, R., Huang, Y., Ng, K.H. (2012). Comparing contractile apparatus-driven cytokinesis mechanisms across kingdoms. *Cytoskeleton.* 69, 942–56.
5. Pollard, T.D. (2017). Nine unanswered questions about cytokinesis. *J. Cell Biol.* 216, 3007–16.
6. Oliferenko, S., Chew, T.G., Balasubramanian, M.K. (2009). Positioning cytokinesis. *Genes Dev.* 23, 660–74.
7. Sagona, A.P., Stenmark, H. (2010). Cytokinesis and cancer. *FEBS Lett.* 584, 2652–61.
8. Daniels, M.J., Wang, Y., Lee, M.Y., Venkitaraman, A.R. (2004). Abnormal cytokinesis in cells deficient in the breast cancer susceptibility protein BRCA2. *Science* (80-.). 306, 876–9.
9. Fujiwara, T., Bandi, M., Nitta, M., Ivanova, E. V., Bronson, R.T., Pellman, D. (2005). Cytokinesis failure generating tetraploids promotes tumorigenesis in p53-null cells. *Nature.* 437, 1043–7.
10. Ganem, N.J., Cornils, H., Chiu, S.Y., O'Rourke, K.P., Arnaud, J., Yimlamai, D., et al. (2014). Cytokinesis failure triggers hippo tumor suppressor pathway activation. *Cell.* 158, 833–48.
11. Wong, C., Stearns, T. (2005). Mammalian cells lack checkpoints for tetraploidy, aberrant centrosome number, and cytokinesis failure. *BMC Cell Biol.* 6, 1–12.
12. Kapoor, S., Panda, D. (2009). Targeting FtsZ for antibacterial

- therapy: a promising avenue. *Expert Opin. Ther. Targets.* *13*, 1037–51.
13. Vollmer, W. (2006). The prokaryotic cytoskeleton: A putative target for inhibitors and antibiotics? *Appl. Microbiol. Biotechnol.* *73*, 37–47.
 14. Erickson, H.P., Anderson, D.E., Osawa, M. (2010). FtsZ in bacterial cytokinesis: cytoskeleton and force generator all in one. *Microbiol. Mol. Biol. Rev.* *74*, 504–28.
 15. Osawa, M., Anderson, D.E., Erickson, H.P. (2008). Reconstitution of Contractile FtsZ Rings in Liposomes. *Science* (80-.). *320*, 792–4.
 16. Osawa, M., Erickson, H.P. (2013). Liposome division by a simple bacterial division machinery. *Proc. Natl. Acad. Sci.* *110*, 11000–4.
 17. Sun, S.X., Walcott, S., Wolgemuth, C.W. (2010). Cytoskeletal cross-linking and bundling in motor-independent contraction. *Curr. Biol.* *20*, 649–54.
 18. Lan, G., Daniels, B.R., Dobrowsky, T.M., Wirtz, D., Sun, S.X. (2009). Condensation of FtsZ filaments can drive bacterial cell division. *Proc. Natl. Acad. Sci.* *106*, 121–6.
 19. Monteiro, J.M., Pereira, A.R., Reichmann, N.T., Saraiva, B.M., Pedro, B., Veiga, H., et al. (2018). Peptidoglycan synthesis drives FtsZ treadmilling-independent step of cytokinesis. *Nature.* *554*, 528–32.
 20. The Arabidopsis Genome Initiative (2000). Analysis of the genome sequence of the flowering plant *Arabidopsis thaliana*. *Nature.* *408*, 796–815.
 21. Smith, L.G. (1999). Divide and conquer: Cytokinesis in plant cells. *Curr. Opin. Plant Biol.* *2*, 447–53.
 22. Jürgens, G. (2005). Plant cytokinesis: Fission by fusion. *Trends Cell Biol.* *15*, 277–83.
 23. Farr, H., Gull, K. (2012). Cytokinesis in trypanosomes. *Cytoskeleton.* *69*, 931–41.
 24. Hardin, W.R., Li, R., Xu, J., Shelton, A.M., Alas, G.C.M., Minin, V.N., et al. (2017). Myosin-independent cytokinesis in *Giardia* utilizes flagella to coordinate force generation and direct membrane

- trafficking. *Proc. Natl. Acad. Sci.* *114*, e5854–63.
25. Pollard, T.D., Wu, J. (2010). Understanding cytokinesis: lessons from fission yeast. *Nat. Rev. Mol. Cell Biol.* *11*, 149–55.
 26. Meitinger, F., Palani, S. (2016). Actomyosin Ring driven Cytokinesis in Budding Yeast. *Semin. Cell Dev. Biol.* *53*, 19–27.
 27. Srivastava, V., Iglesias, P.A., Robinson, D.N. (2016). Cytokinesis: Robust cell shape regulation. *Semin. Cell Dev. Biol.* *53*, 39–44.
 28. Carvalho, A., Desai, A., Oegema, K. (2009). Structural Memory in the Contractile Ring Makes the Duration of Cytokinesis Independent of Cell Size. *Cell.* *137*, 926–37.
 29. Hoffman, C.S., Wood, V., Fantes, P.A. (2015). An ancient yeast for young geneticists: A primer on the *Schizosaccharomyces pombe* model system. *Genetics.* *201*, 403–23.
 30. Pollard, T.D. (2014). The Value of Mechanistic Biophysical Information for Systems-Level Understanding of Complex Biological Processes Such as Cytokinesis. *Biophys. J.* *107*, 2499–507.
 31. Minc, N., Boudaoud, A., Chang, F. (2009). Mechanical forces of fission yeast growth. *Curr. Biol.* *19*, 1096–101.
 32. Liu, J., Wang, H., McCollum, D., Balasubramanian, M.K. (1999). Drc1p/Cps1p, a 1,3- β -glucan synthase subunit, is essential for division septum assembly in *Schizosaccharomyces pombe*. *Genetics.* *153*, 1193–203.
 33. Vangindertael, J., Camacho, R., Sempels, W., Mizuno, H., Dedeker, P., Janssen, K.P.F. (2018). An introduction to optical super-resolution microscopy for the adventurous biologist. *Methods Appl. Fluoresc.* *6*, 22003.
 34. Vavylonis, D., Wu, J.-Q., Hao, S., O’Shaughnessy, B., Pollard, T.D. (2008). Assembly mechanism of the contractile ring for cytokinesis by fission yeast. *Science.* *319*, 97–100.
 35. Stachowiak, M.R., Laplante, C., Chin, H.F., Guirao, B., Karatekin, E., Pollard, T.D., et al. (2014). Mechanism of cytokinetic contractile ring constriction in fission yeast. *Dev. Cell.* *29*, 547–61.

36. Kovar, D.R., Sirotkin, V., Lord, M. (2011). Three's company: The fission yeast actin cytoskeleton. *Trends Cell Biol.* *21*, 177–87.
37. Pelham, R., Chang, F. (2002). Actin dynamics in the contractile ring during cytokinesis in fission yeast. *Nature.* *419*, 82–6.
38. Suarez, C., Carroll, R.T., Burke, T.A., Christensen, J.R., Bestul, A.J., Sees, J.A., et al. (2015). Profilin regulates F-Actin network homeostasis by favoring formin over Arp2/3 complex. *Dev. Cell.* *32*, 43–53.
39. Suarez, C., Kovar, D.R. (2016). Internetwork competition for monomers governs actin cytoskeleton organization. *Nat. Rev. Mol. Cell Biol.* *17*, 799–810.
40. Pelham, J., Chang, F. (2001). Role of actin polymerization and actin cables in actin-patch movement in *Schizosaccharomyces pombe*. *Nat. Cell Biol.* *3*, 235–44.
41. Sirotkin, V., Berro, J., Macmillan, K., Zhao, L., Pollard, T.D. (2010). Quantitative Analysis of the Mechanism of Endocytic Actin Patch Assembly and Disassembly in Fission Yeast. *Mol. Biol. Cell.* *21*, 2894–904.
42. Kaksonen, M., Toret, C.P., Drubin, D.G. (2006). Harnessing actin dynamics for clathrin-mediated endocytosis. *Nat. Rev. Mol. Cell Biol.* *7*, 404–14.
43. Lo Presti, L., Chang, F., Martin, S.G. (2012). Myosin Vs organize actin cables in fission yeast. *Mol. Biol. Cell.* *23*, 4579–91.
44. Feierbach, B., Chang, F. (2001). Roles of the fission yeast formin for3p in cell polarity, actin cable formation and symmetric cell division. *Curr. Biol.* *11*, 1656–65.
45. Kamasaki, T., Osumi, M., Mabuchi, I. (2007). Three-dimensional arrangement of F-actin in the contractile ring of fission yeast. *J. Cell Biol.* *178*, 765–71.
46. Swulius, M.T., Nguyen, L.T., Ladinsky, M.S., Ortega, D.R., Aich, S., Mishra, M., et al. (2018). Structure of the fission yeast actomyosin ring during constriction. *Proc. Natl. Acad. Sci.* 201711218.
47. Chang, F., Drubin, D., Nurse, P. (1997). *cdc12p*, a Protein Required

- for Cytokinesis in Fission Yeast, Is a Component of the Cell Division Ring and Interacts with Profilin. *J. Cell Biol.* *137*, 169–82.
48. Chang, F., Woollard, A., Nurse, P. (1996). Isolation and characterization of fission yeast mutants defective in the assembly and placement of the contractile actin ring. *J. Cell Sci.* *109*, 131–42.
 49. Wu, J., Kuhn, J.R., Kovar, D.R., Pollard, T.D. (2003). Spatial and Temporal Pathway for Assembly and Constriction of the Contractile Ring in Fission Yeast Cytokinesis. *Dev. Cell.* *5*, 723–34.
 50. Wu, J.-Q., Sirotkin, V., Kovar, D.R., Lord, M., Beltzner, C.C., Kuhn, J.R., et al. (2006). Assembly of the cytokinetic contractile ring from a broad band of nodes in fission yeast. *J. Cell Biol.* *174*, 391–402.
 51. Palani, S., Chew, T.G., Ramanujam, S., Kamnev, A., Harne, S., Chapay-Lazo, B., et al. (2017). Motor Activity Dependent and Independent Functions of Myosin II Contribute to Actomyosin Ring Assembly and Contraction in *Schizosaccharomyces pombe*. *Curr. Biol.* *27*, 751–7.
 52. Akamatsu, M., Berro, J., Pu, K.M., Tebbs, I.R., Pollard, T.D. (2014). Cytokinetic nodes in fission yeast arise from two distinct types of nodes that merge during interphase. *J. Cell Biol.* *204*, 977–88.
 53. Pan, K.Z., Saunders, T.E., Flor-Parra, I., Howard, M., Chang, F. (2014). Cortical regulation of cell size by a sizer *cdr2p*. *Elife.* *3*, e02040.
 54. Martin, S.G., Berthelot-Grosjean, M. (2009). Polar gradients of the DYRK-family kinase Pom1 couple cell length with the cell cycle. *Nature.* *459*, 852–6.
 55. Bhatia, P., Hachet, O., Hersch, M., Rincon, S.A., Berthelot-Grosjean, M., Dalessi, S., et al. (2014). Distinct levels in Pom1 gradients limit Cdr2 activity and localization to time and position division. *Cell Cycle.* *13*, 538–52.
 56. Bähler, J., Steever, A.B., Wheatley, S., Wang, Y., Pringle, J.R., Gould, K.L. (1998). Role of Polo Kinase and Mid1p in Determining the Site of Cell Division in Fission Yeast. *J. Cell Biol.* *143*, 1603–16.
 57. Daga, R.R., Chang, F. (2005). Dynamic positioning of the fission

- yeast cell division plane. *Proc. Natl. Acad. Sci. U. S. A.* *102*, .
58. Huang, Y., Yan, H., Balasubramanian, M.K. (2008). Assembly of normal actomyosin rings in the absence of Mid1p and cortical nodes in fission yeast. *J. Cell Biol.* *183*, 979–88.
 59. Hachet, O., Simanis, V. (2008). Mid1p / anillin and the septation initiation network orchestrate contractile ring assembly for cytokinesis. *Genes Dev.* *22*, 3205–16.
 60. Ullal, P., McDonald, N.A., Chen, J.-S., Lo Presti, L., Roberts-Galbraith, R.H., Gould, K.L., et al. (2015). The DYRK-family kinase Pom1 phosphorylates the F-BAR protein Cdc15 to prevent division at cell poles. *J. Cell Biol.* *211*, 653–68.
 61. Huang, Y., Chew, T.G., Ge, W., Balasubramanian, M.K. (2007). Polarity determinants Tea1p, Tea4p, and Pom1p inhibit division-septum assembly at cell ends in fission yeast. *Dev. Cell.* *12*, 987–96.
 62. Laporte, D., Coffman, V.C., Lee, I.-J., Wu, J.-Q. (2011). Assembly and architecture of precursor nodes during fission yeast cytokinesis. *J. Cell Biol.* *192*, 1005–21.
 63. Padmanabhan, A., Bakka, K., Sevugan, M., Naqvi, N.I., D'Souza, V., Tang, X., et al. (2011). IQGAP-related Rng2p organizes cortical nodes and ensures position of cell division in fission yeast. *Curr. Biol.* *21*, 467–72.
 64. Wu, J.-Q., Pollard, T.D. (2005). Counting Cytokinesis Proteins Globally and Locally in Fission Yeast. *Science.* *310*, 310–4.
 65. Laplante, C., Huang, F., Tebbs, I.R., Bewersdorf, J., Pollard, T.D. (2016). Molecular organization of cytokinesis nodes and contractile rings by super-resolution fluorescence microscopy of live fission yeast. *Proc. Natl. Acad. Sci.* *113*, e5876–85.
 66. Chen, Q., Pollard, T.D. (2011). Actin filament severing by cofilin is more important for assembly than constriction of the cytokinetic contractile ring. *J. Cell Biol.* *195*, 485–98.
 67. Ojkic, N., Vavylonis, D. (2010). Kinetics of Myosin Node Aggregation into a Contractile Ring. *Phys. Rev. Lett.* *105*, 048102.
 68. Coffman, V.C., Nile, A.H., Lee, I.-J., Liu, H., Wu, J.-Q. (2009). Roles of

- formin nodes and myosin motor activity in Mid1p-dependent contractile-ring assembly during fission yeast cytokinesis. *Mol. Biol. Cell.* *20*, 5195–210.
69. Huang, J., Huang, Y., Yu, H., Subramanian, D., Padmanabhan, A., Thadani, R., et al. (2012). Nonmedially assembled F-actin cables incorporate into the actomyosin ring in fission yeast. *J. Cell Biol.* *199*, 831–47.
 70. Coffman, V.C., Sees, J. a., Kovar, D.R., Wu, J.Q. (2013). The formins cdc12 and for3 cooperate during contractile ring assembly in cytokinesis. *J. Cell Biol.* *203*, 101–14.
 71. Wang, N., Presti, L. Lo, Zhu, Y.H., Kang, M., Wu, Z., Martin, S.G., et al. (2014). The novel proteins Rng8 and Rng9 regulate the myosin-V Myo51 during fission yeast cytokinesis. *J. Cell Biol.* *205*, 357–75.
 72. Zhou, M., Wang, Y.-L. (2008). Distinct Pathways for the Early Recruitment of Myosin II and Actin to the Cytokinetic Furrow. *Mol. Biol. Cell.* *19*, 318–26.
 73. Cao, L.G., Wang, Y.-L. (1990). Mechanism of the formation of contractile ring in dividing cultured animal cells. I. Recruitment of preexisting actin filaments into the cleavage furrow. *J. Cell Biol.* *110*, 1089–95.
 74. Wachtler, V., Huang, Y., Karagiannis, J., Balasubramanian, M.K. (2006). Cell Cycle-dependent Roles for the FCH-Domain Protein Cdc15p in Formation of the Actomyosin Ring in *Schizosaccharomyces pombe*. *Mol. Biol. Cell.* *17*, 3254–66.
 75. Roberts-Galbraith, R.H., Chen, J.S., Wang, J., Gould, K.L. (2009). The SH3 domains of two PCH family members cooperate in assembly of the *schizosaccharomyces pombe* contractile ring. *J. Cell Biol.* *184*, 113–27.
 76. Ge, W., Balasubramanian, M.K. (2008). Pxl1p, a Paxillin-related Protein, Stabilizes the Actomyosin Ring during Cytokinesis in Fission Yeast. *Mol. Biol. Cell.* *19*, 1680–92.
 77. Berlin, A., Paoletti, A., Chang, F. (2003). Mid2p stabilizes septin rings during cytokinesis in fission yeast. *J. Cell Biol.* *160*, 1083–92.

78. An, H., Morrell, J.L., Jennings, J.L., Link, A.J., Gould, K.L. (2004). Requirements of Fission Yeast Septins for Complex Formation, Localization, and Function. *Mol. Biol. Cell.* *15*, 5551–64.
79. Krapp, A., Simanis, V. (2008). An overview of the fission yeast septation initiation network (SIN). *Biochem. Soc. Trans.* *36*, 411–5.
80. Mishra, M., Karagiannis, J., Trautmann, S., Wang, H., McCollum, D., Balasubramanian, M.K. (2004). The Clp1p/Flp1p phosphatase ensures completion of cytokinesis in response to minor perturbation of the cell division machinery in *Schizosaccharomyces pombe*. *J. Cell Sci.* *117*, 3897–910.
81. Schmidt, S., Sohrmann, M., Hofmann, K., Woollard, A., Simanis, V. (1997). The Spg1p GTPase is an essential, dosage-dependent inducer of septum formation in *Schizosaccharomyces pombe*. *Genes Dev.* *11*, 1519–34.
82. Simanis, V. (2015). Pombe's thirteen - control of fission yeast cell division by the septation initiation network. *J. Cell Sci.* *128*, 1465–74.
83. Roberts-Galbraith, R.H., Ohi, M.D., Ballif, B.A., Chen, J.S., McLeod, I., McDonald, W.H., et al. (2010). Dephosphorylation of F-BAR Protein Cdc15 Modulates Its Conformation and Stimulates Its Scaffolding Activity at the Cell Division Site. *Mol. Cell.* *39*, 86–99.
84. McDonald, N.A., Vander Kooi, C.W., Ohi, M.D., Gould, K.L. (2015). Oligomerization but Not Membrane Bending Underlies the Function of Certain F-BAR Proteins in Cell Motility and Cytokinesis. *Dev. Cell.* *35*, 725–36.
85. Fankhauser, C., Reymond, A., Cerutti, L., Utzig, S., Hofmann, K., Simanis, V. (1995). The *S. pombe* *cdc15* gene is a key element in the reorganization of F-actin at mitosis. *Cell.* *82*, 435–44.
86. Clifford, D.M., Wolfe, B.A., Roberts-Galbraith, R.H., McDonald, W.H., Yates, J.R., Gould, K.L. (2008). The Clp1/Cdc14 phosphatase contributes to the robustness of cytokinesis by association with anillin-related Mid1. *J. Cell Biol.* *181*, 79–88.
87. Mulvihill, D.P., Hyams, J.S. (2003). Role of the two type II myosins,

- Myo2 and Myp2, in cytokinetic actomyosin ring formation and function in fission yeast. *Cell Motil. Cytoskeleton*. 54, 208–16.
88. Liu, J., Tang, X., Wang, H., Oliferenko, S., Balasubramanian, M.K. (2002). The Localization of the Integral Membrane Protein Cps1p to the Cell Division Site is Dependent on the Actomyosin Ring and the Septation-Inducing Network in *Schizosaccharomyces pombe*. *Mol. Biol. Cell*. 13, 989–1000.
 89. Proctor, S. a, Minc, N., Boudaoud, A., Chang, F. (2012). Contributions of turgor pressure, the contractile ring, and septum assembly to forces in cytokinesis in fission yeast. *Curr. Biol*. 22, 1601–8.
 90. Zhou, Z., Laura, E., He, J., Ursell, T., Chang, F., Street, W., et al. (2014). The contractile ring coordinates curvature dependent septum assembly during fission yeast cytokinesis. *Mol. Biol. Cell*. 26, 78–90.
 91. Schroeder, T.E. (1972). The contractile ring. II. Determining its brief existence, volumetric changes, and vital role in cleaving *Arbacia* eggs. *J. Cell Biol*. 53, 419–34.
 92. Huang, J., Chew, T.G., Gu, Y., Palani, S., Kamnev, A., Martin, D.S., et al. (2016). Curvature-induced expulsion of actomyosin bundles during cytokinetic ring contraction. *Elife*. 5, 1–14.
 93. Nakano, K., Mabuchi, I. (2006). Actin-depolymerizing Protein Adf1 Is Required for Formation and Maintenance of the Contractile Ring during Cytokinesis in Fission Yeast. *Mol. Biol. Cell*. 17, 1933–45.
 94. Gunning, P.W., Hardeman, E.C., Lappalainen, P., Mulvihill, D.P. (2015). Tropomyosin - master regulator of actin filament function in the cytoskeleton. *J. Cell Sci*. 128, 2965–74.
 95. Stark, B.C., Sladewski, T.E., Pollard, L.W., Lord, M. (2010). Tropomyosin and myosin-II cellular levels promote actomyosin ring assembly in fission yeast. *Mol. Biol. Cell*. 21, 989–1000.
 96. Clayton, J.E., Pollard, L.W., Murray, G.G., Lord, M. (2015). Myosin motor isoforms direct specification of actomyosin function by tropomyosins. *Cytoskeleton*. 72, 131–45.

97. Clayton, J.E., Sammons, M.R., Stark, B.C., Hodges, A.R., Lord, M. (2010). Differential regulation of unconventional fission yeast myosins via the actin track. *Curr. Biol.* *20*, 1423–31.
98. Clayton, J.E., Pollard, L.W., Sckolnick, M., Bookwalter, C.S., Hodges, A.R., Trybus, K.M., et al. (2014). Fission yeast tropomyosin specifies directed transport of myosin-V along actin cables. *Mol. Biol. Cell.* *25*, 66–75.
99. Balasubramanian, M.K., Helfman, D.M., Hemmingsen, S.M. (1992). A new tropomyosin essential for cytokinesis in the fission yeast *S. pombe*. *Nature.* *360*, 84–7.
100. Laplante, C., Berro, J., Karatekin, E., Hernandez-Leyva, A., Lee, R., Pollard, T.D. (2015). Three Myosins Contribute Uniquely to the Assembly and Constriction of the Fission Yeast Cytokinetic Contractile Ring. *Curr. Biol.* *25*, 1–11.
101. Motegi, F., Mishra, M., Balasubramanian, M.K., Mabuchi, I. (2004). Myosin-II reorganization during mitosis is controlled temporally by its dephosphorylation and spatially by Mid1 in fission yeast. *J. Cell Biol.* *165*, 685–95.
102. Bezanilla, M., Pollard, T.D. (2000). Myosin-II tails confer unique functions in *Schizosaccharomyces pombe*: characterization of a novel myosin-II tail. *Mol. Biol. Cell.* *11*, 79–91.
103. McDonald, N.A., Lind, A.L., Smith, S.E., Li, R., Gould, K.L. (2017). Nanoscale architecture of the *Schizosaccharomyces pombe* contractile ring. *Elife.* *6*, 1–23.
104. Win, T.Z., Gachet, Y., Mulvihill, D.P., May, K.M., Hyams, J.S. (2001). Two type V myosins with non-overlapping functions in the fission yeast *Schizosaccharomyces pombe*: Myo52 is concerned with growth polarity and cytokinesis, Myo51 is a component of the cytokinetic actin ring. *J. Cell Sci.* *114*, 69–79.
105. Takaine, M., Numata, O., Nakano, K. (2015). An actin-myosin-II interaction is involved in maintaining the contractile ring in fission yeast. *J. Cell Sci.* *128*, 2903–18.
106. Zambon, P., Palani, S., Kamnev, A., Balasubramanian, M.K. (2017).

- Myo2p is the major motor involved in actomyosin ring contraction in fission yeast. *Curr. Biol.* 27, r99–100.
107. Wu, J.Q., Bähler, J., Pringle, J.R. (2001). Roles of a fimbrin and an alpha-actinin-like protein in fission yeast cell polarization and cytokinesis. *Mol. Biol. Cell.* 12, 1061–77.
 108. Laporte, D., Ojkic, N., Vavylonis, D., Wu, J.-Q. (2012). α -Actinin and fimbrin cooperate with myosin II to organize actomyosin bundles during contractile-ring assembly. *Mol. Biol. Cell.* 23, 3094–110.
 109. Ren, L., Willet, A.H., Roberts-Galbraith, R.H., McDonald, N.A., Feoktistova, A., Chen, J.-S., et al. (2015). The Cdc15 and Imp2 SH3 domains cooperatively scaffold a network of proteins that redundantly ensure efficient cell division in fission yeast. *Mol. Biol. Cell.* 26, 256–69.
 110. Johnston, A.B., Collins, A., Goode, B.L. (2015). High-speed depolymerization at actin filament ends jointly catalysed by Twinfilin and Srv2/CAP. *Nat. Cell Biol.* 17, 1504–11.
 111. Chaudhry, F., Breitsprecher, D., Little, K., Sharov, G., Sokolova, O., Goode, B.L. (2013). Srv2/cyclase-associated protein forms hexameric shurikens that directly catalyze actin filament severing by cofilin. *Mol. Biol. Cell.* 24, 31–41.
 112. Kanellos, G., Frame, M.C. (2016). Cellular functions of the ADF/cofilin family at a glance. *J. Cell Sci.* 129, 3211–8.
 113. Bernstein, B.W., Bamburg, J.R. (2010). ADF/Cofilin: A functional node in cell biology. *Trends Cell Biol.* 20, 187–95.
 114. De La Cruz, E.M. (2005). Cofilin binding to muscle and non-muscle actin filaments: Isoform-dependent cooperative interactions. *J. Mol. Biol.* 346, 557–64.
 115. McCullough, B.R., Blanchoin, L., Martiel, J.L., De La Cruz, E.M. (2008). Cofilin Increases the Bending Flexibility of Actin Filaments: Implications for Severing and Cell Mechanics. *J. Mol. Biol.* 381, 550–8.
 116. Prochniewicz, E., Janson, N., Thomas, D.D., De La Cruz, E.M. (2005). Cofilin increases the torsional flexibility and dynamics of actin

- filaments. *J. Mol. Biol.* 353, 990–1000.
117. McGough, A., Pope, B., Chiu, W., Weeds, A. (1997). Cofilin changes the twist of F-actin: Implications for actin filament dynamics and cellular function. *J. Cell Biol.* 138, 771–81.
 118. McCullough, B.R., Grintsevich, E.E., Chen, C.K., Kang, H., Hutchison, A.L., Henn, A., et al. (2011). Cofilin-linked changes in actin filament flexibility promote severing. *Biophys. J.* 101, 151–9.
 119. Schramm, A.C., Hocky, G.M., Voth, G.A., Blanchoin, L., Martiel, J.L., De La Cruz, E.M. (2017). Actin Filament Strain Promotes Severing and Cofilin Dissociation. *Biophys. J.* 112, 2624–33.
 120. Wioland, H., Guichard, B., Senju, Y., Myram, S., Lappalainen, P., Jégou, A., et al. (2017). ADF/Cofilin Accelerates Actin Dynamics by Severing Filaments and Promoting Their Depolymerization at Both Ends. *Curr. Biol.* 27, 1956–1967.e7.
 121. Stachowiak, M.R., McCall, P.M., Thoresen, T., Balcioglu, H.E., Kasiewicz, L., Gardel, M.L., et al. (2012). Self-organization of myosin II in reconstituted actomyosin bundles. *Biophys. J.* 103, 1265–74.
 122. Zemel, A., Mogilner, A. (2009). Motor-induced sliding of microtubule and actin bundles. *Phys. Chem. Chem. Phys.* 11, 4821–33.
 123. Oelz, D.B., Rubinstein, B.Y., Mogilner, A. (2015). A Combination of Actin Treadmilling and Cross-Linking Drives Contraction of Random Actomyosin Arrays. *Biophys. J.* 109, 1818–29.
 124. Zumdick, A., Kruse, K., Bringmann, H., Hyman, A. a, Jülicher, F. (2007). Stress generation and filament turnover during actin ring constriction. *PLoS One.* 2, e696.
 125. Lenz, M., Thoresen, T., Gardel, M.L., Dinner, A.R. (2012). Contractile units in disordered actomyosin bundles arise from f-actin buckling. *Phys. Rev. Lett.* 108, 1–5.
 126. Vogel, S.K., Petrasek, Z., Heinemann, F., Schwille, P. (2013). Myosin motors fragment and compact membrane-bound actin filaments. *Elife.* 2013, 1–18.
 127. Ennomani, H., Letort, G., Guérin, C., Martiel, J.-L., Cao, W., Nédélec,

- F., et al. (2016). Architecture and Connectivity Govern Actin Network Contractility. *Curr. Biol.* 1–11.
128. Reichl, E.M., Ren, Y., Morphey, M.K., Delannoy, M., Effler, J.C., Girard, K.D., et al. (2008). Interactions between Myosin and Actin Crosslinkers Control Cytokinesis Contractility Dynamics and Mechanics. *Curr. Biol.* 18, 471–80.
 129. Maupin, P., Pollard, T.D. (1986). Arrangement of Actin Filaments and Myosin-like Filaments in the Contractile Ring and of Actin-like Filaments in the Mitotic Spindle of Dividing HeLa Cells. *J. Ultrastruct. Mol. Struct. Res.* 94, 92–103.
 130. Fallis, A.. (1995). Flexibility of Actin Filaments Derived from Thermal Fluctuations. Effect of Bound Nucleotide, Phalloidin, and Muscle Regulatory Proteins. *J. Biol. Chem.* 270, 11437–44.
 131. Wong, K.C.Y., D’Souza, V.M., Naqvi, N.I., Motegi, F., Mabuchi, I., Balasubramanian, M.K. (2002). Importance of a myosin II-containing progenitor for actomyosin ring assembly in fission yeast. *Curr. Biol.* 12, 724–9.
 132. Thiagarajan, S., Wang, S., O’Shaughnessy, B. (2017). A node organization in the actomyosin contractile ring generates tension and aids stability. *Mol. Biol. Cell.* 28, 3286–97.
 133. Nguyen, L., Swulius, M.T., Aich, S., Mishra, M., Jensen, G.J. (2018). Coarse-grained simulations of actomyosin rings point to a nodeless model involving both unipolar and bipolar myosins. *Mol. Biol. Cell.* 29, .
 134. Thiagarajan, S., Munteanu, E.L., Arasada, R., Pollard, T.D., O’Shaughnessy, B. (2015). The fission yeast cytokinetic contractile ring regulates septum shape and closure. *J. Cell Sci.* 128, 3672–81.
 135. Chew, T.G., Huang, J., Palani, S., Sommes, R., Kamnev, A., Hatano, T., et al. (2017). Actin turnover maintains actin filament homeostasis during cytokinetic ring contraction. *J. Cell Biol.* 216, 2657–67.
 136. Matsuyama, A., Shirai, A., Yashiroda, Y., Kamata, A., Horinouchi, S., Yoshida, M. (2004). pDUAL, a multipurpose, multicopy vector

- capable of chromosomal integration in fission yeast. *Yeast*. *21*, 1289–305.
137. Chen, Y., Wang, G., Hao, H., Chao, C., Wang, Y., Jin, Q. (2017). Facile manipulation of protein localization in fission yeast through binding of GFP-binding protein to GFP. *J. Cell Sci.* *130*, 1003–15.
 138. Wagenmakers, E.-J., Farrell, S. (2004). AIC model selection using Akaike weights. *Psychon. Bull. Rev.* *11*, 192–6.
 139. Lord, M., Pollard, T.D. (2004). UCS protein Rng3p activates actin filament gliding by fission yeast myosin-II. *J. Cell Biol.* *167*, 315–25.
 140. Mishra, M., Kashiwazaki, J., Takagi, T., Srinivasan, R., Huang, Y., Balasubramanian, M.K., et al. (2013). In vitro contraction of cytokinetic ring depends on myosin II but not on actin dynamics. *Nat. Cell Biol.* *15*, 853–9.
 141. Feigelson, E.D., Babu, G.J. (2012). Nonparametric statistics. *Mod. Stat. Methods Astron. With R Appl.*, 2012, p. 105–27 105–27.
 142. Kim, K.Y., Kovács, M., Kawamoto, S., Sellers, J.R., Adelstein, R.S. (2005). Disease-associated mutations and alternative splicing alter the enzymatic and motile activity of nonmuscle myosins II-B and II-C. *J. Biol. Chem.* *280*, 22769–75.
 143. Riedl, J., Crevenna, A.H., Kessenbrock, K., Yu, J.H., Bista, M., Bradke, F., et al. (2010). Lifeact: a versatile marker to visualize F-actin. *Nat. Methods*. *5*, .
 144. Aoi, Y., Sato, M., Sutani, T., Shirahige, K., Kapoor, T.M., Kawashima, S.A. (2014). Dissecting the first and the second meiotic divisions using a marker-less drug-hypersensitive fission yeast. *Cell Cycle*. *13*, 1327–34.
 145. Gu, Y., Yam, C., Oliferenko, S. (2015). Rewiring of cellular division site selection in evolution of fission yeasts. *Curr. Biol.* *25*, 1187–94.
 146. Bubb, M.R., Spector, I., Bershadsky, A.D., Korn, E.D. (1995). Swinholide A is a microfilament disrupting marine toxin that stabilizes actin dimers and severs actin filaments. *J. Biol. Chem.* *270*, 3463–6.
 147. Lim, T.C., Hatano, T., Kamnev, A., Balasubramanian, M.K., Chew, T.G.

- (2018). Equatorial Assembly of the Cell-Division Actomyosin Ring in the Absence of Cytokinetic Spatial Cues. *Curr. Biol.* 28, 955–962.e3.
148. Asadi, F., Chakraborty, B., Karagiannis, J. (2017). Latrunculin A-Induced Perturbation of the Actin Cytoskeleton Mediates Pap1p-Dependent Induction of the Caf5p Efflux Pump in *Schizosaccharomyces pombe*. *Genes|Genomes|Genetics.* 7, 723–30.
 149. Chen, Q., Pollard, T.D. (2013). Actin filament severing by cofilin dismantles actin patches and produces mother filaments for new patches. *Curr. Biol.* 23, 1154–62.
 150. Courtemanche, N., Pollard, T.D., Chen, Q. (2016). Avoiding artefacts when counting polymerized actin in live cells with LifeAct fused to fluorescent proteins. *Nat. Cell Biol.* 18, 676–83.
 151. Jodoin, J.N., Coravos, J.S., Chanet, S., Vasquez, C.G., Tworoger, M., Kingston, E.R., et al. (2015). Stable Force Balance between Epithelial Cells Arises from F-Actin Turnover. *Dev. Cell.* 35, 685–97.
 152. Wiggan, O., Shaw, A.E., DeLuca, J.G., Bamburg, J.R. (2012). ADF/Cofilin Regulates Actomyosin Assembly through Competitive Inhibition of Myosin II Binding to F-Actin. *Dev. Cell.* 22, 530–43.
 153. Mendes Pinto, I., Rubinstein, B., Kucharavy, A., Unruh, J.R., Li, R. (2012). Actin depolymerization drives actomyosin ring contraction during budding yeast cytokinesis. *Dev. Cell.* 22, 1247–60.
 154. Carvalho, A., Olson, S.K., Gutierrez, E., Zhang, K., Noble, L.B., Zanin, E., et al. (2011). Acute drug treatment in the early *C. elegans* embryo. *PLoS One.* 6, .
 155. Yumura, S. (2001). Myosin II dynamics and cortical flow during contractile ring formation in *Dictyostelium* cells. *J. Cell Biol.* 154, 137–45.
 156. Guha, M., Zhou, M., Wang, Y.L. (2005). Cortical actin turnover during cytokinesis requires myosin II. *Curr. Biol.* 15, 732–6.
 157. Srivastava, V., Robinson, D.N. (2015). Mechanical stress and network structure drive protein dynamics during cytokinesis. *Curr. Biol.* 25, 663–70.

158. Wollrab, V., Thiagarajan, R., Wald, A., Kruse, K., Riveline, D. (2016). Still and rotating myosin clusters determine cytokinetic ring constriction. *Nat. Commun.* 7, 1–9.
159. Murthy, K., Wadsworth, P. (2005). Myosin-II-dependent localization and dynamics of F-actin during cytokinesis. *Curr. Biol.* 15, 724–31.
160. Kondo, T., Hamao, K., Kamijo, K., Kimura, H., Morita, M., Takahashi, M., et al. (2011). Enhancement of myosin II/actin turnover at the contractile ring induces slower furrowing in dividing HeLa cells. *Biochem. J.* 435, 569–76.
161. Uehara, R., Goshima, G., Mabuchi, I., Vale, R.D., Spudich, J.A., Griffis, E.R. (2010). Determinants of myosin II cortical localization during cytokinesis. *Curr. Biol.* 20, 1080–5.
162. Zhang, W., Robinson, D.N. (2005). Balance of actively generated contractile and resistive forces controls cytokinesis dynamics. *Proc. Natl. Acad. Sci. U. S. A.* 102, 7186–91.
163. Ma, X., Kovacs, M., Conti, M. a., Wang, a., Zhang, Y., Sellers, J.R., et al. (2012). Nonmuscle myosin II exerts tension but does not translocate actin in vertebrate cytokinesis. *Proc. Natl. Acad. Sci.* 109, 4509–14.
164. Bidone, T.C., Tang, H., Vavylonis, D. (2014). Dynamic Network Morphology and Tension Buildup in a 3D Model of Cytokinetic Ring Assembly. *Biophys. J.* 107, 2618–28.
165. Underhill, P.T., Doyle, P.S. (2004). On the coarse-graining of polymers into bead-spring chains. *J. Nonnewton. Fluid Mech.* 122, 3–31.
166. Behrmann, E., Müller, M., Penczek, P.A., Mannherz, H.G., Manstein, D.J., Raunser, S. (2012). Structure of the rigor actin-tropomyosin-myosin complex. *Cell.* 150, 327–38.
167. Gauger, E., Stark, H. (2006). Numerical study of a microscopic artificial swimmer. *Phys. Rev. E - Stat. Nonlinear, Soft Matter Phys.* 74, 1–10.
168. Friend, J.E., Sayyad, W.A., Arasada, R., McCormick, C.D., Heuser, J.E.,

- Pollard, T.D. (2018). Fission yeast Myo2: Molecular organization and diffusion in the cytoplasm. *Cytoskeleton*. 75, 164–73.
169. Howard, J. (1997). Molecular motors : structural adaptations to cellular functions. *Nature*. 389, 561–7.
 170. Eng, K., Naqvi, N.I., Wong, K.C.Y., Balasubramanian, M.K. (1998). Rng2p, a protein required for cytokinesis in fission yeast, is a component of the actomyosin ring and the spindle pole body. *Curr. Biol*. 8, 611–21.
 171. Takaine, M., Numata, O., Nakano, K. (2009). Fission yeast IQGAP arranges actin filaments into the cytokinetic contractile ring. *EMBO J*. 28, 3117–31.
 172. Zimmermann, D., Homa, K.E., Hocky, G.M., Pollard, L.W., De La Cruz, E.M., Voth, G.A., et al. (2017). Mechanoregulated inhibition of formin facilitates contractile actomyosin ring assembly. *Nat. Commun*. 8, 1–12.
 173. Bryant, D., Clemens, L., Allard, J. (2017). Computational simulation of formin-mediated actin polymerization predicts homologue-dependent mechanosensitivity. *Cytoskeleton*. 74, 29–39.
 174. Hayakawa, K., Tatsumi, H., Sokabe, M. (2011). Actin filaments function as a tension sensor by tension-dependent binding of cofilin to the filament. *J. Cell Biol*. 195, 721–7.
 175. Claessens, M.M.A.E., Bathe, M., Frey, E., Bausch, A.R. (2006). Actin-binding proteins sensitively mediate F-actin bundle stiffness. *Nat. Mater*. 5, 748–53.
 176. Fritzsche, M., Charras, G. (2015). Dissecting protein reaction dynamics in living cells by fluorescence recovery after photobleaching. *Nat. Protoc*. 10, 660–80.
 177. Mogilner, A., Manhart, A. (2016). Agent-based modeling: case study in cleavage furrow models. *Mol. Biol. Cell*. 27, 3379–84.

8. Appendix

8.1. Estimation of observed changes in LAGFP fluorescence from changes in the cellular ratio of [F-actin]:[G-actin]

We previously discussed experiments where we used LAGFP fluorescence as an indicator of the amount of actin that is localised to the actomyosin ring, to provide a comparison between rings in WT and *adf1*-M3 cells (section 3.13). However, because we are using a fluorescently tagged actin binding protein, rather than fluorescently tagged actin itself (because this does not incorporate into the ring), this means that changes in the measured LAGFP fluorescence will not necessarily be proportional to changes in the amount of actin within a given cellular structure.

We can perform a simple calculation to illustrate this, using the previously measured dissociation constants of the LifeAct peptide [143]: LifeAct binds to both F- and G-actin within the cell, and there are separate dissociation constants for each of these processes. The equation for the dissociation of LifeAct from G-actin is

$$K_d^G = L_u G_u / L_G, \quad (A1)$$

whilst for the dissociation of LifeAct from F-actin, the equation is

$$K_d^F = L_u F_u / L_F. \quad (A2)$$

Here, K_d^G (K_d^F) is the dissociation constant of LifeAct from G-actin (F-actin), L_u is the concentration of unbound LifeAct peptide, G_u (F_u) is the concentration of G-actin (F-actin) that is not bound to LifeAct, and L_G (L_F) is the concentration of Lifeact that is bound to G-actin (F-actin).

For the values of G_u and F_u , we can make the following substitutions:

$$G_u = G_{tot} - L_G, \quad (A3)$$

$$F_u = F_{tot} - L_F, \quad (A4)$$

where G_{tot} and F_{tot} are the concentrations of the total amount of G- or F-actin that exists in any state (i.e. bound or unbound) in the cell. Additionally, we can also make the substitution

$$L_u = L_{tot} - L_G - L_F = A_{tot} - L_G - L_F, \quad (A5)$$

where L_{tot} is the concentration of the total amount of LifeAct within the cell, which in our cells is equal to the concentration of total amount of actin in the cell, A_{tot} , because the LAGFP construct is expressed under the *act1* (the *S. pombe* actin gene) promoter.

Substituting equations A3, A4, and A5 into equations A1 and A2, we arrive at

$$K_d^G = (A_{tot} - L_G - L_F)(G_{tot} - L_G)/L_G, \quad (A6)$$

$$K_d^F = (A_{tot} - L_G - L_F)(F_{tot} - L_F)/L_F. \quad (A7)$$

With equations A6 and A7, we can now consider a couple of potential conditions for the values of G_{tot} and F_{tot} , and consider how the values of L_G and L_F vary between these conditions. For our first condition, we can consider a cell where 75% of the total cellular actin is in the G-actin state, and 25% is in the F-actin state (i.e. $G_{tot} = 0.75A_{tot}$ and $F_{tot} = 0.25A_{tot}$), and for our second condition we can consider a cell where the amount of G-actin and F-actin is equal (i.e. $G_{tot} = F_{tot} = 0.5A_{tot}$).

Substituting these conditions into equations A6 and A7, and using values of $A_{tot} = 63.2 \mu\text{M}$ [64], $K_d^g = 0.07 \mu\text{M}$, and $K_d^f = 2 \mu\text{M}$ [143], the only unknowns we are left with are L_G and L_F , which means the pair of equations can be solved simultaneously, using the MATLAB function

‘fsolve’, in order to calculate the corresponding values of L_G and L_F .

For our first condition, we arrive at values of $L_G = 46.8 \mu\text{M}$ and $L_F = 11.3 \mu\text{M}$, whilst for the second condition we get values of $L_G = 31.3 \mu\text{M}$ and $L_F = 24.8 \mu\text{M}$. In other words, doubling the amount of F-actin leads to an apparent increase in the fluorescence signal by a factor of ~ 2.2 (or conversely, halving the amount of F-actin would lead to an apparent decrease in LAGFP fluorescence in F-actin structures by a factor of 2.2). Therefore, using LAGFP as a reporter for the amount of F-actin will tend to overestimate the relative differences in the amount of F-actin between different cells. Because it is not currently possible to differentiate between the signal from unbound LifeAct and G-actin bound LifeAct in fluorescence microscopy experiments, there is no way to correct for this. Therefore, caution must be used when using LifeAct to compare differences in F-actin concentrations between cells where there is a large difference in the ratio of G-actin to F-actin (Figure 3.6A).